Hydrothermal Synthesis and Compositional Engineering of Lithium Iron Orthosilicate as Li-Ion Battery Cathode

Yan Zeng

Department of Mining and Materials Engineering

McGill University, Montreal

November 2019

A thesis submitted to McGill University in partial fulfillment of the requirements of the degree of Doctor of Philosophy

Abstract

In this thesis, lithium iron orthosilicate, Li_2FeSiO_4 (LFS), is synthesized, characterized, and evaluated electrochemically to investigate its capability as a cathode material for Li-ion batteries. Hydrothermal synthesis is employed to produce LFS particles with tailored properties aiming to meet the specifications of Li-ion cathodes. Compositional engineering via doping and non-stoichiometry is exploited on the pursuit of preferable electrochemical performance.

Crystallization mechanism behind hydrothermal formation of LFS is revealed from time-resolved information on structure, composition and morphology via extensive *ex situ* characterizations. X-ray diffraction refinement combined with compositional analyses indicate a gradual transformation from amorphous hydrolysis products of Fe and Si to LFS crystallized in orthorhombic crystal system with space group $Pmn2_1$. Particle size can be varied effectively in the nanometer- to micrometer-range by changing the precursor concentrations, which is attributed to the role of Li activity in adjusting supersaturation and thus kinetics of nucleation and crystal growth. The addition of a complexing agent EDTA is utilized to regulate the activity of Fe, which consequently helps to avoid forming iron oxides and reduce Li-Fe antisite defects in LFS matrix. EDTA is also found to promote the formation of unique hollow mesocrystals that show promise in enhancing Li storage capacity. Electron microscopical characterizations suggest that after initial crystallization, LFS nanoparticles undergo self-assembly via nearly-oriented attachment and evolve to hollow mesocrystals following the Ostwald ripening rule.

The viability of partial substituting into Fe several divalent cations in $Pmn2_1$ LFS is investigated using both first-principles calculations and hydrothermal synthesis. The formation of Co^{2+}-doped $Li_2Fe_{0.94}Co_{0.06}SiO_4$ (CoLFS) is predicted to be energetically favorable, confirmed by successful hydrothermal synthesis. Electrochemical and spectroscopic characterizations on pristine and cycled electrodes are applied to investigate the effect of Co doping on electrochemical properties of LFS. Substitution of Co in LFS is found to enable faster phase transformation to the electrochemically induced phase (inverse $Pmn2_1$) and forms a less resistant and more uniform fluorine-rich cathode-electrolyte interphase (CEI) layer that protects the bulk particle from detrimental reactions with the electrolyte. As a result, Co^{2+}-doped LFS displays enhanced reversibility with 95% capacity retention after 50 cycles as compared to the undoped LFS with

only 80% retention. In the meantime, Mg^{2+}, although can be incorporated into LFS lattice, results in even worse capacity retention. Ni^{2+} or Sr^{2+}-substituted $Pmn2_1$ LFS could not be synthesized due to their high formation energies compared to their competing solid phases.

The effect of non-stoichiometry on crystal structure, electronic structure and Li transport kinetics of LFS is investigated through a combined experimental and computational study. Non-stoichiometric $Pmn2_1$ LFS with up to 8% Fe excess are successfully synthesized by controlled hydrothermal synthesis. In addition to the higher electron capacity from the accessible Fe^{2+}/Fe^{3+} redox couple, the presence of excess Fe enhances the intercalation kinetics compared to the stoichiometric composition. The enhanced kinetics are rationalized by the introduction of the $Fe_{Li}^{\bullet}$ + V_{Li}' defect pair and new electron conducting states from the creation of local Fe–O–Fe configurations. Moreover, the Fe-rich structure facilitates Fe migration to Li-site due to lower energy barrier than stoichiometric LFS, hence leading to faster phase transformation from $Pmn2_1$ towards the cycled inverse $Pmn2_1$. Galvanostatic charge-discharge measurements show that Fe-rich LFS delivers higher capacity than the stoichiometric LFS from low to high current rates, for example 161.8 mA h g^{-1} versus 128.9 mA h g^{-1} at 0.02 C.

Résumé

Dans cette thèse, l'orthosilicate de fer et de lithium, Li_2FeSiO_4 (LFS), est synthétisé, caractérisé et évalué par voie électrochimique afin d'étudier ses capacités en tant que matériau de cathode pour les batteries Li-ion. L'approche hydrothermale est utilisée pour la synthèse de particules de LFS ayant des propriétés répondant aux spécifications des cathodes Li-ion. Le dopage et la synthèse non-stœchiométrique sont exploités afin d'obtenir des performances électrochimiques compétitives.

Entre autres, l'analyse par diffraction des rayons X combinée aux informations sur la composition chimique ont dévoilé une transformation graduelle des composés amorphes de Fe et de Si provenant de l'hydrolyse des cristaux de LFS adoptant une structure orthorombique selon une lattice de type $Pmn2_1$. La variation de la concentration des précurseurs influence la taille des particules, variant de nanomètrique à micrométrique. Ce phénomène est attribué à la contribution de l'activité du Li pour moduler la sursaturation et, par le fait même, la cinétique de nucléation et de croissance des cristaux. L'ajout de l'agent complexant EDTA permet la régulation de l'activité du fer, ce qui par conséquence évite la formation d'oxydes de fer qui compétitionnent avec le LFS pour l'obtention du fer. L'EDTA réduit également l'apparition d'anti-sites dans la structure du LFS et promeut la formation de méso-cristaux creux ayant une capacité d'emmagasinage des ions lithium très prometteuse. La caractérisation par microscopie électronique suggère que les nano-particules de LFS s'assemblent spontanément en attachements quasi-orientés, puis évoluent en meso-cristaux poreux suivant le principe de maturation d'Ostwald.

Les travaux de recherche ont aussi évalué, par les calculs thermodynamiques et l'expérimentation, la possibilité de substituer partiellement les atomes de Fe de la phase LFS $Pmn2_1$ par divers cations divalents. Ainsi, la formation de $Li_2Fe_{0.94}Co_{0.06}SiO_4$ (CoLFS) par dopage au Co^{2+}, prédit énergétiquement favorable selon la thermodynamique, a été réalisée avec succès par la synthèse hydrothermale. Il a été démontré que la substitution par le Co permet une transformation de phase plus rapide vers la phase électrochimique enduite ($Pmn2_1$ inversée) et forme une couche interfaciale cathode-électrolyte (CEI) riche en fluor plus uniforme et moins résistante qui protège les particules de réactions néfastes avec l'électrolyte. Comme résultats, le LFS dopé au Co^{2+} démontre une meilleure réversibilité avec une rétention de capacité de 95%

après 50 cycles comparé au non-dopé (80% de rétention). D'autres parts, l'ion Mg^{2+}, même si il peut être incorporé à la structure du LFS, réduit la rétention de capacité alors que les phases LFS *Pmn*2_1 substituées Ni^{2+} ou Sr^{2+} n'ont pu être synthétisées en raison de leur trop haute énergie de formation.

Ainsi, un LFS *Pmn*2_1 non-stoechiométrique ayant un excès d'au plus 8% de Fe a été synthétisé par voie hydrothermale avec succès. En plus des capacités électroniques plus élevées imputées au couple redox Fe^{2+}/Fe^{3+}, le fer en excès améliore la cinétique d'intercalation. Cette cinétique améliorée est rationalisée par l'introduction des paires de défauts $Fe_{Li}^{\bullet} + V_{Li}'$ et de nouveaux états conducteurs d'électrons à partir de la création de configurations Fe–O–Fe locales. De plus, la structure riche en Fe facilite la migration de Fe vers le site de Li en raison d'une barrière d'énergie inférieure à celle du LFS stœchiométrique, conduisant ainsi à une transformation de phase plus rapide de la phase *Pmn*2_1 vers la phase inverse cyclée *Pmn*2_1. Les mesures de charge-décharge galvanostatiques montrent que le système LFS riche en Fe offre une capacité supérieure à celle du système LFS stœchiométrique pour des courants faibles à élevés, atteignant par exemple 161,8 mA h g^{-1} contre 128,9 mA h g^{-1} à 0,02 C.

Acknowledgements

First of all, I am deeply grateful to my advisor, Professor George P. Demopoulos, for his support and mentoring during my PhD study. This thesis would not have been possible without his guidance and inspiration. I also acknowledge the financial support from McGill Engineering International Doctoral Awards (MEITA), the McGill Sustainability Systems Initiative (MSSI), and Natural Sciences and Engineering Research Council (NSERC).

I thank Professor Raynald Gauvin and Mr. Nicolas Brodusch for their support and invaluable discussions on scanning electron microscopic analysis. I thank Mr. David Liu, Ms. Isabelle Richer, Dr. Lihong Shang, Mr. Petr Fiurasek for their technical training and assistance on various characterization techniques. I am grateful to Professor Tomislav Friščić and Dr. Hatem Titi for providing me the access to their XRD instrument and the help on XRD data analysis. I am thankful to Professor De-Tong Jiang at University of Guelph for arranging the beamline time, guidance at Canadian Light Source, and fruitful discussion on data interpretation of synchrotron XRD data.

I am grateful to Professor Dominic H. Ryan in McGill Physics for teaching me the measurement and interpretation of Mössbauer spectroscopy and the opportunity to participate in Canadian Neutron Diffraction Summer School. I am also thankful for our collaboration on *in operando* Mössbauer experiment and I particularly thank Mr. Richard Talbot for his time and great help on device design.

I thank McGill Materials Engineering administrative staff, Ms. Barbara Hanley, Ms. June Persaud, Ms. Leslie Bernier, and Ms. Heather Holowathy for their kind assistance during my PhD study in this department.

I acknowledge the help I have received from Dr. Fuqiang Guo, Dr. Zhuoran Wang, Marianna Uceda, Christine Wei, Rana Yekani, Konstantina Chalastara, Han Wang, and François Larouche in HydroMET group and I appreciate the great time they have shared with me in the lab and in Montreal. I am very grateful to Dr. Hsien-Chieh (Jay) Chiu for his enormous assistance, guidance, insights, and countless hours that he has dedicated to help me and other group members.

I thank my husband for his support and encouragement during my PhD study and his passion in science that has influenced me greatly. I thank my parents for their mental and financial support, their unconditional love to their daughter, and I thank my younger brother for looking after them during my study abroad for over four years without going home once.

November 2019, Montreal

Yan Zeng

Foreword

This thesis is based on a manuscript-based format that is offered by McGill University as an alternative to the traditional thesis format. Chapter 3 of this thesis has been published, whereas Chapters 4 and 5 have been submitted or are been submitted to peer-reviewed journals.

Authorship contributions

Yan Zeng, Hsien-Chieh Chiu, Majid Rasool, Nicolas Brodusch, Raynald Gauvin, De-Tong Jiang, Dominic H. Ryan, Karim Zaghib, George P. Demopoulos. Hydrothermal crystallization of *Pmn*2_1 Li_2FeSiO_4 hollow mesocrystals for Li-ion cathode application. *Chemical Engineering Journal* **2019**, 359: 1592–1602. DOI: 10.1016/j.cej.2018.11.013.

Yan Zeng, Hsien-Chieh Chiu, Bin Ouyang, Jun Song, Karim Zaghib, George P. Demopoulos. Unveiling the mechanism of improved capacity retention in *Pmn*2_1 Li_2FeSiO_4 cathode by cobalt substitution. *Journal of Materials Chemistry A* **2019**, *7* (44): 25399-25414. DOI: 10.1039/C9TA10287F.

Yan Zeng, Hsien-Chieh Chiu, Bin Ouyang, Karim Zaghib, George P. Demopoulos. Defect engineering of Fe-rich orthosilicate cathode materials with enhanced Li-ion intercalation capacity and kinetics, under review. (*Submitted to ACS Applied Energy Materials on September 23, 2019, MS# ae-2019-01869m*)

All manuscripts have been submitted for publication under the supervision of Professor Demopoulos as the corresponding author. The author of this thesis has designed the experiments, carried out material synthesis, detailed characterizations and electrochemical measurements. Dr. Hsien-Chieh Chiu offered guidance on data interpretation and edited manuscripts. Mr. Nicolas Brodusch performed in-depth scanning electron microscopy characterizations. Dr. Bin Ouyang

assisted with Density-Functional Theory calculations with guidance from Professor Jun Song. Professor Dominic H. Ryan performed experimental measurements and data processing on Mössbauer spectroscopy. Professor De-Tong Jiang arranged and guided synchrotron X-ray diffraction at Canadian Light Source and data interpretation. Dr. Karim Zaghib and Professor Raynald Gauvin offered fruitful discussions.

I hereby give copyright clearance for the inclusion of the above papers, of which I am corresponding author, into the Ph.D. dissertation of Yan Zeng.

Signature: _____ Date: _____

Prof. Dr. George P. Demopoulos

Department of Mining and Materials Engineering

McGill University

Montréal, Québec

Table of Contents

List of Figures

List of Tables

List of Symbols and Abbreviations

Symbols

γ	surface free energy per unit area
γ_{net}	Net effective surface free energy
η	Overpotential
θ	Angle of incidence
λ	wavelength
μ_{Li}	Chemical potential of Li
v	Molecular volume
υ	Scan rate
A	Pre-exponential factor, or
	Surface area
$[A_i]$	Activity of an aqueous specie Ai
C_S	Critical supersaturation
ΔC_{Li^+}	Change in concentration of Li^+
D_{Li^+}	Chemical diffusion coefficient of Li^+
E	Specific energy
E_t	Total energy
$E(t)$	Transient voltage during time t in GITT
$E(x)$	Voltage change with concentration x in GITT
F	Faraday constant
$Fe^{\bullet}_{Li} + V'_{Li}$	Defect pair of an Fe-Li antisite and a Li vacancy
ΔG	Total free energy change
ΔG_{crit}	Critical energy
ΔG_S	Surface free energy change
ΔG_v	Bulk free energy change per unit volume
ΔG_V	Bulk free energy change
I	Current
I_p	Peak current
J^{het}	Heterogeneous nucleation rate

J^{homo}	Homogenous nucleation rate
K_{f}	Formation constant
K_{SP}	Solubility product
L	Length
$\mathrm{Li}'_{\mathrm{Fe}} + \mathrm{Li}^{\bullet}_{\mathrm{i}}$	Defect pair of an Li-Fe antisite and an interstitial Li
M_w	Molecular weight
Q	Specific capacity
R_i	Internal resistance
R_{ct}	Charge-transfer resistance
R_{PT}	Phase transformation resistance
R_{s}	Interface resistance
R_{wp}	Weighted reliability factor
S	Supersaturation, or
	Specific surface area
T	Temperature
V	Voltage, or
	unit cell volume
V_{M}	Molar volume
V_{OC}	Open circuit voltage
Z	Charge number
a	Lattice parameter
b	Lattice parameter
c	Lattice parameter
d	Lattice spacing
f	Structural factor, or
	Recoil-free factor
k_{B}	Boltzmann's constant
k_i	Stoichiometric coefficient
n	Number of charges
r	Radius of a sphere
r_{c}	Critical nuclei size
t	Time

x	Concentration

Abbreviations

AA	Ascorbic acid
AB	Acetylene black
AFM	Atomic force microscopy
BET	Brunauer–Emmett–Teller
BPEI	Branched polyethylenimine
C	Carbon
CBM	Conduction band minimum
CE	Coulombic efficiency
CEI	Cathode electrolyte interphase
ci-NEB	climbed image Nudged Elastic Band
CNF	Carbon nanofiber
CPA	Crystallization by particle attachment
CTAB	Hexadecyl trimethyl ammonium bromide
CV	Cyclic voltammetry
CoLFS	$Li_2Fe_{0.94}Co_{0.06}SiO_4$
DEC	Diethyl carbonate
DFT	Density functional theory
DMC	Dimethyl carbonate
DOD	Depth of discharge
EC	Ethylene carbonate

EDS	Energy-dispersive X-ray spectroscopy
EDTA	Ethylenediaminetetraacetic acid
EIS	Electrochemical impedance spectroscopy
ESR	X-band electronic spin resonance
EVs	Electric vehicles
FTIR	Fourier transform infrared
G	Graphene
GGA-PBE	Generalized gradient approximation Perdew−Burke−Ernzerhof
GITT	Galvanostatic intermittent titration technique
ICP	Inductively coupled plasma
LCO	$LiCoO_2$
LFP	$LiFePO_4$
LFS	Li_2FeSiO_4
LiBOB	Lithium bis(oxalato)borate
LIBs	Lithium-ion batteries
LMO	$LiMn_2O_4$
IS	Isomer shifts
MEPs	Minimum energy paths
MgLFS	$Li_2Fe_{0.94}Mg_{0.06}SiO_4$
MWCNT	Multi-wall carbon nanotubes
NCA	$LiNi_{0.8}Co_{0.15}Al_{0.05}O_2$
NMC	$LiNi_xMn_yCo_{(1-x-y)}O_2$
NMP	N-methyl pyrrolidinone

OCV	Open circuit voltage
PAW	Projector augmented wave
PC	Polycarbonate
PDOS	Projected density of states
PEDOT	Poly(3,4-ethylenedioxythiophene)
PTFE	Polytetrafluoroethylene
PVDF	Polyvinylidene fluoride
QS	Quadrupole splitting
rGO	Reduced graphene oxide
SAED	Selected area electron diffraction
SDBS	Sodium dodecyl benzene sulfonate
SEI	Solid electrolyte interphase
SEM	Scanning electron microscopy
SOC	State of charge
TEM	Transmission electron microscopy
TEOS	Tetraethyl orthosilicate
TM	Transition metal
VASP	Vienna *ab initio* simulation package
VBM	Valence band maximum
XANES	X-ray absorption near edge structure
XPS	X-ray photoelectron spectroscopy
XRD	X-ray diffraction

Chapter 1. Introduction

1.1 Motivation

Rechargeable Li-ion batteries (LIBs), with their exceptional ability to store energy per given weight or volume, have advanced widespread technologies from portable electronic devices to electric vehicles (EVs), and to greener storage systems for renewable solar and wind energies.[1-4] The LIBs market has grown tremendously over the last three decades and is expected to increase even more rapidly within the next years with the increasing market segment of EVs.[1] Moreover, the global grid-scale energy storage systems is predicted to grow thirteenfold over the next six years, from a 12 GW h market in 2018 to a 158 GWh market in 2024 ($71 billion).[5]

In LIBs, lithium ions are pulled out of the battery's cathode (positive electrode) during the charge process and returned to the cathode when power is drained.[2] The cathode is the key element that determines the performance of a LIB and its fabrication cost.[6] To meet the demands of long lifetime, short charging time, high safety, and low cost for application in diverse energy storage technologies, the cathode materials are desired to have high energy density, good power capability, long cycle lifetime, good stability, and made by inexpensive and abundant elements.[7] Since the first commercialization of LIBs in 1990,[8-9] the search for better cathode materials has drawn intensive attention in academia and industry. At present, the commercialized LIBs are limited to a few types of cathode materials, including layered $LiCoO_2$ (LCO), $LiNi_xMn_yCo_{(1-x-y)}O_2$ (NMC), $LiNi_{0.8}Co_{0.15}Al_{0.05}O_2$ (NCA), spinel $LiMn_2O_4$ (LMO), and olivine $LiFePO_4$ (LFP), but none of these materials can meet all the criteria for future energy storage solutions.[3]

LCO delivers an energy density of about 600 W h kg^{-1}, but the major drawbacks of LCO are the high cost and toxicity of cobalt as well as poor thermal stability that can induce explosion and fire hazard.[10-11] By partially replacing cobalt with Ni/Mn or Al in the layered oxide structure, the deployments of NMC and NCA have reduced the cost and enhanced the energy density but safety is still an issue to be addressed.[12] LMO has more profound cost advantage over LCO but its low energy density and short cycling life do not allow broad applications.[13-14] Different to the oxide compounds, LFP is built on the polyanionic structure Upon overcoming the intrinsic poor electronic conductivity via conductive carbon coating[16] and nano-structuring[17], LFP soon became a sustainable cathode material of choice, which shares a large portion of the whole LIBs market

(36% in 2016).[1] Yet, even the energy density of LFP has been optimized towards its theoretical limit (i.e. 560 W h kg^{-1}), this energy density is relatively low and cannot meet the demand for long-range EVs.

It was the need to increase the limited energy density of LFP that motivated Michel Armand supported by Hydro-Québec to initiate the study on the silicate family Li_2MSiO_4 (M = Mn, Fe, Co) as alternative cathode materials.[18-19] Li_2MSiO_4 have two lithium per formula unit, which means double theoretical specific capacity compared with their phosphate counterpart (i.e. ~333 mA h g^{-1} vs. 170 mA h g^{-1}) if both lithium ions are extracted. The silicate framework makes the release of oxygen more difficult and thus provides enhanced stability upon charge-discharge. In the silicate family, Li_2MnSiO_4 has suffered from irreversible structural distortion from MnO_4 tetrahedra during initial cycling, while Li_2CoSiO_4 contains expensive Co and requires high voltage that exceeds the safety window of current electrolytes.[20] Li_2FeSiO_4 has drawn the most attention among the silicates not only because of the abundance of Fe and the better stability compared to Li_2MnSiO_4, but also due to the possibility in utilizing the second Li at a reasonably high voltage (~4.8 V vs. Li^+/Li), which would lead to an energy density of about 1120 W h kg^{-1}.[21] Yet, practical application of Li_2FeSiO_4 has been hampered by low electronic and ionic conductivities and the difficulty in extracting reversibly more than one Li.[20]

To pursue the full potential of LFS as a LIB cathode material, synthesis is the key part because it controls the properties of the particles and hence the electrochemical performance. In this context, hydrothermal synthesis conducted in pressure reactors is a favorable approach as it can produce nanoparticles with tunable stoichiometry, purity, morphology, and particle size. Hydrothermal synthesis can be performed on a large scale at relatively reasonable costs and more importantly in an environmentally benign manner.[22] A featured example is the hydrothermal production of high quality $LiFePO_4$ with tunable particle size and morphology, which enabled the achievement of its full electrochemical potential and commercial success.[23] In the meantime, compositional engineering via doping and off-stoichiometry have been proved to be effective strategies to tune the intrinsic properties of intercalation compounds.[6, 24] Thus there exists the opportunity to apply these two compositional designs also to LFS in order to enhance its electrochemical performance.

1.2 Objectives

The overall goal of this thesis is to design, synthesize, and optimize Li_2FeSiO_4-based compounds as cathode materials for LIBs with the focus on a low-temperature orthorhombic phase (*Pmn*2_1 space group) using hydrothermal synthesis. More specifically, the objectives of this thesis are to

1. Synthesize Li_2FeSiO_4 by hydrothermal method with controlled properties including purity, composition, particle size, morphology, and defects and advance the insights into the crystallization mechanism.

2. Search for promising cation dopants and investigate the cation doping effect on improving the electrochemical properties of Li_2FeSiO_4.

3. Optimize the electrochemical properties of Li_2FeSiO_4 by Fe-rich compositional design and elucidate the role of the excess Fe in alternating the electronic structure and Li storage capability.

1.3 Thesis Organization

This thesis is presented in six chapters, followed by Appendices of supporting information. Chapter 1 gives a general introduction to the motivation and objectives of this thesis. Chapter 2 provides a literature review on the fundamentals of LIBs with the focus on cathode materials, present research status and issues of LFS as an emerging cathode material, and the basics of hydrothermal synthesis accompanied by its application in preparing materials for LIB cathodes.

In Chapter 3, hydrothermal synthesis and property optimization of LFS particles are demonstrated. The crystal formation mechanism is unveiled via extensive *ex situ* characterizations. Key synthesis parameters are manipulated to control purity, particle size, morphology, and defects. The electrochemical activity of the as-synthesized LFS is briefly evaluated.

In Chapter 4, doping with several divalent cations are attempted by hydrothermal synthesis, guided by a first-principle calculations-enabled pre-screening. The enhancement in electrochemical performance via cobalt doping is discussed.

In Chapter 5, synthesis and electrochemistry of non-stoichiometric LFS are discussed. The enhancement by Fe-rich compositional design are rationalized to the role of excess Fe in altering the electron capacity, local bonding environment, and Li transport kinetics.

Chapter 6 summarizes the overall work with conclusions and suggestions for future investigations.

1.4 References

1. Matthew, L.; Jun, L.; Zhongwei, C.; Khalil, A., 30 Years of Lithium‐Ion Batteries. *Advanced Materials* **2018,** *0* (0), 1800561.

2. Goodenough, J. B., How we made the Li-ion rechargeable battery. *Nature Electronics* **2018,** *1* (3), 204-204.

3. Blomgren, G. E., The Development and Future of Lithium Ion Batteries. *Journal of The Electrochemical Society* **2017,** *164* (1), A5019-A5025.

4. Larcher, D.; Tarascon, J. M., Towards greener and more sustainable batteries for electrical energy storage. *Nature Chemistry* **2015,** *7* (1), 19-29.

5. John, J. S., Global Energy Storage to Hit 158 Gigawatt-Hours by 2024, Led by US and China. *GTM: A Wood Mackenzie Business* 2019.

6. Nitta, N.; Wu, F.; Lee, J. T.; Yushin, G., Li-ion battery materials: present and future. *Materials Today* **2015,** *18* (5), 252-264.

7. Kostiantyn Turcheniuk; Dmitry Bondarev; Vinod Singhal; Yushin, G., Ten years left to redesign lithium-ion batteries. *Nature* **2018,** *559*, 467-470.

8. Mizushima, K.; Jones, P. C.; Wiseman, P. J.; Goodenough, J. B., Li_xCoO_2 ($0<x<1$): A new cathode material for batteries of high energy density. *Materials Research Bulletin* **1980,** *15* (6), 783-789.

9. Ozawa, K., Lithium-ion rechargeable batteries with $LiCoO_2$ and carbon electrodes: the $LiCoO_2$/C system. *Solid State Ionics* **1994,** *69* (3), 212-221.

10. Bang, H. J.; Joachin, H.; Yang, H.; Amine, K.; Prakash, J., Contribution of the Structural Changes of $LiNi_{0.8}Co_{0.15}Al_{0.05}O_2$ Cathodes on the Exothermic Reactions in Li-Ion Cells. *Journal of The Electrochemical Society* **2006,** *153* (4), A731-A737.

11. Schipper, F.; Erickson, E. M.; Erk, C.; Shin, J.-Y.; Chesneau, F. F.; Aurbach, D., Review—Recent Advances and Remaining Challenges for Lithium Ion Battery Cathodes: I. Nickel-Rich, $LiNi_xCo_yMn_zO_2$. *Journal of The Electrochemical Society* **2017,** *164* (1), A6220-A6228.

12. Whittingham, M. S., Ultimate limits to intercalation reactions for lithium batteries. *Chemical reviews* **2014,** *114* (23), 11414-11443.

13. Amatucci, G.; Tarascon, J.-M., Optimization of Insertion Compounds Such as $LiMn_2O_4$ for Li-Ion Batteries. *Journal of The Electrochemical Society* **2002,** *149* (12), K31-K46.

14. MacNeil, D. D.; Hatchard, T. D.; Dahn, J. R., A Comparison Between the High Temperature Electrode /Electrolyte Reactions of Li_xCoO_2 and $Li_xMn_2O_4$. *Journal of The Electrochemical Society* **2001,** *148* (7), A663-A667.

15. Zaghib, K.; Guerfi, A.; Hovington, P.; Vijh, A.; Trudeau, M.; Mauger, A.; Goodenough, J. B.; Julien, C. M., Review and analysis of nanostructured olivine-based lithium recheargeable batteries: Status and trends. *Journal of Power Sources* **2013,** *232*, 357-369.

16. Wang, J.; Sun, X., Understanding and recent development of carbon coating on $LiFePO_4$ cathode materials for lithium-ion batteries. *Energy & Environmental Science* **2012,** *5* (1), 5163-5185.

17. Lee, K. T.; Kan, W. H.; Nazar, L. F., Proof of Intercrystallite Ionic Transport in $LiMPO_4$ Electrodes (M = Fe, Mn). *Journal of the American Chemical Society* **2009,** *131* (17), 6044-6045.

18. Armand, M., Lithium insertion electrode materials based on orthosilicate derivatives. *U.S. Patent 6 085 015* **2000**.

19. Nytén, A.; Abouimrane, A.; Armand, M.; Gustafsson, T.; Thomas, J. O., Electrochemical performance of Li_2FeSiO_4 as a new Li-battery cathode material. *Electrochemistry Communications* **2005,** *7* (2), 156-160.

20. Islam, M. S.; Dominko, R.; Masquelier, C.; Sirisopanaporn, C.; Armstrong, A. R.; Bruce, P. G., Silicate cathodes for lithium batteries: alternatives to phosphates? *Journal of Materials Chemistry* **2011,** *21* (27), 9811-9818.

21. Ni, J.; Zhang, L.; Fu, S.; Savilov, S. V.; Aldoshin, S. M.; Lu, L., A review on integrating nano-carbons into polyanion phosphates and silicates for rechargeable lithium batteries. *Carbon* **2015,** *92*, 15-25.

22. Byrappa, K.; Adschiri, T., Hydrothermal technology for nanotechnology. *Progress in Crystal Growth and Characterization of Materials* **2007,** *53* (2), 117-166.

23. Chen, J., A Review of Nanostructured Lithium Ion Battery Materials via Low Temperature Synthesis. *Recent Patents on Nanotechnology* **2013**, *7* (1), 2-12.

24. Seo, D.-H.; Lee, J.; Urban, A.; Malik, R.; Kang, S.; Ceder, G., The structural and chemical origin of the oxygen redox activity in layered and cation-disordered Li-excess cathode materials. *Nature Chemistry* **2016,** *8*, 692.

Chapter 2. Literature Review

In this chapter, the fundamentals of Li-ion batteries and the most commonly used cathode materials are introduced. This is followed by a review of Li_2FeSiO_4 (LFS) as an emerging cathode material, with the focus on the preparation methods as well as structural and electrochemical properties. The final part of this chapter is concerned with the hydrothermal synthesis method, the crystallization theory behind this synthesis approach, and its application in preparation of cathode materials, particularly LFS.

2.1 Li-ion batteries

2.1.1 Working principles of Li-ion batteries

A battery is a device that stores electrical energy as chemical energy in the chemical bonds. It usually consists of several identical electrochemical cells that are interconnected in series and/or in parallel. Each cell is comprised of a positive electrode (cathode) and a negative electrode (anode) that are immersed in an electrolyte while kept apart by a separator. Li-ion batteries are rechargeable batteries that use lithium intercalation compounds as electrodes in which lithium ions can be inserted/extracted into/from the host matrix reversibly during charge/discharge without significant lattice change. Figure 2.1 shows the configuration of a typical Li-ion cell using $LiCoO_2$ as the cathode and graphite (represented as C_6) as the anode.[1] The cathode material is coated on aluminum foil while the anode material is coated on copper foil. The electrolyte consists a lithium salt, such as $LiPF_6$, dissolved in a nonaqueous solvent, such as mixed ethylene carbonate and dimethyl carbonate (EC/DMC). The separator is normally a porous material made by polyethylene that blocks electricity while allows lithium ions to travel through. During charge process, lithium ions are extracted from $LiCoO_2$, transport through the electrolyte and separator, and then intercalated into graphite. Simultaneously, electrons are donated by Co^{3+} in the cathode and transfer to the anode through the external circuit. During discharge, the reverse reactions occur. The two half-reactions in the Li-ion cell during charge can be described as:

$$\text{Cathode: } LiCoO_2 \rightarrow Li_{1-x}CoO_2 + x\ Li^+ + x\ e^- \quad (2.1)$$

$$\text{Anode: } y\ C_6 + x\ Li^+ + x\ e^- \rightarrow y\ Li_{x/y}C_6 \quad (2.2)$$

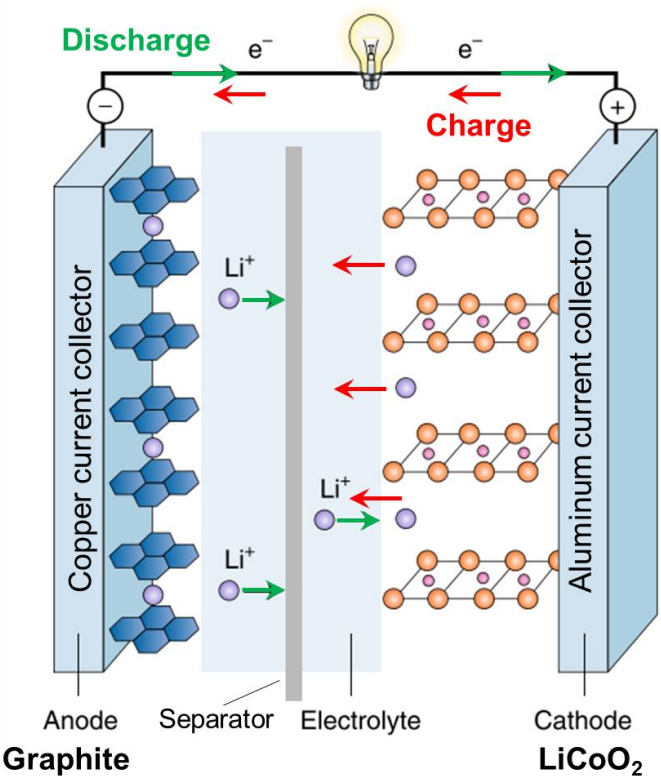

Figure 2.1. Schematic of a Li-ion cell with a graphite anode (left) and a $LiCoO_2$ cathode (right).[1] Lithium ions and electrons transport from the cathode to the anode during charge while in the opposite direction during discharge.

The choice of electrode materials is crucial for the performance of a Li-ion cell. Key properties of a Li-ion cell include voltage, specific capacity, energy density, power density, cycle lifetime, safety, and cost. These properties are highly correlated to the chemical composition and crystal/electronic structure of the electrode materials.

The open-circuit voltage (V_{OC}, V) of a cell is the voltage between the cell terminals with no current applied. V_{OC} is determined by the difference in the lithium chemical potential between the anode (μ_{Li}^{Anode}) and cathode ($\mu_{Li}^{Cathode}$):

$$V_{OC} = \frac{-\left(\mu_{Li}^{Cathode} - \mu_{Li}^{Anode}\right)}{nF} \tag{2.3}$$

where n is the number of charge (n = 1 for Li^+) and F is Faraday constant of 96,485 C mol^{-1}. V_{OC} increases with the state of charge (SOC) while decreases with the depth of discharge (DOD) for single-phase reactions.

Specific capacity (sometimes simplified as capacity) is the amount of charge that a cell contains in a unit weight, often expressed as Q in mA h g^{-1}. Based on Faraday's first law, Q is calculated by:

$$Q = \frac{nF}{M_w}\left(\frac{A \cdot s}{g}\right) \tag{2.4}$$

where M_w is the molecular weight (g mol^{-1}). Take Li_2FeSiO_4 as an example, the theoretical specific capacity delivered from 2 Li^+/f.u. is:

$$Q_{Li2FeSiO4} = \frac{2(mol)\times 96485(\frac{C}{mol})}{161.81(\frac{g}{mol})} \times \left(\frac{1000}{3600}\right) = 331.3(\frac{mA \cdot h}{g}) \tag{2.5}$$

Energy density or specific energy (E) is the energy per unit volume (W h L^{-1}) or per unit weight (W h kg^{-1}). The output energy density (E_{dis}) is determined by the discharge voltage (V_{dis}) and the specific discharge capacity (Q_{dis}):[2]

$$E_{dis} = \int_0^{Q_{dis}} V_{dis}(q)dq = \int_0^{t_{dis}} V_{dis}(q)I_{dis}dt \tag{2.6}$$

where q is the specific capacity, t is the discharge time, and I_{dis} is the constant current drawn from the cell in the galvanostatic mode. It should be noted that V_{dis} is distinct from V_{OC} due to the existence of internal resistance (R_i). This internal resistance lowers V_{dis} from V_{OC} by an overpotential (η).[2]

2.1.2 Cathode materials for Li-ion batteries

The positive electrode (cathode) is considered to be the bottleneck of the battery's performance due to its determinant role in energy density and the cost.[3] The cathode materials that are currently used in the market are $LiCoO_2$ (LCO), $LiNi_xMn_yCo_{(1-x-y)}O_2$ (NMC), $LiNi_{0.8}Co_{0.15}Al_{0.05}O_2$ (NCA), $LiMn_2O_4$ (LMO), and $LiFePO_4$ (LFP).[4] Figure 2.2 presents the world-wide market share of these cathode materials. As it is shown, NMC and LFP occupy a large share of the market with a total mass percentage of 62% in 2016 and are expected to grow to 65% in 2025.[5] Each cathode material has its own advantages and disadvantages, as summarized in Table 2.1.

The first commercialized Li-ion battery was made by $LiCoO_2$ as the cathode and graphite as the anode (as shown in Figure 2.1). LCO as a cathode was first invented by Goodenough et al.[6] in 1980 and commercialized by Sony Corporation in 1991[7]. The practical capacity of LCO is about

140 mA h g^{-1} (vs theoretical capacity of 270 mA h g^{-1}) at intercalation voltage of about 3.9 V (vs Li^+/Li).[7] LCO has high tap density which allows for high volumetric energy densities that is desired for small portable electronic devices. The major drawbacks of LCO include its poor thermal stability and the high cost of cobalt. LCO has a layered structure, as illustrated in Figure 2.3a, in which Li^+ transports in 2D planes. LCO is normally charged to a half-delithiated state (i.e. $Li_{0.5}CoO_2$) at a cut-off voltage of 4.2 V (vs Li^+/Li) in order to maintain a good cycling stability. Charging above 4.2 V can extract more Li^+ and deliver higher capacity but will also cause irreversible structural change, oxygen evolution, and electrolyte degradation, which ultimately leads to capacity fading and safety issues.[8-10]

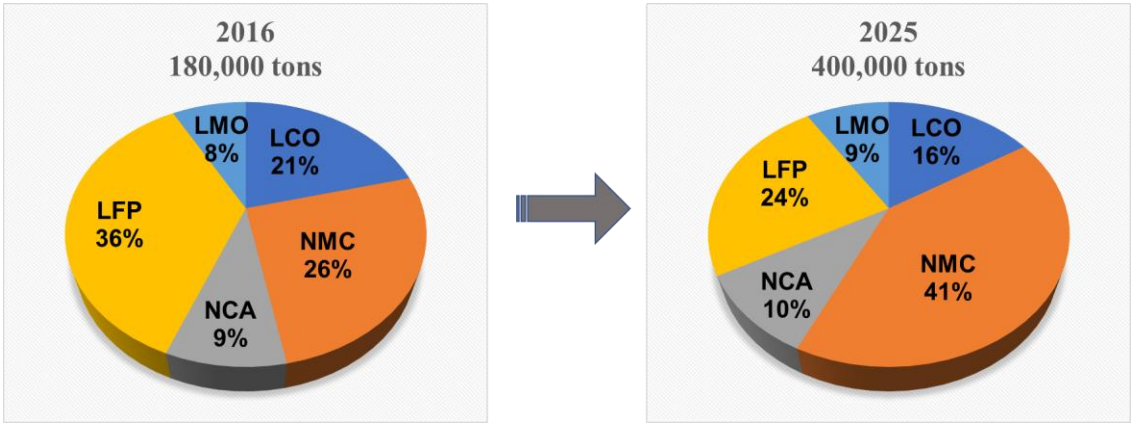

Figure 2.2. World-wide market shares (mass percentage) of Li-ions batteries in 2016 and forecasted to 2025. Bar charts were plotted based on the data reported in reference[5].

With the aim to reduce the cost, increase the energy density while improving the thermal stability of LCO, NMC was developed and has become one of the most advanced cathode materials in the present battery market.[11] NMC shares the same layered structure as LCO (Figure 2.3a). The ratio of Ni/Mn/Co can be varied and that leads to a series of NMC materials, such as NMC811 (Ni = 0.8, Mn = Co = 0.1) and NMC111 (Ni = Mn = Co = 1/3). Each transition metal plays different role in determining the electrochemical properties of the whole NMC materials.[12-14] In general, nickel provides most of the capacity via reversible Ni^{2+}/Ni^{3+} and Ni^{3+}/Ni^{4+} redox reactions. Cobalt prevents the undesired cation mixing between Ni^{2+} and Li^+ and provides additional capacity from Co^{3+}/Co^{4+} redox. Manganese remains electrochemically inert in Mn^{4+} and stabilizes the crystal structure especially when the cell is charged to a highly delithiated state; it also lowers the total cost. The challenge for NMC cathode materials is to optimize the composition to yield electrochemical properties that meet the requirements of specific applications. In recent years,

high-Ni NMC has been pursued due to its higher energy density. However, high-Ni content suffers from poor thermal stability and capacity fading.[15] Achieving higher energy density while keeping good cyclability remains a grand challenge for Ni-rich NMC.[13]

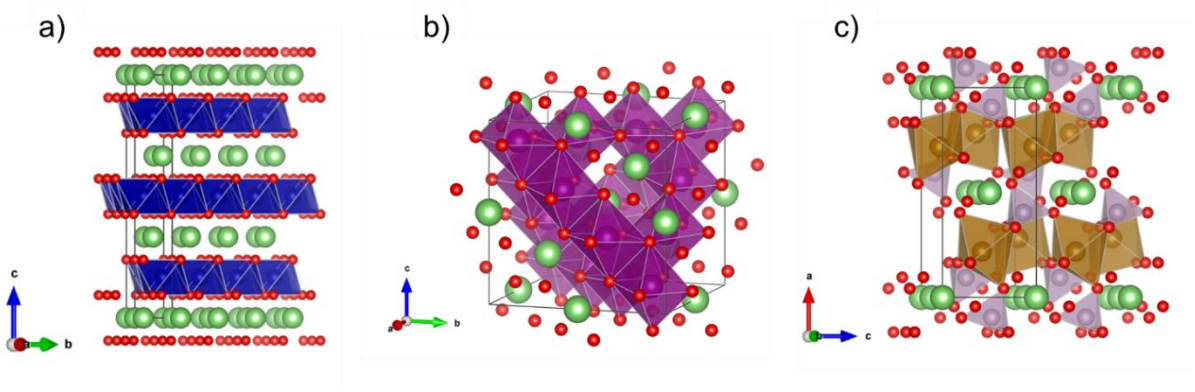

Figure 2.3. Crystal structure of (a) layered $LiCoO_2$ (trigonal S.G. $R\bar{3}m$), (b) spinel $LiMn_2O_4$ (cubic S.G. $Fd\bar{3}m$), and (c) olivine $LiFePO_4$ (orthorhombic S.G. *Pnma*). Colors represent: CoO_6 (blue), MnO_6 (dark purple), FeO_6 (brown), PO_4 (light purple), oxygen (red), and lithium (green). Crystal structures are drawn with the VESTA software.[33]

NCA is another popular layered oxide for LIBs. NCA usually has the composition of $LiNi_{0.8}Co_{0.15}Al_{0.05}O_2$.[16] It has been mostly manufactured by Panasonic and used in Tesla EVs. NCA has slightly higher energy density than NMC due to higher Ni content, but it also results in several drawbacks. The thermal stability of NCA is inferior than NMC's, except NMC811.[17] The surface of NCA particles is sensitive to moisture and CO_2 and can form insulating layers containing LiOH and Li_2CO_3.[18] Coating with resistive compounds such as SiO_2 has been investigated to overcome the surface sensitivity of NCA.[19]

LMO has the intrinsic cost advantage over LCO due to low cost manganese vs. expensive cobalt. It also has good thermal stability that ensures safety during usage. However, low energy density and poor cycle life have limited the application of LMO.[20-21] Mn tends to dissolve under the attack of HF acid produced by side reactions of $LiPF_6$, and the dissolved Mn ions would migrate and deposit on the anode, resulting in capacity loss.[22] In contrast to the layered oxides, LMO adopts a 3D spinel structure (see Figure 2.3b) with Mn occupying half of the octahedral sites while Li occupying one eighth of the tetrahedral sites in a cubic closed-packed (ccp) oxygen framework. Li can transport in 3D channels in spinel LMO, and this gives rise to the high-power capability of LMO.

LFP possesses excellent thermal stability thanks to the strong P—O bonds that prohibit the oxygen release and minimize the heat release which could occur in layered oxides.[23] The use of inexpensive and abundant iron instead of cobalt and/or nickel lowers the cost significantly. Bare LFP particles suffer from low ionic and electronic conductivities,[24-26] but this problem has been overcome via coating with a thin conductive carbon layer[27-28] combined with nanosizing[29]. Modified LFP has good cycle life and power capability, however, its low energy density due to a moderate voltage (3.4 V vs Li^+/Li) and low tap density originated from small particle sizes has hindered its application in areas where high energy density is required, such as portable electronics. Application of LFP in EVs is also limited. LFP has an olivine structure in orthorhombic *Pnma* space group, as shown in Figure 2.3c. Li and Fe occupy octahedral sites while P occupies tetrahedral sites in hexagonal closed-packed (hcp) oxygen framework. In LFP, Li^+ moves in an 1D trajectory along [010] direction.[30] Thus, the diffusion of Li^+ is highly sensitive to the defects and impurities in the [010] channels. The antisite defect (Fe on Li-site) has dramatic effect on the electrochemical performance of LFP.[31-32] Therefore, synthesis of defect and impurity-free LFP is a key to realize its capacity. Detailed reviews on the synthesis of LFP will be discussed in next section. During (de)lithiation, LFP undergoes a two-phase reaction and this results in a unique feature of a voltage plateau.

Table 2.1. Properties of cathode materials used in commerlized Li-ion batteries[4]

Cathode	Midpoint voltage (vs Li^+/Li, C/20)	Capacity (mA h g^{-1})	Advantages	Disadvantages	Applications
LCO	3.9	155	Long lifetime, good energy density	Poor thermal stability, cost	Portable electronics
NMC	3.8	160	Long lifetime, good energy and power, thermal stabiltiy	Patent issue	EVs, portable electronics, power tools
NCA	3.7	180	Good cycle life, energy, and power	Moderate thermal stability, moisture-sensitivity	EVs (Tesla)
LMO	4.0	100-120	Good thermal stability, good power capability, inexpensive	Low energy density, capacity fading	Power tools, electric motive power
LFP	3.4	160	Excellent thermal stability, good power capability, inexpensive, long lifetime	Low energy density	EVs, power tools, energy storage systems

2.2 Lithium iron orthosilicate (Li_2FeSiO_4)

In an effort to find cathode materials that are cheaper and safer than $LiCoO_2$ while with higher energy density than $LiFePO_4$, Li_2MSiO_4 (*M* = Fe, Mn, Co, or Ni) was proposed by Armand et al.[34-35] in 2000. Li_2MSiO_4, having two Li per transition metal, could potentially lead to a high theoretical capacity of *ca.* 331 mA h g^{-1}. The rigid framework constructed by silicate polyanions ensures a good structural and thermal stability. Of the silicate family, Li_2FeSiO_4 has recognized as the most promising one. Fe and Si are two of the most abundant elements in the earth crust. The (de)lithiation associated with redox reactions occur at 2.8 V (vs. Li^+/Li, $Fe^{2+/3+}$) and around 4.8 V (vs. Li^+/Li, $Fe^{3+/4+}$ or $O^{2-/-}$), which results in energy density of approximately 1120 W h kg^{-1}.[36] Other silicates have the similar framework and energy density, but some key factors have hindered their practical application. Li_2MnSiO_4 suffers from considerable capacity fading upon cycling due to the remarkable instability introduced by Mn^{3+},[37-40] while Li_2CoSiO_4[41-43] and Li_2NiSiO_4[44] are high-priced and their redox voltages are two high for current electrolytes.

2.2.1 Crystal structures of Li_2FeSiO_4

Li_2FeSiO_4 exhibits rich polymorphism with variation in the distribution of cations (Li, Fe, Si) in tetrahedral sites of the hexagonal close-packed (hcp) framework of oxygen.[45] The as-synthesized Li_2FeSiO_4 has been commonly found to crystallize in three polymorphs— β_{II} (orthorhombic, S.G. $Pmn2_1$)[46], γ_s (monoclinic, S.G. $P2_1/n$)[47], and γ_{II} (orthorhombic, S.G. *Pmnb*)[48], designated on the basis of β and γ polymorphs of Li_3PO_4. The formation of each polymorph strongly depends on the synthesis approach and particularly temperature history. As an example, in the study reported by Sirisopanaporn et al., $Pmn2_1$ was obtained via hydrothermal synthesis at 200°C, whereas $P2_1/n$ and *Pmnb* were produced by subsequent annealing at 700°C and 900°C, respectively, after the hydrothermal treatment.[46]

Crystal structures of the three synthesizable polymorphs are presented in Figure 2.4(a-c).[49] Li, Fe, and Si are all coordinated with O as tetrahedra, the connection manners of the LiO_4, FeO_4, and SiO_4 tetrahedra, however, are different among these three polymorphs. To be specific, in $Pmn2_1$, all the tetrahedra point in the same direction, perpendicular to the close-packed planes, and share only corners with each other; chains of LiO_4 along the a-axis parallel to chains of alternating FeO_4 and SiO_4. In $P2_1/n$, half of the tetrahedra point in opposite directions to the other half and there are edge-sharing tetrahedra pairs of LiO_4/FeO_4 and LiO_4/LiO_4. In *Pmnb*, there are three edge-

sharing tetrahedra of $LiO_4/FeO_4/LiO_4$. The average Fe−O bond length and the degree of FeO_4 distortion are varied, among which *Pmn*2_1 has the longest bond distance and the lowest distortion, whereas *Pmnb* has the shortest bond and the highest distortion.[46] It was also demonstrated that the variation of FeO_4 arrangement affects the equilibrium potential of Fe^{2+}/Fe^{3+} redox couple, leading to 3.1 V, 3.0 V, and 2.9 V (vs. Li^+/Li) for *Pmn*2_1, *P*2_1/*n*, and *Pmnb*, respectively.

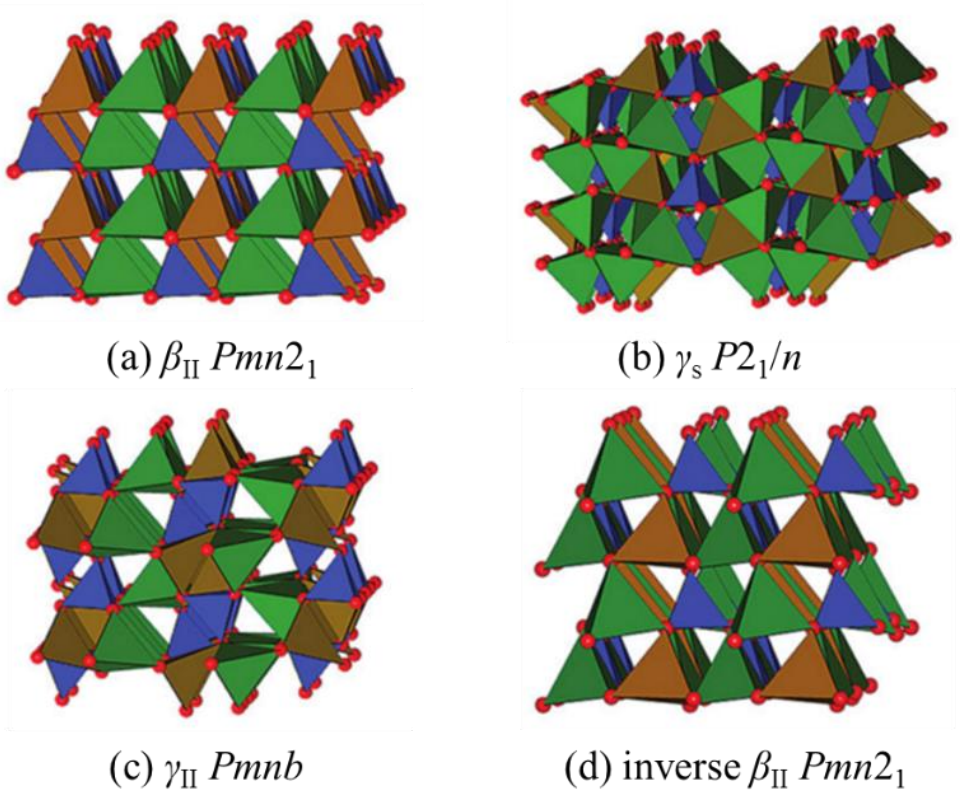

Figure 2.4. Crystal structures of Li_2FeSiO_4 polymorphs. Synthesizable structures of (a) orthorhombic β_{II} *Pmn*2_1; (b) monoclinic γ_s *P*2_1/*n*; and (c) orthorhombic γ_{II} *Pmnb*. (d) A possible cycled structure: orthorhombic inverse β_{II} *Pmn*2_1. Colors are shown as SiO_4 (blue), FeO_4 (brown), LiO_4 (green), and oxygen (red).[49]

Regardless of the starting structures, during electrochemical cycling, Li_2FeSiO_4 undergoes changes of the equilibrium voltage (i.e. thermodynamics) and the polarization (i.e. kinetics) within the first few cycles and then stabilizes. Such changes have been linked to structural transformation to a new phase.[50] To resolve the cycled structure, Armstrong et al.[51] conducted a postmortem study on cycled electrodes made by *P*2_1/*n* Li_2FeSiO_4. By using a combination of powder X-ray diffraction and neutron scattering, they found that the structure of cycled Li_2FeSiO_4 was essentially the same as β_{II} Li_2CoSiO_4 and similar to β_{II} Li_2FeSiO_4. The difference between the cycled

Li_2FeSiO_4 and the pristine β_{II} Li_2FeSiO_4 is that upon cycling the original Fe-sites are all occupied by Li, whereas half Li-sites are occupied by Fe. Because the relationship between the cycled β_{II} and the pristine β_{II} Li_2FeSiO_4 is analogous to the relationship between normal and inverse spinel, the cycled β_{II} Li_2FeSiO_4 is sometimes called inverse β_{II} or inverse *Pmn*2_1. Regarding the Fe/Li ordering scheme on the sharing Li-site, they found via simulations the lowest-energy ordering to be Li and Fe alternating regularly along the *a*-axis. This proposed cycled structure of Li_2FeSiO_4 is shown in Figure 2.4d. Several subsequent studies supported the same inverse *Pmn*2_1 structure of cycled Li_2FeSiO_4,[52-53] even though other cycled structures have also been proposed. For example, Kojima et al.[54] suggested that the cycled Li_2FeSiO_4 (after one charge-discharge cycle at 0.07 C rate) was in the same *P*2_1/*n* space group as the pristine but with significant Fe/Li disordering. 2.3% volume expansion from the pristine (335.16 $Å^3$) to the discharged (343.06 $Å^3$) was resolved from *ex situ* XRD. It is noted that the studied cycled structures were exclusively built on analyzing electrodes starting from the pristine *P*2_1/*n* polymorph. Even though all three polymorphs exhibit similar voltage change manner upon cycling, it has not been evidenced yet if the pristine *Pmn*2_1 and *Pmnb* will evolve to the same inverse *Pmn*2_1 structure after cycling.

2.2.2 Synthesis of Li_2FeSiO_4

Various synthesis routes have been used for the preparation of Li_2FeSiO_4 with different structural properties and electrochemical performance. The most commonly utilized methods are solid-state, sol-gel, and hydrothermal/solvothermal synthesis.

Solid-state reaction is the most conventional and robust method to synthesize powder ceramic materials. In a typical solid-state synthesis of Li_2FeSiO_4, precursor chemicals containing Li, Fe, Si, and O are mixed by grinding in an organic solvent for several hours. The resulting mixture is then dried and subjected to high temperature annealing. After several hours annealing followed by quenching to room temperature, the products are obtained. Precursors can be $FeC_2O_4 \cdot 2H_2O + Li_2SiO_3$[55-56], $FeC_2O_4 \cdot 2H_2O + Li_2CO_3 + SiO_2$[47] or $Fe_{0.97}O + Li_2SiO_3$.[48] To suppress the oxidation of Fe^{2+} during thermal annealing, reducing or inert gas such as CO/CO_2[57] and Ar[52] are often used. Annealing at 700°C and 900°C results in the formation of monoclinic *P*2_1/*n* and orthorhombic *Pmnb*,[58] , respectively, while annealing at 800°C leads to the formation of a mixture of these two phases.[48] The disadvantage of solid-state reaction includes the limited diffusion and interaction of species, formation of undesired impurities such as Fe_xO_y, Li_2SiO_3 and $LiFeSi_2O_6$,

and uncontrolled crystal growth which leads to inhomogeneous composition, irregular morphology and agglomeration.[55-57]

Sol-gel method is another popular approach to synthesize Li_2FeSiO_4. In this approach, precursors (e.g. $CH_3COOLi{\cdot}2H_2O$ + TEOS + $Fe(NO_3)_3{\cdot}9H_2O$) are dissolved in solvent (e.g. ethanol) and mixed for several hours to obtain a clear sol. The sol is then dried to form a gel. The gel is grinded to powders and subjected to thermal treatment at *ca.* 700°C.[59] Carbon sources can be added during the formation of the sol-gel, and carbon coating is formed after the thermal treatment. Carbon sources such as P123[59] and resols[60-61] have been used. The sol-gel route followed by high temperature treatment usually leads to the formation of monoclinic (S.G. $P2_1/n$) Li_2FeSiO_4 as micro-sized particles assembled by smaller particles and porous interiors. Nevertheless, complexity, time-consuming, and use of toxic chemicals hinder sol-gel method to be used in large scale production.

Compared to solid-state and sol-gel methods which require high-temperature annealing to enable the crystallization of Li_2FeSiO_4, hydrothermal/solvothermal method can crystallize Li_2FeSiO_4 at temperatures as low as 150-250°C, producing a low-temperature orthorhombic phase (S.G. $Pmn2_1$).[36] Hydrothermal/solvothermal synthesis is conducted in pressure reactors at temperatures above the boiling point of the solution. Hydrothermal refers to the processes in which water is used as the solvent, whereas solvothermal refers to those use organic solvents. Inorganic salts such as $LiOH{\cdot}H_2O$, SiO_2 and $FeCl_2{\cdot}4H_2O$ are the typical precursors.[46, 62] Hydrothermal/solvothermal synthesis is capable of producing nanoparticles with controlled stoichiometry, purity, desirable morphology, and narrow particle size distribution. Hydrothermal synthesis in particular provides the potential for scalable production at low cost and in an environmentally benign manner. More discussion on hydrothermal synthesis and the conditions for producing Li_2FeSiO_4 is given in the next section.

The as-synthesized Li_2FeSiO_4 is sensitive to exposure to air. Nytén et al.[63] observed significant amount of Li_2CO_3 associated with Fe^{3+} on the surface of Li_2FeSiO_4 particles in contact with air for one month. Deng et al. found out that Li_2FeSiO_4 was severely oxidized after one-year exposure to air, but the pristine phase could be recovered through annealing at 700°C in Ar gas.[64] Nevertheless, attention must be taken to minimize the air-exposure of pristine Li_2FeSiO_4 during handling and storage. Storage in inert atmosphere such as Ar-filled glovebox is suggested.

2.2.3 Electrochemical performance of Li_2FeSiO_4

Li_2FeSiO_4 has a wide bandgap of about 3 eV[65] and a small electronic conductivity of about 6×10^{-14} S cm^{-1} at room temperature and about 2×10^{-12} S cm^{-1} at 60°C[40]. Due to this poor intrinsic conductivity, nanosizing and carbon-coating are required to achieve one-Li capacity. Figure 2.5a shows galvanostatic charge-discharge profile of the first three cycles of $P2_1/n$ Li_2FeSiO_4/C composite cycling at C/20 at 60°C.[40] Under this cycling condition, slightly above 0.7 Li was extracted/inserted, resulting in a capacity of about 120 mA h g^{-1}. The voltage plateau of charge appears at about 3.1 V in the first cycle while drops to 2.8 V in the third cycle. This voltage drop has been originated to phase transformation to a lower energy phase such as inverse $Pmn2_1$ as discussed above (see Figure 2.4d). The capacity decreases with the increase of current density, as shown in Figure 2.5b. Without carbon coating or cycling at room temperature tends to lead to remarkable reduced capacity.[66-67]

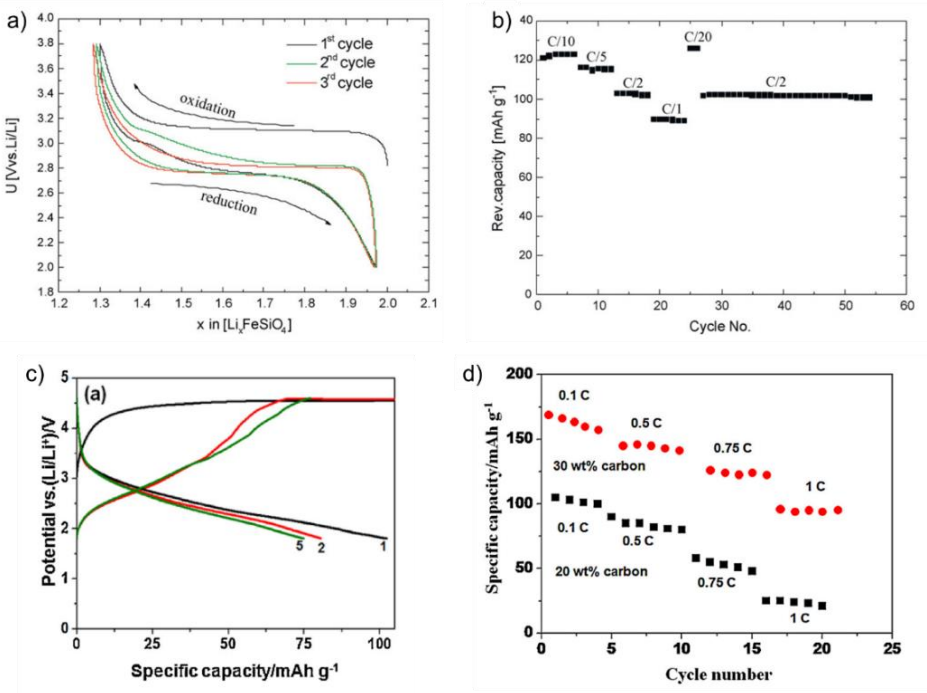

Figure 2.5. (a) Galvanostatic charge-discharge curves and (b) cycling performance of $P2_1/n$ Li_2FeSiO_4/C composite cycled between 2 V and 3.8 V at 60°C in LiBOB EC/DEC electrolyte.[40] (c) Galvanostatic charge-discharge curves of non-carbon-coated and (d) cycling performance of carbon-coated $Pmn2_1$ Li_2FeSiO_4 cycled between 1.5 V and 4.8 V at room temperature in $LiClO_4$ EC/DEC electrolyte.[68]

Electrochemical performance of $Pmn2_1$ phase is in general inferior to that of $P2_1/n$ phase in terms of capacity and cyclability.[68-71] Yet it has not been elucidated whether the poor

performance of *Pmn*2$_1$ Li_2FeSiO_4 originates from the intrinsic properties of this crystal structure, or from the lack of conductive coating. *Pmn*2$_1$ Li_2FeSiO_4 is unstable above 500^{o}C, while current carbon coating techniques require processing temperatures above 650^{o}C.[36] Shown in Figures 2.5c and 2.5d, Devaraju et al.[68] found that mixing with large amount of carbon (30wt%, including MWCNT, CNF and PEDOT) increased the initial discharge capacity of *Pmn*2$_1$ nanorods from 102 mA h g^{-1} to 177 mA h g^{-1} which then dropped to 40 mA h g^{-1} and 150 mA h g^{-1}, respectively, after 30 cycles. The *Pmn*2$_1$ nanorods of Li_2FeSiO_4 were synthesized by supercritical fluid method at 380^{o}C, cycled at C/20 between 1.5 V and 4.8 V in $LiClO_4$ EC/DEC at room temperature.

For the first Li extraction process (i.e. from Li_2FeSiO_4 to $LiFeSiO_4$), it has been evidenced by employing Mössbauer spectroscopy and X-ray absorption spectroscopy that one electron is taken out from Fe-3*d* band and results in the oxidation from Fe^{2+} to Fe^{3+}.[72] The elucidation of Li storage mechanism in Li_2FeSiO_4, however, has been only based on DFT simulations. In the structure model of inverse *Pmn*2$_1$ Li_2FeSiO_4, Armstrong et al. identified two major Li migration paths as shown in Figure 2.6.[51] The first path involves hops (A) to (B) along zig-zag c-axis between corner-sharing LiO_4 tetrahedra sites with Li-Li separation distances of 3.03 Å + 3.04 Å and migration barrier of 0.91 eV. The second path involves hops (C) to (D) along b-axis between corner-sharing LiO_4 tetrahedra sites with Li-Li separation distances of 3.03 Å + 3.33 Å and migration barrier of 1.55 eV. Other paths were found to have migration barriers larger than 3.0 eV. As a comparison, the migration barrier in $LiFePO_4$ is 0.55 eV,[73] much lower than the 0.91 eV in Li_2FeSiO_4.

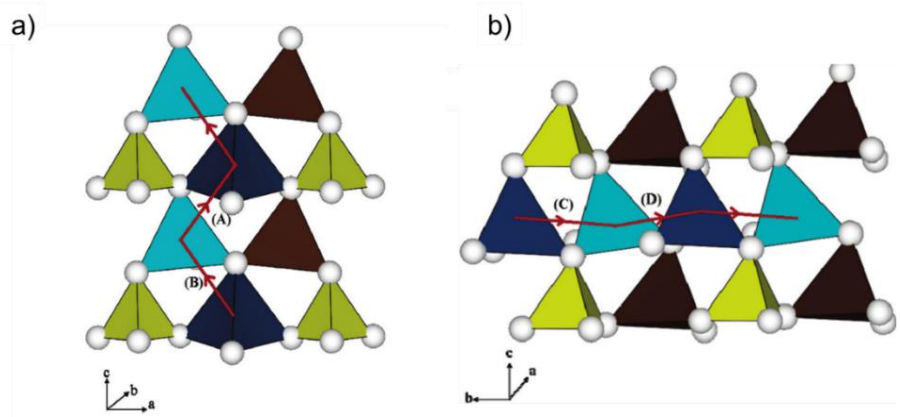

Figure 2.6. Pathways for lithium ion migration in the cycled structure of inverse *Pmn*2$_1$ Li_2FeSiO_4. (a) The first path involves hops (A) and (B) in the zig-zag *c* direction. (b) The second path involves hops (C) and (D) in the *b* direction. SiO_4 tetrahedra, yellow; Li(1)O_4 tetrahedra, dark blue; Li(2)O_4 tetrahedra, light blue; FeO_4 tetrahedra, brown).[51]

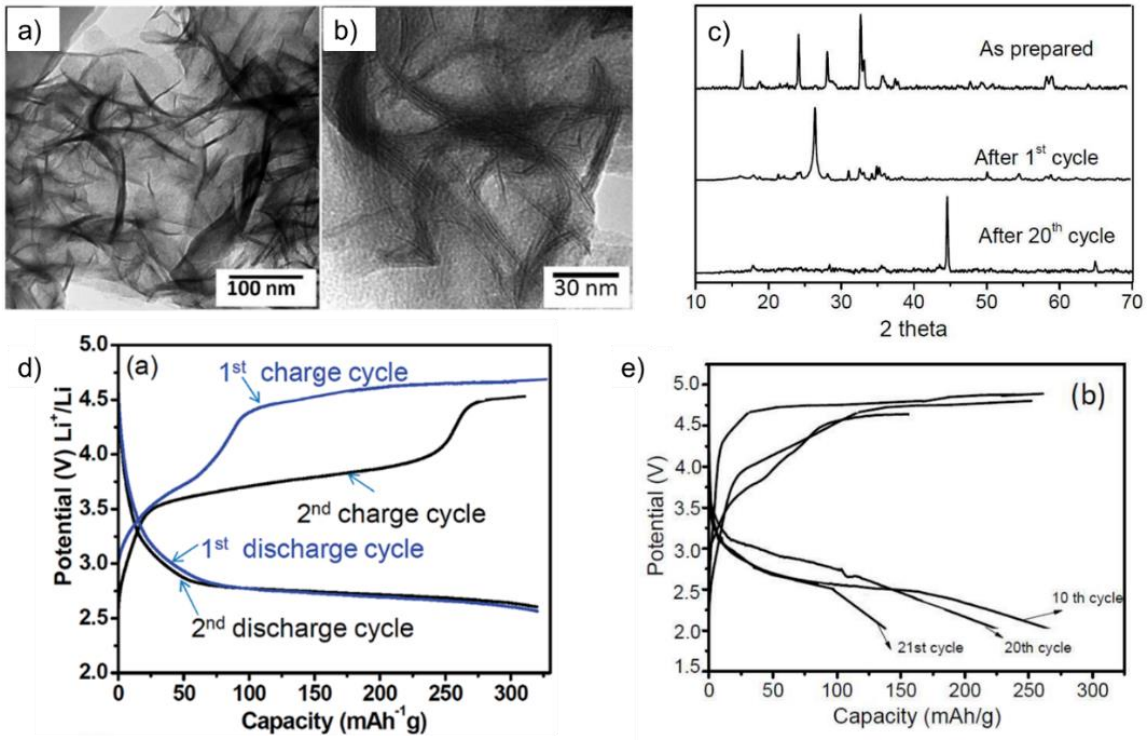

Figure 2.7. (a, b) TEM images of Li_2FeSiO_4 nanosheets synthesized by supercritical fluid method. (c) XRD patterns of as prepared and cycled Li_2FeSiO_4 nanosheets. Charge-discharge curves of (d) the 1st and the 2nd cycles and (e) the 10th, 20th, and the 21st cycles cycled at C/50 at 45±5°C in $LiClO_4$ EC/DEC.[74]

To achieve higher capacity and energy density, many efforts have been made to extract more than one Li-ions from Li_2FeSiO_4 and insert these Li-ions back reversibly. Theoretically, (de)lithiation of the second Li requires cell voltage above 4.8 V.[44] Charge to such high voltage could cause degradation of electrolytes. Nevertheless, some studies have shown that nanosizing and conductive carbon-coating can help to deliver more than one-Li capacity. Table 2.2 summarizes the studies which reported above one-Li capacity. All of the high-capacity specimens were carbon-coated $P2_1/n$ phase except the one reported by Rangappa et al. in 2012.[74] As shown in Figure 2.7, Rangappa et al.[74] prepared ultrathin nanosheets of Li_2FeSiO_4 in $Pmn2_1$ phase via supercritical fluid method using ethanol-water mixed-solvent and found these nanosheets delivered discharge capacity of about 320 mA h g^{-1} in the initial cycles, corresponding to 1.93 Li being intercalated at 45±5°C and C/50. These nanosheets have an average thickness of 3 nm as determined by Atomic Force Microscopy (AFM). With this 2D feature, the (de)intercalation reactions of Li would be surface dominant which defers from the bulk materials. Therefore, it is no surprise to find out large polarization between charge and discharge even after 20 cycles.

Moreover, the Li_2FeSiO_4 nanosheets went through phase transformation after the 1st cycle, as indicated by the significant change of XRD patterns, while after 20 cycles, most of the peaks diminished and one new strong peak showing up. The dramatic structural change may be the cause for the 60% capacity loss after 21 cycles. This study shows the promise of realizing the theoretical capacity of Li_2FeSiO_4, while it also leaves the question to whether this high capacity can be delivered in a reversible mode.

Table 2.2. Summary of studies reporting more-than-one lithium capacity from Li_2FeSiO_4

Reference	Specimen	Initial discharge capacity, retention (cycle)	Cycling condition	Charge compensation, exp evidence	Comments
Ding, 2018[75]	LFS/C mesocrystal plates	315, 95% (5th)	1.5-4.7 V, C/5, $LiPF_6$ in EC/DMC	Fe^{4+}, N/A	
Kumar, 2016[60]	LFS/C	275, 93% (2nd)	1.5-4.8 V, C/30, $LiPF_6$ in EC/DMC	O^{2-}/O_2^-, N/A	Only 2 cycles
Yang, 2015[76]	Graphene-LFS	327, 106% (5th)	1.5-4.8 V, C/10, $LiPF_6$ in EC/DMC	No Fe^{4+}, Mössbauer and ESR	Start with 45% Fe^{3+} but delivered 2-Li capacity
Masese, 2015[52]	LFS/C	330, N/A	1.3-4.8 V, C/50, 55ºC, $LiClO_4$ in PC	ligand hole in O-2p, ex situ XANES	Only 2 charge and 1 discharge cycles
Ding, 2015[60]	3DOM-LFS/C**	237, 96.3% (20th)	1.5-4.8 V, C/10, $LiPF_6$ in EC/DMC	Fe^{4+}, N/A	
Zhu, 2014[77]	3DOM-G-LFS/C	313, 85% (15th)	1.5-4.8 V, C/10, $LiPF_6$ in EC/DMC	Fe^{4+}, N/A	
Zhu, 2014[78]	LFS/G/C	310, 93% (15th)	1.5-4.8 V, C/10, $LiPF_6$ in EC/DMC	Fe^{4+}, N/A	30wt% G+C in the composite
Zhang, 2013[79]	LFS(C+rGO)	178, 94.5% (40th)	1.5-4.8 V, C/10, $LiPF_6$ in EC/DMC	Fe^{4+}, N/A	
Lv, 2013[80]	LFS/C	195, N/A	1.5-4.8 V, ~C/11, RT, $LiPF_6$ in EC/DMC	Fe^{4+}, in situ XANES	XAS of oxygen was unavailable
Rangappa, 2012[74]	Nanosheets, supercritical fluid, PEDOT + MWCNT	320, 70% (20th), 40% (21st)	1.5(?)*-4.8 V, C/50, 45±5ºC, $LiClO_4$ in EC/DEC	N/A	Drastic fading after 21 cycles. Inconsistent results between figures and text

* In the experimental section, the lowest voltage was claimed to be 1.5 V, but in the figures, it was shown as 2.5 V and 2.0 V in the article and the SuppInfo, respectively.

** 3DOM stands for three-dimensionally ordered macroporous.

Unlike the evidence of Fe^{2+}/Fe^{3+} redox responsible for removing the first Li, charge compensation mechanism for the second Li remains unclear and is still under debate if the extra capacity is from the active material itself or from the degradation of the electrolyte. As listed in

Table 2.2, there are basically three explanations for the above one-Li capacity: (i) Fe^{3+}/Fe^{4+} redox, (ii) oxygen participation, and (iii) electrolyte degradation.

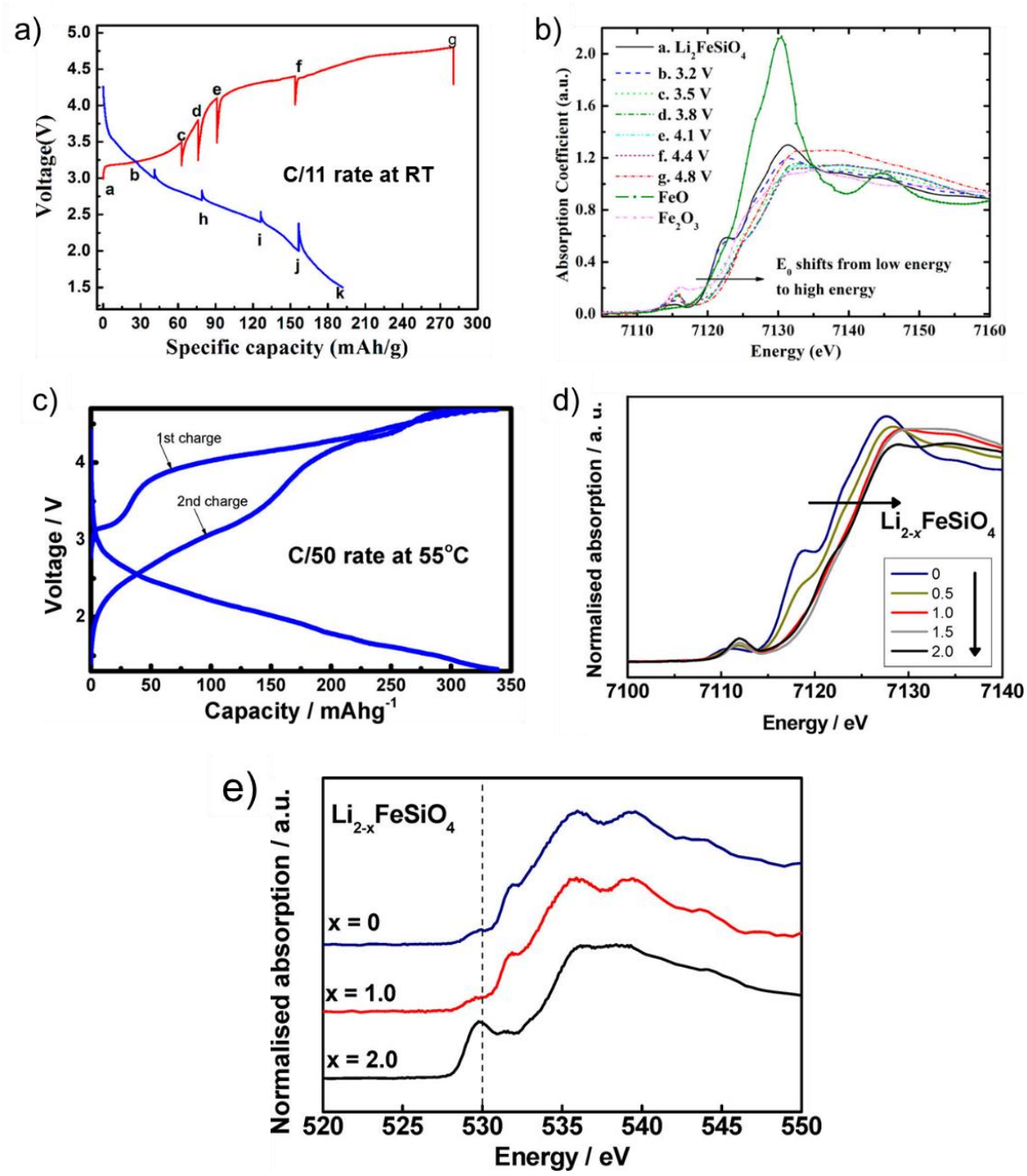

Figure 2.8. Charge compensation mechanism of LFS during (de)lithiation. (a) Charge-discharge curve of Li_2FeSiO_4/C by Lv et al.[80] at C/11 at room temperature in $LiPF_6$ EC/DMC for *in situ* XANES study showing in (b) XANES of Fe K-edge and reference spectra. (c) Charge-discharge curve of Li_2FeSiO_4/C by Masese et al.[52] at C/50 at 55ºC in $LiClO_4$ PC and *ex situ* XANES of (d) Fe K-edge spectra and (e) O K-edge spectra.

Lv et al.[80] utilized *in situ* XANES to monitor the change of Fe oxidation states and ascribed the capacity above one Li extraction to the formation of Fe^{4+} as there was a subtle change of Fe K-edge in XANES when charging the cell above 4.1 V (Figure 2.8 a,b). However, other *ex situ* or *in situ* XANES studies did not observe Fe^{4+}.[52, 81] Mössbauer spectroscopy has been used to identify the oxidation state of Fe. Lv et al.[72] assigned a new doublet to Fe^{4+} when charging to 4.2 V. However, this doublet may originate from low-spin Fe^{3+} because it overlaps with high-spin Fe^{4+}.[76, 82] Yang et al.[76] further confirmed with X-band electronic spin resonance (ESR) that no high-spin Fe^{4+} was detected but rather increasing signals from low-spin Fe^{3+} with increasing charge voltage.

Using *ex situ* EXANES, Masese et al.[52] observed that there was no change in the Fe-3d band but rather forming ligand holes on O-2p band during the second Li extraction (Figure 2.8 c-e). Lu et al. also observed oxygen participation from *ex situ* XANES study.[83] It is noticed that in the study by Masese et al.,[52] fully delithiated $FeSiO_4$ was obtained and the structure was described as orthorhombic *Pnma*. However, only one discharge cycle was reported, and the quality of the structure refinement was not satisfactory. Moreover, first principle computations indicate the optimized structure of $FeSiO_4$ is unstable.[44]

Recently, Liivat et al.[82] performed *in situ* Mössbauer spectroscopy on symmetric cells of $Li(1)FeSiO_4$ || $Li(1)FeSiO_4$ and $Li(0)FeSiO_4$ || $Li(0)FeSiO_4$. They found that a large portion of the cycled lithium did not originate from the electrode but rather from the high-voltage degradation of the electrolyte (1M $LiPF_6$ in EC/DEC at room temperature). Electrolyte degradation was proposed by another study as well.[81]

2.3 Hydrothermal Synthesis

Hydrothermal synthesis refers to the synthesis method that produces materials via chemical reactions performed in aqueous solutions where the reagents are heated at temperatures above the boiling point of water and at pressures above 1 atm.[84] Hydrothermal synthesis is a low cost and environmentally benign method for producing a variety of inorganic materials. It offers the opportunity to alter many important characteristics of the solid products, such as purity, composition, crystal structure, particle size, and morphology, to name a few, by adjusting synthesis parameters including temperature, pressure, precursor concentration, reaction time, and additives. When using in producing functional materials for various applications, the synthesis parameters need to be selected to produce particles with quality and properties that give the desired

functionality. In order to manipulate the synthesis process, it is important to understand the fundamental mechanism of particle formation and growth rather than trial-and-error. This section will review the basic principles of hydrothermal synthesis and particle formation and growth theory, including the well-known classical and recently developed nonclassical theories. Various applications of hydrothermal method in producing Li-ion cathode materials are discussed. Furthermore, the hydrothermal method employed in Li_2FeSiO_4 synthesis and the relations of synthesis parameters and resultant properties of Li_2FeSiO_4 particles are reviewed.

2.3.1 Principles of hydrothermal synthesis

The term hydrothermal synthesis usually refers to heterogeneous reactions in the presence of aqueous solvents or mineralizers under high-pressure-high-temperature conditions to dissolve and reprecipitate materials that are relatively insoluble under ordinary conditions.[85] Historically, hydrothermal growth has been used to grow large crystals, such as quartz and zeolites. In the recent decades, nanocrystals and submicron-crystals are also made by hydrothermal synthesis with crystal size controlled due to the advancement in nanotechnology. The solvent- usually refers to water, plays a vital role in the hydrothermal process. Water not only works as a medium that provide a certain environment for dissolution and growth of substances, but also works as an absorbent or reactant. Under elevated temperature and pressure, the fundamental properties of water such as the dielectric constant, viscosity, ionic product, thermal conductivity, and heat capacity change.[86] Figure 2.9a summarizes the multiple roles that water plays under hydrothermal conditions.[87] Figure 2.9b shows the static dielectric constant of water as a function of pressure at various temperatures. It is clearly shown that the dielectric constant of water increases slightly with pressure while drops rapidly with temperature.[88] The dielectric constant of water is 78 at 25^{o}C, which favors the dissolution of ionic or polar compounds. As the temperature increases, the dielectric constants reduce to 55.4 and 34.7, respectively, for saturated water at 100^{o}C (101.42 kPa) and 200^{o}C (1554.9 kPa). Under near-supercritical conditions, taking 370^{o}C (21044 kPa) as an example, the dielectric constant drops to 8.7. Higher temperature leads to lower dielectric constant of water, which would result in the precipitation of ionic or polar compounds because they become less soluble. The critical temperature and pressure of water are 374^{o}C and 22.1 MPa.

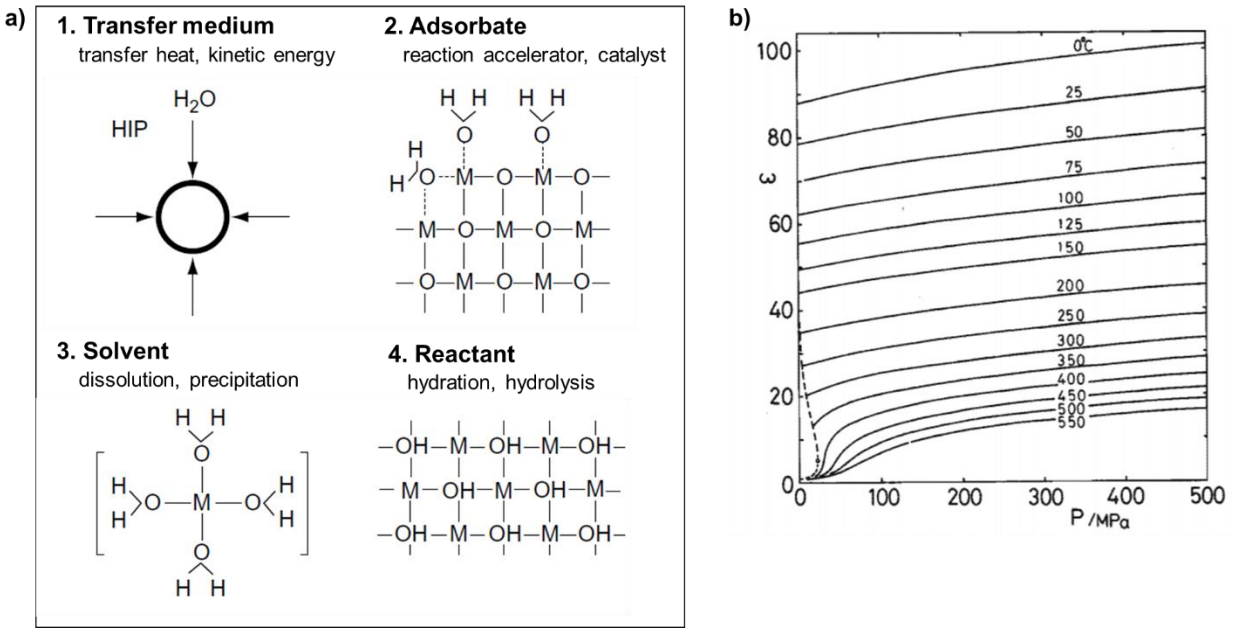

Figure 2.9. (a) Multiple roles of hydrothermal water and their actions on solid substances. Edited from reference[87]. (b) Static dielectric constant of water as a function of pressure at various temperatures[88].

2.3.2 Reactors for hydrothermal synthesis

Most hydrothermal processes are performed in a sealed reactor, known as an autoclave, a pressure vessel, or a high-pressure bomb. These reactors are made by metal (particularly stainless steel) with PTFE or alloy linings or containing an extra container putting inside made of PTFE or alloy to protect the metal body from corrosion at high temperature and pressure. Figure 2.10 presents several examples of autoclaves. For laboratory hydrothermal synthesis, the reactor can be as simple as the one on the left side, with solely a metal-made vessel and a PTFE liner inside. This reactor is then heated up in an oven. The reactor can also be equipped with a pressure gauge and a thermocouple to monitor and control the pressure and temperature as shown on the right side. In some cases, a stirred is equipped to provide agitation to minimize the concentration gradience. As *in situ* synthesis and characterizations are becoming more and more popular in the field of crystal growth of advanced materials, reactors made by quartz or sapphire or other materials with a transparent window have been used. The choice of a hydrothermal reactor depends on the temperature and pressure of a specific experiment, as well as the corrosive resistance of the internal materials (e.g. liner, stirrer, thermocouple, etc.) towards the nature of the solution (e.g. acidic, alkaline, corrosion species such as chlorine).

Figure 2.10. Typical reactors for hydrothermal synthesis. On the left is a simple closed-vessel that can be heated in an oven, while on the right is a more complex autoclave equipped with temperature and pressure sensors and a stirrer, which is heated by a heating mantle with temperature control.[89]

2.3.3 Crystal nucleation and growth theory

An understanding of the crystal formation mechanism is essential to manipulating the synthesis parameters and producing particles with desired purity, particle size and morphology. The formation of a solid phase out of a solution involves nucleation, growth, and assembly of particles. Nucleation is a process whereby the molecules or ion-pairs in a supersaturated solution combine together to form clusters which constantly form and disappear until achieving a critical size.[90] According to the classical nucleation theory, there are two different mechanisms, namely, homogeneous or heterogeneous nucleation, depending on which site the nucleation occurs.[91] Homogeneous nucleation occurs when nuclei form uniformly throughout the parent phase, whereas heterogeneous nucleation occurs at a foreign surface (e.g. seeds, impurities, container surfaces, bubbles, etc.). Although many approximations and assumptions must be considered, the classical nucleation theory is helpful for understanding the basic phenomenon happening during hydrothermal synthesis and serves as a powerful tool in the optimization of synthesis parameters.

Homogeneous nucleation can be considered thermodynamically by looking at the Gibbs free energy change during the formation of a cluster (Figure 2.11a).[92] The total free energy change ΔG is a sum of the surface free energy change ΔG_S, associated with the formation of new surfaces that costs energy, and the bulk free energy change ΔG_V, associated with the formation of a bulk volume that lowers the energy

$$\Delta G = \Delta G_S + \Delta G_V \tag{2.6}$$

The change of each free energy as a function of the nuclei size is presented in Figure 2.11b.

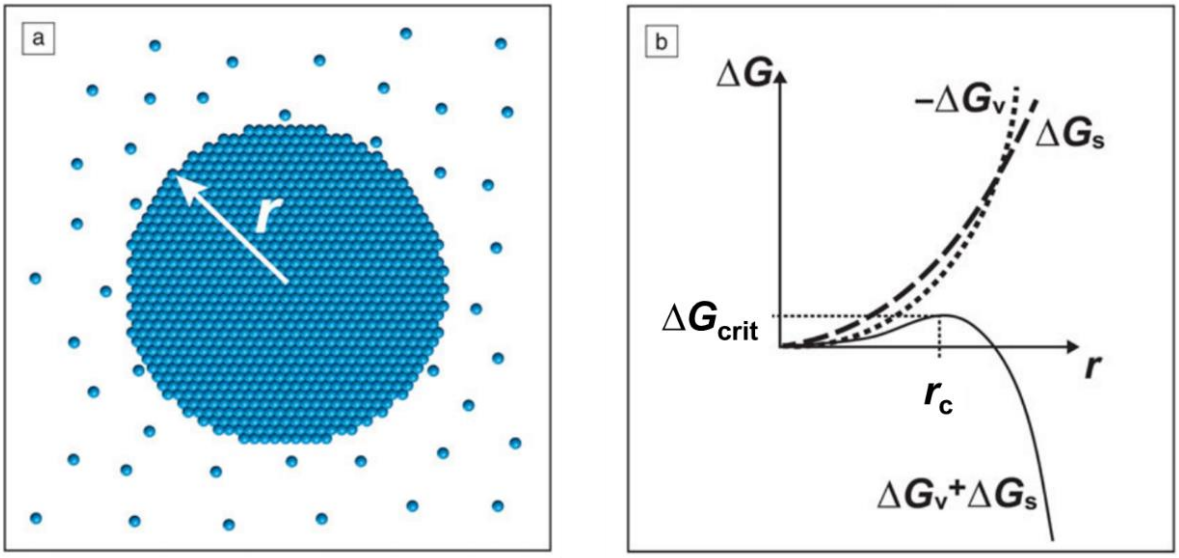

Figure 2.11. (a) Schematics of the formation of a spherical cluster with radius *r* from solution. (b) Gibbs free energy changes as a function of *r*.[92]

ΔG_S and ΔG_V are further described as

$$\Delta G_S = 4\pi r^2 \gamma \tag{2.7}$$

$$\Delta G_V = \frac{4}{3}\pi r^3 \Delta G_v = \frac{4}{3}\pi r^3 \left(-\frac{k_B T ln S}{v}\right) \tag{2.8}$$

where r is the radius of a spherical cluster, γ is the surface free energy per unit area, ΔG_v is the bulk free energy change per unit volume between the new and the old phases, k_B is Boltzmann's constant of 1.38×10^{-23} J K^{-1}, T is the absolute temperature, S is supersaturation, and v is the molecular volume. As shown in Figure 2.11b, because ΔG_S is always positive while ΔG_V is always negative, there is a maximum ΔG at which the cluster will pass through to form a stable nucleus. The critical nuclei size r_c represents the minimum size of a stable nucleus. Nuclei with size smaller than r_c will dissolve, whereas those larger than r_c will continue to grow to minimize the total free energy. Therefore, r_c can be calculated by setting $\frac{d\Delta G}{dr} = 0$, which leads to

$$r_c = -\frac{2\gamma}{\Delta G_v} = \frac{2\gamma v}{k_B T ln S} \tag{2.9}$$

The critical energy, ΔG_{crit}, which represents the activation energy barrier of nucleation process, is therefore given by

$$\Delta G_{crit} = \frac{16\pi\gamma^3 v^2}{3(k_B T ln S)^2} \tag{2.10}$$

The intrinsic homogenous nucleation rate J^{homo}, which represents the number of nuclei formed per unit time and unit volume, can be expressed as an Arrhenius-type equation by

$$J^{homo} = Aexp\left(-\frac{\Delta G_{crit}}{k_B T}\right) = Aexp\left(-\frac{16\pi\gamma^3 v^2}{3{k_B}^3 T^3 (lnS)^2}\right) \tag{2.11}$$

where *A* is a pre-exponential factor. It can be seen from equation 2.11 that there are three main experimental parameters that govern the nucleation rate, namely, temperature *T*, supersaturation *S*, and surface free energy γ. It has been reported that the largest effect comes from supersaturation. A change from S = 2 to S = 4 could cause an increase in the nucleation rate by 10^{70}.[93] Supersaturation is the driving force for the formation of a phase. For the following reaction[94]

$$k_1 A_1 + k_2 A_2 + \cdots + k_i A_i = [(A_1)_{k_1}(A_2)_{k_2} \ldots (A_i)_{k_i}] \tag{2.12}$$

where A_i is an aqueous species, k_i is the stoichiometric coefficient, and $[(A_1)_{k_1}(A_2)_{k_2} \ldots (A_i)_{k_i}]$ is the new phase. Supersaturation can by expressed by

$$S = \frac{\prod_i [A_i]^{k_i}}{K_{SP}} \tag{2.13}$$

where $[A_i]$ is the activity of an aqueous species, and K_{SP} is the solubility product of the new phase. For approximation, concentration, instead of activity, might be used for the calculation of supersaturation. According to eq 2.9, higher supersaturation could result in smaller critical nuclei size.

In the presence of any heterogeneities in the parent phases, the height of the nucleation barriers will be reduced and leads to heterogeneous nucleation. The rate of heterogenous nucleation can by expressed by considering a structural factor *f* while assigning a net effective surface free energy γ_{net}[95]

$$J^{het} = Aexp\left(-\frac{\Delta G_{crit}}{k_B T} f\right) = Aexp\left(-\frac{16\pi\gamma_{net}^3 v^2 f}{3{k_B}^3 T^3 (lnS)^2}\right) \tag{2.14}$$

Once stable nuclei have formed, the particles will start to grow. The growth of particles could follow different mechanisms depending on the conditions such as supersaturation, surrounding species, and temperature. Of the classical crystallization theory, LaMer mechanism has been widely used in interpreting crystallization of nanoparticles. LaMer mechanism[96] separates the process into three stages, as demonstrated in Figure 2.12:[97] (I) the concentration of free monomers increases rapidly and reaches a critical supersaturation (C_S); (II) the saturation level reaches C_{min} at which the energy barrier for nucleation can be overcome, resulting in rapid self-nucleation of the monomers; and (III) the saturation decreases to a level that is insufficient for self-nucleation, so that particle growth occurs through diffusion of monomers from solution.

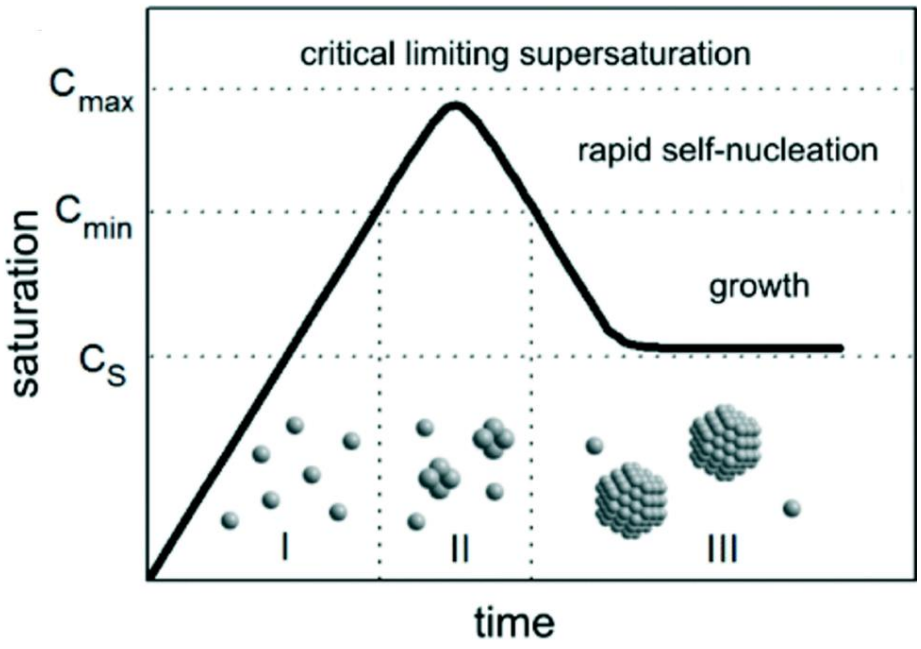

Figure 2.12. Classical crystal growth mechanism: The LaMer mechanism.[97]

Classical nucleation and growth models consider only the monomer-by-monomer addition, which are not commonly observed in realistic experiments. More and more experimental observations in diverse solution systems support a set of nonclassical crystal nucleation and growth mechanisms– crystallization by particle attachment (CPA), as summarized in Figure 2.13.[98] There are a variety of plausible building blocks, ranging from ion-complexes to amorphous and to nanocrystals. The pathways for these building blocks to attach with each other are governed by the free-energy landscapes and the reaction dynamics including particle diffusion and relaxation.

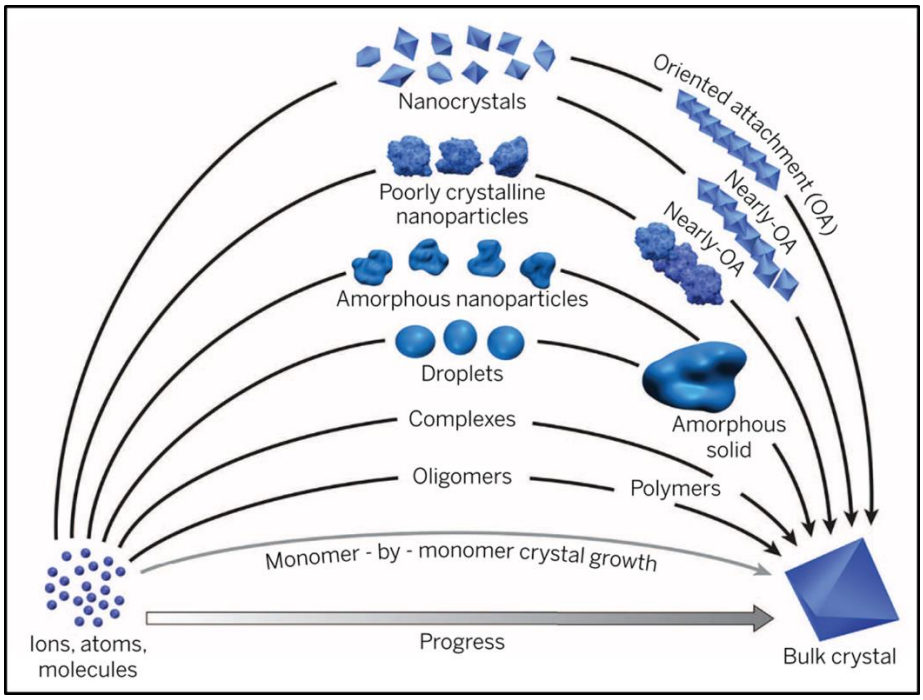

Figure 2.13. Pathways to crystallization by particle attachment (CPA).[98] There are a range of pathways through which various forms of particles attach with each other and form the final bulk crystals. The classical nucleation and growth through monomer-by-monomer addition is shown as the grey curve at bottom.

2.3.4 Hydrothermal synthesis of cathode materials

Hydrothermal method had been widely applied to synthesis cathode materials for Li-ion batteries from oxides to polyanions. Hydrothermal synthesis is capable to produce particles with high purity at relatively low temperature, and more importantly it allows for the control of particle size and morphology. Nanosizing engineering plays a key role in achieving theoretical performance of a cathode materials because the particle size affects the distance for Li-ion to transport while the surface area determines the exterior contact between electrode and electrolyte.[99] Nanoparticles used as cathode materials for Li-ion batteries are usually considered to have at least one dimension less than 100 nm.[100] In addition, reducing the particle size can also decrease the length of the tunneling barrier for electrons to travel between the surface layer and the core of the particles, which is especially useful to improve the electrochemical performance of materials that suffer from low intrinsic electrical conductivity, such as $LiFePO_4$.[101] At the meantime, morphology can also be crucial if Li-ion has a certain transport direction across the electrode.

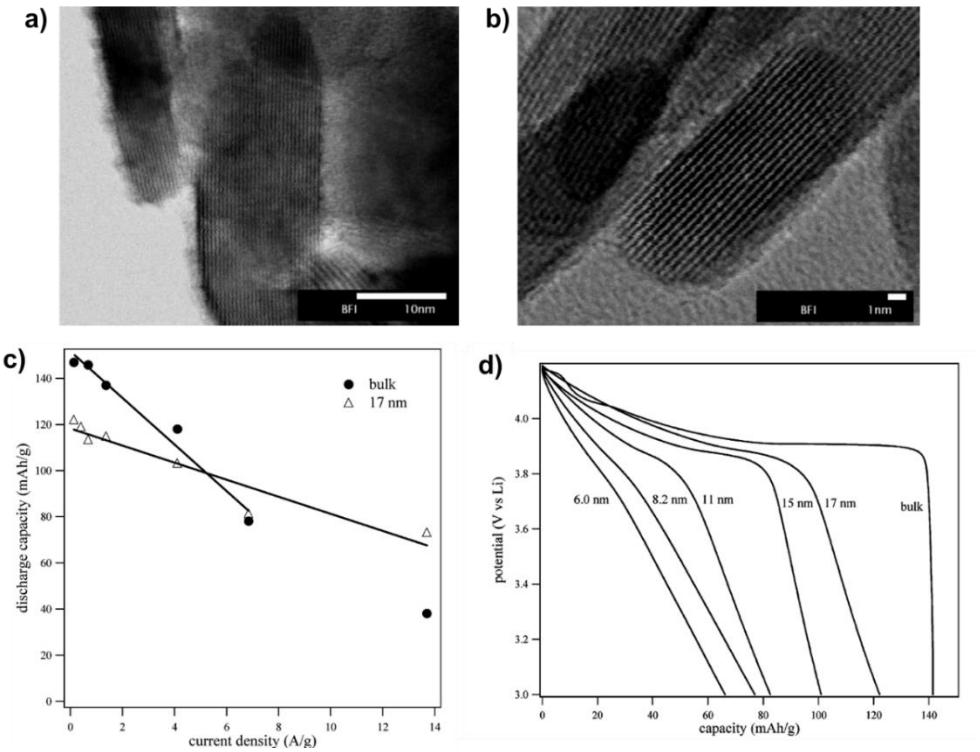

Figure 2.14. Size-controlled hydrothermal synthesis of $LiCoO_2$ and its performance as cathode. (a) TEM of $LiCoO_2$ with thickness of 17 nm obtained with 1M LiOH. (b) TEM of $LiCoO_2$ with thickness of 11 nm obtained with 5 M LiOH. (c) Rate capacity of bulk and nanosized $LiCoO_2$. (d) Discharge curves of $LiCoO_2$ in various size.[102]

For a typical hydrothermal synthesis of Li-based materials, the reactants are dissolved or dispersed in water, the resultant precursor mixture is then heated up in an autoclave to temperatures above 100^{o}C and is held for a desired duration. The properties of the produced particles can be tuned by varying temperature, reaction time, the type of reactants, concentrations, pH, additives, stirring speed, etc. In some cases, nonaqueous solvents, such as ethylene glycol, are utilized as alternatives to water and such process is referred to as solvothermal synthesis. This review gives emphasize on hydrothermal synthesis in aqueous media only. Table 2.3 summarizes the reported work on hydrothermal synthesis of common Li-ion cathode materials from oxides to polyanionic compounds. A size-controlled hydrothermal synthesis of $LiCoO_2$ by Okubo et al.[102] showed that smaller particles were obtained by using higher LiOH concentration, shorter reaction time, or lower reaction temperature, demonstrating a dissolution-recrystallization formation mechanism (Figure 2.14). Using LiOH concentration of 0.1, 1, and 5M, respectively, resulted in crystallite size of 27, 17, and 11 nm in thickness. Nanosizing demonstrated strong impact on the electrochemical performance of $LiCoO_2$. The authors found crystallite sizes between 15 and 20 nm to be

appropriate for high-rate performance. Further decreasing of the crystallite size to smaller than 15 nm resulted in remarkable capacitor behavior and capacity reduction, as shown in Figure 2.14.

Table 2.3. Li-based cathode materials prepared by hydrothermal synthesis

Type	Compound	Precursor and concentration	Additives	Temp./ time	Particle size	Morphology
Oxide	$LiCoO_2$ [102]	$LiOH{\cdot}H_2O$ 1M, CoOOH 0.067M	-	170ºC, 12h	17nm thick, 40nm wide	Nanoplate
	$LiMnO_2$ [103]	$LiOH{\cdot}H_2O$ 3.5M, Mn_3O_4 0.02M	-	170ºC, 4d	0.1-0.5μm	Irregular cubic
	$LiMn_2O_4$ [104]	$LiOH{\cdot}H_2O$ 0.8M, MnO_2 0.5M $Mn(NO_3)_2$ 0.17M	-	280ºC, 36h	50-300nm	Octahedral
Phosphate	$LiFePO_4$ [31] *	$LiOH{\cdot}H_2O$ 1.2M, $FeSO_4{\cdot}7H_2O$ 0.4M, H_3PO_4 0.4M	Ascorbic acid	180ºC, 5h	2μm long, ~0.5μm wide	Rhombic
	$LiCoPO_4$ [105]	$LiOH{\cdot}H_2O$ 0.1M, $Co(NO_3)_2{\cdot}6H_2O$ 0.05M, H_3PO_4 0.05M	-	220ºC, 5h	1-6μm	Orthorhombic prism
	$LiMnPO_4$ [106]	$Li_2SO_4{\cdot}H_2O$ 1.3M, $MnSO_4{\cdot}H_2O$ 0.67M, $NH_4H_2PO_4$ 0.67M, $Na_2S{\cdot}9H_2O$ 0.57M	-	200ºC, 10h	1.5μm long, 0.2μm wide	Wedge-like single or meso-crystal, change with concentration
	$Li_3V_2(PO_4)_3$ [107]	Li_2CO_3, V_2O_5, H_3PO_4 (concentration unknown)	$C_2H_2O_4{\cdot}2H_2O$	180ºC, 24h	60 nm wide	Nanorod
Silicate	Li_2FeSiO_4 [69]*	$LiOH{\cdot}H_2O$ 0.4M, $FeCl_2{\cdot}4H_2O$ 0.1M, SiO_2 0.1M	BPEI	150ºC, 16h	1000 nm long, 100 nm thick	Six-armed mesocrystal
	Li_2MnSiO_4 [38]	$LiOH{\cdot}H_2O$ 2.5M, $MnCl_2{\cdot}4H_2O$ 0.6M, SiO_2 0.6M	EDTA-4Na	170ºC, 48h	40-60 nm wide, 200-400nm long	Nanorod
	Li_2CoSiO_4	$LiOH{\cdot}H_2O$ 1.33M, $CoCl_2{\cdot}6H_2O$ 0.33M, SiO_2, 0.33M	-	180ºC, 20h	2-4μm	Irregular single crystals with impurities
Oxyphosphate	$LiVOPO_4$ [108]	$LiOH{\cdot}H_2O$ 0.7M, V_2O_5 0.04M, H_3PO_4 0.23M	$N_2H_2{\cdot}2H_2O$	250ºC, 48h	12μm	Hollow sphere mesocrystal

* Hydrothermal synthesis of $LiFePO_4$ and Li_2FeSiO_4 will be discussed in detail in the following section.

Of the cathode materials, hydrothermal synthesis of $LiFePO_4$ has been studied the most extensively.[101, 109-110] In the crystal structure of *Pnma* $LiFePO_4$, Li-ion follows an 1D diffusion mechanism and preferably transports along the *b*-direction.[73] Therefore, minimizing the crystal dimension in *b*-direction is crucial for reducing the Li transport length. For this reason, hydrothermal method is superior than solid-state reaction because the former allows for the control of particle size and morphology while the latter does not. To synthesize $LiFePO_4$ with desired properties, a range of critical parameters have been investigated. Chen and Whittingham[101] found

temperature higher than 180°C was necessary to effectively eliminate Li/Fe antisite defects and avoid blockage in Li-diffusion channel. pH of the precursor solution/suspension has shown profound impact on the purity, particle size, morphology, and defects of $LiFePO_4$. Liu et al.[111] showed that pure phase of $LiFePO_4$ could only be obtained at neutral or slightly alkaline conditions. Similarly, $LiCoPO_4$, which is an analogue to $LiFePO_4$, can be hydrothermally synthesized with a starting pH of 8.5. When a lower pH, i.e. pH = 5.7, was applied, $Co_3(OH)_2(PO_3OH)_2$ was obtained instead.[105] Increasing the concentration of precursors can lead to the formation of smaller particles, as reported by Dokko et al.[112] and Ellis et al.[113] Stirring speed is also an important parameter during hydrothermal synthesis. Vediappan et al. found that optimum stirring speed favored the production of particles with smaller size and less agglomeration.[114]

With the aim to modify the morphology of $LiFePO_4$, a range of hydrothermal studies have been focusing on the role of organic additives. For example, polyethylene glycol (PEG) was found to work as a capping agent to inhibit the crystal growth of $LiFePO_4$ and thus resulted in smaller particle size.[115] The addition of hexadecyl trimethyl ammonium bromide (CTAB) in hydrothermal treatment enabled the formation of $LiFePO_4$ nanoparticles that delivered high capacity close to the theoretical value.[116] Sodium dodecyl benzene sulfonate (SDBS) was found to serve as an anionic surfactant that can adsorb on the particle surface to affect the particle growth, thus tuning the particle size and morphology.[117] As shown in Figure 2.15, by varying the concentration of SDBS, nanoparticles, nanorods, and nanoplates of $LiFePO_4$ with varied *b*-axis thickness were prepared, amongst which the nanoplates presented the highest capacity of 162.9 mA h g^{-1} at 0.1C, respectively. Fagot-like $LiFePO_4$ mesocrystals formed by the oriented assembly of smaller rod-like units were prepared by using $Fe_3(PO_4)_2 \cdot 8H_2O$ and LiOH as the precursors in the presence of ascorbic acid.[118] Ascorbic acid was proposed to absorb on (001) and (010) faces and suppress the growth along the [001] and [010] directions. The formation of $LiFePO_4$ mesocrystals was explained by a branching growth mechanism on the precursor surface. Ascorbic acid is also commonly used as a reducing agent to the precursor to prevent the undesirable oxidation of Fe^{2+} species during hydrothermal treatment.[31, 113, 119] Degassing by bubbling N_2 or Ar gas is also an effective way to minimize oxidation.

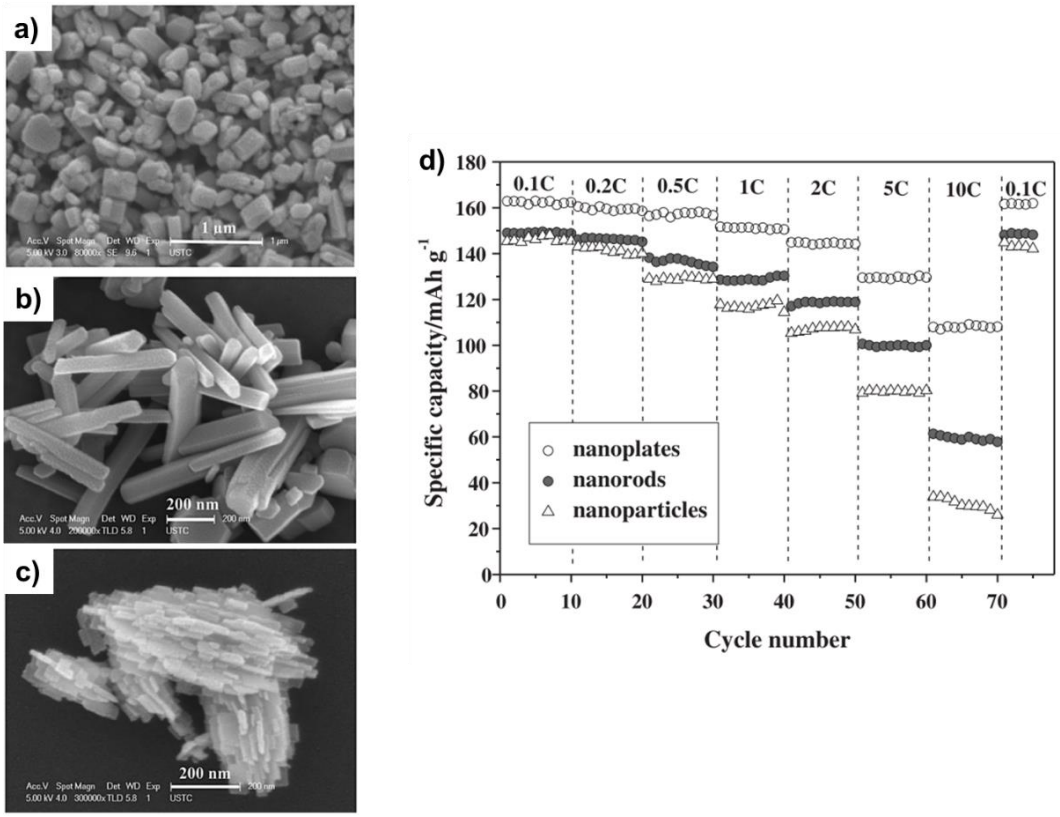

Figure 2.15. Hydrothermally synthesized $LiFePO_4$ using various concentrations of SDBS surfactant resulted in different morphology and electrochemical performance. SEM images of (a) nanoparticles, (b) nanorods, and (c) nanoplates. (d) Rate capacity and cycling performance.[117]

2.3.5 Hydrothermal synthesis of Li_2FeSiO_4

Hydrothermal synthesis has been applied on producing Li_2FeSiO_4 in orthorhombic *Pmn*2_1 polymorph. Table 2.4 summarizes the synthesis conditions, post treatment, particle properties and electrochemical performance of Li_2FeSiO_4 obtained by hydrothermal methods without post high temperature annealing.[46, 68-69, 71, 120-124] $LiOH{\cdot}H_2O$ is usually used as a Li precursor and a base to control pH in alkaline range. While for Fe precursors, various Fe-based salts have been studied, including $FeCl_2{\cdot}4H_2O$, $FeSO_4{\cdot}7H_2O$, and $(NH_4)_2Fe(SO_4)_2{\cdot}6H_2O$. For Si precursors, SiO_2 was used the most, whereas tetraethyl orthosilicate (TEOS) and Li_2SiO_3 were also used. To obtain LFS with minimum impurities, two times excess amount of lithium in the precursor is needed to synthesize Li_2FeSiO_4.[70-71] That is to say, the molar ratio between Li: (Fe or Si) > 4. Otherwise, significant amount of $FeOOH/Fe_2O_3/Fe_3O_4$ and Li_2SiO_3 were obtained. It is noticed that the types of Fe and Si precursors have profound effect on the morphology of the obtained Li_2FeSiO_4 particles. SiO_2 may favor the formation of mesocrystals, whereas TEOS and Li_2SiO_3 may lead to single crystal

nanoparticles, as shown in Figure 2.16a to 2.16c and 2.16d. On the other hand, depending on the Fe source ($FeCl_2$ in Figure 2.16a vs. $FeSO_4$ in Figure 2.16b), the mesocrystals formed in the presence of SiO_2 have different morphologies. This indicates that the properties of the starting materials, such as solubility, dissociated species and morphology, have direct impact on the nucleation and growth of Li_2FeSiO_4 crystals from hydrothermal conditions. Yet the mechanism behind the crystal formation has not been clearly demonstrated in the literature. The hydrothermally synthesized Li_2FeSiO_4 is usually subjected to post annealing with organic compounds to achieve carbon coating. This will induce phase transformation from orthorhombic $Pmn2_1$ to monoclinic $P2_1/n$ or orthorhombic *Pmnb* polymorphs depending on the temperature. There were only a few studies that reported the electrochemical performance of hydrothermal Li_2FeSiO_4 without high-temperature annealing.

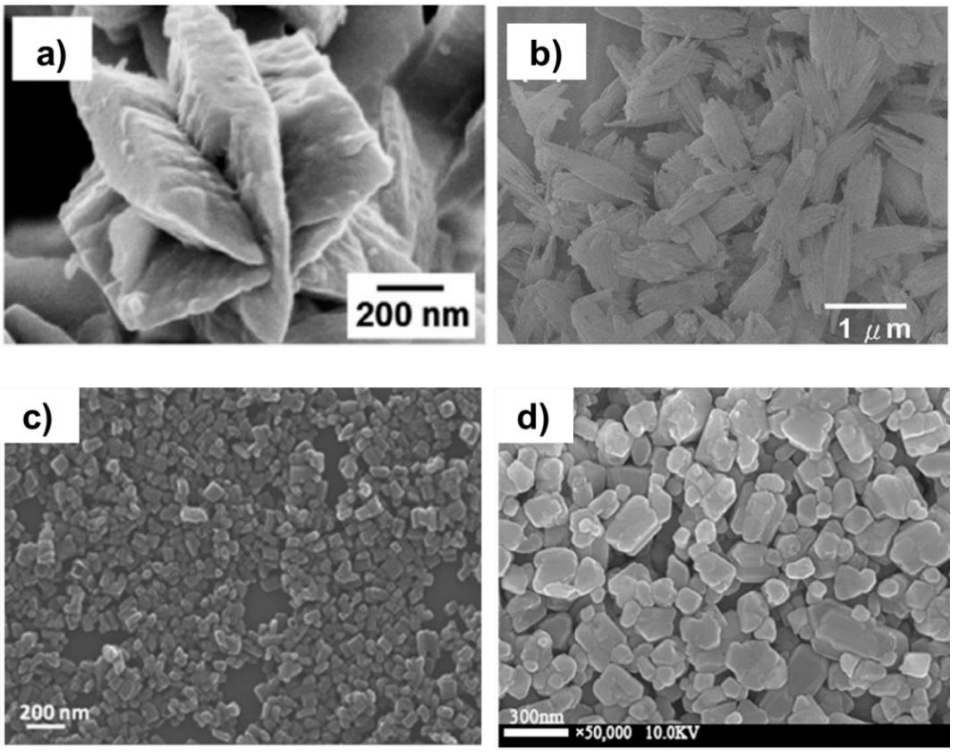

Figure 2.16. Effect of precursor on the morphology of hydrothermal synthesized LFS. (a) Six-armed mesocrystal synthesized by LiOH, $FeCl_2$ and SiO_2.[69] (b) Shuttle-like mesocrystals synthesized by LiOH, $FeSO_4$ and SiO_2.[70] (c) Nanoparticles synthesized by LiOH, $FeCl_2$ and TEOS.[123] (d) Nanoparticles synthesized by LiOH, $FeCl_2$ and Li_2SiO_3.[124]

Table 2.4. Summary of reported hydrothermal synthesis studies of Li_2FeSiO_4

Precursors	Temp./ time	Carbon mixing	Impurities	Size	Morphology	Discharge capacity mAh/g, cycle, rate, temp.*	Year
$LiOH{\cdot}H_2O$ 1.33M, $FeCl_2{\cdot}4H_2O$ 0.33M, SiO_2 0.33M	150°C/72h	-	Fe_3O_4	-	-	91, 3rd, C/30, RT	2006 [120]
$LiOH{\cdot}H_2O$ 1.33M, $FeCl_2{\cdot}4H_2O$ 0.33M, SiO_2 0.33M	150°C/72h	Ball-milled with acetylene black (600rpm, 24h)	Fe_3O_4 or Fe_2O_3	1μm	Agglomerate	130, 10th, C/20, RT	2010 [71]
$LiOH{\cdot}H_2O$ 0.27M, $FeCl_2{\cdot}4H_2O$ 0.07M, SiO_2 0.07M	200°C/6h	Ball-milled with Ketjen black (600 rpm, 6h)	pure	-	-	--	2011 [46]
$LiOH{\cdot}H_2O$, $FeCl_2{\cdot}4H_2O$, TEOS, ascorbic acid, sucrose	380°C/30min (SCF)	Coated within situ sucrose and ball-milled with MWCNT, CNF, and PEDOT	pure	20-60 nm wide, 50-500 nm long	Nanorod	120, 30th, C/20, RT	2013 [68]
$LiOH{\cdot}H_2O$ 0.4M, $(NH_4)_2Fe(SO_4)_2{\cdot}6H_2O$ 0.1M, SiO_2 0.1M	190°C /24h	-	pure	300nm wide, 1.6μm long	Spindle-like mesocrystal	20, 3rd, C/10, RT	2014 [122]
$LiOH{\cdot}H_2O$ 0.4M, $FeCl_2{\cdot}4H_2O$ 0.1M, SiO_2 0.1M, BPEI	150°C/16h	-	Fe_3O_4	1000 nm long, 100 nm thick	Six-armed mesocrystal	120, 20th, C/20, 60°C	2015 [69]
$LiOH{\cdot}H_2O$ 0.67M, $FeCl_2{\cdot}4H_2O$ 0.17M, TEOS 0.17M,	180°C /24h	-	pure	50-200 nm	Nanoparticle	-	2015 [123]
$LiOH{\cdot}H_2O$, $FeCl_2{\cdot}4H_2O$, Li_2SiO_3	250°C /3h	Ball-milled with acetylene black (380rpm, 24h)	Fe_3O_4, Li_2SiO_3	50-300 nm	Nanoparticle	144, 50th, C/10, N/A	2018 [124]

*Capacity noted here corresponds to the material without high temperature annealing that will induce phase transformation to monoclinic phase. 1C = 166 mA g^{-1}.

2.4 References

1. Goodenough, J. B., How we made the Li-ion rechargeable battery. *Nature Electronics* **2018,** *1* (3), 204-204.

2. Kasnatscheew, J.; Rodehorst, U.; Streipert, B.; Wiemers-Meyer, S.; Jakelski, R.; Wagner, R.; Laskovic, I. C.; Winter, M., Learning from Overpotentials in Lithium Ion Batteries: A Case Study on the $LiNi_{1/3}Co_{1/3}Mn_{1/3}O_2$ (NCM) Cathode. *Journal of The Electrochemical Society* **2016,** *163* (14), A2943-A2950.

3. Nitta, N.; Wu, F.; Lee, J. T.; Yushin, G., Li-ion battery materials: present and future. *Materials Today* **2015,** *18* (5), 252-264.

4. Blomgren, G. E., The Development and Future of Lithium Ion Batteries. *Journal of The Electrochemical Society* **2017,** *164* (1), A5019-A5025.

5. Matthew, L.; Jun, L.; Zhongwei, C.; Khalil, A., 30 Years of Lithium‐Ion Batteries. *Advanced Materials* **2018,** *0* (0), 1800561.

6. Mizushima, K.; Jones, P. C.; Wiseman, P. J.; Goodenough, J. B., Li_xCoO_2 ($0<x<-1$): A new cathode material for batteries of high energy density. *Materials Research Bulletin* **1980,** *15* (6), 783-789.

7. Ozawa, K., Lithium-ion rechargeable batteries with $LiCoO_2$ and carbon electrodes: the $LiCoO_2$/C system. *Solid State Ionics* **1994,** *69* (3), 212-221.

8. Amatucci, G. G.; Tarascon, J. M.; Klein, L. C., CoO_2, The End Member of the Li_xCoO_2 Solid Solution. *Journal of The Electrochemical Society* **1996,** *143* (3), 1114-1123.

9. Chebiam, R. V.; Kannan, A. M.; Prado, F.; Manthiram, A., Comparison of the chemical stability of the high energy density cathodes of lithium-ion batteries. *Electrochemistry Communications* **2001,** *3* (11), 624-627.

10. Reimers, J. N.; Dahn, J. R., Electrochemical and In Situ X‐Ray Diffraction Studies of Lithium Intercalation in Li x CoO2. *Journal of The Electrochemical Society* **1992,** *139* (8), 2091-2097.

11. Lu, Z.; MacNeil, D. D.; Dahn, J. R., Layered Cathode Materials Li $[Ni_xLi_{(1/3-2x/3)}Mn_{(2/3-x/3)}]O_2$ for Lithium-Ion Batteries. *Electrochemical and Solid-State Letters* **2001,** *4* (11), A191-A194.

12. Goonetilleke, D.; Sharma, N.; Pang, W. K.; Peterson, V. K.; Petibon, R.; Li, J.; Dahn, J. R., Structural evolution and high voltage structural stability of $Li(Ni_xMn_yCo_z)O_2$ electrodes. *Chemistry of Materials* **2019**, *31* (2), 376-386

13. Schipper, F.; Erickson, E. M.; Erk, C.; Shin, J.-Y.; Chesneau, F. F.; Aurbach, D., Review—Recent Advances and Remaining Challenges for Lithium Ion Battery Cathodes: I. Nickel-Rich, $LiNi_xCo_yMn_zO_2$. *Journal of The Electrochemical Society* **2017,** *164* (1), A6220-A6228.

14. Manthiram, A.; Song, B.; Li, W., A perspective on nickel-rich layered oxide cathodes for lithium-ion batteries. *Energy Storage Materials* **2017,** *6*, 125-139.

15. Li, Z.; Chernova, N. A.; Roppolo, M.; Upreti, S.; Petersburg, C.; Alamgir, F. M.; Whittingham, M. S., Comparative Study of the Capacity and Rate Capability of $LiNi_yMn_yCo_{1-2y}O_2$ (y = 0.5, 0.45, 0.4, 0.33). *Journal of The Electrochemical Society* **2011,** *158* (5), A516-A522.

16. Lee, K. K.; Yoon, W. S.; Kim, K. B.; Lee, K. Y.; Hong, S. T., Characterization of $LiNi_{0.85}Co0.10M_{0.05}O_2$ (M = Al, Fe) as a cathode material for lithium secondary batteries. *Journal of Power Sources* **2001,** *97-98*, 308-312.

17. Inoue, T.; Mukai, K., Roles of positive or negative electrodes in the thermal runaway of lithium-ion batteries: Accelerating rate calorimetry analyses with an all-inclusive microcell. *Electrochemistry Communications* **2017,** *77*, 28-31.

18. Zhuang, G. V.; Chen, G.; Shim, J.; Song, X.; Ross, P. N.; Richardson, T. J., Li_2CO_3 in $LiNi_{0.8}Co_{0.15}Al_{0.05}O_2$ cathodes and its effects on capacity and power. *Journal of Power Sources* **2004,** *134* (2), 293-297.

19. Cho, Y.; Cho, J., Significant Improvement of $LiNi_{0.8}Co_{0.15}Al_{0.05}O_2$ Cathodes at 60 ° C by SiO2 Dry Coating for Li-Ion Batteries. *Journal of The Electrochemical Society* **2010,** *157* (6), A625-A629.

20. Amatucci, G.; Tarascon, J.-M., Optimization of Insertion Compounds Such as $LiMn_2O_4$ for Li-Ion Batteries. *Journal of The Electrochemical Society* **2002,** *149* (12), K31-K46.

21. MacNeil, D. D.; Hatchard, T. D.; Dahn, J. R., A Comparison Between the High Temperature Electrode/Electrolyte Reactions of Li_xCoO_2 and $Li_xMn_2O_4$. *Journal of The Electrochemical Society* **2001,** *148* (7), A663-A667.

22. Blyr, A.; Sigala, C.; Amatucci, G.; Guyomard, D.; Chabre, Y.; Tarascon, J. M., Self‐Discharge of $LiMn_2O_4$/C Li‐Ion Cells in Their Discharged State: Understanding by Means of Three‐Electrode Measurements. *Journal of The Electrochemical Society* **1998,** *145* (1), 194-209.

23. A. K. Padhi, K. N., and J. B. Goodenough, Phospho-olivines as Positive‐Electrode Materials for Rechargeable Lithium Batteries. *Journal of The Electrochem Society* **1997**, *144* (4), 1188-1194.

24. Zhou, F.; Kang, K.; Maxisch, T.; Ceder, G.; Morgan, D., The electronic structure and band gap of $LiFePO_4$ and $LiMnPO_4$. *Solid State Communications* **2004,** *132* (3), 181-186.

25. Yamada, A.; Chung, S. C.; Hinokuma , K., Optimized $LiFePO_4$ for Lithium Battery Cathodes. *Journal of The Electrochemical Society* **2001,** *148* (3), A224-A229.

26. Zaghib, K.; Mauger, A.; Goodenough, J. B.; Gendron, F.; Julien, C. M., Electronic, optical, and magnetic properties of $LiFePO_4$: Small magnetic polaron effects. *Chemistry of Materials* **2007,** *19* (15), 3740-3747.

27. Wang, J.; Sun, X., Understanding and recent development of carbon coating on $LiFePO_4$ cathode materials for lithium-ion batteries. *Energy & Environmental Science* **2012,** *5* (1), 5163-5185.

28. Herstedt, M.; Stjerndahl, M.; Nytén, A.; Gustafsson, T.; Rensmo, H.; Siegbahn, H.; Ravet, N.; Armand, M.; Thomas, J. O.; Edström, K., Surface Chemistry of Carbon-Treated $LiFePO_4$ Particles for Li-Ion Battery Cathodes Studied by PES. *Electrochemical and Solid-State Letters* **2003,** *6* (9), A202-A206.

29. Delacourt, C.; Poizot, P.; Levasseur, S.; Masquelier, C., Size effects on carbon-free $LiFePO_4$ powders: The key to superior energy density. *Electrochemical and Solid-State Letters* **2006,** *9* (7), A352-A355.

30. Nishimura, S.; Kobayashi, G.; Ohoyama, K.; Kanno, R.; Yashima, M.; Yamada, A., Experimental visualization of lithium diffusion in Li_xFePO_4. *Nature Matererials* **2008,** *7* (9), 707-11.

31. Paolella, A.; Turner, S.; Bertoni, G.; Hovington, P.; Flacau, R.; Boyer, C.; Feng, Z.; Colombo, M.; Marras, S.; Prato, M.; Manna, L.; Guerfi, A.; Demopoulos, G. P.; Armand, M.; Zaghib, K., Accelerated removal of Fe-antisite defects while nanosizing hydrothermal $LiFePO_4$ with Ca^{2+}. *Nano Letters* **2016,** *16* (4), 2692–2697.

32. Axmann, P.; Stinner, C.; Wohlfahrt-Mehrens, M.; Mauger, A.; Gendron, F.; Julien, C. M., Nonstoichiometric $LiFePO_4$: Defects and Related Properties. *Chemistry of Materials* **2009,** *21* (8), 1636-1644.

33. Momma, K.; Izumi, F., VESTA 3 for three-dimensional visualization of crystal, volumetric and morphology data. *Journal of Applied Crystallography* **2011,** *44* (6), 1272-1276.

34. Armand, M., Lithium insertion electrode materials based on orthosilicate derivatives. *U.S. Patent 6 085 015* **2000**.

35. Simoneau, M.; Hovington, P.; Armand, M.; Michot, C.; Ravet, N.; Christopher, M. New lithium insertion-type electrode material with an orthosilicate structure for use in redox reactions. US6085015-A, 04 Jul **2000**.

36. Girish, H. N.; Shao, G. Q., Advances in high-capacity Li_2MSiO_4 (M = Mn, Fe, Co, Ni, ...) cathode materials for lithium-ion batteries. *Rsc Advances* **2015,** *5* (119), 98666-98686.

37. Chen, Q.; Xiao, P.; Pei, Y.; Song, Y.; Xu, C.-Y.; Zhen, L.; Henkelman, G., Structural transformations in Li_2MnSiO_4: evidence that a Li intercalation material can reversibly cycle through a disordered phase. *Journal of Materials Chemistry A* **2017,** *5* (32), 16722-16731.

38. Pei, Y.; Chen, Q.; Xu, C.-Y.; Wang, H.-X.; Fang, H.-T.; Zhou, C.; Zhen, L.; Cao, G., Chelate-induced formation of Li2MnSiO4 nanorods as a high capacity cathode material for Li-ion batteries. *Journal of Materials Chemistry A* **2016,** *4* (24), 9447-9454.

39. Saracibar, A.; Wang, Z.; Carroll, K. J.; Meng, Y. S.; Dompablo, M. E. A.-d., New insights into the electrochemical performance of Li2MnSiO4: effect of cationic substitutions. *Journal of Materials Chemistry A* **2015,** *3* (11), 6004-6011.

40. Dominko, R., Li_2MSiO_4 (M=Fe and/or Mn) cathode materials. *Journal of Power Sources* **2008,** *184* (2), 462-468.

41. He, G.; Popov, G.; Nazar, L. F., Hydrothermal synthesis and electrochemical poperties of Li_2CoSiO_4/C nanospheres. *Chemistry of Materials* **2013,** *25* (7), 1024-1031.

42. Armstrong, A. R.; Lyness, C.; Ménétrier, M.; Bruce, P. G., Structural polymorphism in Li_2CoSiO_4 intercalation electrodes: A combined diffraction and NMR study. *Chemistry of Materials* **2010,** *22* (5), 1892-1900.

43. Gong, Z. L.; Li, Y. X.; Yang, Y., Synthesis and electrochemical performance of Li_2CoSiO_4 as cathode material for lithium ion batteries. *Journal of Power Sources* **2007,** *174* (2), 524-527.

44. Arroyo-de Dompablo, M. E.; Armand, M.; Tarascon, J. M.; Amador, U., On-demand design of polyoxianionic cathode materials based on electronegativity correlations: An exploration of the Li_2MSiO_4 system (M=Fe, Mn, Co, Ni). *Electrochemistry Communications* **2006,** *8* (8), 1292-1298.

45. Armstrong, A. R.; Sirisopanaporn, C.; Adamson, P.; Billaud, J.; Dominko, R.; Masquelier, C.; Bruce, P. G., Polymorphism in Li_2MSiO_4 (M = Fe, Mn): A variable temperature diffraction study. *Zeitschrift für anorganische und allgemeine Chemie* **2014,** *640* (6), 1043-1049.

46. Sirisopanaporn, C.; Masquelier, C.; Bruce, P. G.; Armstrong, A. R.; Dominko, R., Dependence of Li_2FeSiO_4 electrochemistry on structure. *Journal of the American Chemical Society* **2011,** *133* (5), 1263-1265.

47. Nishimura, S.-i.; Hayase, S.; Kanno, R.; Yashima, M.; Nakayama, N.; Yamada, A., Structure of Li_2FeSiO_4. *Journal of the American Chemical Society* **2008,** *130* (40), 13212-13213.

48. Boulineau, A.; Sirisopanaporn, C.; Dominko, R.; Armstrong, A. R.; Bruce, P. G.; Masquelier, C., Polymorphism and structural defects in Li_2FeSiO_4. *Dalton Transactions* **2010,** *39* (27), 6310-6316.

49. Eames, C.; Armstrong, A. R.; Bruce, P. G.; Islam, M. S., Insights into changes in voltage and structure of Li_2FeSiO_4 polymorphs for lithium-ion batteries. *Chemistry of Materials* **2012,** *24* (11), 2155-2161.

50. Islam, M. S.; Dominko, R.; Masquelier, C.; Sirisopanaporn, C.; Armstrong, A. R.; Bruce, P. G., Silicate cathodes for lithium batteries: alternatives to phosphates? *Journal of Materials Chemistry* **2011,** *21* (27), 9811-9818.

51. Armstrong, A. R.; Kuganathan, N.; Islam, M. S.; Bruce, P. G., Structure and lithium transport pathways in Li_2FeSiO_4 cathodes for lithium batteries. *Journal of the American Chemical Society* **2011,** *133* (33), 13031-13035.

52. Masese, T.; Tassel, C.; Orikasa, Y.; Koyama, Y.; Arai, H.; Hayashi, N.; Kim, J.; Mori, T.; Yamamoto, K.; Kobayashi, Y.; Kageyama, H.; Ogumi, Z.; Uchimoto, Y., Crystal structural changes and charge compensation mechanism during two lithium extraction/insertion between Li_2FeSiO_4 and $FeSiO_4$. *The Journal of Physical Chemistry C* **2015,** *119* (19), 10206-10211.

53. Chen, R.; Heinzmann, R.; Mangold, S.; Chakravadhanula, V. S. K.; Hahn, H.; Indris, S., Structural Evolution of $Li_2Fe_{1-y}Mn_ySiO_4$ (y = 0, 0.2, 0.5, 1) Cathode Materials for Li-Ion Batteries upon Electrochemical Cycling. *The Journal of Physical Chemistry C* **2013,** *117* (2), 884-893.

54. Kojima, A.; Kojima, T.; Sakai, T., Structural Analysis during Charge-Discharge Process of Li_2FeSiO_4 Synthesized by Molten Carbonate Flux Method. *Journal of The Electrochemical Society* **2012,** *159* (5), A525-A531.

55. Zaghib, K.; Ait Salah, A.; Ravet, N.; Mauger, A.; Gendron, F.; Julien, C. M., Structural, magnetic and electrochemical properties of lithium iron orthosilicate. *Journal of Power Sources* **2006,** *160* (2), 1381-1386.

56. Nytén, A.; Abouimrane, A.; Armand, M.; Gustafsson, T.; Thomas, J. O., Electrochemical performance of Li_2FeSiO_4 as a new Li-battery cathode material. *Electrochemistry Communications* **2005,** *7* (2), 156-160.

57. Nytén, A.; Kamali, S.; Häggström, L.; Gustafsson, T.; Thomas, J. O., The lithium extraction/insertion mechanism in Li_2FeSiO_4. *Journal of Materials Chemistry* **2006,** *16* (23), 2266-2272.

58. Sirisopanaporn, C.; Boulineau, A.; Hanzel, D.; Dominko, R.; Budic, B.; Armstrong, A. R.; Bruce, P. G.; Masquelier, C., Crystal Structure of a New Polymorph of Li_2FeSiO_4. *Inorganic Chemistry* **2010,** *49* (16), 7446-7451.

59. Li, D.; Zhang, W.; Sun, R.; Yong, H.-T.-H.; Chen, G.; Fan, X.; Gou, L.; Mao, Y.; Zhao, K.; Tian, M., Soft-template construction of three-dimensionally ordered inverse opal structure from Li_2FeSiO_4/C composite nanofibers for high-rate lithium-ion batteries. *Nanoscale* **2016,** *8* (24), 12202-12214.

60. Ding, Z.; Liu, J.; Ji, R.; Zeng, X.; Yang, S.; Pan, A.; Ivey, D. G.; Wei, W., Three-dimensionally ordered macroporous Li_2FeSiO_4/C composite as a high performance cathode for advanced lithium ion batteries. *Journal of Power Sources* **2016,** *329*, 297-304.

61. Chen, Z.; Qiu, S.; Cao, Y.; Qian, J.; Ai, X.; Xie, K.; Hong, X.; Yang, H., Hierarchical porous Li_2FeSiO_4/C composite with 2 Li storage capacity and long cycle stability for advanced Li-ion batteries. *Journal of Materials Chemistry A* **2013,** *1* (16), 4988.

62. Jiang, X. L.; Xu, H. Y.; Yang, J.; Liu, J.; Mao, H. Z.; Qian, Y. T., Synthesis of novel morphologies of Li_2FeSiO_4/C micro/nano composites by a facile hydrothermal method. *Rsc Advances* **2014,** *4* (75), 39889-39893.

63. Nytén, A.; Stjerndahl, M.; Rensmo, H.; Siegbahn, H.; Armand, M.; Gustafsson, T.; Edström, K.; Thomas, J. O., Surface characterization and stability phenomena in Li_2FeSiO_4 studied by PES/XPS. *Journal of Materials Chemistry* **2006,** *16* (34), 3483-3488.

64. Deng, C.; Zhang, S.; Gao, Y.; Wu, B.; Ma, L.; Sun, Y. H.; Fu, B. L.; Wu, Q.; Liu, F. L., Regeneration and characterization of air-exposed Li_2FeSiO_4. *Electrochimica Acta* **2011,** *56* (21), 7327-7333.

65. Arroyo-de Dompablo, M. E.; Armand, M.; Tarascon, J. M.; Amador, U., On-demand design of polyoxianionic cathode materials based on electronegativity correlations: An exploration of the Li_2MSiO_4 system (M = Fe, Mn, Co, Ni). *Electrochemistry Communications* **2006,** *8* (8), 1292-1298.

66. Yabuuchi, N.; Yamakawa, Y.; Yoshii, K.; Komaba, S., Low-temperature phase of Li_2FeSiO_4: Crystal structure and a preliminary study of electrochemical behavior. *Dalton Transactions* **2011,** *40* (9), 1846-1848.

67. Dominko, R.; Conte, D. E.; Hanzel, D.; Gaberscek, M.; Jamnik, J., Impact of synthesis conditions on the structure and performance of Li_2FeSiO_4. *Journal of Power Sources* **2008,** *178* (2), 842-847.

68. Devaraju, M. K.; Tomai, T.; Honma, I., Supercritical hydrothermal synthesis of rod like Li_2FeSiO_4 particles for cathode application in lithium ion batteries. *Electrochimica Acta* **2013,** *109*, 75-81.

69. Kageyama, H.; Hashimoto, Y.; Oaki, Y.; Imai, H., Six-armed twin crystals composed of lithium iron silicate nanoplates and their electrochemical properties. *Crystengcomm* **2015,** *17* (44), 8486-8491.

70. Hsu, C.-H.; Shen, Y.-W.; Chien, L.-H.; Kuo, P.-L., Li_2FeSiO_4 nanorod as high stability electrode for lithium-ion batteries. *Journal of Nanoparticle Research* **2015,** *17* (1), 1-9.

71. Yabuuchi, N.; Yamakawa, Y.; Yoshii, K.; Komaba, S., Hydrothermal synthesis and characterization of Li_2FeSiO_4 as positive electrode materials for Li-ion batteries. *Electrochemistry* **2010,** *78* (5), 363-366.

72. Lv, D.; Wen, W.; Huang, X.; Bai, J.; Mi, J.; Wu, S.; Yang, Y., A novel Li_2FeSiO_4/C composite: Synthesis, characterization and high storage capacity. *Journal of Materials Chemistry* **2011,** *21* (26), 9506-9512.

73. Islam, M. S.; Driscoll, D. J.; Fisher, C. A. J.; Slater, P. R., Atomic-scale investigation of defects, dopants, and lithium transport in the $LiFePO_4$ olivine-type battery material. *Chemistry of Materials* **2005,** *17* (20), 5085-5092.

74. Rangappa, D.; Murukanahally, K. D.; Tomai, T.; Unemoto, A.; Honma, I., Ultrathin Nanosheets of Li_2MSiO_4 (M = Fe, Mn) as High-Capacity Li-Ion Battery Electrode. *Nano Letters* **2012,** *12* (3), 1146-1151.

75. Ding, Z.; Zhang, D.; Feng, Y.; Zhang, F.; Chen, L.; Du, Y.; Ivey, D. G.; Wei, W., Tuning anisotropic ion transport in mesocrystalline lithium orthosilicate nanostructures with preferentially exposed facets. *Npg Asia Mater* **2018,** *10* (7), 606-617.

76. Yang, J.; Kang, X.; He, D.; Zheng, A.; Pan, M.; Mu, S., Graphene activated 3D-hierarchical flower-like Li_2FeSiO_4 for high-performance lithium-ion batteries. *Journal of Materials Chemistry A* **2015,** *3* (32), 16567-16573.

77. Zhu, H.; Wu, X.; Zan, L.; Zhang, Y., Three-Dimensional Macroporous Graphene–Li2FeSiO4 Composite as Cathode Material for Lithium-Ion Batteries with Superior Electrochemical Performances. *ACS Applied Materials & Interfaces* **2014,** *6* (14), 11724-11733.

78. Zhu, H.; Wu, X.; Zan, L.; Zhang, Y., Superior electrochemical capability of Li_2FeSiO_4/C/G composite as cathode material for Li-ion batteries. *Electrochimica Acta* **2014,** *117*, 34-40.

79. Zhang, L.-L.; Duan, S.; Yang, X.-L.; Peng, G.; Liang, G.; Huang, Y.-H.; Jiang, Y.; Ni, S.-B.; Li, M., Reduced graphene oxide modified Li_2FeSiO_4/C composite with enhanced electrochemical performance as cathode material for lithium ion batteries. *ACS Applied Materials & Interfaces* **2013,** *5* (23), 12304-12309.

80. Lv, D. P.; Bai, J. Y.; Zhang, P.; Wu, S. Q.; Li, Y. X.; Wen, W.; Jiang, Z.; Mi, J. X.; Zhu, Z. Z.; Yang, Y., Understanding the high Capacity of Li_2FeSiO_4: in situ XRD/XANES study combined with first-principles calculations. *Chemistry of Materials* **2013,** *25* (10), 2014-2020.

81. Brownrigg, A. W.; Mountjoy, G.; Chadwick, A. V.; Alfredsson, M.; Bras, W.; Billaud, J.; Armstrong, A. R.; Bruce, P. G.; Dominko, R.; Kelder, E. M., In situ Fe K-edge X-ray absorption spectroscopy study during cycling of Li_2FeSiO_4 and $Li_{2.2}Fe_{0.9}SiO_4$ Li ion battery materials. *Journal of Materials Chemistry A* **2015,** *3* (14), 7314-7322.

82. Liivat, A.; Thomas, J.; Guo, J.; Yang, Y., Novel insights into higher capacity from the Li-ion battery cathode material Li2FeSiO4. *Electrochimica Acta* **2017,** *223*, 109-114.

83. Lu, X.; Chiu, H.-C.; Arthur, Z.; Zhou, J.; Wang, J.; Chen, N.; Jiang, D.-T.; Zaghib, K.; Demopoulos, G. P., Li-ion storage dynamics in metastable nanostructured Li_2FeSiO_4 cathode: Antisite-induced phase transition and lattice oxygen participation. *Journal of Power Sources* **2016,** *329*, 355-363.

84. Suchanek, W. L.; Lencka, M. M.; Riman, R. E., Chapter 18 - Hydrothermal synthesis of ceramic materials A2 - Palmer, Donald A. In *Aqueous Systems at Elevated Temperatures and Pressures*, Fernández-Prini, R.; Harvey, A. H., Eds. Academic Press: London, 2004; pp 717-744.

85. Byrappa, K.; Yoshimura, M., 1 - Hydrothermal Technology—Principles and Applications. In *Handbook of Hydrothermal Technology (Second Edition)*, William Andrew Publishing: Oxford, 2013; pp 1-49.

86. Byrappa, K.; Yoshimura, M., 4 - Physical Chemistry of Hydrothermal Growth of Crystals. In *Handbook of Hydrothermal Technology*, William Andrew Publishing: Norwich, NY, 2001; pp 161-197.

87. Yoshimura, M.; Byrappa, K., Hydrothermal processing of materials: Past, present and future. *Journal of Materials Science* **2008,** *43* (7), 2085-2103.

88. Uematsu, M.; Frank, E. U., Static Dielectric Constant of Water and Steam. *Journal of Physical and Chemical Reference Data* **1980,** *9* (4), 1291-1306.

89. Parr Instrument Company. https://www.parrinst.com/products/ (accessed 2019 June).

90. Demopoulos, G. P., Aqueous precipitation and crystallization for the production of particulate solids with desired properties. *Hydrometallurgy* **2009,** *96* (3), 199-214.

91. Mullin, J. W., 5 - Nucleation. In *Crystallization (Fourth Edition)*, Butterworth-Heinemann: Oxford, 2001; pp 181-215.

92. De Yoreo, J.; Whitelam, S., Nucleation in atomic, molecular, and colloidal systems. *MRS Bulletin* **2016,** *41* (05), 357-360.

93. Kwon, S. G.; Hyeon, T., Formation Mechanisms of Uniform Nanocrystals via Hot-Injection and Heat-Up Methods. *Small* **2011,** *7* (19), 2685-2702.

94. Whittaker, M. L.; Dove, P. M.; Joester, D., Nucleation on surfaces and in confinement. *MRS Bulletin* **2016,** *41* (5), 388-392.

95. Sear, R., What do crystals nucleate on? What is the microscopic mechanism? How can we model nucleation? *MRS Bulletin* **2016,** *41* (5), 363-368.

96. LaMer, V. K.; Dinegar, R. H., Theory, Production and Mechanism of Formation of Monodispersed Hydrosols. *Journal of the American Chemical Society* **1950,** *72* (11), 4847-4854.

97. Polte, J., Fundamental growth principles of colloidal metal nanoparticles – a new perspective. *CrystEngComm* **2015,** *17* (36), 6809-6830.

98. De Yoreo, J. J.; Gilbert, P. U. P. A.; Sommerdijk, N. A. J. M.; Penn, R. L.; Whitelam, S.; Joester, D.; Zhang, H.; Rimer, J. D.; Navrotsky, A.; Banfield, J. F.; Wallace, A. F.; Michel, F. M.; Meldrum, F. C.; Cölfen, H.; Dove, P. M., Crystallization by particle attachment in synthetic, biogenic, and geologic environments. *Science* **2015,** *349* (6247), aaa6760.

99. Zaghib, K.; Guerfi, A.; Hovington, P.; Vijh, A.; Trudeau, M.; Mauger, A.; Goodenough, J. B.; Julien, C. M., Review and analysis of nanostructured olivine-based lithium recheargeable batteries: Status and trends. *Journal of Power Sources* **2013,** *232*, 357-369.

100. Lee, K. T.; Cho, J., Roles of nanosize in lithium reactive nanomaterials for lithium ion batteries. *Nano Today* **2011,** *6* (1), 28-41.

101. Chen, J.; Whittingham, M. S., Hydrothermal synthesis of lithium iron phosphate. *Electrochemistry Communications* **2006,** *8* (5), 855-858.

102. Okubo, M.; Hosono, E.; Kim, J.; Enomoto, M.; Kojima, N.; Kudo, T.; Zhou, H.; Honma, I., Nanosize Effect on High-Rate Li-Ion Intercalation in $LiCoO_2$ Electrode. *Journal of the American Chemical Society* **2007,** *129* (23), 7444-7452.

103. Myung, S.-T.; Komaba, S.; Kumagai, N., Hydrothermal synthesis and electrochemical behavior of orthorhombic $LiMnO_2$. *Electrochimica Acta* **2002,** *47* (20), 3287-3295.

104. Wu, H. M.; Tu, J. P.; Yuan, Y. F.; Chen, X. T.; Xiang, J. Y.; Zhao, X. B.; Cao, G. S., One-step synthesis $LiMn_2O_4$ cathode by a hydrothermal method. *Journal of Power Sources* **2006,** *161* (2), 1260-1263.

105. Huang, X.; Ma, J.; Wu, P.; Hu, Y.; Dai, J.; Zhu, Z.; Chen, H.; Wang, H., Hydrothermal synthesis of $LiCoPO_4$ cathode materials for rechargeable lithium ion batteries. *Materials Letters* **2005,** *59* (5), 578-582.

106. Gao, Z.; Pan, X.; Li, H.; Xie, S.; Yi, R.; Jin, W., Hydrothermal synthesis and electrochemical properties of dispersed $LiMnPO_4$ wedges. *CrystEngComm* **2013,** *15* (38), 7808-7814.

107. Liu, H.; Cheng, C.; Huang, X.; Li, J., Hydrothermal synthesis and rate capacity studies of $Li_3V_2(PO_4)_3$ nanorods as cathode material for lithium-ion batteries. *Electrochimica Acta* **2010,** *55* (28), 8461-8465.

108. Ren, M. M.; Zhou, Z.; Gao, X. P.; Liu, L.; Peng, W. X., $LiVOPO_4$ Hollow Microspheres: One-Pot Hydrothermal Synthesis with Reactants as Self-Sacrifice Templates and Lithium Intercalation Performances. *The Journal of Physical Chemistry C* **2008,** *112* (33), 13043-13046.

109. Chen, J.; Wang, S.; Whittingham, M. S., Hydrothermal synthesis of cathode materials. *Journal of Power Sources* **2007,** *174* (2), 442-448.

110. Devaraju, M. K.; Honma, I., Hydrothermal and solvothermal process towards development of $LiMPO_4$ (M = Fe, Mn) nanomaterials for lithium-ion batteries. *Advanced Energy Materials* **2012,** *2* (3), 284-297.

111. Liu, J.; Jiang, R.; Wang, X.; Huang, T.; Yu, A., The defect chemistry of $LiFePO_4$ prepared by hydrothermal method at different pH values. *Journal of Power Sources* **2009,** *194* (1), 536-540.

112. Dokko, K.; Koizumi, S.; Kanamura, K., Electrochemical Reactivity of $LiFePO_4$ Prepared by Hydrothermal Method. *Chemistry Letters* **2006,** *35* (3), 338-339.

113. Ellis, B.; Kan, W. H.; Makahnouk, W. R. M.; Nazar, L. F., Synthesis of nanocrystals and morphology control of hydrothermally prepared $LiFePO_4$. *Journal of Materials Chemistry* **2007,** *17* (30), 3248-3254.

114. Vediappan, K.; Guerfi, A.; Gariépy, V.; Demopoulos, G. P.; Hovington, P.; Trottier, J.; Mauger, A.; Zaghib, K.; Julien, C. M., Effect of the stirring during the hydrothermal synthesis of C-$LiFePO_4$. *ECS Transactions* **2014,** *58* (14), 67-72.

115. Tajimi, S.; Ikeda, Y.; Uematsu, K.; Toda, K.; Sato, M., Enhanced electrochemical performance of $LiFePO_4$ prepared by hydrothermal reaction. *Solid State Ionics* **2004,** *175* (1), 287-290.

116. Meligrana, G.; Gerbaldi, C.; Tuel, A.; Bodoardo, S.; Penazzi, N., Hydrothermal synthesis of high surface $LiFePO_4$ powders as cathode for Li-ion cells. *Journal of Power Sources* **2006,** *160* (1), 516-522.

117. Pei, B.; Yao, H.; Zhang, W.; Yang, Z., Hydrothermal synthesis of morphology-controlled LiFePO4 cathode material for lithium-ion batteries. *Journal of Power Sources* **2012,** *220*, 317-323.

118. Uchiyama, H.; Imai, H., Preparation of $LiFePO_4$ Mesocrystals Consisting of Nanorods through Organic-Mediated Parallel Growth from a Precursor Phase. *Crystal Growth & Design* **2010,** *10* (4), 1777-1781.

119. Paolella, A.; Bertoni, G.; Hovington, P.; Feng, Z.; Flacau, R.; Prato, M.; Colombo, M.; Marras, S.; Manna, L.; Turner, S.; Van Tendeloo, G.; Guerfi, A.; Demopoulos, G. P.; Zaghib, K., Cation exchange mediated elimination of the Fe-antisites in the hydrothermal synthesis of $LiFePO_4$. *Nano Energy* **2015,** *16*, 256-267.

120. Dominko, R.; Bele, M.; Gaberšček, M.; Meden, A.; Remškar, M.; Jamnik, J., Structure and electrochemical performance of Li_2MnSiO_4 and Li_2FeSiO_4 as potential Li-battery cathode materials. *Electrochemistry Communications* **2006,** *8* (2), 217-222.

121. Zhang, M.; Chen, Q. P.; Xi, Z. X.; Hou, Y. G.; Chen, Q. L., One-step hydrothermal synthesis of Li_2FeSiO_4/C composites as lithium-ion battery cathode materials. *Journal of Materials Science* **2012,** *47* (5), 2328-2332.

122. Gao, H. Y.; Hu, Z.; Zhang, K.; Cheng, F. Y.; Tao, Z. L.; Chen, J., Hydrothermal synthesis of spindle-like Li_2FeSiO_4-C composite as cathode materials for lithium-ion batteries. *Journal of Energy Chemistry* **2014,** *23* (3), 274-281.

123. Xu, Y.; Shen, W.; Wang, C.; Zhang, A.; Xu, Q.; Liu, H.; Wang, Y.; Xia, Y., Hydrothermal synthesis and electrochemical performance of nanoparticle Li_2FeSiO_4/C cathode materials for lithium ion batteries. *Electrochimica Acta* **2015,** *167*, 340-347.

124. Liu, L.; Wang, P.; Li, J.; Shi, G.; Ma, L.; Zhao, J.; An, H., Hydrothermal preparation and intrinsic transport properties of nanoscale Li_2FeSiO_4. *Solid State Ionics* **2018,** *320*, 353-359.

Chapter 3. Hydrothermal Crystallization of *Pmn*2$_1$ Li_2FeSiO_4 Hollow Mesocrystals for Li-Ion Cathode Application

As reviewed in Chapter 2, LFS is a promising cathode material which has high theoretical energy density and sustainable features for energy storage applications. To achieve the full potential LFS, it is essential to be able to synthesize the material with desired properties. In this chapter, we apply hydrothermal synthesis due to its advantages on tailoring particle size, morphology, and crystal structure. The crystallization mechanism of LFS is unveiled through *ex situ* characterizations to provide insights into the evolution of crystal structure, composition, and morphology. The understanding of the underlying formation mechanism enables us to identity the key synthesis parameters that control the particle size, phase purity, and defects. In the end of this chapter, a preliminary charge-discharge test is performed to evaluate the electrochemical activity of the hydrothermal synthesized LFS.

This chapter was published as **Yan Zeng**, Hsien-Chieh Chiu, Majid Rasool, Nicolas Brodusch, Raynald Gauvin, De-Tong Jiang, Dominic H. Ryan, Karim Zaghib, George P. Demopoulos. Hydrothermal crystallization of *Pmn*2$_1$ Li_2FeSiO_4 hollow mesocrystals for Li-ion cathode application. *Chemical Engineering Journal* **2019**, 359: 1592–1602.

3.1 Abstract

Lithium transition metal orthosilicates such as Li_2FeSiO_4 (LFS) have been recognized as promising cathode materials for application in Li-ion batteries because of their high theoretical energy density, safety, and benign/abundant element composition. Their development however has been hampered by the challenge of obtaining phase-pure and defect-free Li_2FeSiO_4 nanoparticles as non-optimized crystal properties have an adverse effect on structure stability and electrochemical performance. Considering the sustainable potential of hydrothermal synthesis in producing electrode materials, here we employ this process to systematically study critical synthesis parameters for optimal control of particle size, morphology, phase purity, and defects of Li_2FeSiO_4 crystallized in the orthorhombic crystal system with space group *Pmn*2$_1$. It is shown that via a combination of elevated $FeSO_4$ concentration regime and use of EDTA as complexing agent, phase-pure *Pmn*2$_1$ particle formation can be controlled. Synchrotron-based XRD Rietveld refinement and ^{57}Fe Mössbauer spectroscopy reveal significant reduction in Li-Fe antisite defects

and presence of Fe^{3+}. Additionally, the use of EDTA promotes the formation of unique peanut-shell looking hollow mesocrystals that are advantageous in maximizing electrode/electrolyte contact resulting in higher Li-ion storage capacity than dense LFS particles. On the basis of detailed XRD, SEM, and TEM characterizations, a four-step crystallization mechanism is proposed to explain the formation of the hollow mesocrystals. These findings bring new insight in our pursuit of optimization of Li_2FeSiO_4 as a cathode material for Li-ion batteries.

3.2 Introduction

Developing sustainable and safe cathode materials with high energy and power density is among the primary targets for next-generation rechargeable Li-ion batteries to be used in large-scale stationary energy storage and electric transportation.[1-3] In this context, transition metal orthosilicates Li_2MSiO_4 (M = Fe, Mn, or Co) are receiving increasing attention as cathode materials in view of their high theoretical capacity (~333 mA h g^{-1}) arising from the possibility to extract two Li-ions per formula unit.[4-7] Within the silicate family, Li_2FeSiO_4 (LFS) is the most promising one because of its relatively high stability and the abundant non-toxic nature of Fe and Si. Li_2FeSiO_4 is known however to exhibit complex polymorphism, with at least three crystal structures identified, namely one low temperature orthorhombic phase (β_{II}) with space group $Pmn2_1$[8] and two high temperature phases including a monoclinic phase (γ_s) with space group $P2_1/n$[9] and an orthorhombic phase (γ_{II}) with space group $Pmnb$[10]. Most of the reported work has focused on the $P2_1/n$ structure either because of its direct formation during high temperature synthesis processes such as solid-state reaction or due to the phase transformation during the subsequent annealing to achieve carbon coating.[11] However, it has been found that during cycling the $P2_1/n$ phase transforms to a more stable inverse-$Pmn2_1$ phase.[12-15] This cycled inverse-$Pmn2_1$ phase is isostructural with $Pmn2_1$, except that all the Fe have exchanged sites with half of Li. This has therefore prompted our interest into the $Pmn2_1$ phase which can only be produced at temperatures below 500°C.[16]

It is known from a wide range of studies that the morphology and particle size of cathode materials have a direct impact on their electrochemical performance. For example, the formation of $LiFePO_4$ particles of nanometre size or 2D nanoplatelets is considered to enhance electrochemical performance by reducing the Li-ion transport path length.[17-20] In this context, controlling synthesis to produce nanostructured particles suitable for high performance Li-ion

batteries is a critical step in the development of new electrode materials such as Li_2FeSiO_4. Various synthesis methods have been applied to produce Li_2FeSiO_4. While high-temperature solid-state reaction is the most robust and conventional method, it does not allow for the control of particle size and morphology.[8, 15, 21-23] The complexity of sol-gel process and the toxic chemicals involved in it may hinder its further application in large scale production.[5, 24-25] In addition, neither solid-state reaction nor the sol-gel method can produce *Pmn*2$_1$ Li_2FeSiO_4 because of the high temperatures (600-900ºC) used.[11, 26] By comparison, hydrothermal synthesis constitutes a sustainable option to produce nanomaterials with specific properties on a large scale at a reasonable cost and in an environmentally benign manner.[27-28] Several authors have discussed the importance of applying hydrothermal processing to the synthesis of Li-ion battery materials [29-31], including polyanionic compounds such as the silicates and phosphates.[32] Supercritical hydrothermal synthesis conducted at 350-420ºC at a pressure of 38 MPa has been applied to produce LFS nanosheets of the *Pmn*2$_1$ polymorph,[33] but the method does not lend itself to large scale application.

To date, a number of studies on the hydrothermal preparation of Li_2FeSiO_4 have appeared.[34-38] However, the formation of phase-pure Li_2FeSiO_4 is relatively difficult to achieve during hydrothermal synthesis due to undesirable side reactions, which lead to hydrolytic co-precipitation of impurity phases like Li_2SiO_3, Fe_3O_4, Fe_2O_3, and FeOOH.[36-38] Such impurities are also encountered in solvothermal synthesis, where ethylene glycol-water solution instead of pure water is used.[39-41] Solvothermal synthesis can produce Li_2FeSiO_4 particles with hierarchical morphologies but long reaction time from 4 to 8 days is required for the completion of crystallization. Even when phase-pure Li_2FeSiO_4 is obtained, as reported by Sirisopanaporn *et al*., intersite exchange between Li and Fe occurs, resulting in undesirable defects as was the case of *Pmn*2$_1$ phase hydrothermally synthesized at 200ºC.[34-35] The occurrence of such antisite defects has been widely investigated in the case of $LiFePO_4$ in terms of their impact on Li-ion diffusion and electrochemical performance.[17, 42] Luckily, in the case of $LiFePO_4$ or the high-temperature monoclinic (*P*2$_1$/*n*) form of Li_2FeSiO_4, these antisite defects are removed effectively during subsequent annealing at ~700ºC. This approach cannot however be applied to the low-temperature orthorhombic (*Pmn*2$_1$) Li_2FeSiO_4 phase as it is not stable at high temperatures.

With the overriding goal of producing defect-free *Pmn*2$_1$ Li_2FeSiO_4 to evaluate its electrochemical performance as intercalation cathode, herein we report a systematic study on the

hydrothermal synthesis of this material. Synthesis parameters including temperature, reaction time, precursor concentration, and the addition of EDTA as complexing agent are investigated. The hydrothermal treatment leads to reactive crystallization of LFS in the form of mesocrystals via oriented nanocrystallite assembly,[43] whilst the presence of EDTA allows the formation of unique hollow structure. The formation mechanism is investigated by taking samples during hydrothermal operation. Synchrotron-based XRD with Rietveld refinement, and Mössbauer spectroscopy have allowed for quantification of Li-Fe antisite defects and Fe^{3+} as an impurity enabling the synthesis of phase-pure and defect-free LFS with promising charge and discharge characteristics.

3.3 Experimental Section

3.3.1 Synthesis

Lithium iron silicate (Li_2FeSiO_4, LFS) was prepared by hydrothermal synthesis from starting materials of lithium hydroxide monohydrate (98% $LiOH{\cdot}H_2O$), fumed silica (99% SiO_2), iron(II) sulfate heptahydrate (98% $FeSO_4{\cdot}7H_2O$), ascorbic acid (99% $C_6H_8O_6$), and ethylenediaminetetraacetic acid calcium disodium salt (99% EDTA-Ca-2Na). All the chemicals were purchased from Sigma-Aldrich.

In a typical synthesis test, SiO_2 powder was dissolved in 160 mL of LiOH aqueous solution in an ultrasonic bath for 1.5 hours. Then 40 mL of $FeSO_4$ solution was added dropwise with a peristaltic pump to the $LiOH/SiO_2$ solution in a N_2-filled glovebox to avoid oxidation of the ferrous iron. The molar ratio of Li: Fe: Si was kept at 4: 1: 1 for all syntheses. Ascorbic acid (AA) with the molar ratio AA: Fe = 0.16: 1 was added as a reducing agent to further prevent ferrous iron oxidation. The concentration of Li^+ was varied from 0.4 to 1.6M in the mixed precursor solution and the obtained LFS product powders were denoted as LFS04M, LFS08M, LFS12M, and LFS16M, correspondingly. EDTA was used with all other conditions being the same as in LFS08M. The molar ratio of EDTA: Fe was 0.16: 1 and the product was denoted as LFSEDTA. Hydrothermal synthesis was performed in a 450 mL Teflon-lined stirred autoclave (Parr Instruments, Moline, IL) at different temperatures (up to 200^{o}C) for variable times (0 to 12 hours) and stirring speed of 300 rpm. The stirring feature allows for uniform distributions of reactants and products. Moreover, the autoclave is equipped with a dip tube, which permits sampling during the hydrothermal operation.[44] A Parr 4848 reactor controller was used to allow for continuous control and monitoring of temperature and pressure. After completion of hydrothermal

precipitation, the autoclave was cooled down to room temperature within 30 min. The obtained slurry was separated in a centrifuge. The wet solids were rinsed twice with deoxygenate deionized water (again to avoid undesirable oxidation of ferrous iron) and once with acetone for one time, followed by drying in a vacuum oven at 80^{o}C for 12 hours. The dried powders were stored in a glovebox to minimize exposure to oxygen and moisture.

For the investigation of the particle formation mechanism, slurry samples were collected from the dip tube during the heat-up period at various times/temperatures, namely at 100°C (after 20 min), 120°C (after 30 min), 160°C (after 40 min), and 200°C (after 50 min, which is the end of the heating ramp). To avoid oxidation of ferrous iron, a custom-made container filled with argon gas was used to collect the slurry products and was transferred to a glovebox immediately. Dried powder for subsequent characterization or electrochemical evaluation was obtained after centrifugation, washing with deoxygenated/deionized water, and drying in a vacuum oven at 80^{o}C for 12 hours.

3.3.2 Characterizations

Synchrotron X-ray diffraction (XRD) measurements were taken at the Hard X-ray Micro-Analysis (HXMA) beamline at Canadian Light Source (CLS). The wavelength of the X-ray was λ = 0.6889 Å. A mar345 image plate detector was used to record the Debye-Scherrer rings from thin pellet samples made from the pristine powders. Calibration was done by using the synchrotron XRD pattern of LaB_6 powder sample. Laboratory XRD was performed on a Bruker D8-Advantage powder diffractometer using Co-Kα radiation (λ = 1.78892 Å, 35 kV; 15 mA) from 2θ = 10 to 100° in a step of 0.02°. Rietveld refinement was done using TOPAS Academic V.5.0 program.

A Hitachi SU-8230 cold-field emission scanning electron microscope (CFE-SEM) (Hitachi High Technologies) was employed for particle morphology characterization. Transmission electron microscope (TEM) and high-resolution TEM (HR-TEM) images were acquired in a FEI Tecnai 12 BioTwin TEM at 200 kV. Brunauer–Emmett–Teller (BET) specific surface area measurements were performed using a TriStar 3000 analyzer (Micromeritics) in N_2 (-196^{o}C). Inductively coupled plasma optical emission spectroscopy (ICP-OES, Thermo Scientific iCAP 6500 ICP spectrometer) was applied for elemental analysis. Prior to ICP measurements, LFS powders were digested by using mixed concentrated acid HCl: HF (3: 1 vol%) at 95^{o}C for 3 hours, followed by dilution with 4 vol% HNO_3.

^{57}Fe transmission Mössbauer spectroscopy was collected in an in-house facility in a constant acceleration mode at room temperature with ^{57}Co Rh source. 0.03 g of LFS powders were used for each measurement. Velocity calibration and isomer shifts (IS) were quoted with respect to α-iron foil. Parameter fittings were performed using a standard least-squares minimisation with Lorentzian lines.

3.3.3 Electrochemistry

The pristine powder products were mixed with acetylene black (AB) in a weight ratio of 0.8: 0.2 and ball milled at 250 rpm for 3 hours using planetary micro mill (Fritsch, Pulverisette 7 premium line). 100 g of 1 mm ZrO_2 grinding balls were used for per 1 g of LFS-AB mixture in 15 mL of isopropanol. This procedure enables mechanical carbon coating and simultaneous nanosizing of the LFS particles while preserving the low-T orthorhombic phase ($Pmn2_1$). The working electrodes were prepared by spreading a slurry of the active material (ball-milled C-LFS), acetylene black, and poly(vinylidenedifluoride) (PVDF) in a weight ratio of (C-LFS: AB: PVDF) 0.8: 0.1: 0.1 onto aluminum foil. Metallic lithium was used as the counter electrode. A polypropylene film (Celgard 2200) was used as the separator. Each final electrode contained approximately 2.5 mg cm^{-2} of active Li_2FeSiO_4 material. A standard electrolyte solution made of 1M $LiPF_6$/ethylene carbonate (EC)/dimethyl carbonate (DMC) (1: 1 by volume) was used. The data of the galvanostatic charge and discharge profile was collected on an 8-Channel Battery Analyzer (MTI Corporation, USA). The charge and discharge cycling were performed at C/50 rate (1 C = 166 mA h g^{-1}) in the voltage range of 1.5 to 4.5 V at 55^{o}C. Electrochemical Impedance Spectroscopy (EIS) measurements performed on electrodes before cycling (after a 6-hour relaxation period) were carried out on an electrochemical workstation (Bio-Logic) in potentiostatic mode between 1 MHz and 20 mHz at open circuit voltage (OCV). The resistances are determined by fitting the Nyquist plot with the Equivalent Electric Circuit by Z-fit method provided by EC-Lab software.

3.4 Results and Discussion

3.4.1 Reactive crystallization of Li_2FeSiO_4

To investigate the hydrothermal formation mechanism of crystalline Li_2FeSiO_4 particles, slurry products were collected during the heating up of the pressure reactor from room temperature to the target temperature (200^{o}C) and characterized by synchrotron XRD, SEM, TEM and ICP

techniques. Figure 3.1 shows the evolution of XRD patterns of precipitates collected from solution with 0.8M LiOH at different reaction time and temperature. In the beginning (i.e. before heating starts), the drop-wise addition of $FeSO_4$ aqueous solution to the $LiOH/SiO_2$ solution (pH = 11.8) resulted in spontaneous formation of a colloidal white suspension, which gradually changed to a pale green color at the final pH = 11.2 of the mixed solution. This spontaneous reaction can be attributed to forced hydrolysis of iron(II) representing the formation of $Fe(OH)_2$ colloids.[45] After washing and drying, the collected precursor powder, denoted as LFSRT, was characterized by synchrotron XRD (Figure 3.1). As shown in the bottom pattern in Figure 3.1, one broad XRD band at around $2\theta = 15.5°$ was observed. When using a laboratory Co source XRD instrument over wider 2θ range, two broad XRD bands were observed (Figure A1).

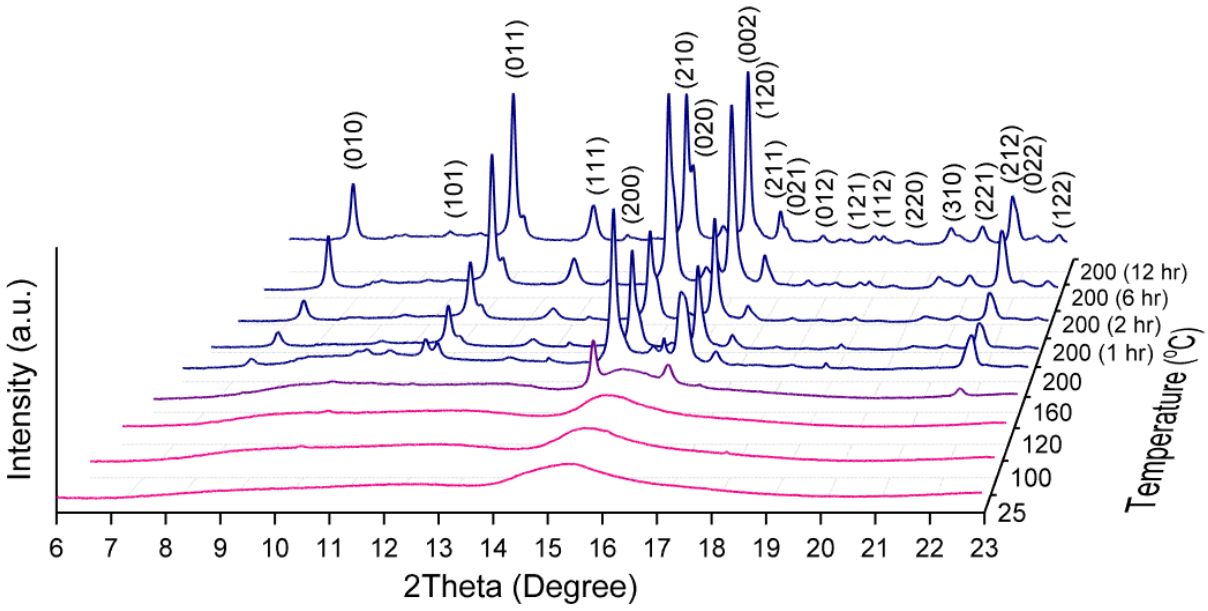

Figure 3.1. Synchrotron XRD (λ = 0.6889 Å) patterns of hydrothermal precipitates obtained at different temperatures and times from 25 to 200ºC (heat-up period) and held at 200ºC for (1, 2, 6, and 12) hours. Bragg peak positions correspond to *Pmn*2_1 Li_2FeSiO_4 (reference PDF# 01-080-6279).

Elemental analysis using ICP (Figure A2) shows that this precursor precipitate contains a Li to Fe mole ratio of 0.43: 1 and a Si to Fe ratio of 0.74: 1. ICP analysis of the filtrate confirms that all the Fe (less than 2×10^{-5} mol L^{-1} in filtrate) had precipitated, whereas the respective amounts for Si and Li were 81.5% and 17.5%. On the basis of this analysis it is proposed that the spontaneously formed hydrolytic precipitate (LFSRT) consists mainly of poorly crystalline ferrous

hydroxide along with the adsorbed or co-precipitated silicate and lithium species (possibly as one or more of silica, ferrous silicate, and lithium silicate) as commonly observed in multi-ion hydrolytic precipitation systems.[46-47] Following the precursor precipitation in glove box, the slurry was transferred to autoclave and heated up to 200°C in 50 min, during which products were collected and characterized. As can be seen from Figure 3.1 (but also Figure A1), the powders obtained at 100 and 120°C, denoted as LFS100C and LFS120C, respectively, have broad XRD features similar to the room temperature precursor precipitate, LFSRT. ICP analysis of the solids (Figure A2) shows that the Li to Fe mole ratio was still around 0.4~0.45: 1, whereas the Si to Fe mole ratio increased to 1: 1 as the reaction temperature increased to 100 and 120°C. The concentrations of Fe and Si in the solution were insignificant, indicating that all of the Fe and Si had precipitated out.

The first signs of nucleation-crystallization of Li_2FeSiO_4 appear after 40 min when the temperature has reached 160°C (LFS160C) as revealed in Figure 3.1. More specifically, three diffraction peaks emerge at $2\theta = 14.6°$, 16.1° and 21.8° corresponding to the (210), (002) and (022) facets, respectively, of *Pmn*2_1 Li_2FeSiO_4.[35] It should be noted however that the diffraction peaks is rather weak reflecting the early stages of nucleation of a nanocrystalline phase. In addition, the coexistence of the broad background feature, indicates that not all the precursor precipitate has been rearranged into a crystalline structure. Ten minutes later with the temperature reaching 200°C (LFS200C), we can see crystallization has accelerated as now all the diffraction peaks of *Pmn*2_1 LFS appear and their intensities have increased. These results indicate that the crystallization of LFS is not progressing through homogeneous nucleation but rather through the precipitation of a poorly crystalline ferrous hydroxide/silicate intermediate that undergoes solution-mediated heterogeneous transformation upon heating into crystalline LFS. The crystallinity of the LFS can be seen (in Figure 3.1) to improve as the holding time at 200°C is extended to 1, 2, and 6 hours as evidenced by the increased peak intensity. No further improvement is observed when hydrothermal time at 200°C is extended to 12 hours. The XRD pattern of Li_2FeSiO_4 synthesized at 200°C for 6 hours (denoted as LFS08M) is very well indexed as the *Pmn*2_1 LFS.[35] Rietveld refinement of the XRD data will be discussed in a later section.

We further confirmed the reactive crystallization mechanism of LFS by identifying the evolution of morphology and crystal structure. Figure A3 shows low-magnification features of the

reaction intermediates from the precursor precipitate (LFSRT) to one-hour hydrothermally treated product (LFS200C1H). It reveals that before reaching 200°C, the precipitated particles have an irregular size and shape. Clearly, conversion occurred when the temperature reached 200°C as we can see that the precipitates are dominantly smaller round-shape particles. After holding at 200°C for 1 hour, the chunk-like particles have almost disappeared, and the precipitate is composed of dispersed uniform round-shaped particles. These morphological analyses, combined with the XRD results, provide a clue that a critical conversion of the amorphous intermediate to crystalline LFS happened right before 200°C.

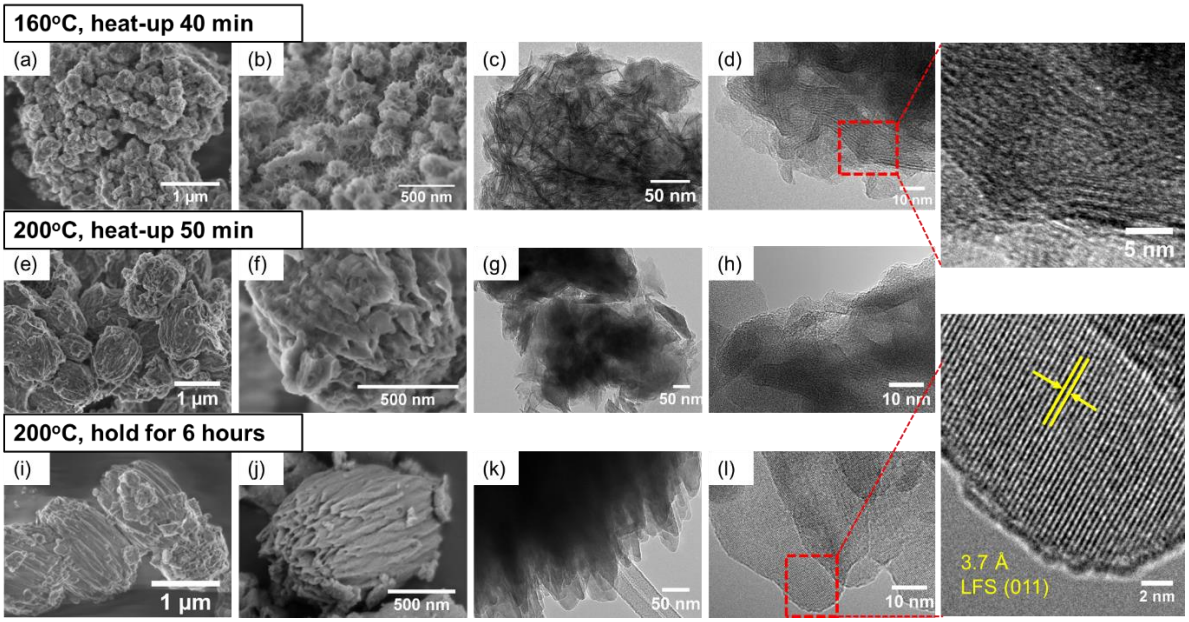

Figure 3.2. SEM, TEM, and HR-TEM images of hydrothermal precipitates obtained either during heat-up period at (a-d) 160°C (LFS160C, 40 min) and at (e-h) 200°C (LFS200C, 50 min); and (i-l) at 200°C after 6 hours (LFS08M).

For further confirmation and understanding of the conversion process, high-magnification SEM and high-resolution TEM were performed on LFS160C (40 min heat-up), LFS200C (50 min heat-up), and LFS08M (6 hours holding time). Figure 3.2a shows the surface morphology of LFS160C, revealing that the freshly nucleated nanocrystalline LFS is in the form of aggregates of smaller 100-150 nm (primary) particles. Higher magnification SEM image (Figure 3.2b) reveals the LFS160C having a honeycomb-like nanoarchitecture. With further observation through TEM (Figure 3.2c) and HR-TEM (Figure 3.2d), the nanoparticles are seen to be made of sub-nm thick nanocrystalline fibers interweaved together. BET specific surface area of LFS160C is 111.16 m^2

g^{-1}, approximately ten-fold greater than that of the final LFS product. This extremely high surface area can be attributed to the 2-D nanofiber features of LFS160C.

As the temperature increased to 200°C (LFS200C), elliptical bulk particles form (Figure 3.2e) via the evolution of LFS160C. These (primary) particles are now about 1 μm in diameter and have very rough surface (Figure 3.2f). TEM and HR-TEM images (Figure 3.2g, h) of LFS200C show that the primary particles are made of assemblies of smaller irregular shape components with the characteristic crystalline fiber nanostructure that have been bonded together apparently via secondary nucleation. Additionally, the BET surface area was found to drop dramatically to 6-8 m^2/g, further confirming the transformation of 2-D nanofibers to 3-D crystalline particles.

SEM images of LFS08M (LFS obtained after 6 hours hydrothermal processing at 200°C) reveal that the as-synthesized fully crystalline primary particles are elliptical (or barrel-like) in shape with size about 800 nm in waist diameter and 1.2 μm in length (Figure 3.2i, j). The barrel-like shape is built from elongated nanocrystals with width ranging from 20 to 50 nm, as can be seen in Figure 3.2k. HR-TEM image of the edge of a LFS08M particle (Figure 3.2l) reveals that the nanocrystals have high crystallinity and all the adjacent nanocrystals are assembled in the same crystallographic orientation. This special feature is characteristic of mesocrystals, a rather unique class of crystalline materials made up via alignment of nanocrystals along the same crystallographic order over a microscopic scale.[43] The lattice fringe shown in the HR-TEM image has a d-spacing of 3.7 Å, which corresponds to the (011) plane of LFS. Analysis of the synchrotron XRD by Rietveld refinement indicates that the crystallite size of LFS08M is 45.4(6) nm.

3.4.2 Effect of precursor concentration

In the attempt to control the morphology and size of LFS particles via supersaturation adjustment, a series of experiments at different precursor concentrations were conducted. The reaction time was kept at 6 hours, the temperature at 200°C, and the molar ratio of Li: Fe: Si at 4: 1: 1, i.e. Fe and Si were at stoichiometric ratio and Li at 100% excess. Yabuuchi *et al.* found that 100% excess of Li is required for the synthesis of LFS under hydrothermal treatment.[48] Four Li^+ concentrations were examined, namely 0.4, 0.8, 1.2, and 1.6M, and the samples are denoted as LFS04M, LFS08M, LFS12M, and LFS16M, respectively. Figure 3.3 shows the XRD patterns of the as-synthesized products. All the four products can be indexed to the $Pmn2_1$ LFS. Interestingly fewer peaks (labeled with an *) denoting the presence of minor iron oxide impurities are found in

the products obtained at the high range of precursor concentrations. By far the LFS04M product obtained with 0.4M Li^+ was found to be the least pure.

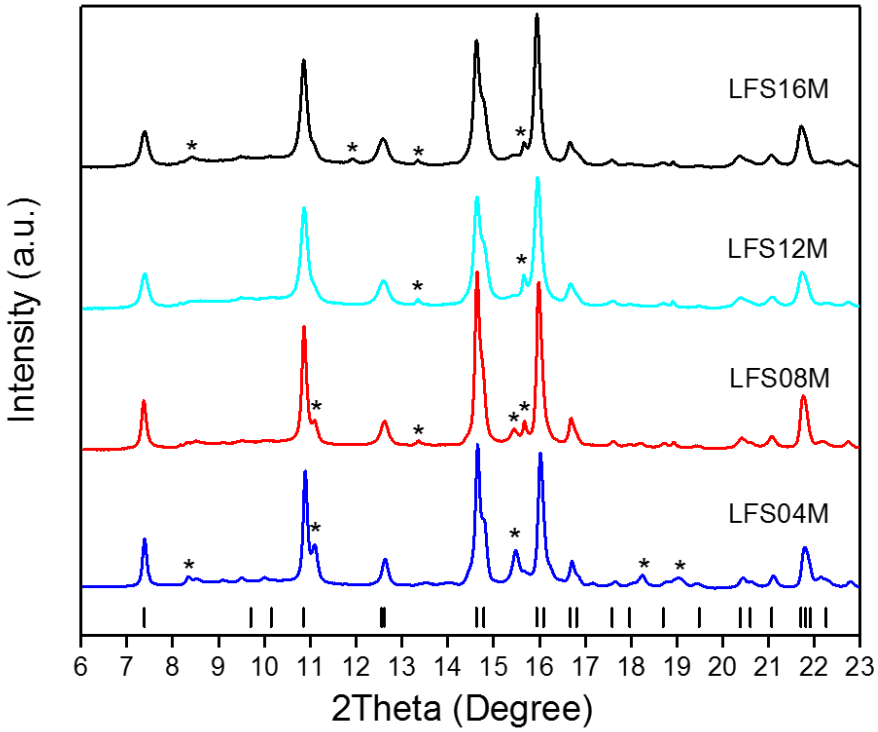

Figure 3.3. Synchrotron XRD (λ = 0.6889 Å) patterns of LFS prepared from precursor solution containing Li^+ concentration of 0.4, 0.8, 1.2, and 1.6M, denoted as LFS04M, LFS08M, LFS12M, and LFS16M, respectively. Black streaks at the bottom represent the Bragg peak positions of *Pmn*2_1 Li_2FeSiO_4 (reference PDF# 01-080-6279). Star symbols shown represent iron (hydr)oxide impurities.

Concentration determines the supersaturation of the crystallization system which ultimately controls the kinetics of particle nucleation and growth.[49] Particle morphological characteristics as a function of precursor concentrations are presented in Figure 3.4. It can be seen that LFS04M and LFS08M have similar shape and particle size –about 1200 nm long and 600 nm diameter (Figure 3.4a, b). BET specific areas of LFS04M and LFS08M are 7.22 and 8.66 m^2 g^{-1}, respectively. Nitrogen adsorption-desorption isotherms associated with the BET analysis can be found in the Supplementary Data (Figure A4). However, when the starting concentration of Li^+ was increased to 1.2M, the particle size of LFS decreased significantly to ~200 nm in diameter and ~400 nm in length (Figure 3.4c) and the BET specific surface area increased to 26.05 m^2 g^{-1}, which is almost 3× of the magnitude of the lower concentration LFS products. No further change in

particle size (Figure 3.4d) and surface area (27.16 m^2 g^{-1}) was observed when the precursor Li concentration was raised from 1.2 to 1.6M. TEM images of LFS08M and LFS16M are compared in Figure 3.4e and 3.4f. Similar to LFS08M, LFS16M particles are assembled by oriented attachment of elongated nanocrystals, although the size of the nanocrystals is smaller than those assembled in LFS08M.

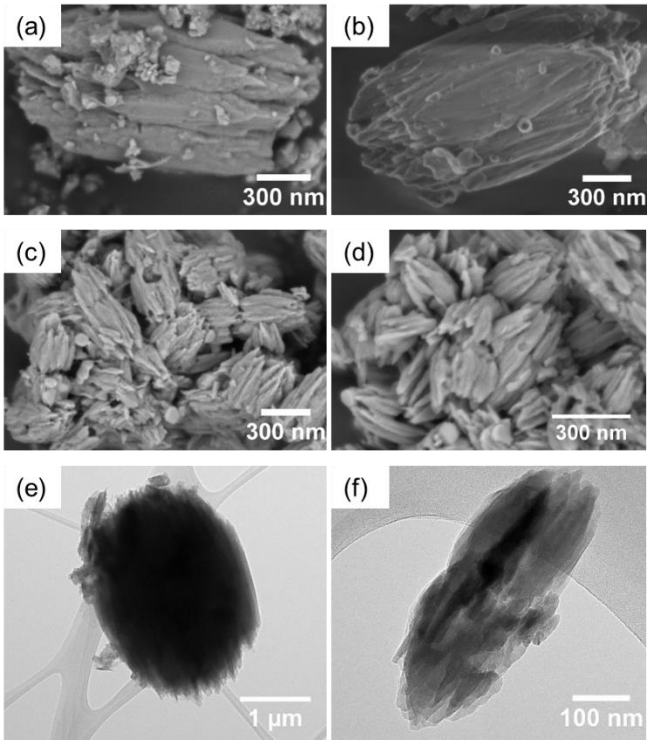

Figure 3.4. SEM images of LFS prepared from precursor solutions containing Li^+ concentration of (a) 0.4M, (b) 0.8M, (c) 1.2M, and (d) 1.6M, denoted as LFS04M, LFS08M, LFS12M, and LFS16M, respectively. TEM images of (e) LFS08M and (f) LFS16M.

3.4.3 Effect of EDTA complexing additive

The purity and morphology of the hydrothermally synthesized LFS crystals was further optimized when EDTA was added into the reaction mixture as complexing agent. The XRD data of the EDTA-produced LFS (denoted as LFSEDTA) is analyzed and discussed in terms of crystal structure and purity in the next section 3.4.4. Here we describe the crystal morphological effects of EDTA. As the SEM images in Figures 3.5a,b indicate the ellipsoidal LFSEDTA were formed from many elongated crystals looking similar to LFS08M in terms of their exterior. The particle size is about 1 μm in length and 500 nm in diameter. Remarkably, some of the particles were broken in half revealing a unique hollow structure resembling with peanut shell. As a result, the

BET surface area of LFSEDTA increased to 11.70 m^2 g^{-1}, higher than that of LFS08M (i.e. 8.66 m^2 g^{-1}). Figure 3.5c (TEM) clearly illustrates the hollow structure which can be seen from the contrast between the inner sphere and the outer shell. In HR-TEM images, d-spacings of 3.7 Å, 4.1 Å (Figure 3.5d, e), and 5.3 Å (Figure 3.5f, g) can be observed, which correspond to the (011), (110), and (010) facets, respectively, of *Pmn*2_1 LFS.

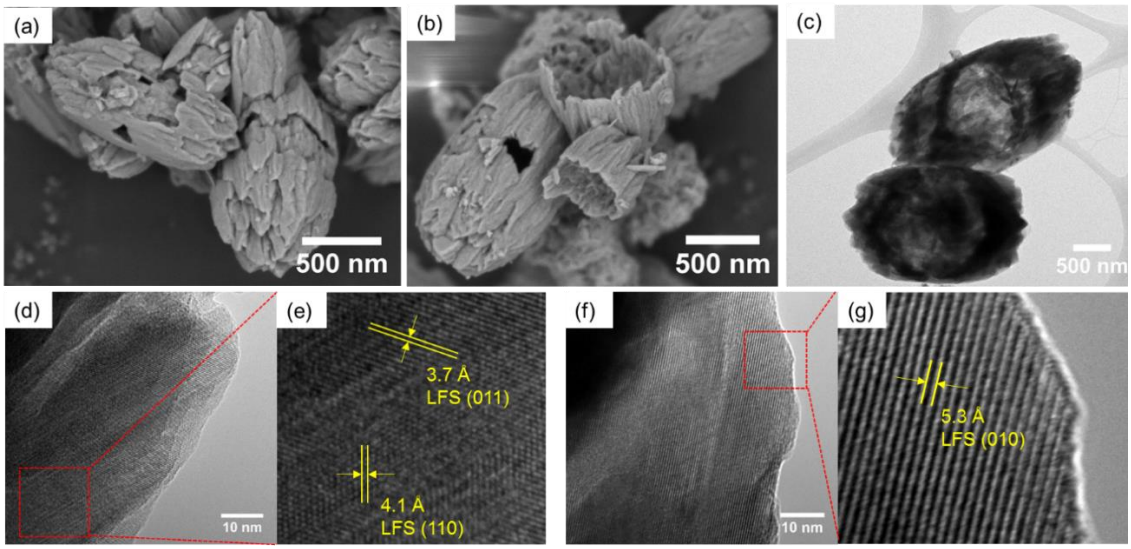

Figure 3.5. Morphology and crystal structure of LFSEDTA particles. (a, b) SEM images. (c) TEM image. (d, e) HR-TEM image and its larger magnification showing two d-spacings, 3.7 Å and 4.1 Å, corresponding to the (011) and (110) facets, respectively, of *Pmn*2_1 Li_2FeSiO_4. (f, g) HR-TEM image and its larger magnification showing a d-spacing of 5.3 Å, corresponding to the (010) facet of *Pmn*2_1 Li_2FeSiO_4.

Hollow nanostructured materials hold a lot of promise as Li-ion storage electrode materials as they allow for intimate interfacing with the electrolyte phase while their thin shell walls provide short diffusion length for larger Li-ion storage capacities provoking the interest of a number of studies. Some notable examples in this regard are the preparation of nanoporous γ-MnO_2 and nano-cage $NiCo_2O_4$ as anode materials,[50-51] hollow-structured Co_3O_4 nanoparticles and the study of their capacity fade,[52] the synthesis of hollow nanospheres of Li_2CoSiO_4/C as cathode material,[53] and the nanoengineering of some unique hollow nanoboxes of Li_2MnSiO_4@C as high capacity cathode.[54] Typically however synthesis of hollow particles is accomplished via template-based or other complex multi-step methods that are not amenable to scale up. The only attempt to produce hollow Li_2FeSiO_4 particles has been reported by Xu et al.[39] The authors produced their hollow LFS particles in mixed solvent media (1/3 ethylene glycol-2/3 water) after 3-days hydrothermal reaction that were further sintered at 650°C for 10 hours to promote their C-coating that resulted

in obtaining the monoclinic ($P2_1$) phase. Questions are raised if their hollow spherical particles had not densified due to sintering upon annealing as no detailed data were presented. Notwithstanding this issue, we do not as yet have a study that reports template-free or organic solvent-free hydrothermal synthesis of hollow nanostructured LFS particles crystallized in the $Pmn2_1$ system as done here. The mechanism of EDTA-mediated formation of the hollow (peanut-shell like) LFS particles is discussed at a later section.

3.4.4 Rietveld refinement and Mössbauer spectroscopy

Rietveld refinement of the synchrotron XRD data was applied to extract crystal structure information of three LFS products, namely LFSEDTA, LFS08M, and LFS16M. Figure 3.6a-c shows comparisons between observed and fitted patterns of LFSEDTA, LFS08M, and LFS16M with R_{wp} values of 3.821%, 5.429%, and 3.821%, respectively. The starting atomic coordinates are taken from Sirisopanaporn *et al.*[35] Only the orthorhombic crystalline Li_2FeSiO_4 phase with space group $Pmn2_1$ was found to fit the data. The minor iron oxide impurities observed in some samples were not taken into account for the refinement. The extracted unit cell parameters of LFSEDTA are a = 6.26451(16) Å, b = 5.34467(15) Å, and c = 4.96216(8) Å, which agree well with the reported results for $Pmn2_1$ structure.[35, 55] During refinement, Fe and Li were allowed to occupy on each other's site and it was assumed that each site is fully occupied. Table A1 lists the atomic fractional coordinates and site occupancies of LFSMEDTA.

In the ideal $Pmn2_1$ structure of Li_2FeSiO_4, Li and Fe atoms occupy different crystallographic sites, denoted as Li1 (4b site) and Fe1 (2a site), respectively. During electrochemical lithiation/delithiation, Li migrates in either a straight *a*-direction or a zig-zag *c*-direction according to DFT computational studies as illustrated in Figure A5a.[12, 56] However, intersite exchange of Li and M has been reported in orthorsilicates Li_2MSiO_4 (M = Fe, Mn, or Co) and identified as the most energetically favourable defect in atomistic simulations of Li_2MnSiO_4.[57-58] In a recent study of post-mortem synchrotron-based XRD and XANES characterizations on monoclinic and orthorhombic phases of Li_2FeSiO_4, Lu *et al.* demonstrated that Li-Fe antisite defects can be induced during cycling and play an important role in the phase transformation.[14] Sirisopanaporn *et al.*[35] observed that 5% of the Li1 site was occupied by Fe and 10% of the Fe1 site was occupied by Li in the $Pmn2_1$ Li_2FeSiO_4 that was hydrothermally synthesized at 200°C using 0.4M starting Li concentration. After electrochemical cycling, all the Fe will exchange sites

with half of the Li, leading to an inverse-*Pmn*2$_1$ structure.[12-13] In the inverse-*Pmn*2$_1$ LFS, Li may migrate in a zig-zag *c*-direction or a zig-zag *b*-direction (Figure A5b).[12, 56] However, if there are local Fe/Li antisite defects, resulting in a non-established b-migration channel, the nearby Li-ions could be blocked (see Figure A5c). Hence to address this concern, it should be beneficial to minimize the formation of antisite defects during synthesis.

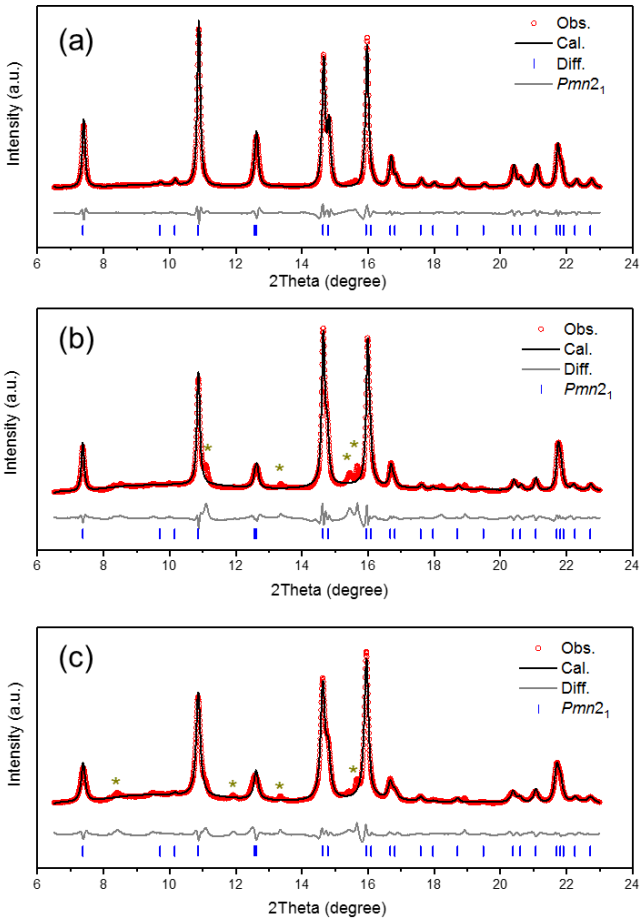

Figure 3.6. Rietveld refinement of synchrotron XRD ($\lambda = 0.6889$ Å) patterns of Li_2FeSiO_4 products of (a) LFSEDTA; (b) LFS08M; and (c) LFS16M. Red open symbols represent the experimental observation, black curve is the calculation results, grey curve is the difference between observation and calculation, and blue streaks at the bottom represent the Bragg peak positions of *Pmn*2$_1$ Li_2FeSiO_4. Star symbols shown in (b) and (c) represent iron (hydr)oxide impurities.

According to the present Rietveld refinement analysis, all three as-synthesized LFS materials (Figure 3.6) were also found to have certain Li-Fe antisite defects. The concentration of Fe antisite defect (Fe on Li1 site) is of particular interest as it may block the Li diffusion pathway

during electrochemical cycling and thereby degrade the performance of the cell. Thus, as depicted in Figure 3.7 (detailed data is listed in Table A2), the Fe antisite defect (atom%) was determined to be 3.6%, 10.1%, and 8.9%, respectively, for LFSEDTA, LFS08M, and LFS16M. Li occupancy on Fe1 site (Li antisite defect) was found to be 11.5%, 20.8%, and 30.3%, respectively, for LFSEDTA, LFS08M, and LFS16M. However, it is noted that is difficult to acquire a totally accurate refinement for Li antisite defects with only XRD data because Li atoms are weakly scattered by X-rays. One possible origin of the rather high concentrations of Li antisite defects could be the difficulty to differentiate a vacancy from a Li-occupancy. Simultaneous analysis with X-ray and neutron diffraction would make the analysis of Li-occupancy more accurate. Nevertheless, there is clear indication that tuning the synthesis conditions can reduce the formation of Li-Fe antisite defects in LFS. Recently, Paolella *et al*. studied the formation of antisite defects of $LiFePO_4$ during hydrothermal synthesis and found that the addition of Ca^{2+} helped to alter the crystallization path, leading to substantial reduction of antisite defects.[17] In this work, the use of EDTA as an additive has proven to be an effective alternative strategy to reduce the occurrence of antisite defects during hydrothermal synthesis without contaminating the final nanostructured cathode material.

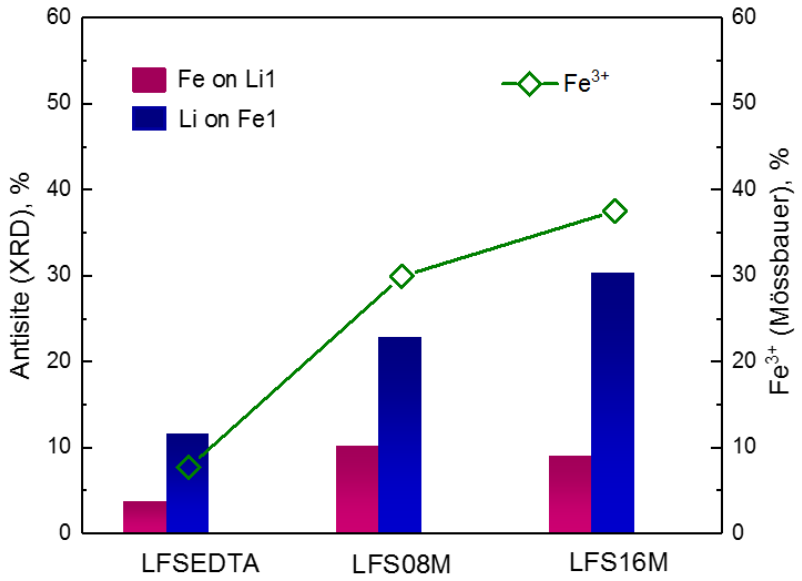

Figure 3.7. Percent antisite defect concentrations determined by Rietveld refinement and percent Fe^{3+} contents determined from Mössbauer spectra for LFSEDTA, LFS08M, and LFS16M.

^{57}Fe Mössbauer spectroscopy was applied to further demonstrate the beneficial effects of EDTA on the properties of the hydrothermally prepared LFS products. Figure 3.8 shows the Mössbauer spectra obtained from three LFS samples. The parameters extracted from Mössbauer spectra include isomer shift (IS, mm/s), quadrupole splitting (QS, mm s^{-1}), and intensities (atom%). These results are tabulated in Table A3. The overall shape of the spectra suggests a dominant Fe^{2+} component (solid green lines) and a minor Fe^{3+} component (dash bluelines). The IS values of Fe^{2+} in the three products range from 0.959(3) to 0.991(1) mm s^{-1}, which are typical for Fe^{2+} in tetrahedral coordination with oxygen. For Fe^{3+} doublets, IS values range from 0.28(2) to 0.330(8) mm s^{-1}, whereas QS is in the range of 0.69(1) to 0.85(5) mm s^{-1}, which are indication of Fe^{3+} in the environment of iron-oxygen tetrahedra.[23, 55] From the area ratios of the Fe^{2+} and Fe^{3+} absorption doublets, Mössbauer results indicate that the LFS produced in the absence of EDTA contain a significant amount of Fe^{3+} ranging from 29.9% to 37.5% in LFS08M and LFS16M, respectively. The Fe^{3+} content is remarkably lower in LFSEDTA, only 7.7%.

The existence of Fe^{3+} in the LFS has been reported in many studies involving different synthesis methods such as via hydrothermal,[55, 59] solvothermal,[41] solid-state,[23] or sol-gel[60]. Dominko *et al.* reported 19.2% of Fe^{3+} in the LFS sample synthesized at 150^{o}C for 14 days.[59] Liivat *et al.*[61] observed 22% and Yang *et al.*[41] even found 45.5% Fe^{3+} in the fresh electrodes. It is possible that some Fe^{3+} came from the oxidation of nanocrystalline LFS after synthesis during handling despite the caution taken as described in the Experimental part.[62] During Mössbauer measurement, the powder was exposed to the air which could also cause the oxidation of Fe^{2+} on the material surface. It is suggested that during future Mössbauer measurements of air-sensitive materials such as LFS, a special air-free sample holder should be used. It should be noted that the relative intensity of the two doublets not only depends on the atomic fraction of these two Fe components, but also their recoil-free factor, *f*. So far, the fitting procedure of relative ratio of Fe^{2+} and Fe^{3+} has been always made on the assumption that they have the same recoil-free factor, which could lead to an overestimation or underestimation of the Fe^{3+} concentration as pointed out by Mysen.[63]

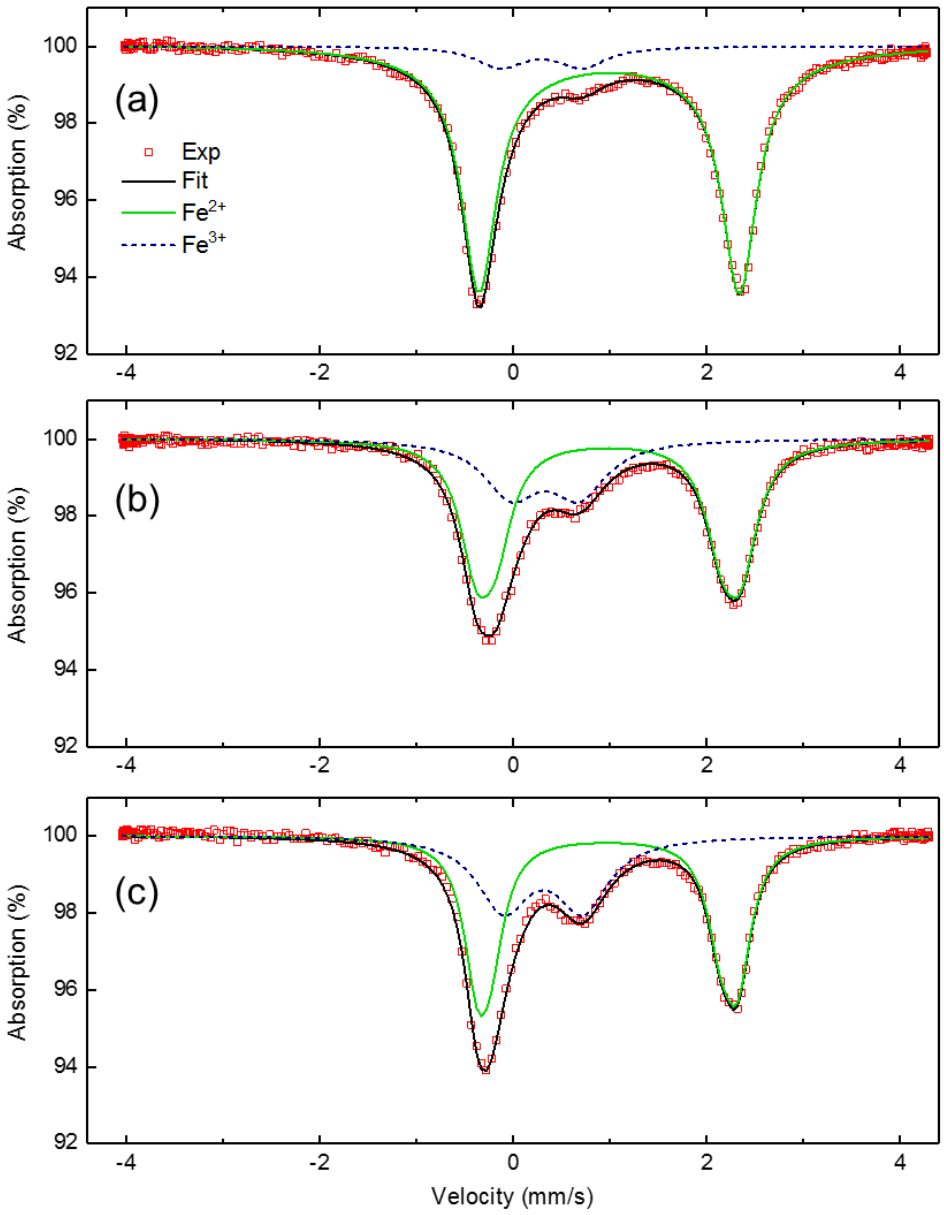

Figure 3.8. ^{57}Fe Mössbauer spectra of (a) LFSEDTA; (b) LFS08M; and (c) LFS16M. Red symbols are data measured from experiment, black lines stand for the overall fitting results, while solid green and dash blue lines represent Fe^{2+} and Fe^{3+} components respectively.

As discussed above, the limitation of current characterization techniques could lead to an overestimation of the antisite defects and Fe^{3+} components. Nevertheless, the relative defect concentrations of LFSEDTA, LFS08M and LFS16M is still valid. Figure 3.7 demonstrates that the relative antisite defects amount follows the trend of Fe^{3+} concentration with LFSEDTA having the least amount of antisite defects and Fe^{3+}. The detailed data can be found in Table A2.

3.4.5 Formation mechanism of LFS mesocrystals

A 4-step mechanism as illustrated in Figure 3.9 is proposed to account for the formation of LFS mesocrystals by hydrothermal crystallization. Mesocrystals is a special class of crystalline materials with highly ordered nanoparticle superstructure formed via aligned assembly of nanocrystallites.[43] They have only the last ten years that have been identified and described.[43] Their unique particle morphology gives them interesting physical, chemical, and electrochemical properties as candidate materials for energy storage application.[43, 64-65] The underlying mesocrystal formation mechanism was determined via sampling and analysis of intermediates as function of hydrothermal reaction progress. The role that EDTA plays in regulating the crystallization of defect-free LFS mesocrystals with hollow structure is elaborated.

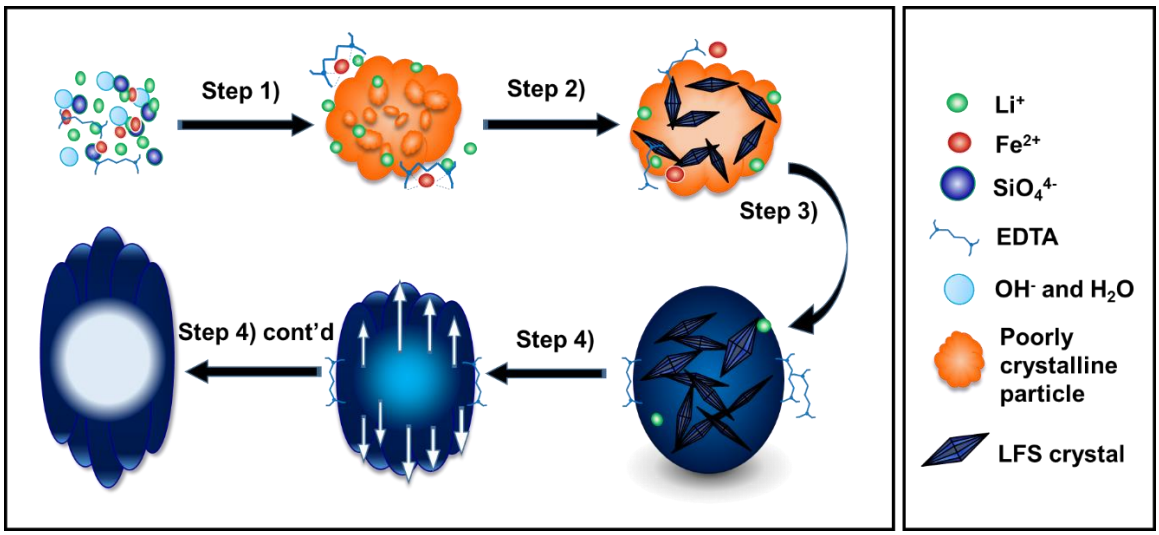

Figure 3.9. Proposed scheme for the crystallization of LFS in EDTA-mediated hydrothermal system. Step 1): nucleation and aggregation of poorly crystalline intermediates; Step 2): crystallization of LFS non-bulk 2D nanocrystals out from the intermediates; Step 3): nearly-oriented attachment to assemble bulk LFS mesocrystals; Step 4): dissolution of inner particles and growth of the outer shell into peanut shell-like hollow mesocrystals.

Step 1): In the beginning, spontaneous nucleation and aggregation occur to form a hydrolytic precipitate containing mainly ferrous hydroxides along with adsorbed or co-precipitated silicate and lithium species (Figure A3). These metastable solid phases form as intermediates because the barriers for their nucleation are smaller than that for the more stable phases. In the presence of EDTA, however, Fe^{2+} is partially chelated forming soluble $[Fe^{II}(EDTA)]^{2-}$ complex. The formation constant of $[Fe^{II}(EDTA)]^{2-}$ at 25°C is log K_f = 14.32.[66] The complexation of Fe species alters the reactivity of Fe^{2+} hence modifying the LFS crystallization pathway.

Step 2): As the temperature and pressure increase during hydrothermal treatment, heterogeneous nucleation of the more stable crystalline phase (i.e. LFS) takes place from the metastable intermediate solid species through local dissolution and recrystallization (refer to Figure 3.2a-d). During this stage, more Li ions are supplied from the solution to complete the formation of stoichiometric LFS, as evidenced by ICP elemental analysis (Figure A2). The phase transformation from metastable to more stable phases can be referred to as the Stranski's or Ostwald step rule which states that more often the thermodynamically unstable phases occur first, followed by the thermodynamically stable phases.[49, 67] Simultaneously, the $[Fe^{II}(EDTA)]^{2-}$ complex undergoes hydrothermal decomposition at elevated temperature and releases Fe^{2+}.[68-69] Thus unlike the system where EDTA is absent, the Fe^{2+} cations that are required for the crystallization of LFS are provided not only by the *in situ* dissolution of iron hydroxide but also by the dissociation of the $[Fe^{II}(EDTA)]^{2-}$ complex. The regulation of the Fe^{2+} concentration in the solution can control the supersaturation of the LFS crystallization. In consequence, the product LFSEDTA has the lowest occurrence of defects including Li-Fe antisite defects and oxidized iron species Fe^{3+}.

Step 3): The newly formed non-bulk nanoparticles of LFS act as building blocks and attach to each other through nearly-oriented attachment to produce larger mesocrystals, releasing the surface energies associated with their free surfaces (Figure 3.2e-h).[70] This step can be considered as the initial growth stage of LFS.

Step 4): The initially formed mesocrystal is not in a fully crystalline state. With further time progression, according to the Ostwald ripening process,[71] the particles in the center have lower crystallinity than the outside and thus prefer to dissolve, thereby promote the growth of outer shell which has higher crystal stability. As we can see by comparing the morphology of LFS08M (Figure 3.4c) with that of LFSEDTA (Figure 3.5e), the hollow structure is formed only in the presence of EDTA. This suggests that beyond regulating the crystal structure, EDTA also plays a role in modifying the crystal growth pattern of LFS. It has been reported that EDTA can bind to a specific surface of magnetite during its hydrothermal synthesis resulting in dodecahedral nanocrystals.[72] Hollow microspheres of $BiVO_4$ were synthesized through microwave hydrothermal method by manipulating the chelating effect of EDTA with Bi^{3+}.[73] For the growth of LFS, it is reasonable to suspect that EDTA may bind to a preferred crystal surface thus

facilitating the growth of the 2D nanocrystals. The controlled release of Fe^{2+} may also contribute to the hollow structure. Consequently, ellipsoidal peanut-shell-like hollow mesocrystals are formed (Figure 3.2i-l and Figure 3.5).

3.4.6 Electrochemical Performance

The hydrothermally synthesized pristine powders were examined as cathode materials by performing galvanostatic charge and discharge tests. All of the measurements were carried out at C/50 rate in the voltage range of 1.5 to 4.5 V (vs. Li/Li^+) at 55ºC. The first discharge and the second charge curves are shown in Figure 3.10a. Charging and discharging capacities up to 6 cycles can be found in Figure A6. LFSEDTA exhibited an initial discharge capacity of 164 mA h g^{-1}, which is 98.6% of the theoretical capacity (166 mA h g^{-1}, assuming that one Li^+ is intercalated into the structure). This capacity is superior than previously reported values measured under similar conditions (e.g. current rate and temperature) on *Pmn*2_1 LFS materials[36, 59, 74] that have not been submitted to annealing[36] or coating with conductive materials[74]. This is attributed to the well controlled crystallization process enabling the unique hollow and defect-free mesocrystal structure. Here we may remark that in some previous studies, Li_2FeSiO_4 with $P2_1/n$ crystal structure has been shown to deliver enhanced initial capacity corresponding to the extraction of more than one Li^+ per formula unit.[75-77] It remains unclear, however, whether this extra capacity is a result of the redox reactions of Fe^{3+}/Fe^{4+} and/or O^{2-}/O^- or can be at least partly attributed to electrolyte degradation.[15, 61, 77-78] The latter cannot be excluded because typically all the studies that achieved capacity beyond 166 mA h g^{-1} were conducted at a rather high voltage cut-off, *ca*. 4.8 V. In this study, we applied a relatively safe voltage range, i.e. 1.5-4.5 V, focusing only on the extraction-insertion of the first Li^+.

In comparison, the EDTA-free synthesized LFS materials, LFS08M and LFS16M, exhibited lower discharge capacities than LFSEDTA in the first cycle, which were 137 and 130 mA h g^{-1} (82.6% and 78.2% of the theoretical capacity), respectively. It is proposed that the absence of impurities, but more importantly the lower amount of antisite defects and the hollow structure of the LFSEDTA particles are responsible for the superior performance vis-a-vis the LFS08M and LFS16M materials. Moreover, LFSEDTA shows a higher area below the discharge curve (more plateau-like shape), which denotes a higher energy density compared with the other two products. It is noted however that upon cycling (Figure A6), the capacity of LFSEDTA

decreased to 146 mA h g^{-1}, close to that of LFS08M. To probe the origin of the initial enhanced performance exhibited by the hollow LFSEDTA mesocrystals vis-à-vis the LFS08M mesocrystals the two pristine electrodes were subjected to EIS analysis. As it can be seen in Figure 3.10b, the EDTA-controlled mesocrystals revealed a lower charge-transfer resistance as evident by the relative size of the semicircle in the high-to-middle frequency range that represents R_s and R_{ct}, the interface resistance and charge-transfer resistance, respectively. While LFSEDTA is found to have R_s = 17.9 Ω and R_{ct} = 2.3 Ω, LFS08M has higher values of both resistances with R_s = 25.5 Ω and R_{ct} = 12.3 Ω. Having developed the new crystallization process, attention will be shifted next to surface modification to fully exploit the potential of *Pmn*2_1 LFS mesocrystals as higher energy density cathode materials.

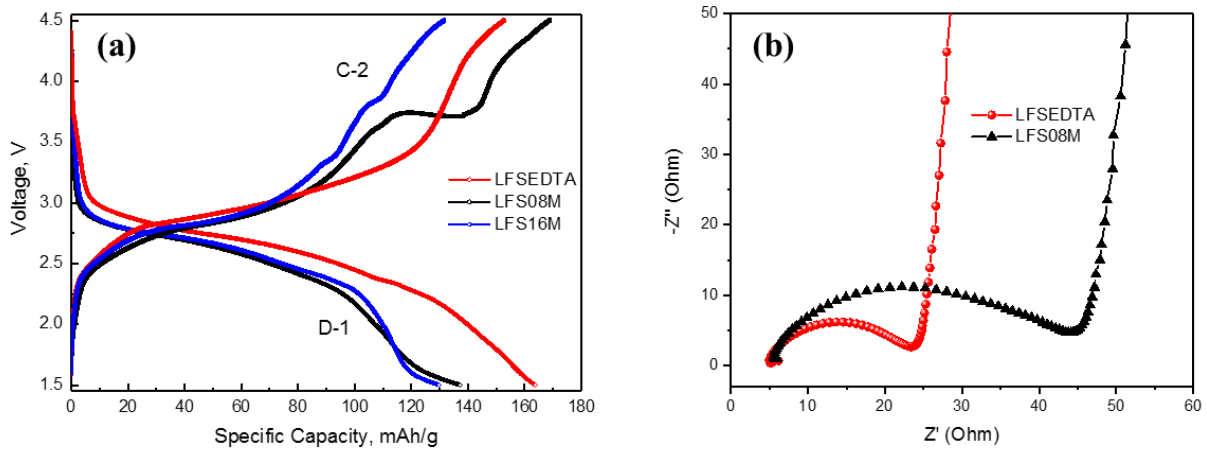

Figure 3.10. (a) Galvanostatic curves of the first discharge and the second charge cycles of LFSEDTA, LFS08M, and LFS16M at C/50 rate in the voltage range of 1.5 to 4.5 V at 55ºC. (b) Electrochemical impedance spectroscopy (EIS) of pristine LFSEDTA and LFS08M electrodes.

3.5 Conclusions

With the systematic study on hydrothermal synthesis of Li_2FeSiO_4, we were able to control the size, purity, and defect concentration in *Pmn*2_1 orthorhombic phase particles characterized by unique mesocrystal morphology. By increasing the precursor concentration, crystallization favored the production of smaller nanoparticles with a higher surface area. Rietveld refinement of synchrotron XRD data was used to examine the effects of precursor concentration and EDTA additive on the Li-Fe antisite defects concentrations. Fe oxidation states were analysed by ^{57}Fe

Mössbauer spectroscopy. The application of EDTA as a complexing agent allowed for effective control of LFS crystallization process enabling the production of high purity mesocrystals with a unique hollow structure and minimized occurrence of defect formation and Fe^{2+} oxidation. As a result, the EDTA-assisted synthesized LFS material exhibited superior initial discharge capacity of nearly 1-Li storage (164 mA h g^{-1}) owing to reduced interfacial charge transfer resistance as confirmed by EIS. The formation mechanism of LFS mesocrystals under EDTA-mediated hydrothermal conditions was proposed to involve four steps: 1) spontaneous precipitation of metastable intermediate phases, 2) local dissolution and transformation of intermediate phases to stable LFS phase, 3) initial growth by nearly-oriented attachment of nanocrystallites into mesocrystals, and 4) further growth to form hollow structure by Ostwald ripening.

3.6 Acknowledgements

This work is funded by a Hydro-Québec/Natural Sciences & Engineering Research Council of Canada (NSERC) Collaborative R&D research grant (463484-2014). YZ and GPD acknowledge additional support by the McGill Engineering International Tuition Award (MEITA) and McGill Sustainability Systems Initiative (MSSI) programs. Synchrotron radiation measurements were performed at the Canadian Light Source (CLS), which is supported by CFI, NSERC, University.

3.7 References

1. Armand, M.; Tarascon, J. M., Building better batteries. *Nature* **2008,** *451* (7179), 652-657.

2. Dunn, B.; Kamath, H.; Tarascon, J.-M., Electrical energy storage for the grid: A battery of choices. *Science* **2011,** *334* (6058), 928-935.

3. Choi, J. W.; Aurbach, D., Promise and reality of post-lithium-ion batteries with high energy densities. *Nature Reviews Materials* **2016,** *1*, 16013.

4. Arroyo-de Dompablo, M. E.; Armand, M.; Tarascon, J. M.; Amador, U., On-demand design of polyoxianionic cathode materials based on electronegativity correlations: An exploration of the Li_2MSiO_4 system (M = Fe, Mn, Co, Ni). *Electrochemistry Communications* **2006,** *8* (8), 1292-1298.

5. Dominko, R.; Bele, M.; Gaberšček, M.; Meden, A.; Remškar, M.; Jamnik, J., Structure and electrochemical performance of Li_2MnSiO_4 and Li_2FeSiO_4 as potential Li-battery cathode materials. *Electrochemistry Communications* **2006,** *8* (2), 217-222.

6. Dominko, R., Li_2MSiO_4 (M=Fe and/or Mn) cathode materials. *Journal of Power Sources* **2008,** *184* (2), 462-468.

7. Islam, M. S.; Dominko, R.; Masquelier, C.; Sirisopanaporn, C.; Armstrong, A. R.; Bruce, P. G., Silicate cathodes for lithium batteries: alternatives to phosphates? *Journal of Materials Chemistry* **2011,** *21* (27), 9811-9818.

8. Nytén, A.; Abouimrane, A.; Armand, M.; Gustafsson, T.; Thomas, J. O., Electrochemical performance of Li_2FeSiO_4 as a new Li-battery cathode material. *Electrochemistry Communications* **2005,** *7* (2), 156-160.

9. Nishimura, S.-i.; Hayase, S.; Kanno, R.; Yashima, M.; Nakayama, N.; Yamada, A., Structure of Li_2FeSiO_4. *Journal of the American Chemical Society* **2008,** *130* (40), 13212-13213.

10. Boulineau, A.; Sirisopanaporn, C.; Dominko, R.; Armstrong, A. R.; Bruce, P. G.; Masquelier, C., Polymorphism and structural defects in Li_2FeSiO_4. *Dalton Transactions* **2010,** *39* (27), 6310-6316.

11. Girish, H. N.; Shao, G. Q., Advances in high-capacity Li_2MSiO_4 (M = Mn, Fe, Co, Ni, ...) cathode materials for lithium-ion batteries. *Rsc Advances* **2015,** *5* (119), 98666-98686.

12. Armstrong, A. R.; Kuganathan, N.; Islam, M. S.; Bruce, P. G., Structure and lithium transport pathways in Li_2FeSiO_4 cathodes for lithium batteries. *Journal of the American Chemical Society* **2011,** *133* (33), 13031-13035.

13. Eames, C.; Armstrong, A. R.; Bruce, P. G.; Islam, M. S., Insights into changes in voltage and structure of Li_2FeSiO_4 polymorphs for lithium-ion batteries. *Chemistry of Materials* **2012,** *24* (11), 2155-2161.

14. Lu, X.; Chiu, H.-C.; Arthur, Z.; Zhou, J.; Wang, J.; Chen, N.; Jiang, D.-T.; Zaghib, K.; Demopoulos, G. P., Li-ion storage dynamics in metastable nanostructured Li_2FeSiO_4 cathode: Antisite-induced phase transition and lattice oxygen participation. *Journal of Power Sources* **2016,** *329*, 355-363.

15. Masese, T.; Tassel, C.; Orikasa, Y.; Koyama, Y.; Arai, H.; Hayashi, N.; Kim, J.; Mori, T.; Yamamoto, K.; Kobayashi, Y.; Kageyama, H.; Ogumi, Z.; Uchimoto, Y., Crystal structural changes and charge compensation mechanism during two lithium extraction/insertion between Li_2FeSiO_4 and $FeSiO_4$. *The Journal of Physical Chemistry C* **2015,** *119* (19), 10206-10211.

16. Armstrong, A. R.; Sirisopanaporn, C.; Adamson, P.; Billaud, J.; Dominko, R.; Masquelier, C.; Bruce, P. G., Polymorphism in Li_2MSiO_4 (M = Fe, Mn): A variable temperature diffraction study. *Zeitschrift für anorganische und allgemeine Chemie* **2014,** *640* (6), 1043-1049.

17. Paolella, A.; Turner, S.; Bertoni, G.; Hovington, P.; Flacau, R.; Boyer, C.; Feng, Z.; Colombo, M.; Marras, S.; Prato, M.; Manna, L.; Guerfi, A.; Demopoulos, G. P.; Armand, M.; Zaghib, K., Accelerated removal of Fe-antisite defects while nanosizing hydrothermal $LiFePO_4$ with Ca^{2+}. *Nano Letters* **2016,** *16* (4), 2692–2697.

18. Delacourt, C.; Poizot, P.; Levasseur, S.; Masquelier, C., Size effects on carbon-free $LiFePO_4$ powders: The key to superior energy density. *Electrochemical and Solid-State Letters* **2006,** *9* (7), A352-A355.

19. Gaberscek, M.; Dominko, R.; Jamnik, J., Is small particle size more important than carbon coating? An example study on $LiFePO_4$ cathodes. *Electrochemistry Communications* **2007,** *9* (12), 2778-2783.

20. Örnek, A., Positive effects of a particular type of microwave-assisted methodology on the electrochemical properties of olivine $LiMPO_4$ (M=Fe, Co and Ni) cathode materials. *Chemical Engineering Journal* **2018,** *331*, 501-509.

21. Jugović, D.; Milović, M.; Ivanovski, V. N.; Avdeev, M.; Dominko, R.; Jokić, B.; Uskoković, D., Structural study of monoclinic Li_2FeSiO_4 by X-ray diffraction and Mössbauer spectroscopy. *Journal of Power Sources* **2014,** *265*, 75-80.

22. Zaghib, K.; Ait Salah, A.; Ravet, N.; Mauger, A.; Gendron, F.; Julien, C. M., Structural, magnetic and electrochemical properties of lithium iron orthosilicate. *Journal of Power Sources* **2006,** *160* (2), 1381-1386.

23. Nytén, A.; Kamali, S.; Häggström, L.; Gustafsson, T.; Thomas, J. O., The lithium extraction/insertion mechanism in Li_2FeSiO_4. *Journal of Materials Chemistry* **2006,** *16* (23), 2266-2272.

24. Kumar, A.; Jayakumar, O. D.; Naik, V. M.; Nazri, G. A.; Naik, R., Improved electrochemical properties of solvothermally synthesized Li_2FeSiO_4/C nanocomposites: A comparison between solvothermal and sol-gel methods. *Solid State Ionics* **2016,** *294*, 15-20.

25. Bini, M.; Ferrari, S.; Ferrara, C.; Mozzati, M. C.; Capsoni, D.; Pell, A. J.; Pintacuda, G.; Canton, P.; Mustarelli, P., Polymorphism and magnetic properties of Li_2MSiO_4 (M = Fe, Mn) cathode materials. *Scientific Reports* **2013,** *3*, 03452.

26. Sun, S.; Matei Ghimbeu, C.; Vix-Guterl, C.; Sougrati, M.-T.; Masquelier, C.; Janot, R., Synthesis of Li_2FeSiO_4/carbon nano-composites by impregnation method. *Journal of Power Sources* **2015,** *284*, 574-581.

27. Byrappa, K.; Adschiri, T., Hydrothermal technology for nanotechnology. *Progress in Crystal Growth and Characterization of Materials* **2007,** *53* (2), 117-166.

28. Yoshimura, M.; Byrappa, K., Hydrothermal processing of materials: Past, present and future. *Journal of Materials Science* **2008,** *43* (7), 2085-2103.

29. Chen, J., A review of nanostructured lithium ion battery materials via low temperature synthesis. *Recent Patent on Nanotechnology* **2013,** *7* (1), 2-12.

30. Chen, J.; Wang, S.; Whittingham, M. S., Hydrothermal synthesis of cathode materials. *Journal of Power Sources* **2007,** *174* (2), 442-448.

31. Devaraju, M. K.; Honma, I., Hydrothermal and solvothermal process towards development of $LiMPO_4$ (M = Fe, Mn) nanomaterials for lithium-ion batteries. *Advanced Energy Materials* **2012,** *2* (3), 284-297.

32. Masquelier, C.; Croguennec, L., Polyanionic (phosphates, silicates, sulfates) frameworks as electrode materials for rechargeable Li (or Na) batteries. *Chemical reviews* **2013,** *113* (8), 6552-6591.

33. Rangappa, D.; Murukanahally, K. D.; Tomai, T.; Unemoto, A.; Honma, I., Ultrathin Nanosheets of Li_2MSiO_4 (M = Fe, Mn) as High-Capacity Li-Ion Battery Electrode. *Nano Letters* **2012,** *12* (3), 1146-1151.

34. Sirisopanaporn, C.; Dominko, R.; Masquelier, C.; Armstrong, A. R.; Mali, G.; Bruce, P. G., Polymorphism in $Li_2(Fe,Mn)SiO_4$: A combined diffraction and NMR study. *Journal of Materials Chemistry* **2011,** *21* (44), 17823-17831.

35. Sirisopanaporn, C.; Masquelier, C.; Bruce, P. G.; Armstrong, A. R.; Dominko, R., Dependence of Li_2FeSiO_4 electrochemistry on structure. *Journal of the American Chemical Society* **2011,** *133* (5), 1263-1265.

36. Yabuuchi, N.; Yamakawa, Y.; Yoshii, K.; Komaba, S., Low-temperature phase of Li_2FeSiO_4: Crystal structure and a preliminary study of electrochemical behavior. *Dalton Transactions* **2011,** *40* (9), 1846-1848.

37. Kageyama, H.; Hashimoto, Y.; Oaki, Y.; Imai, H., Six-armed twin crystals composed of lithium iron silicate nanoplates and their electrochemical properties. *Crystengcomm* **2015,** *17* (44), 8486-8491.

38. Xu, Y.; Shen, W.; Wang, C.; Zhang, A.; Xu, Q.; Liu, H.; Wang, Y.; Xia, Y., Hydrothermal synthesis and electrochemical performance of nanoparticle Li_2FeSiO_4/C cathode materials for lithium ion batteries. *Electrochimica Acta* **2015,** *167*, 340-347.

39. Xu, Y.; Shen, W.; Zhang, A.; Liu, H.; Ma, Z., Template-free hydrothermal synthesis of Li_2FeSiO_4 hollow spheres as cathode materials for lithium-ion batteries. *Journal of Materials Chemistry A* **2014,** *2* (32), 12982-12990.

40. Yang, J.; Kang, X.; He, D.; Peng, T.; Hu, L.; Mu, S., Hierarchical shuttle-like Li_2FeSiO_4 as a highly efficient cathode material for lithium-ion batteries. *Journal of Power Sources* **2013,** *242*, 171-178.

41. Yang, J.; Kang, X.; He, D.; Zheng, A.; Pan, M.; Mu, S., Graphene activated 3D-hierarchical flower-like Li_2FeSiO_4 for high-performance lithium-ion batteries. *Journal of Materials Chemistry A* **2015,** *3* (32), 16567-16573.

42. Zaghib, K.; Guerfi, A.; Hovington, P.; Vijh, A.; Trudeau, M.; Mauger, A.; Goodenough, J. B.; Julien, C. M., Review and analysis of nanostructured olivine-based lithium recheargeable batteries: Status and trends. *Journal of Power Sources* **2013,** *232*, 357-369.

43. Sturm, E. V.; Cölfen, H., Mesocrystals: structural and morphogenetic aspects. *Chemical Society Reviews* **2016,** *45* (21), 5821-5833.

44. Vediappan, K.; Guerfi, A.; Gariépy, V.; Demopoulos, G. P.; Hovington, P.; Trottier, J.; Mauger, A.; Zaghib, K.; Julien, C. M., Effect of the stirring during the hydrothermal synthesis of C-$LiFePO_4$. *ECS Transactions* **2014,** *58* (14), 67-72.

45. Encina, E. R.; Distaso, M.; Klupp Taylor, R. N.; Peukert, W., Synthesis of goethite α-FeOOH particles by air oxidation of ferrous hydroxide $Fe(OH)_2$ suspensions: Insight on the formation mechanism. *Crystal Growth & Design* **2015,** *15* (1), 194-203.

46. Meng, X.; Bang, S.; Korfiatis, G. P., Effects of silicate, sulfate, and carbonate on arsenic removal by ferric chloride. *Water Research* **2000,** *34* (4), 1255-1261.

47. Dzombak D. A. , M. F. o. M. M., *Surface complexation modeling: Hydrous ferric oxide*. Wiley: New York, 1990.

48. Yabuuchi, N.; Yamakawa, Y.; Yoshii, K.; Komaba, S., Hydrothermal synthesis and characterization of Li_2FeSiO_4 as positive electrode materials for Li-ion batteries. *Electrochemistry* **2010,** *78* (5), 363-366.

49. Demopoulos, G. P., Aqueous precipitation and crystallization for the production of particulate solids with desired properties. *Hydrometallurgy* **2009,** *96* (3), 199-214.

50. Zhao, J.; Tao, Z.; Liang, J.; Chen, J., Facile synthesis of nanoporous γ-MnO_2 structures and their application in rechargeable Li-ion batteries. *Crystal Growth & Design* **2008,** *8* (8), 2799-2805.

51. Hou, X.; Xue, S.; Liu, M.; Shang, X.; Fu, Y.; He, D., Hollow irregular octahedra-like $NiCo_2O_4$ cages composed of mesoporous nanosheets as a superior anode material for lithium-ion batteries. *Chemical Engineering Journal* **2018,** *350*, 29-36.

52. Kim, Y.; Lee, J.-H.; Cho, S.; Kwon, Y.; In, I.; Lee, J.; You, N.-H.; Reichmanis, E.; Ko, H.; Lee, K.-T.; Kwon, H.-K.; Ko, D.-H.; Yang, H.; Park, B., Additive-free hollow-structured Co_3O_4 nanoparticle Li-ion battery: The origins of irreversible capacity loss. *ACS Nano* **2014,** *8* (7), 6701-6712.

53. He, G.; Popov, G.; Nazar, L. F., Hydrothermal synthesis and electrochemical poperties of Li_2CoSiO_4/C nanospheres. *Chemistry of Materials* **2013,** *25* (7), 1024-1031.

54. Yang, X.-F.; Yang, J.-H.; Zaghib, K.; Trudeau, M. L.; Ying, J. Y., Synthesis of phase-pure Li_2MnSiO_4@C porous nanoboxes for high-capacity Li-ion battery cathodes. *Nano Energy* **2015,** *12*, 305-313.

55. Mali, G.; Sirisopanaporn, C.; Masquelier, C.; Hanzel, D.; Dominko, R., Li_2FeSiO_4 polymorphs probed by Li-6 MAS NMR and Fe-57 Mössbauer spectroscopy. *Chemistry of Materials* **2011,** *23* (11), 2735-2744.

56. Liivat, A.; Thomas, J. O., Li-ion migration in Li_2FeSiO_4-related cathode materials: A DFT study. *Solid State Ionics* **2011,** *192* (1), 58-64.

57. Armstrong, A. R.; Lyness, C.; Ménétrier, M.; Bruce, P. G., Structural polymorphism in Li_2CoSiO_4 intercalation electrodes: A combined diffraction and NMR study. *Chemistry of Materials* **2010,** *22* (5), 1892-1900.

58. Fisher, C. A. J.; Kuganathan, N.; Islam, M. S., Defect chemistry and lithium-ion migration in polymorphs of the cathode material Li_2MnSiO_4. *Journal of Materials Chemistry A* **2013,** *1* (13), 4207-4214.

59. Dominko, R.; Conte, D. E.; Hanzel, D.; Gaberscek, M.; Jamnik, J., Impact of synthesis conditions on the structure and performance of Li_2FeSiO_4. *Journal of Power Sources* **2008,** *178* (2), 842-847.

60. Chen, R.; Heinzmann, R.; Mangold, S.; Chakravadhanula, V. S. K.; Hahn, H.; Indris, S., Structural evolution of $Li_2Fe_{1-y}Mn_ySiO_4$(y = 0, 0.2, 0.5, 1) cathode materials for Li-ion batteries upon electrochemical cycling. *The Journal of Physical Chemistry C* **2013,** *117* (2), 884-893.

61. Liivat, A.; Thomas, J.; Guo, J.; Yang, Y., Novel insights into higher capacity from the Li-ion battery cathode material Li2FeSiO4. *Electrochimica Acta* **2017,** *223*, 109-114.

62. Deng, C.; Zhang, S.; Gao, Y.; Wu, B.; Ma, L.; Sun, Y. H.; Fu, B. L.; Wu, Q.; Liu, F. L., Regeneration and characterization of air-exposed Li_2FeSiO_4. *Electrochimica Acta* **2011,** *56* (21), 7327-7333.

63. Mysen, B. O., The structural behavior of ferric and ferrous iron in aluminosilicate glass near meta-aluminosilicate joins. *Geochimica et Cosmochimica Acta* **2006,** *70* (9), 2337-2353.

64. Uchaker, E.; Gu, M.; Zhou, N.; Li, Y.; Wang, C.; Cao, G., Enhanced intercalation dynamics and stability of engineered micro/nano-structured electrode materials: vanadium oxide mesocrystals. *Small* **2013,** *9* (22), 3880-6.

65. Tachikawa, T.; Majima, T., Metal oxide mesocrystals with tailored structures and properties for energy conversion and storage applications. *Npg Asia Mater* **2014,** *6*, e100.

66. Hart, J. R., Ethylenediaminetetraacetic acid and related chelating Agents. In *Ullmann's Encyclopedia of Industrial Chemistry*, 2011.

67. Thanh, N. T. K.; Maclean, N.; Mahiddine, S., Mechanisms of nucleation and growth of nanoparticles in solution. *Chemical reviews* **2014,** *114* (15), 7610-7630.

68. Chirita, M.; Banica, R.; Ieta, A.; Grozescu, I., Fe-EDTA thermal decomposition, a route to highly crystalline hematite (alpha Fe_2O_3) nanoparticle synthesis. *Particulate Science and Technology* **2010,** *28* (3), 217-225.

69. Fujishiro, Y.; Sato, T.; Okuwaki, A., Homogeneous precipitation of transition metal (Co^{2+}, Fe^{2+}, Ni^{2+} and Zn^{2+}) phosphates under hydrothermal conditions utilizing metal polyaminocarboxylate complex as a precursor. *Phosphorus Research Bulletin* **1994,** *4*, 1-6.

70. De Yoreo, J. J.; Gilbert, P. U. P. A.; Sommerdijk, N. A. J. M.; Penn, R. L.; Whitelam, S.; Joester, D.; Zhang, H.; Rimer, J. D.; Navrotsky, A.; Banfield, J. F.; Wallace, A. F.; Michel, F. M.; Meldrum, F. C.; Cölfen, H.; Dove, P. M., Crystallization by particle attachment in synthetic, biogenic, and geologic environments. *Science* **2015,** *349* (6247), aaa6760.

71. Voorhees, P. W., The theory of Ostwald ripening. *Journal of Statistical Physics* **1985,** *38* (1), 231-252.

72. Chen, F.; Gao, Q.; Hong, G.; Ni, J., Synthesis and characterization of magnetite dodecahedron nanostructure by hydrothermal method. *Journal of Magnetism and Magnetic Materials* **2008,** *320* (11), 1775-1780.

73. Zhu, Z.; Du, J.; Li, J.; Zhang, Y.; Liu, D., An EDTA-assisted hydrothermal synthesis of $BiVO_4$ hollow microspheres and their evolution into nanocages. *Ceramics International* **2012,** *38* (6), 4827-4834.

74. Devaraju, M. K.; Tomai, T.; Honma, I., Supercritical hydrothermal synthesis of rod like Li_2FeSiO_4 particles for cathode application in lithium ion batteries. *Electrochimica Acta* **2013,** *109*, 75-81.

75. Ding, Z.; Zhang, D.; Feng, Y.; Zhang, F.; Chen, L.; Du, Y.; Ivey, D. G.; Wei, W., Tuning anisotropic ion transport in mesocrystalline lithium orthosilicate nanostructures with preferentially exposed facets. *Npg Asia Mater* **2018,** *10* (7), 606-617.

76. Yang, J.; Kang, X.; Hu, L.; Gong, X.; Mu, S., Nanocrystalline-Li_2FeSiO_4 synthesized by carbon frameworks as an advanced cathode material for Li-ion batteries. *Journal of Materials Chemistry A* **2014,** *2* (19), 6870-6878.

77. Lv, D. P.; Bai, J. Y.; Zhang, P.; Wu, S. Q.; Li, Y. X.; Wen, W.; Jiang, Z.; Mi, J. X.; Zhu, Z. Z.; Yang, Y., Understanding the high Capacity of Li_2FeSiO_4: in situ XRD/XANES study combined with first-principles calculations. *Chemistry of Materials* **2013,** *25* (10), 2014-2020.

78. Brownrigg, A. W.; Mountjoy, G.; Chadwick, A. V.; Alfredsson, M.; Bras, W.; Billaud, J.; Armstrong, A. R.; Bruce, P. G.; Dominko, R.; Kelder, E. M., In situ Fe K-edge X-ray absorption spectroscopy study during cycling of Li_2FeSiO_4 and $Li_{2.2}Fe_{0.9}SiO_4$ Li ion battery materials. *Journal of Materials Chemistry A* **2015,** *3* (14), 7314-7322.

Chapter 4. Unveiling the Mechanism of Improved Capacity Retention in *Pmn*2$_1$ Li_2FeSiO_4 Cathode by Cobalt Substitution

In Chapter 3, we focused on the hydrothermal synthesis of LFS with a brief evaluation of the electrochemical activity of the as-synthesized LFS. It is found that although the optimized LFS could deliver approximately 1 Li^+ per formula unit at high temperature (55ºC) and a slow current rate (C/50) in the first discharge, capacity fading occurred in the following cycles with decline of voltage plateau. In this chapter, we are aiming to improve the capacity retention of LFS by employing the cation doping strategy that has been shown as an effective way to tune the intrinsic properties of intercalation cathode materials. First-principles DFT calculations integrated with experimental synthesis are integrated to select dopants that could be practically doped to the lattice of *Pmn*2$_1$ LFS via hydrothermal method. Co^{2+}-doped $Li_2Fe_{0.94}Co_{0.06}SiO_4$ (CoLFS) is successfully synthesized and stands out as the most promising doped-compound by showing notable enhancement in capacity retention. The mechanism behind this enhancement is then revealed by in-depth electrochemical and spectroscopic analyses on the pristine and cycled electrodes. It is noticed that a more practical cycling condition is applied in this chapter, namely, 45ºC and C/10 to reduce the undesired side reactions that can be accelerated with increasing temperature and accumulated in a long charge-discharge duration.

This chapter was published as **Yan Zeng**, Hsien-Chieh Chiu, Bin Ouyang, Jun Song, Karim Zaghib, George P. Demopoulos. Unveiling the mechanism of improved capacity retention in *Pmn*2$_1$ Li_2FeSiO_4 cathode by cobalt substitution. *Journal of Materials Chemistry A* **2019**, *7* (44): 25399-25414. DOI: 10.1039/C9TA10287F.

4.1 Abstract

Li_2FeSiO_4 (LFS) is a sustainable Li-ion cathode material composed of earth-abundant elements with potentially high-energy-density but suffers from limited reversible storage capacity (less than one Li), low intrinsic conductivities, and cycling instability. In search of deeper understanding of the structural chemistry of LFS towards overcoming some of these challenges, the viability of Fe-site doping by Co and other dopants in *Pmn*2$_1$ LFS is investigated using both first-principles calculations and experimental testing. Computational results suggest that the

formation of $Li_2Fe_{1-x}Co_xSiO_4$ is energetically favorable, predictions confirmed by successful hydrothermal synthesis. Substitution of Co in LFS is revealed to have a dual effect; firstly catalyzing faster electrochemically induced phase transformation to the stable inverse-$Pmn2_1$ phase; and secondly enabling the formation of a low-resistant, uniform and stable fluorine-rich cathode-electrolyte interphase (CEI) layer that inhibits detrimental reactions between the cathode and electrolyte. As a result, Co-substituted LFS displays enhanced reversibility with 95% capacity retention after 50 cycles as compared to 80% of the undoped LFS.

4.2 Introduction

The demand for cost-competitive LIBs with enhanced energy density and high safety has motivated extensive research into various advanced cathode materials.[1-4] In this context, the discovery and commercial success of olivine $LiFePO_4$ has been instrumental in directing considerable research activities on cathode materials built on three-dimensional frameworks of polyanions (XO_4^{n-}, X = Si, P, and S).[5] The positive attributes of polyanionic frameworks include their structural stability, increased redox potential as a result of inductive effect, and versatility toward cation and anion substitution.[5] $LiFePO_4$, however, has reached its limitation of energy density.[6] In search of higher capacity polyanionic materials, transition metal orthosilicates, particularly Li_2FeSiO_4 (LFS), are promising candidates as they can accommodate two Li-ions per transition metal, so theoretically having capacity of ~330 mAh g^{-1}, twice the capacity of LFP.[7-16] Yet, the attainment of such high theoretical capacity from LFS has been hindered by several obstacles including low intrinsic electronic and ionic conductivities,[10] high voltage (~4.8 V vs. Li^+/Li) required for accessing the above one-Li-capacity,[17] which could cause decomposition of the electrolyte,[18-20] and plausible participation of oxygen redox associated with structural instability.[14-15]

One strategy that has been pursued to overcome these material challenges with the electrochemical performance of Li_2FeSiO_4 is Fe^{2+}-site cation doping. In this regard, various cations have been evaluated as dopants for the monoclinic LFS phase, $P2_1/n$ but not for the less common orthorhombic $Pmn2_1$ phase. Among the dopants evaluated for $P2_1/n$ are divalent cations such as Mg^{2+}, Co^{2+}, Ni^{2+}, Cu^{2+}, Zn^{2+}, Cd^{2+}, and Sr^{2+}, and aliovalent cations such as Al^{3+}, Cr^{3+}, Y^{3+}, Ti^{4+}, and Sn^{4+}.[21-34] Some of these cations were found to improve the electrochemical properties of $P2_1/n$ LFS. For example, aliovalent doping with Ti^{4+} was reported to profoundly enhance the

structural stability and electrochemical activity of $P2_1/n$ LFS, attributed to the strong hybridization between Ti 3d and 4s orbitals and O 2p orbital.[32] On the other hand, Co^{2+} was found to be the most effective divalent dopant in improving the rate capability of LFS,[24] as in the case of Co^{2+} doping in Li_2MnSiO_4[35] and LFP.[36] The beneficial effect of Co^{2+} substitution in these previous studies have been attributed mainly to enhanced electronic and ionic conductivities via the introduction of defects.[24] But this conductivity enhancement effect does not shed light as to the structural stabilization effect Co^{2+} is known of and which is important to understand in our pursuit of Co-free cathode materials.[37]

It is the scope of this work to address this mechanistic gap in our understanding of the complex material chemistry effects Co substitution has by focusing on another important polymorph of LFS, i.e. a low-temperature orthorhombic structure in S.G. $Pmn2_1$.[13] $Pmn2_1$ LFS has been found to be less electrochemically active in terms of capacity and cyclability than $P2_1/n$ LFS[9] and suffer also from capacity fading - the origin of which has not been elucidated,[38-39] hence offering an interesting intercalation host structure to study the effect of Co doping. Other than seeking to enhance its electrochemical performance and more generally the Co-doping chemistry of $Pmn2_1$, it is of interest to examine how the solubility of Co substitution may differ from one LFS phase to the other and how it is influenced by the synthesis temperature.[40-41] In this context, first-principles DFT calculations can provide useful guideline for the selection of dopants via examination of the thermodynamic stability and other properties of the cation-substituted LFS compounds.[42-45]

In this work, we carried out first-principles calculations to examine the solubility of various cation dopants in $Pmn2_1$ LFS and subsequently prepared them via hydrothermal synthesis.[46] As per computational guidelines, high-purity $Li_2Fe_{0.94}Co_{0.06}SiO_4$ (denoted as CoLFS) and $Li_2Fe_{0.94}Mg_{0.06}SiO_4$ (denoted as MgLFS) were successfully prepared and electrochemically tested. In the meantime, Ni^{2+} or Sr^{2+}-substituted $Pmn2_1$ LFS could not be synthesized due to their high formation energies compared to other competing phases. A preliminary evaluation on the electrochemical performance of MgLFS revealed that the cyclability of MgLFS was even worse than the undoped LFS. Therefore, we focused on CoLFS which showed promise in enhancing the electrochemical performance and offering the opportunity to shed light on the stabilization effect Co doping plays. Galvanostatic charge-discharge, cyclic voltammetry (CV), and electrochemical

impedance spectroscopy (EIS) were applied to unveil the role of Co-substitution in improving the cyclability of LFS. Surface characterization by X-ray photoelectron spectroscopy (XPS) and Fourier Transform Infrared (FTIR) spectroscopy provided evidence of cobalt-enabled formation of a protective thin cathode-electrolyte interphase (CEI) contributing to cathode stability. DFT calculations provided insight as to the structural and electrochemical effects of cobalt in terms of energetics, redox potential, and structural changes during Li-extraction in both *Pmn*2_1 and inverse-*Pmn*2_1 polymorphs.

4.3 Experimental

4.3.1 Synthesis

Li_2FeSiO_4 and $Li_2Fe_{0.94}M_{0.06}SiO_4$ (M = Mg, Co, Ni) were prepared by employing a hydrothermal method[46]. The starting materials used were lithium hydroxide monohydrate (98% $LiOH{\cdot}H_2O$), fumed silica (99% SiO_2), iron(II) sulfate heptahydrate (98% $FeSO_4{\cdot}7H_2O$), magnesium sulfate heptahydrate (98% $MgSO_4{\cdot}7H_2O$), cobalt(II) sulfate heptahydrate (98% $CoSO_4{\cdot}7H_2O$), and nickel sulfate hexahydrate (99% $NiSO_4{\cdot}6H_2O$). For the preparation of $Li_2Fe_{0.94}Sr_{0.06}SiO_4$, Fe and Sr precursors were iron(II) chloride tetrahydrate (99% $FeCl_2{\cdot}4H_2O$) and strontium chloride hexahydrate (99% $SrCl_2{\cdot}6H_2O$) because of the limited solubility of strontium sulfate in water. All the chemicals were purchased from Sigma-Aldrich and used without purification. In a typical synthesis, SiO_2 powder was dissolved in LiOH aqueous solution.[46] Mixed-metal solutions were prepared by mixing the required metal salts and dissolving them in water. The mixed-metal solution was then dropped wisely added to the $LiOH/SiO_2$ solution. The concentration of Li^+ was 0.8 M in the precursor solution. The molar ratio of Li: (Fe+M): Si was kept at 4: 1: 1 for all the syntheses. The as-formed precursor suspension was loaded to a 450 mL PTFE-lined stirred autoclave (Parr Instrument Company, Moline, IL). All these preparation steps were performed in a nitrogen-filled glovebox to avoid the oxidation of Fe(II) in alkaline solution. Hydrothermal synthesis was performed at 200^{o}C for 6 hours at a stirring speed of 300 rpm. A Parr 4848 reactor controller was used to control and monitor the temperature and pressure within the autoclave. After the completion of hydrothermal precipitation, the autoclave was cooled down to room temperature within 30 min. The obtained beige-greyish slurry was separated by centrifugation. The wet solid was rinsed with deoxygenated LiOH solution for two times and with acetone for one time, followed by drying in a vacuum oven at 80^{o}C for 12 hours. The obtained

powders of LFS, CoLFS, and MgLFS were further subjected to annealing at 400^{o}C for 6 hours under Ar atmosphere and subsequently quenched to room temperature in a tube furnace. All the products were stored in glovebox to prevent the exposure to oxygen and moisture.

4.3.2 Characterizations

X-ray Diffraction (XRD) characterizations were performed with a Bruker D8-Advantage powder diffractometer using Co-Kα radiation (λ = 1.78892 Å, 35 kV; 15 mA) from 2θ = 15 to 100° in a step size of 0.01°. XRD patterns were refined by Le Bail method with TOPAS Academic V.5.0 program to extract lattice parameters of the unit cell and check phase purity. A Hitachi SU-8230 cold-field emission Scanning Electron Microscope (CFE-SEM) (Hitachi High Technologies, Rexdale, Canada) was employed for morphology characterization and Energy-Dispersive X-ray Spectroscopy (EDS). X-ray Photoelectron Spectroscopy (XPS) measurements were performed on a PHI 5500 system using monochromatized Al-Kα at 1486.6 eV. The applied X-ray spot size was 400 μm. Electron flood gun was used for charge compensation. The spectrometer energy scale was calibrated using C1s characteristic peak at 284.8 eV (C-C). Spectra of C 1s, O 1s, F 1s, P 2p, and Si 2p were fitted with single or multiple peaks. XPS data processing was performed with Thermo Avantage Software. Fourier Transform Infrared (FTIR) spectroscopy was carried out with Bruker's ALPHA platinum module in the wavenumber range of 400 to 4000 cm^{-1}.

4.3.3 Electrochemical measurements

The pristine powders collected after annealing were mixed with acetylene black (AB) in a weight ratio of 0.8: 0.2 and ball-milled at 250 rpm for 3 hours using a planetary micro mill (Fritsch, Pulverisette 7 premium line). The working electrodes were prepared by spreading slurry of the ball-milled LFS (BM-LFS), acetylene black, and poly (vinylidene difluoride) (PVDF) in a weight ratio of BM-LFS: AB: PVDF = 0.8: 0.1: 0.1 onto aluminum foil. The resultant composite contains 64 wt% of active materials (LFS or CoLFS), 26 wt% of AB, and 10 wt% of PVDF. Each final electrode contains approximately 2.5 mg cm^{-2} of active materials. Electrochemical testing was performed on Swagelok type half-cells using metallic lithium as the counter and reference electrode and two pieces of polypropylene film (Celgard 2200) as the separator in a standard electrolyte solution made of 1M $LiPF_6$/ethylene carbonate (EC)/dimethyl carbonate (DMC) (1: 1 by volume). Galvanostatic charge-discharge was conducted with an Arbin battery cycler at C/10 (16.6 mA g^{-1}) or C/30 (5.5 mA g^{-1}) rate in the voltage range between 1.5 – 4.5 V. The reported

capacity values are based on the weight of active materials, excluding acetylene black and PVDF. Cyclic Voltammetry (CV) and Electrochemical Impedance Spectroscopy (EIS) measurements were carried out on an electrochemical workstation (Bio-Logic). CV was performed between 1.5 – 4.5 V at a scan rate of 0.2 mV s^{-1} for the first ten sweeps and then scanned at 0.1, 0.2, 0.3, 0.4, and 0.5 mV s^{-1} successively. EIS measurements were made in the potentiostatic mode at open circuit voltage (OCV) after a 6-hour rest before and after the CV test. The frequency of EIS was between 1 MHz and 20 mHz. All the electrochemical measurements were performed at 45ºC.

For the *ex situ* characterizations of the cycled electrodes after CV tests, Swagelok cells were disassembled in an argon-filled glovebox. The electrodes were rinsed with DMC solvent and dried inside the antechamber under vacuum for 12 hours. The dried electrodes were then sealed and stored in the glovebox for further analyses.

4.3.4 Computational methods

Spin polarized density functional theory (DFT) calculations were performed in the Vienna *ab initio* simulation package (VASP) using the projector augmented wave (PAW) method.[47-48] Generalized gradient approximation Perdew−Burke−Ernzerhof (GGA-PBE) functional was employed.[49] Hubbard parameter correlation (GGA + *U*) was used to correct the interactions inside the *d*-orbitals of the transition metals. *U* values for Co, Fe, Mn, and Ni are 3.32, 5.3, 3.9, and 6.2 eV, respectively.[50-51] The cutoff energy was kept at 700 eV for all the calculations. A calculation is treated as converged if the forces on all of the nuclei were smaller than 0.01 eV/Å.

The initial atomic configurations of *Pmn*2_1 and inverse-*Pmn*2_1 Li_2FeSiO_4 for the present calculations were adopted from Eames *et al*.[52] The difference between *Pmn*2_1 and inverse-*Pmn*2_1 is that in inverse-*Pmn*2_1 half of the Li-ions interchange positions with all of the Fe-ions. Doping with a series of dopants, namely, divalent Mg, Mn, Co, Ni, and Sr and aliovalent Ti and Zr were envisaged here. 2×2×2 supercells were constructed, and in each supercell one Fe was substituted by one dopant, giving a doping concentration of 6.25 atom% (shown in Figure 4.1). This doping concentration was chosen as a comprise between the effectiveness of doping and the theoretical specific capacity; too low content of dopants may dilute the effect of doping while too high content would sacrifice the capacity from Fe^{2+}/Fe^{3+} redox reaction. The nominal formula of a doped Li_2FeSiO_4 is represented as $Li_2Fe_{0.94}M_{0.06}SiO_4$, where M denotes the doping element. To evaluate the phase stability of the doped structures, all of the competing phases under the Li-Fe-Si-O-M

compositional space were involved to build the energy convex hull.[50] In this case, the energy above the hull represents the thermodynamic driving force for a compound to decompose into the competing phases at the hull. This will therefore offer more accurate description about the stability and the potential phase transition of the compounds during synthesis. The structures of all the potential competing phases were taken from Materials Project database[50] with followed-up DFT relaxation to ensure higher precision criterion as described above. In the assessment of delithiation process, particularly energy and volume changes, one or two Li-ions per formula unit was removed from Li_2FeSiO_4, resulting in $LiFeSiO_4$ or $FeSiO_4$. All of the structures were fully relaxed prior to further calculations. Note that in the delithiated inverse-*Pmn*2_1 $LiFeSiO_4$, Li-ion occupies the original Li-site, which means it is the Li-ion on the Fe-site that has been removed from the host structure of Li_2FeSiO_4. Same approach was applied on $Li_2Fe_{0.94}Co_{0.06}SiO_4$ to understand its delithiation process.

4.4 Results and Discussion

4.4.1 DFT-guided screening of potential dopants and experimental validation

First the theoretical feasibility of synthesizing a series of M doped-LFS in *Pmn*2_1 symmetry with 6.25% dopant concentration was evaluated using DFT calculations. The evaluated dopants (M) include divalent Mg, Mn, Co, Ni, Sr, and aliovalent Ti and Zr. The atomic configuration of *Pmn*2_1 $Li_2Fe_{0.94}M_{0.06}SiO_4$ is shown in Figure 4.1a. The *Pmn*2_1 phase has a lower energy than the inverse-*Pmn*2_1 phase for all the dopants considered according to DFT calculations (results reported in Table B1), hence we have assumed the *Pmn*2_1 will likely form during synthesis regardless of the dopant type. The experimental synthesis results presented later proved this hypothesis. Energies above the hull calculated for $Li_2Fe_{0.94}M_{0.06}SiO_4$ are depicted in Figure 4.1a. The values of energies and the potential decomposition phases are listed in Table B2. As shown in Figure 4.1a, doping of Zr is associated with extremely high energy above the hull of approximately 583 meV/atom. As energy above the hull represents the thermodynamic driving force for a compound to decompose into its competing phases at the convex hull, it is suggested that Zr-doped LFS is unlikely to form, even if higher synthesis temperatures and low doping concentrations are applied. Ti-doped LFS also shows a relatively high energy above the hull of about 33 meV/atom. An estimation based on Boltzmann distribution[53] suggests that only 0.2% of Ti is possible to be doped into LFS at accessible hydrothermal temperatures (e.g. 200^{o}C). However, if the temperature is

raised to 700°C, the doping concentration can be increased to 4.3%. This may explain why Ti-doped $P2_1/n$ LFS materials were reported by studies using high-temperature synthesis method.[32-33] Nevertheless, doping with high-valence cations seem to be limited to very low concentrations. Interestingly, a computational study on doping in the related $LiFePO_4$ system revealed that the substitution of high-valence dopants on either Li- or Fe-site is highly unfavorable.[40] Sr- or Ni-substituted LFS possesses moderate energies above their competing phases. The lowest energies are found for substitution by Mn, Co, and Mg, which are less than 10 meV/atom above their energy hulls. This result suggests the possibility of doping a certain concentration of Mn, Co, or Mg into $Pmn2_1$ LFS under hydrothermal conditions. This finding is in agreement with a reported experimental study on $Li_2Fe_{1-x}Mn_xSiO_4$ (x = 0 - 1) in which solid solutions were found to form by hydrothermal synthesis at 180°C.[54]

To further validate this prediction, we examined experimentally the dopants identified to have relatively low formation energies (i.e. Mg, Co, Ni, and Sr that have less positive E above hull) with a nominal composition $Li_2Fe_{0.94}M_{0.06}SiO_4$ (M = Mg, Co, Ni, Sr) via hydrothermal synthesis at 200°C. XRD patterns of the as prepared powders are shown in Figure 4.1b. Le Bail method was employed to refine the unit cell and check phase purity (see Figure B1). As shown in Figure 4.1b and Figure B1, Mg- and Co-doped LFS materials have similar patterns as LFS, with all the diffraction peaks ascribed to Li_2FeSiO_4 in space group $Pmn2_1$. The similarity in XRD patterns suggests that Mg and Co being doped into LFS host lattice, which will be further evidenced by EDS elemental mapping presented in later section. As a comparison, XRD patterns from Ni- and Sr-involved samples show obvious signals from other Ni- or Sr-containing phases. The solubility of Ni in LFS is probably limited by the preferred formation of other compounds such as $NiFe_2O_4$ and NiO which are more stable under the synthesis condition. As for Sr it formed a separate phase, $SrSiO_3$, rather than becoming incorporated in LFS lattice. These experimental results are consistent with the calculated formation energies (Figure 4.1a), proving the validity and usefulness of the DFT calculations using in predicting new materials and material properties.

To this end, only MgLFS and CoLFS are concluded to be synthesizable by the hydrothermal process. A moderate post-annealing at 400°C was conducted on the hydrothermally synthesized powders with the aim to achieve improved electrochemical performance without changing the $Pmn2_1$ crystal structure. However, preliminary electrochemical evaluations revealed

that the cyclability of MgLFS was even worse than the undoped LFS (Figure B2). Severe capacity loss associated with enlarging polarization were observed in MgLFS cycled at C/10. The cause for the observed adverse effect of Mg doping in LFS remains unclear. We chose CoLFS to further study the electrochemical performance of doped-LFS and compared it to LFS.

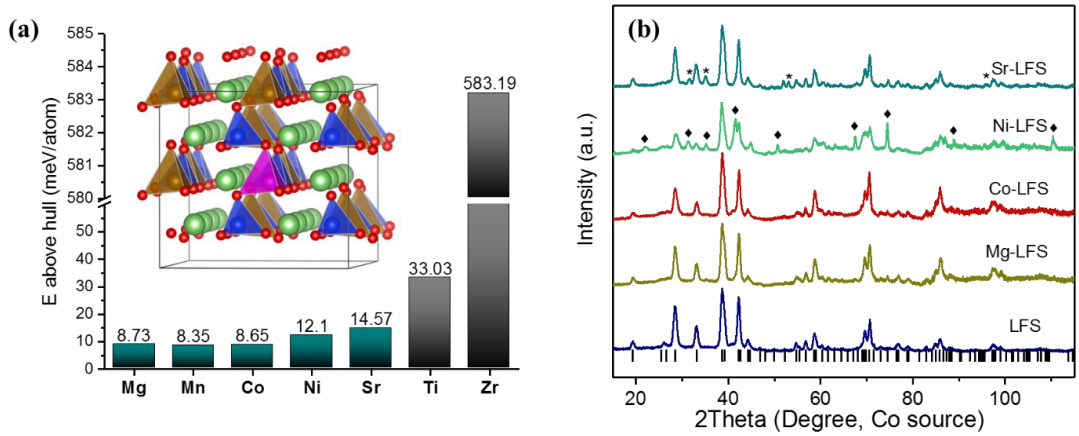

Figure 4.1. Synthesis of different metal-substituted LFS compounds. (a) Energy above the hull of *Pmn*2$_1$ $Li_2Fe_{0.94}M_{0.06}SiO_4$ (M = Mg, Mn, Co, Ni, Sr, Ti, and Zr) calculated by DFT. The inset shows atomic configuration of *Pmn*2$_1$ $Li_2Fe_{0.94}M_{0.06}SiO_4$, in which one Fe atom is replaced by one dopant in a 2 × 2 × 2 supercell. (b) XRD of Mg, Co, Ni, or Sr-involved Li_2FeSiO_4 samples obtained by hydrothermal synthesis at 200°C. Sticks at the bottom belong to the reference pattern of *Pmn*2$_1$ Li_2FeSiO_4 (PDF# 01-080-3671). Stars and diamonds represent the impurities observed in Sr-LFS and Ni-LFS, respectively.

4.4.2 Structural characterizations

XRD patterns of the annealed LFS and CoLFS, shown in Figure 4.2a, prove that both retained the *Pmn*2$_1$ crystal structure after annealing at 400°C for 6 hours. It is consistent with previous studies that the *Pmn*2$_1$ phase of LFS is stable up to 500°C.[55] We constructed a quaternary phase diagram of the Li-Fe-Co-Si-O system (Figure 4.2b) via the first principles DFT method. The thermodynamically stable phases within this chemical space are noted in the phase diagram. We can see from Figure 4.2b that the major competing reaction for the formation of $Li_2Fe_{1-x}Co_xSiO_4$ solid solution is its phase separation into a mixture of Li_2FeSiO_4 and Li_2CoSiO_4. This indicates that even if Co cannot be introduced into Li_2FeSiO_4 lattice, it could still combine with other elements and form Li_2CoSiO_4, and this will give rise to a similar XRD pattern as $Li_2Fe_{1-x}Co_xSiO_4$ due the similar electron densities between Co^{2+} and Fe^{2+}. Thus, SEM and EDS mappings were used to further confirm the substitution of Co in LFS lattice. SEM images in Figures 4.1c reveal

that LFS and CoLFS particles exhibit similar crystal size and morphology– both crystallized as mesocrystals (~1μm) assembled by irregular nanoplates. Details about the hydrothermal formation of LFS mesocrystals can be found in our previous work.[46] EDS elemental mappings on CoLFS particles (Figure 4.2d) demonstrate uniform distributions of Fe, Co, Si and O, confirming that Co has been successfully incorperated to the host matrix of LFS, rather than forming seperared Li_2CoSiO_4 particles.

Although XRD patterns of both LFS and CoLFS can be indexed to the $Pmn2_1$ symmetry, a careful comparison between these two patterns reveals that several peaks exhibit different intensities between LFS and CoLFS. As demonstrated in the enlarged 2theta region (Figure 4.2a), three peaks at 19.1°, 28.4° and 33.1° in CoLFS have lower intensities than those in LFS. In $Pmn2_1$ polymorph, peaks at 19.1°, 28.4° and 33.1° (λ = 1.7889 Å) correspond to the reflections from (010), (011) and (200) lattice planes, respectively. The difference in the peak intensity indicates that LFS and CoLFS have different electron densities in the corresponding lattice planes. Considering that Fe^{2+} and Co^{2+} have similar electron densities, variation in peak intensities would originate from different amount of Fe/Li and/or Co/Li antisite defects.[56] The lower XRD peak intensities from CoLFS than LFS suggest that there are more antisite defects in CoLFS than LFS. To confirm this hypothesis, we simulated the XRD patterns of CoLFS in ideal $Pmn2_1$ structure where Co sits on the Fe-site vs. CoLFS with a local Co/Li antisite defect (one Co exchanges site with one Li) using VESTA software.[57] As shown in Figure 4.3, the presence of Co/Li antisite defect results in lower reflection intensities from (010), (011), and (200) planes. The simulation results (Figure 4.3b) agree very well with the experimental XRD (Figure 4.2a). From the energetic point of view, we calculated the total energies of Li_2FeSiO_4 and Li_2CoSiO_4 in both $Pmn2_1$ and inverse-$Pmn2_1$ structures. Inverse-$Pmn2_1$ is formed when all the Fe and Co exchange sites with Li. Interestingly, the stable structure for Li_2FeSiO_4 is $Pmn2_1$, which has energy ~0.04 eV/f.u. lower than inverse-$Pmn2_1$ (i.e. -53.13 eV/f.u. vs. -53.09 eV/f.u.). On the contrary, Li_2CoSiO_4 is more stable in inverse-$Pmn2_1$ structure rather than in $Pmn2_1$ structure (-51.68 eV/f.u. vs. -51.65 eV/f.u.). This energy difference suggests that when Co is incorporated into LFS matrix during synthesis, it may prefer to take the Li-site and leads to the formation of a Co/Li antisite.

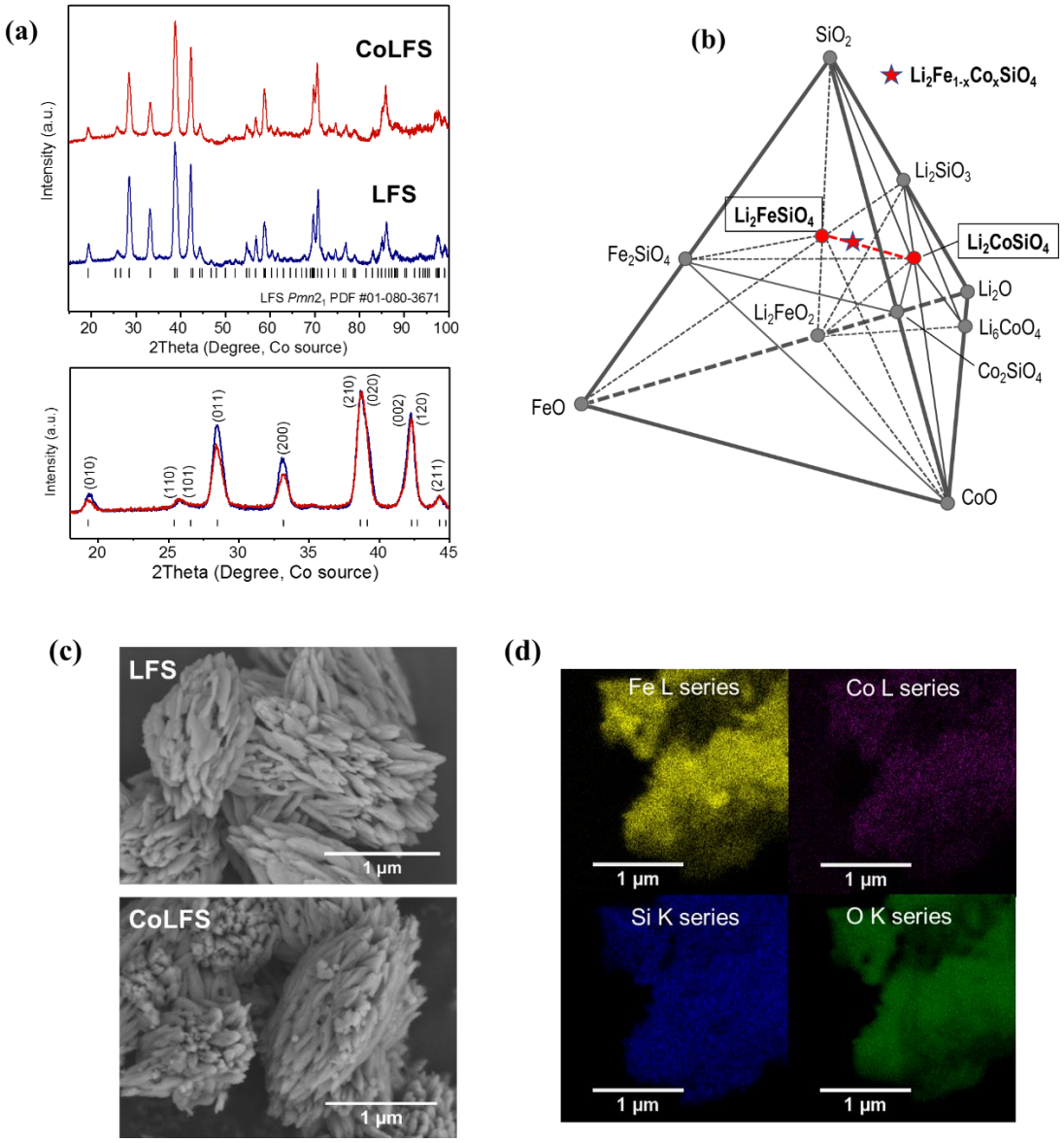

Figure 4.2. Structural and morphological characterizations of LFS and CoLFS. (a) X-ray diffraction patterns of LFS and CoLFS prepared by hydrothermal synthesis at 200°C followed by annealing at 400°C. The enlarged 2theta area from 25 to 45 degree are shown at the bottom. Sticks at the bottom belong to a reference pattern of *Pmn*2$_1$ Li_2FeSiO_4 (PDF# 01-080-3671). Different peak intensities associated with (010), (011), and (200) planes are observed. (b) Calculated quaternary phase diagram of the Li-Fe-Co-Si-O system in accordance to Li_2O, FeO, CoO, and SiO_2. Dashed red line in the phase diagram presents $Li_2Fe_{1-x}Co_xSiO_4$ (x = 0 - 1), in which the star presents the composition of $Li_2Fe_{0.94}Co_{0.06}SiO_4$. (c) Scanning electron microscopy images of LFS and CoLFS. (d) Energy dispersive spectroscopic mappings of Fe, Co, Si, and O in CoLFS.

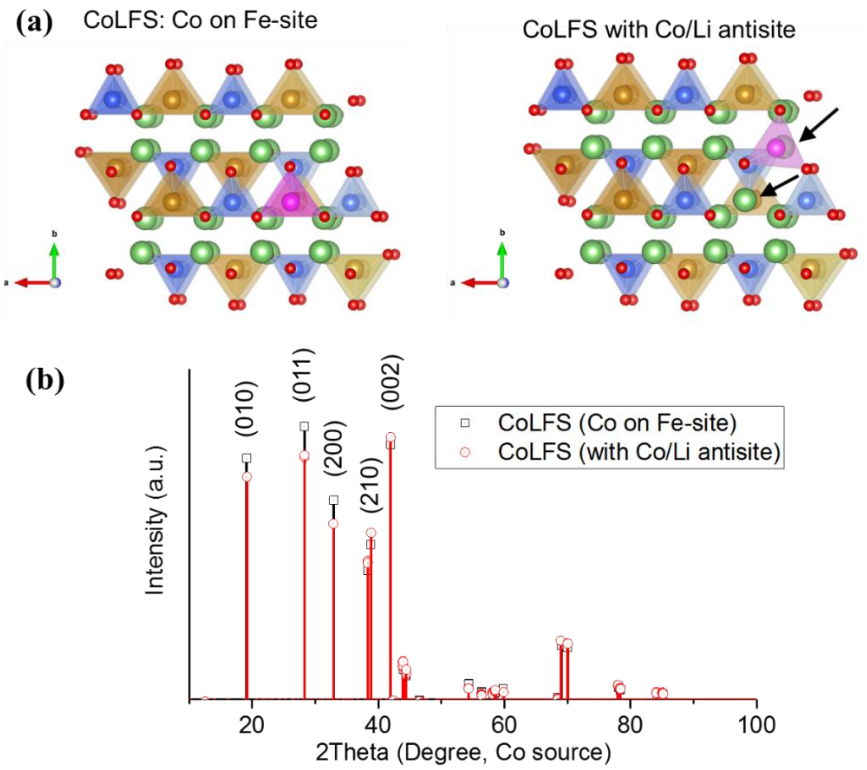

Figure 4.3. Effect of the position of Co on the corresponding peak intensities in XRD. (a) Crystal structures of *Pmn*2$_1$ $Li_2Fe0_{.94}Co_{0.06}SiO_4$ (CoLFS) in which Co occupies Fe-site (left) vs. CoLFS with a Co/Li antisite defect (right). Li (green), Fe (brown), Si (blue), O (red), and Co (purple). Co/Li antisite is pointed out by arrows. (b) Simulated X-ray diffraction patterns by VESTA software.[57] The existence of Co/Li antisite defect results in lower reflection intensities from (010), (011), and (200) planes.

4.4.3 Electrochemical properties

The influence of Co substitution on the electrochemical activity of *Pmn*2$_1$ LFS was evaluated by galvanostatic charging-discharging of LFS and CoLFS half-cells using Li metal as the counter and reference electrodes. Figures 4.4a and 4.4d present the voltage profiles of LFS and CoLFS during galvanostatic cycling at C/10 in the range of 1.5 – 4.5 V, respectively. Both cells delivered discharge capacity of about 100 mAh g^{-1} in their initial cycles, corresponding to the intercalation of 0.6 Li/f.u. The low material utilization at C/10 is a consequence of poor intrinsic electronic and ionic conductivities that result in high polarizations as can be observed in Figures 4.4a and 4.4d. At a lower current rate of C/30, higher capacities up to 125 mAh g^{-1} can be achieved (see Figure B3). Figures 4.4b and 4.4e show that LFS encountered serious capacity loss that there was only 80% capacity retention after 50 cycles at C/10, while CoLFS exhibited correspondingly

at least 95% capacity retention. The same phenomenon of capacity loss in *Pmn*2$_1$ LFS has been reported in other studies,[38-39] but an in-depth elucidation of the underlying mechanism responsible for this behavior remains unclear.

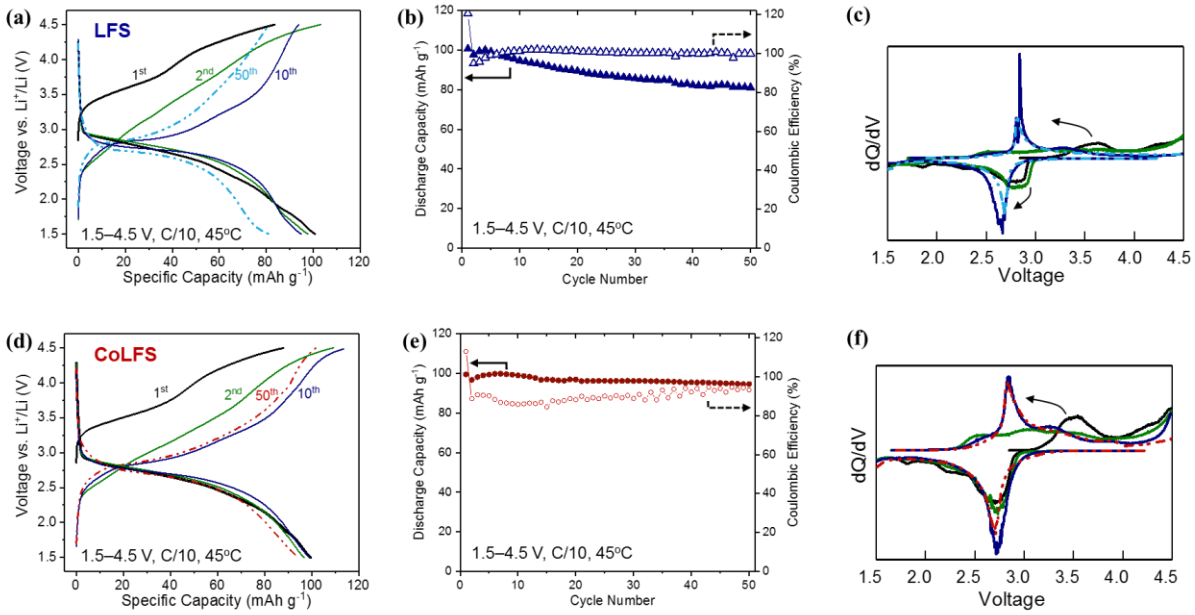

Figure 4.4. Electrochemical cycling performance of LFS and CoLFS. (a, d) Voltage profiles in the 1st, 2nd, 10th and 50th cycles at C/10 between 1.5-4.5 V at 45ºC. (b, e) Discharge capacity retention (solid symbols, left) and Coulombic efficiency (open symbols, right) of LFS (blue) and CoLFS (red) in 50 cycles cycled at C/10 between 1.5 – 4.5 V at 45ºC. (c, f) Differential capacity, dQ/dV vs. voltage corresponding to (a) and (d), respectively. Arrows point out the shift of charge and discharge voltages in the initial cycles.

It is noticed that the charge voltage profiles of both LFS and CoLFS shift downward after the formation cycle. Similar voltage drop is quite typical in *P*2$_1$/*n* LFS, as a result of phase transformation to inverse-*Pmn*2$_1$ phase based on experimental and computational studies.[58] Such electrochemically induced phase transformation is driven by the energy difference (~0.3 eV/f.u.) between *P*2$_1$/*n* and inverse-*Pmn*2$_1$ symmetries in the delithiated LFS with composition $LiFeSiO_4$, hence resulting in a ~0.3 V voltage drop after the phase transformation. We hypothesized that similar phase transformation, from the mother matrix of *Pmn*2$_1$ to the inverse-*Pmn*2$_1$ phase, would occur as well upon cycling. This indeed is supported by our calculation results. We calculated the energetics of $Li_yFe_{1-x}Co_xSiO_4$ (x = 0, 0.0625; y = 0, 1, 2) and found a similar energy trend as that in *P*2$_1$/*n* LFS. Figure B3 shows that for the fully lithiated composition, i.e. $Li_2Fe_{1-x}Co_xSiO_4$, the

total energy of inverse-*Pmn*2$_1$ phase is only about 0.04 eV/f.u. higher than the *Pmn*2$_1$ phase. These similar energies could explain why a certain content of Fe/Li or Co/Li antisite is found in the as-synthesized LFS. On the contrary, when one Li is extracted, corresponding to the composition $LiFe_{1-x}Co_xSiO_4$, the total energy of inverse-*Pmn*2$_1$ is about 0.3 eV/f.u. lower than that of *Pmn*2$_1$. Because of the substantial lower energy, phase transformation from *Pmn*2$_1$ to inverse-*Pmn*2$_1$ could take place upon delithiation. Cell voltages (vs. Li^+/Li) can be calculated from total energies according to the following equations.

$$V\ (y = 2 \rightarrow 1, V) = E_{\mathrm{t}}\ (\mathrm{Li_2Fe_{1-x}Co_xSiO_4}, eV) - E_{\mathrm{t}}\ (\mathrm{LiFe_{1-x}Co_xSiO_4}, eV) - E_{\mathrm{t}}\ (\mathrm{Li}, eV) \quad (4.1)$$

$$V\ (y = 1 \rightarrow 0, V) = E_{\mathrm{t}}\ (\mathrm{LiFe_{1-x}Co_xSiO_4}, eV) - E_{\mathrm{t}}\ (\mathrm{Fe_{1-x}Co_xSiO_4}, eV) - E_{\mathrm{t}}\ (\mathrm{Li}, eV) \quad (4.2)$$

The calculated cell voltages are shown in Figure B4 and listed in Table B3 together with the reported values in the literature for comparison. As the cell voltage is proportional to the energy change associated with (de)lithiation, the voltage of Fe^{2+}/Fe^{3+} redox couple in inverse-*Pmn*2$_1$ is about 0.3 V lower than that in *Pmn*2$_1$. After doping with Co, the calculated cell voltage is slightly higher than the undoped compound, while the difference between two phases remains as ~0.3 V.

Crystal structure stability is one of the key factors that affect capacity retention. To evaluate the structural stability of LFS and CoLFS in the one-Li extraction region, volume changes between Li_2FeSiO_4 and $LiFeSiO_4$ in either *Pmn*2$_1$ or inverse-*Pmn*2$_1$ structure were calculated by DFT and plotted in Figure B4. It is found that upon the removal of one Li, Li_2FeSiO_4 undergoes 1.68% and 3.19% volume expansions in its *Pmn*2$_1$ and inverse-*Pmn*2$_1$ polymorphs, respectively. It is consistent with the results reported by Eames *et al.* that the inverse structure was found to go through larger volume expansion than the normal *Pmn*2$_1$.[52] In regard to $Li_2Fe_{0.94}Co_{0.06}SiO_4$, its *Pmn*2$_1$ structure expands by 1.68%, whereas its inverse-*Pmn*2$_1$ structure expands by 3.16% upon the removal of one Li. If the assumption of taking inverse-*Pmn*2$_1$ as the cycled structure is true, the minor volume changes infer that LFS and CoLFS in either *Pmn*2$_1$ or inverse-*Pmn*2$_1$ are structurally stable when removing one Li. Within the applied voltage range (i.e. 1.5 - 4.5 V), only the first Li charged was compensated by Fe^{2+}/Fe^{3+}. In this regard then, irreversibility caused by plausible oxygen redox activity could be ruled out.

4.4.4 Electrochemical activation by structural evolution

The voltage-capacity profiles in Figures 4.4a and 4.4d reflect a progressive variation in the initial 10 cycles during charge, which suggest the cathode compounds have experienced an electrochemical activation process. Such electrochemical activation is enabled by the phase transformation in the bulk and surface reconstruction. To understand this activation process more clearly, dQ/dV curves (Figures 4.4c, 4.4f) were derived from the corresponding voltage profiles. Upon the first charge cycle from the open-circuit voltage at ~2.8 V to the cut-off voltage at 4.5 V, a rather diffused peak appears at ~3.6 V for LFS and ~3.5 V for CoLFS, respectively. Considering that the theoretical charge voltage is at ~3.0 V (Figure B4), the average overpotential due to internal resistances is about 0.5 V and 0.4 V for LFS and CoLFS, respectively. Such diffused peaks associated with high overpotentials indicate very sluggish and complex kinetics of Li transport in the formation cycle. In a previous study, we found spontaneous reaction between LPF_6-EC/DMC electrolyte and uncharged LFS prior to any cycling treatment that resulted in de-lithiation and Fe oxidation to Fe^{3+}.[59] Moreover, pristine LFS particles synthesized by hydrothermal method have always been found to contain a certain level of Fe^{3+} even though a careful handling was taken.[13, 46] A deactivated surface will not only obstruct the mass transfer through the surface but also interfere with intercalation in the bulk. This also explains why the Coulombic efficiency (CE) in the first cycle is larger than 100% (i.e. discharge capacity > charge capacity) for either of LFS or CoLFS (Figures 4.4b and 4.4e). Thus, a surface reconstruction process is required to reactivate the delithiation and the subsequent re-lithiation process. After the formation cycle, the charge peak at 3.5 V/3.6 V transforms into a broad shoulder appearing in the range of 2.5 – 4 V. In the 10^{th} cycle, dQ/dV curve of charge shows a peak at ~2.8 V, corresponding to the inverse-*Pmn*2_1 phase which has theoretical charge voltage at ~2.7 V. The better resolved peak and the lowered overpotential reflect that upon cycling, re-ordering between Fe and Li gives rise to better-established channels that have low energy barriers for Li-ion diffusion, and thus enhanced delithiation kinetics.

Contrary to the variation observed in charge voltage profiles, the evolution of discharge profiles is relatively stable with only subtle changes for both LFS and CoLFS. The asymmetric shape of charge and discharge voltage curves (Figures 4.4a, 4.4d) implies that the kinetics of Li-ion storage and phase transformation during lithiation (discharge) are completely distinct from the delithiation (charge) process. The corresponding dQ/dV curves (Figure 4.4c vs. 4.4f) confirm the

steady discharge process upon cycling while notably, obvious distinction between LFS and CoLFS during discharge is revealed. As it is shown, CoLFS reached a stable discharge voltage at ~2.7 V even in the first cycle, whereas LFS proceeded through a progressive voltage drop from ~2.9 V to ~2.6 V. This indicates that CoLFS may complete the phase transformation in the first cycle and avoid unnecessary intermediate phases, while the un-doped LFS experienced rather slow phase transformation across multiple intermediate stages between the initial and the final structures. Such structure-dependent phase transformation kinetics have been reported previously for the three polymorphs of LFS: $P2_1/n$ and *Pmnb* exhibited faster phase transformation than $Pmn2_1$ due to higher disorder degrees in the cation connectivity.[13] It is therefore reasonable to assume that, for the present study, substituting a small amount of Co for Fe induces more TM/Li antisite defects in the as-synthesized material (Figure 4.1a), and these pre-existing TM/Li antisite defects work as nuclei that facilitate the phase transformation to inverse-$Pmn2_1$ as a consequence of cation rearrangement upon cycling. Evidence of creation of antisites serves as nucleation "catalyst" in phase transformation of $P2_1/n$ to inverse $Pmn2_1$ has been noted also by Lu et al.[14] A rapid phase transition is preferred because it could avoid the formation undesired intermediate phases that would cause blockage of Li diffusion and unnecessary energy losses.

The distinction between charge and discharge as well as the difference between LFS and CoLFS are further revealed by cyclic voltammetry (CV), shown in Figure 4.5. CV was conducted at a scanned rate of 0.2 mV s^{-1} from 1.5 V to 4.5 V for ten sweeps. In the voltage window of 1.5 – 4.5 V vs. Li^+/Li, the only redox-active couple in the active materials is Fe^{2+}/Fe^{3+} because the oxidation of Co^{2+} would require a voltage higher than 4.5 V.[60] For either LFS or CoLFS (Figures 4.5a, 4.5b), a wide but well-resolved cathodic (= reduction) peak is shown. This peak remains stable upon cycling, which is similar to the steady discharge voltage profiles shown in Figure 4.4, although the peak shift observed in LFS is only slightly reflected in its CV curves. On the contrary, the anodic (= oxidation) curves go through significant changes in shape and intensities in the first 10 sweeps. This is again, consistent with the general trend observed in galvanostatic charge voltage profiles (Figure 4.4). For both LFS and CoLFS, it takes about six CV scans for the anodic curves to become stable. The 1st scan, giving rise to poorly resolved anodic peaks, confirms that the starting structures are nearly electrochemical inactive. After a few cycles, multiple peaks can be observed along with enhanced intensities, demonstrating a progressive activation process. The

existence of multiple anodic peaks and their evolution can be attributed to the continuous surface reconstruction and phase transformation occurring during cycling which ultimately affect the kinetics of Li-ion diffusion. As discussed earlier, such phase transformation could be promoted by the TM/Li cation mixing.

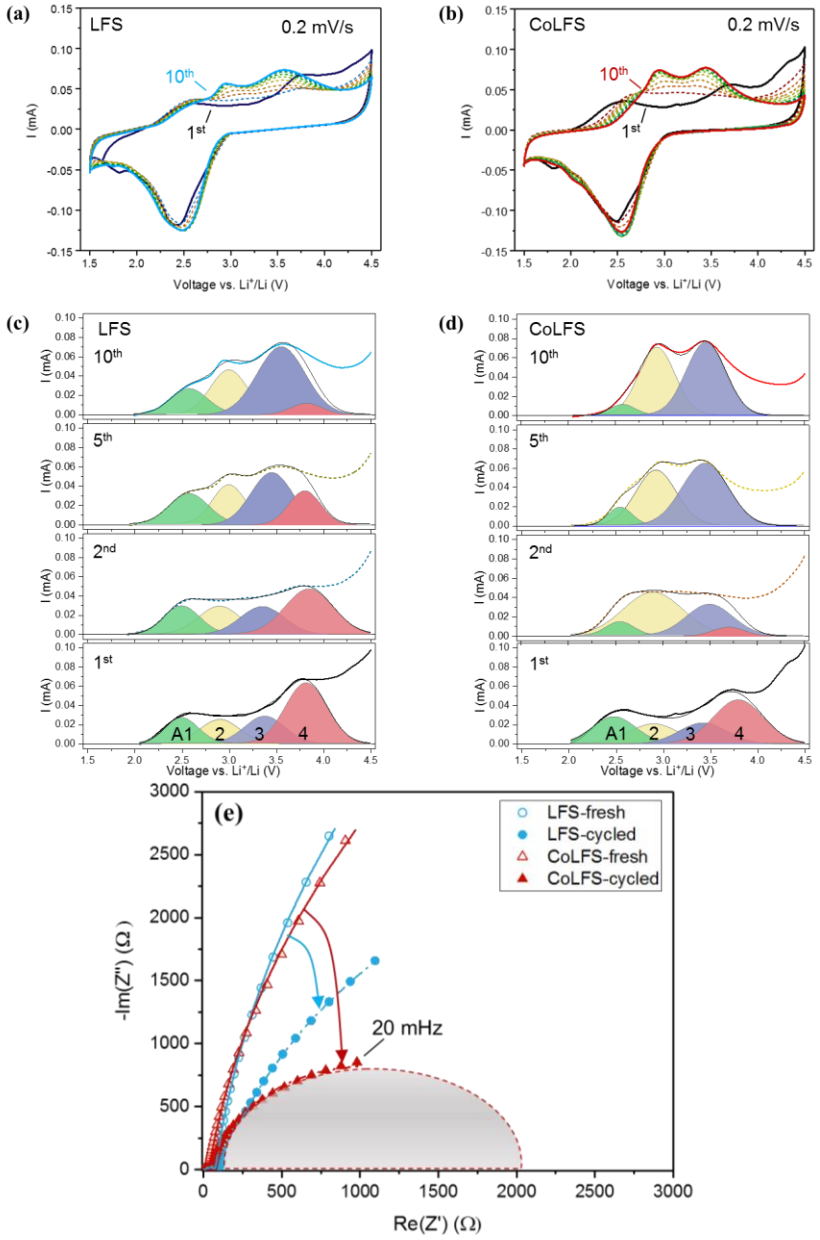

Figure 4.5. Structural evolution activates electrochemical properties. Cyclic voltammograms of (a) LFS and (b) CoLFS in the first 10 cycles at a scan rate of 0.2 mV/s between 1.5 - 4.5 V. (c, d) Anodic (oxidation) curves fitted by three-four peaks for the 1st, 2nd, 5th, and 10th cycles corresponding to (a, b). (e) Electrochemical impedance spectra of LFS (blue) and CoLFS (red) cells before and after cycling in a frequency range of 1 MHz to 20 mHz. Solid and dashed lines represent the fitting results. Grey-filled half-circle represents the fitted resistance of CoLFS-cycled.

The asymmetry between anodic and cathodic curves indicate different diffusion mechanisms during delithiation and lithiation processes. Different to the delithiation process, the lithiation process is more stable and progresses at enhanced kinetics from the beginning. This could be attributed to surface reconstruction taking place in the preceding delithiation cycle and also to the Li-vacancies that are generated after delithiation, both factors facilitating Li-ion transport. This phenomenon is also reflected in the galvanostatic charge-discharge results (Figures 4.4a, 4.4b), where most of changes take place during charging rather than discharging process.

To demonstrate the evolution of anodic peak more clearly, the anodic curves of the 1st, 2nd, 5th, and 10th cycles were deconvoluted to four Gaussian peaks denoted as A_1, A_2, A_3, and A_4 and shown in Figures 4.5c and 4.5d. Detailed deconvolution process can be found in Supporting Information. The four peaks can be seen there to be centered at approximately 2.5 V, 2.9 V, 3.5 V, and 3.8 V, respectively. In the 1st sweep, A_4 occupies the largest area, with the other three peaks sharing similar areas. The dominant presence of A_4 is seen slightly more pronounced in LFS than that in CoLFS. In the following cycles, one can see that A_4 slowly fades out till the 10th anodic sweep in LFS, while it almost disappears from the 2nd sweep in CoLFS. Simultaneously, A_3 (at ~3.5 V) increases with scanning cycles, and the buildup of A_3 seems related to the reduction of A_4. The A_4, centering at ~3.8 V, is considered to be associated to the delithiation (oxidation) reaction occurring in the initial surface of the active particles. Thus, the decreasing intensities of A_4 imply structural reconstruction in the surface layer, which is apparently much faster in CoLFS than LFS. The A_3 (~3.5 V) could be linked to the delithiation reaction from the *Pmn*2_1-dominant bulk region, whereas the A_2 (~2.9 V) can be assigned to inverse-*Pmn*2_1-dominant region. A_2 grows with number of cycles due to continuous phase transformation. Again, the relatively fast kinetics in CoLFS is attributed to the pre-existing TM/Li antisite defects -created by Co substitution - that function as nuclei for phase transformation. The fundamental cause for A_1 (~2.5 V), the peak at the lowest voltage, is still unclear, implying that some crystallographic information is missing. Nevertheless, the difference between LFS and CoLFS reveals that the electrochemical activation process is strongly correlated to the local structural changes caused by Co incorporation.

Figure B5 shows the variation of CV at various scan rates from 0.1 mV s^{-1} to 0.5 mV s^{-1}. The chemical diffusion coefficient of Li^+ (D_{Li^+}) can be estimated from the slope of the linear lines of the peak current, i.e., I_C, I_{A2}, or I_{A3}, vs. the square root of the scan rate $\upsilon^{1/2}$. The calculated results

are listed in Table B4. As it can be seen, diffusion coefficient of lithiation is larger than that of delithiation for both LFS and Co-LFS, although all the calculated D_{Li^+} are around 10^{-13} cm^2 s^{-1}.

Electrochemical impedance spectra (EIS) before and after CV tests were measured and presented in Nyquist format in Figure 4.5e. We focus firstly at the unfinished loop that cut at 20 mHz, which is ascribed to the impedance related to solid-state diffusion of Li^+ which is coupled with phase transformation.[61] This information is of great importance because the transport of Li-ions in LFS crystals will be correlated with the movement of grain boundaries between different phases. From the equivalent circuit model fitting (showing later in Figure 4.6b), the resistance from phase transformation (denoted as R_{PT}) declines from 17 kΩ to 7 kΩ in LFS, while more dramatically, from 14 kΩ to 2 kΩ in CoLFS. These results clearly point out two benefits brought by Co substitution: (i) improved phase transformation kinetics and (ii) enhanced electrochemical activation. Such electrochemical activation by structural evolution during cycling has been observed in other materials that involve TM/Li re-ordering, such as $LiFeSO_4F$.[62] Thus, incorporation of Co in LFS can effectively suppress the formation of unnecessary intermediate phases, hence making the transformation pathway more energetic efficient.

4.4.5 Characteristics of CEIs formed on cycled electrodes

It is noted that at high voltage region, a rising oxidation tail starting from ~4.2 V is observed in both dQ/dV and CV curves (Figure 4.4 and Figure 4.5). This tail could be attributed to electrolyte oxidation that contributes a parasitic charge capacity fraction. Electrolyte oxidation has been observed in multiple cathode materials when charging above 4.2 V and the starting voltage for the parasitic oxidation is highly dependent on the nature of the electrode materials.[18] The most common parasitic electrolyte oxidation reaction is the oxidation of ethylene carbonate (EC), which could go through ring-opening leading to evolution of CO_2/CO gas.[63] As the oxidation tail is the most significant in the 1st cycle subsequently fading out with cycling, one can assume that the extent of parasitic electrolyte oxidation is reduced with successive cycling. The presence of this extra capacity fraction results in low Coulombic efficiencies (CEs) from the 2nd to ~15th cycle in both LFS and CoLFS (see Figures 4.4c and 4.4f). Surprisingly, LFS reaches ~100% CE which then remains stable, but CoLFS possesses rather poor CE (~95%) till the 50th cycle. However, CoLFS has substantially better discharge capacity retention than LFS (95% vs. 80%). This contradiction implies that the fundamental cause for the continuous capacity loss in LFS is not the

electrolyte oxidation. Indeed, more detrimental side reactions between electrode and electrolyte can come from the electrolyte decomposition associated with PF_6^--based species.[64] More specifically, PF_6^- in the electrolyte is sensitive to moisture and heat, which can generate HF acid. HF could attack the cathode and result in the loss of active materials.[20, 65] Simultaneously, a surface film, called cathode electrolyte interphase (CEI), will form on the surface of the cathode. The functionality of this CEI depends on its composition, thickness, and structure. Thus, a desired CEI could work as a protection buffer layer that prohibit further attack from HF while allow Li^+ to pass through. On the other hand, an undesired CEI may be incapable of blocking detrimental reaction while even worse, been resistive to Li^+ transport.

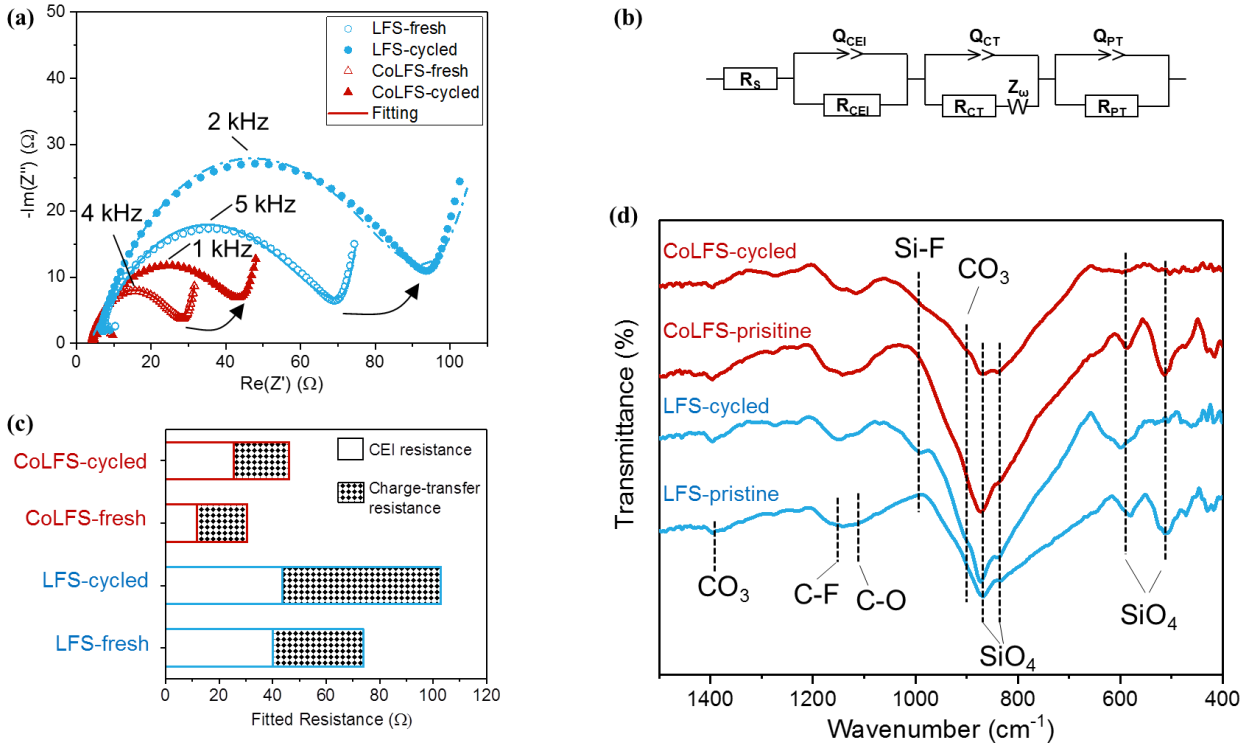

Figure 4.6. Characteristics of the cathode-electrolyte interphases (CEIs) and the surface of electrodes. (a) Nyquist plots in the high-to-medium-frequency region of EIS spectra of LFS and CoLFS half-cells before and after cycling in $LiPF_6$ EC-DMC electrolyte at 45°C. Arrows indicate increases of impedances upon cycling. (b) Equivalent circuit used to fit the Nyquist plots. (c) Deconvolution results of the loop composed of two depressed half-circles: one from CEI resistance (R_{CEI}) and the other from charge-transfer resistance (R_{CT}). (d) FTIR spectra of the pristine and cycled electrodes. Noted that "fresh" electrodes are those in the half-cells before cycling, while "pristine" electrodes are those electrodes that have not been in contact with electrolyte.

Figure 4.6a shows the Nyquist plots of LFS and CoLFS EIS measurements which can be interpreted using a common equivalent circuit model as shown in Figure 4.6b for a Li half-cell.[66-68] It should be noted that Figure 4.6a is a magnification from the high-to-medium frequency range in Figure 4.5a. The fitted spectra are the convolution of two depressed semicircles, followed by a tail with ~60-degree angle. The semicircle at high frequency can be assigned to the contact resistance between cathode interface (CEI layer) and current collector, denoted as R_{CEI}. The semicircle at medium frequency is ascribed to the charge-transfer resistance at the surface of cathode, denoted as R_{CT}. Figure 4.6c shows the fitting results of LFS and CoLFS before and after CV tests. LFS electrode exhibits larger overall impedance than CoLFS before and after cycling, more specifically in both R_{CEI} and R_{CT}. Upon cycling, R_{CEI} in CoLFS increases from about 12 Ω to 25 Ω while R_{CT} almost remains at about 20 Ω. As a comparison, LFS goes through a small increase in R_{CEI} from 40 Ω to 44 Ω, whereas its R_{CT} is almost doubled from 34 Ω to 60 Ω upon cycling. CoLFS exhibits lower and more stable R_{CT} than LFS. This means that Co substitution helps to establish a well-structured CEI/CoLFS interphase that facilitates charge transfer. It has been reported that in $P2_1/n$ LFS, Co-doping could introduce more defects and enhance the electronic and ionic conductivities.[24] In other materials, such as $LiFePO_4$[36] and $LiMn_2O_4$[69], doping small amount of Co was found to decrease the charge-transfer resistance.

FTIR (Figure 4.6d) was employed to reveal compositional and structural features of the surface on LFS and CoLFS and the CEI layer formed after cycling. In the pristine LFS electrode (denoted as LFS-pristine), the characteristic vibration bands from SiO_4 polyanion can be observed in the range of 400 – 1000 cm^{-1}, which contains stretching vibrations at ~835 cm^{-1} and ~870 cm^{-1} and bending vibrations at ~510 cm^{-1} and ~580 cm^{-1}. CO_3 in Li_2CO_3 contributes to the bending vibration at ~900 cm^{-1} and the stretching vibration at ~1400 cm^{-1}.[70] Stretching band of C-F from PVDF binder is found at ~1150 cm^{-1}.[71] After the CV tests at 45ºC between 1.5 – 4.5 V, all the features found in LFS-pristine remains in LFS-cycled but with changes in their relative intensities. The most noticeable changes are from the vibrations of SiO_4 which show substantial intensity reduction at ~510 cm^{-1} while intensity growth at ~870 cm^{-1}. This change implies that the surface chemistry of LFS has changed significantly upon cycling in the electrolyte. In the meantime, a small band at ~1000 cm^{-1} emerges in LFS-cycled, which can be designated to Si-F stretching vibration.[71] The formation of Si-F bonds should originate from the attack by HF acid that is

produced by the decomposition of $LiPF_6$. The reaction between LFS and HF was evidenced in a previous study and Li_2SiF_6 was found to be the product.[72] Moreover, among the three common polymorphs of LFS, *Pmn*2_1 was the least stable polymorph upon the attack by HF.[72]

As shown in Figure 4.6d, substituting 6% Co for Fe leads to insignificant variations in the FTIR spectra of the pristine electrodes (CoLFS-pristine vs. LFS-pristine), but the evolution of FTIR spectra upon cycling are different. In CoLFS-cycled, bending vibrations from SiO_4 in the range of 400 – 700 cm^{-1} almost disappear, while stretching vibrations from SiO_4 in the range of 800 – 900 cm^{-1} diminish. Considering SiO_4 signals are only from the bulk of the electrode particles, reduction of SiO_4 vibrations could be attributed to a complete coverage of CEI layers on CoLFS particles. In addition, it is worth noting that there is only a diffused shoulder from Si-F vibration at ~1000 cm^{-1}, suggesting that the content of Si-F-bearing species in CoLFS-cycled is considerably less than that in LFS-cycled. Therefore, the lower quantity of Si-F found in CoLFS indicates that CoLFS has an improved tolerance towards HF. FTIR data in combination with the EIS results suggest that CoLFS formed relatively conductive and well-constructed CEI layers, whereas un-doped LFS appeared to have formed resistive, porous or even fractured CEI layers. It is also revealed that Li_2CO_3 is one of the major components in the CEIs on both LFS and CoLFS. Li_2CO_3 is a common component found in CEIs and SEIs, which can form during air exposure before electrochemical tests. With an appropriate content of Li_2CO_3, CEIs would have better interfacial stability and kinetics of carrier transport at the CEI/electrode interphases as well as endow the electrodes with improved high-temperature tolerance.[73]

XPS was applied to elucidate the surface chemistry and structures of CEIs. It is noted that XPS spectra usually represent surface chemistry in the top 1-10 nm layers from the studied substances.[74] Figure 4.7 compares the XPS spectra of pristine and cycled electrodes of LFS and CoLFS (view from bottom to top). From the schematic summary of the chemical compositions of each sample given in the bar chart in Figure 4.7, new signals from element P emerge and increasing signals from element F show up after cycling, both of which can be attributed to decomposition of the $LiPF_6$-based electrolyte. Spectra on the right and bottom provide more specific information of the components and their changes after cycling. It is shown that signals belonging to LiF (~685.5 eV) and $Li_xPO_yF_z$ (~135 eV) emerge in F 1s and P 2p spectra only after cycling.[72, 75] In the pristine electrodes, F 1s spectra are dominated by a peak at ~688 eV which is attributed to CF_2 from the

binder PVDF, i.e. -$(C_2H_2F_2)_n$-. After cycling, the newly formed $Li_xPO_yF_z$ contributes additional signals to the peak at 688 eV in F 1s and that at 135 eV in P 2p. There is more LiF in the CEI of CoLFS than that in LFS after cycling by comparing F 1s spectra between the two cycled electrodes. More specifically, as summarized in Figure 4.7 and Table B5, CoLFS-cycled contains 24% of F, whereas LFS contains 19.2% of F in the sum of C, O, F, P, and Si. Remarkably, LiF in CoLFS-cycled (13.6%) is almost double of that in LFS-cycled (7.2%). CoLFS-cycled also bears higher P content (5.9%) than LFS-cycled (3.6%), which also reflects a higher content of $Li_xPO_yF_z$ in CoLFS. LiF and $Li_xPO_yF_z$ (e.g. $LiPO_2F_2$) derive from the decomposition of $LiPF_6$ in the electrolyte triggered by moisture and thermal sensitivities.[20, 76-77] Recent studies have revealed that the presence of fluorine species in the surface layer of electrode materials have positive impact on electrochemical performance.[19, 76-78] The presence of Li_2CO_3, which was detected by the FTIR results, was also confirmed by XPS in C 1s and O 1s spectra.

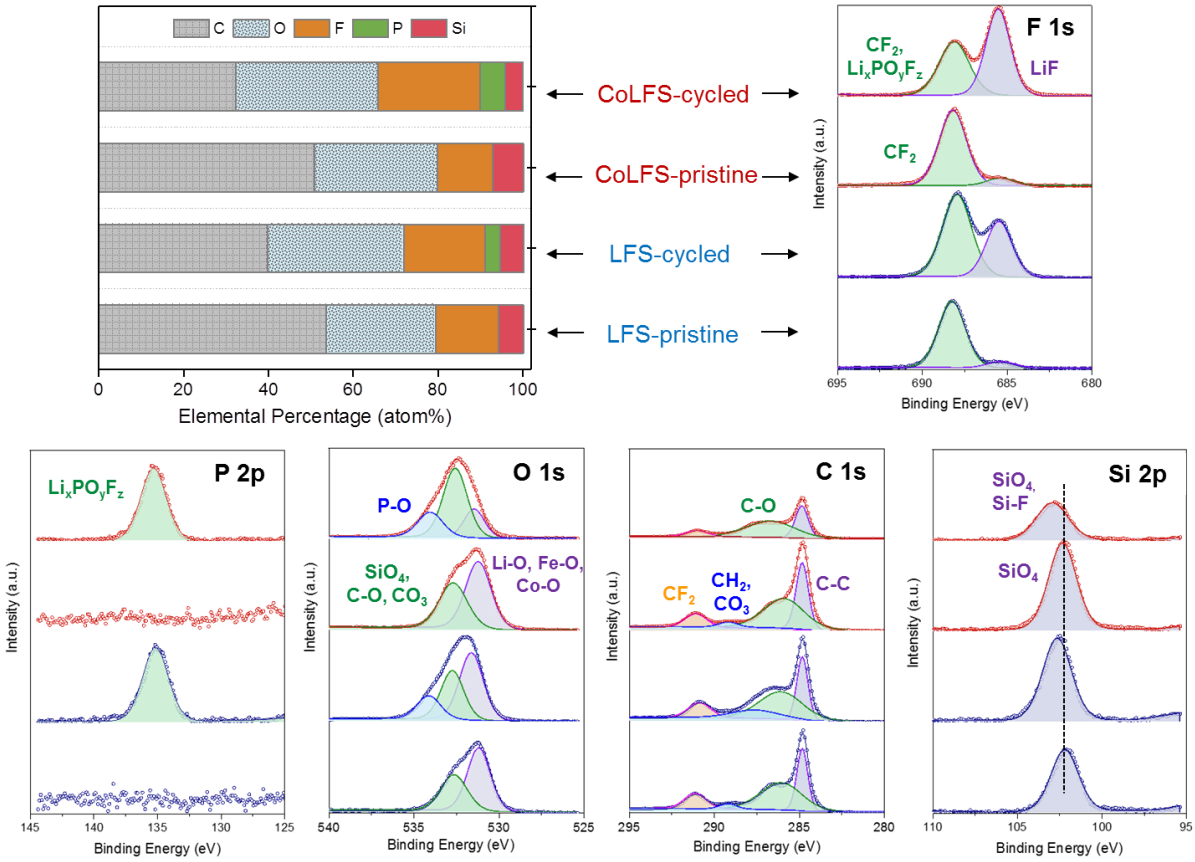

Figure 4.7. XPS surface analysis of the pristine and cycled electrodes of LFS and CoLFS. Top left figure is the elemental percentages of C, O, F, P, and Si derived from XPS. The rest of the figures show XPS spectra of F 1s, P 2p, O 1s, C 1s, and Si 2p of the pristine and cycled electrodes.

As discussed above, FTIR (Figure 4.6d) shows a sign of newly formed Si-F bonds as a result of reaction between LFS and HF. As shown in Figure 4.7, Si 2p peak shifts to higher energy after cycling. This suggests formation of new Si-containing compounds that have higher-binding-energy bonds such as Si-F. Ensling *et al.*[79] reported the formation of Si-F groups (at 103 eV if using C-C at 284.8 eV as reference) in the LFS/C cells cycled at 55°C in $LiPF_6$ electrolyte. Our previous work[59] also showed that spontaneous reactions can occur even between the uncharged LFS and $LiPF_6$ electrolyte at room temperature, resulting in the reduction of electrolyte components and oxidation of Fe^{2+}. Not only the attack of HF on LFS is responsible for material degradation such as mass loss of the active material but also is responsible for an increase of internal resistance, and consequently diminished capacity observed in various Li-ion intercalation compounds, such as $Li_4Ti_5O_{12}$, $LiCoO_2$, $LiNiO_2$, $LiNi_{0.5}Mn_{0.5}O_2$, $LiMn_2O_4$, $LiNi_{0.5}Mn_{1.5}O_4$, and $LiFePO_4$.[65] Moreover, compared with the oxides, the affinity of F- to Si-O bonds in LFS would lead to more detrimental effect on the degradation of LFS and electrolyte.

The CEI layers, which is usually only a few nanometers thick, also affects the performance of the electrodes.[80-81] By analyzing the ratio of XPS signals between LiF plus $Li_xPO_yF_z$, which are part of the CEI layer, and Fe plus SiO_4, which are part of the bulk electrode particles (Figure 4.7 and Figure B6), it can be seen that CoLFS-cycled contains more signals from CEI than from the bulk, while LFS-cycled does not. As listed in Table B5, the atomic percentage of Si in LFS almost remains the same (5.9% vs. 5.5%) before and after cycling. On the contrary, Si detected from CoLFS decreases from 7.3% to 4.2% after cycling, indicating that there is less amount of Si in the XPS sensitive region due to the coverage of the CoLFS surface by the better formed CEI layer. In addition, the SiO_4 vibration detected by FTIR (Figure 4.6d) becomes significantly weaker in CoLFS-cycled due to the coverage of CEI. Combined with the EIS results where CoLFS was found to have lower CEI resistance than LFS, we believe that CoLFS was covered with more complete and thinner CEI layers that allowed Li-ion transport while adequately protecting the active particles from further detrimental reactions with electrolyte. By contrast undoped LFS formed a fractured CEI which failed to serve as protection layer.

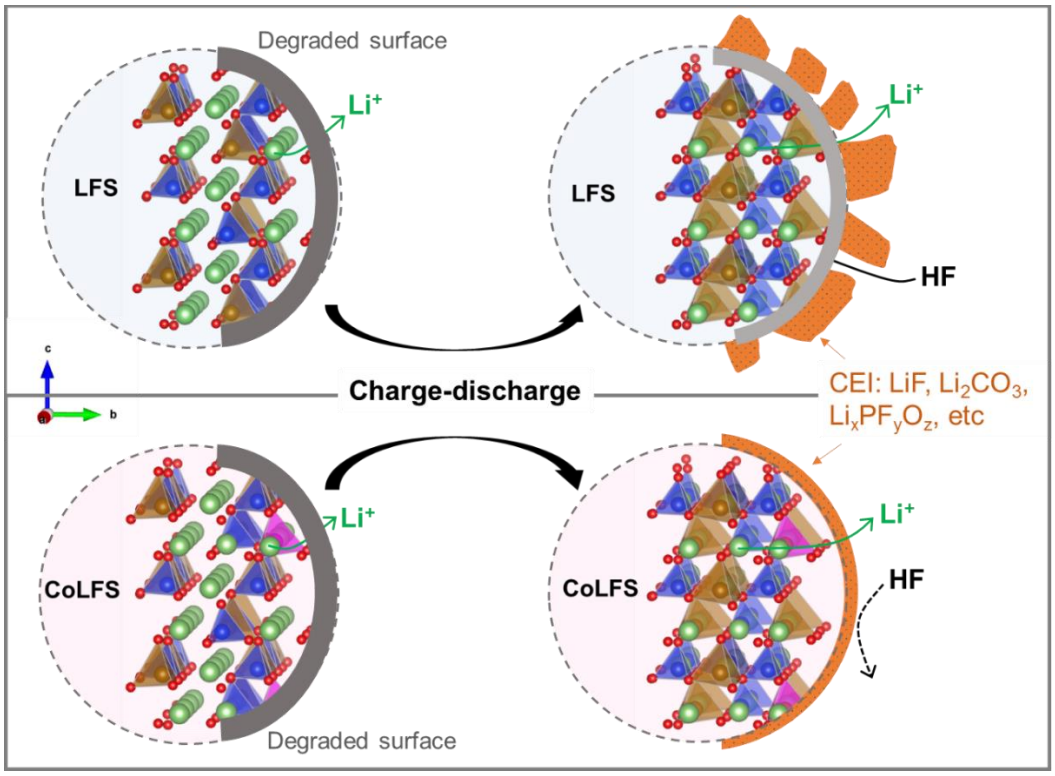

Figure 4.8. Electrochemical structural activation mechanism: Schematic illustration of structural evolution, surface reactivation, and formation of CEIs in LFS and CoLFS upon charge-discharge cycling in $LiPF_6$ EC/DMC electrolyte.

Based on the results and discussions above, we propose a schematic illustration presented in Figure 4.8 for the cobalt-catalyzed electrochemical activation and CEI formation in CoLFS and LFS during cycling. We find that substituting a small amount of Co for Fe induced more TM/Li antisite defects in the pristine materials, thus facilitating the phase transformation to the cycled structure and avoiding unnecessary intermediate phases. Surface reconstruction is progresses with cycling and is completed faster in CoLFS than LFS. Moreover, Co in LFS catalyzed the formation of more conductive and well-constructed CEI layers that serve as a protection film to prevent further attack by HF. The CEI layers are mainly composed of LiF, $Li_xPO_yF_z$, and Li_2CO_3. We hypothesize that Co ions on the surface may play catalytic site roles that favor the formation and deposition of conductive CEI components. This protection layer leads to enhanced capacity retention of CoLFS vis-a-vis the unprotected LFS. Nevertheless, the presence of Co also leads to some parasitic electrolyte oxidation which although does not diminish the discharge capacity still consumes electrolyte. Therefore, some electrolyte additives are still needed to optimize the electrolyte/CoLFS interphases.

4.5 Conclusions

In this work, we demonstrate the effect of Co-substitution on LFS via theoretical modeling and experimental testing. $Li_2Fe_{0.94}Co_{0.06}SiO_4$ solid solution in $Pmn2_1$ polymorph was successfully synthesized by hydrothermal method. Larger quantities of pre-existing TM/Li antisite defects were found in CoLFS, which during cycling served as nuclei for the phase transformation from $Pmn2_1$ to the electrochemically induced phase. The surface of both LFS and CoLFS was degraded upon contact with electrolyte thus exhibiting sluggish kinetics in the initial cycles, but upon cycling the surface was reconstructed. By careful examination of the surface on the cycled electrodes, we found that the substitution of Co tuned the CEI formation ability and resulted in a coverage of conductive and uniform protecting layer over the active particles. This CEI layer, mainly composed by LiF, Li_2CO_3 and $Li_xPO_yF_z$, not only helped to prevent the active materials from corrosion attack by HF, but also possessed lower interphase resistance thus facilitating charge-transfer. As a consequence, CoLFS showed profoundly enhanced capacity retention performance compared to undoped LFS (95% vs. 80%). We attempted to synthesize LFS doped with other elements according to their theoretical synthesizability predicted by DFT calculations. However, only Mg was successfully substituted into LFS under hydrothermal condition, but the presence of Mg introduced severe capacity loss, probably due to the lack of protective CEI layer. The new insight provided in this work opens new optimization avenues for LFS via investigation of surface coating with compatible and robust materials.

4.6 Acknowledgements

This work is funded by a Hydro-Québec/Natural Sciences & Engineering Research Council of Canada (NSERC) Collaborative R&D research grant (463484-2014). YZ and GPD acknowledge additional support by the McGill Engineering International Tuition Award (MEITA) and McGill Sustainability Systems Initiative (MSSI) programs.

4.7 References

1. Choi, J. W.; Aurbach, D., Promise and reality of post-lithium-ion batteries with high energy densities. *Nature Reviews Materials* **2016,** *1*, 16013.

2. Yoo, H. D.; Markevich, E.; Salitra, G.; Sharon, D.; Aurbach, D., On the challenge of developing advanced technologies for electrochemical energy storage and conversion. *Materials Today* **2014,** *17* (3), 110-121.

3. Dunn, B.; Kamath, H.; Tarascon, J.-M., Electrical energy storage for the grid: A battery of choices. *Science* **2011,** *334* (6058), 928-935.

4. Armand, M.; Tarascon, J.-M., Building better batteries. *Nature* **2008,** *451* (7179), 652-657.

5. Masquelier, C.; Croguennec, L., Polyanionic (phosphates, silicates, sulfates) frameworks as electrode materials for rechargeable Li (or Na) batteries. *Chemical reviews* **2013,** *113* (8), 6552-6591.

6. Whittingham, M. S., Ultimate limits to intercalation reactions for lithium batteries. *Chemical Reviews* **2014,** *114* (23), 11414-11443.

7. Arroyo-de Dompablo, M. E.; Armand, M.; Tarascon, J.-M.; Amador, U., On-demand design of polyoxianionic cathode materials based on electronegativity correlations: An exploration of the Li_2MSiO_4 system (M = Fe, Mn, Co, Ni). *Electrochemistry Communications* **2006,** *8* (8), 1292-1298.

8. Dominko, R.; Bele, M.; Gaberšček, M.; Meden, A.; Remškar, M.; Jamnik, J., Structure and electrochemical performance of Li_2MnSiO_4 and Li_2FeSiO_4 as potential Li-battery cathode materials. *Electrochemistry Communications* **2006,** *8* (2), 217-222.

9. Dominko, R., Li_2MSiO_4 (M=Fe and/or Mn) cathode materials. *Journal of Power Sources* **2008,** *184* (2), 462-468.

10. Islam, M. S.; Dominko, R.; Masquelier, C.; Sirisopanaporn, C.; Armstrong, A. R.; Bruce, P. G., Silicate cathodes for lithium batteries: alternatives to phosphates? *Journal of Materials Chemistry* **2011,** *21* (27), 9811-9818.

11. Nytén, A.; Abouimrane, A.; Armand, M.; Gustafsson, T.; Thomas, J. O., Electrochemical performance of Li_2FeSiO_4 as a new Li-battery cathode material. *Electrochemistry Communications* **2005,** *7* (2), 156-160.

12. Nytén, A.; Kamali, S.; Häggström, L.; Gustafsson, T.; Thomas, J. O., The lithium extraction/insertion mechanism in Li_2FeSiO_4. *Journal of Materials Chemistry* **2006,** *16* (23), 2266-2272.

13. Sirisopanaporn, C.; Masquelier, C.; Bruce, P. G.; Armstrong, A. R.; Dominko, R., Dependence of Li_2FeSiO_4 electrochemistry on structure. *Journal of the American Chemical Society* **2011,** *133* (5), 1263-1265.

14. Lu, X.; Chiu, H.-C.; Arthur, Z.; Zhou, J.; Wang, J.; Chen, N.; Jiang, D.-T.; Zaghib, K.; Demopoulos, G. P., Li-ion storage dynamics in metastable nanostructured Li_2FeSiO_4 cathode: Antisite-induced phase transition and lattice oxygen participation. *Journal of Power Sources* **2016,** *329*, 355-363.

15. Masese, T.; Tassel, C.; Orikasa, Y.; Koyama, Y.; Arai, H.; Hayashi, N.; Kim, J.; Mori, T.; Yamamoto, K.; Kobayashi, Y.; Kageyama, H.; Ogumi, Z.; Uchimoto, Y., Crystal structural changes and charge compensation mechanism during two lithium extraction/insertion between Li_2FeSiO_4 and $FeSiO_4$. *The Journal of Physical Chemistry C* **2015,** *119* (19), 10206-10211.

16. Billaud, J.; Eames, C.; Tapia-Ruiz, N.; Roberts, M. R.; Naylor, A. J.; Armstrong, A. R.; Islam, M. S.; Bruce, P. G., Evidence of enhanced ion transport in Li-rich silicate intercalation materials. *Advanced Energy Materials* **2017**, 1601043.

17. Arroyo-de Dompablo, M. E.; Armand, M.; Tarascon, J.-M.; Amador, U., On-demand design of polyoxianionic cathode materials based on electronegativity correlations: An exploration of the Li_2MSiO_4 system (M=Fe, Mn, Co, Ni). *Electrochemistry Communications* **2006,** *8* (8), 1292-1298.

18. Li, W.; Song, B.; Manthiram, A., High-voltage positive electrode materials for lithium-ion batteries. *Chemical Society Reviews* **2017,** *46* (10), 3006-3059.

19. Wang, C.; Meng, Y. S.; Xu, K., Perspective—Fluorinating Interphases. *Journal of The Electrochemical Society* **2019,** *166* (3), A5184-A5186.

20. Xu, K., Electrolytes and interphases in Li-ion batteries and beyond. *Chemical reviews* **2014,** *114* (23), 11503-11618.

21. Zhang, S.; Deng, C.; Fu, B. L.; Yang, S. Y.; Ma, L., Doping effects of magnesium on the electrochemical performance of Li_2FeSiO_4 for lithium ion batteries. *Journal of Electroanalytical Chemistry* **2010,** *644* (2), 150-154.

22. Qu, L.; Luo, D.; Fang, S.; Liu, Y.; Yang, L.; Hirano, S.-i.; Yang, C.-C., Mg-doped Li_2FeSiO_4/C as high-performance cathode material for lithium-ion battery. *Journal of Power Sources* **2016,** *307*, 69-76.

23. Kumar, A.; Jayakumar, O. D.; Jagannath, J.; Bashiri, P.; Nazri, G. A.; Naik, V. M.; Naik, R., Mg doped Li_2FeSiO_4/C nanocomposites synthesized by the solvothermal method for lithium ion batteries. *Dalton Transactions* **2017,** *46* (38), 12908-12915.

24. Zhang, L.-L.; Duan, S.; Yang, X.-L.; Liang, G.; Huang, Y.-H.; Cao, X.-Z.; Yang, J.; Li, M.; Croft, M. C.; Lewis, C., Insight into cobalt-doping in Li_2FeSiO_4 cathode material for lithium-ion battery. *Journal of Power Sources* **2015,** *274*, 194-202.

25. Deng, C.; Zhang, S.; Yang, S. Y.; Fu, B. L.; Ma, L., Synthesis and characterization of $Li_2Fe_{0.97}M_{0.03}SiO_4$ (M = Zn^{2+}, Cu^{2+}, Ni^{2+}) cathode materials for lithium ion batteries. *Journal of Power Sources* **2011,** *196* (1), 386-392.

26. Li, L.-m.; Guo, H.-j.; Li, X.-h.; Wang, Z.-x.; Peng, W.-j.; Xiang, K.-x.; Cao, X., Effects of roasting temperature and modification on properties of Li_2FeSiO_4/C cathode. *Journal of Power Sources* **2009,** *189* (1), 45-50.

27. Zhang, L. L.; Duan, S.; Yang, X. L.; Liang, G.; Huang, Y. H.; Cao, X. Z.; Yang, J.; Ni, S. B.; Li, M., Systematic investigation on Cadmium-incorporation in Li_2FeSiO_4/C cathode material for lithium-ion batteries. *Scientific Reports* **2014,** *4*.

28. Qu, L.; Li, M.; Bian, L.; Du, Q.; Luo, M.; Yang, B.; Yang, L.; Fang, S.; Liu, Y., A strontium-doped Li_2FeSiO_4/C cathode with enhanced performance for the lithium-ion battery. *Journal of Solid State Electrochemistry* **2017,** *21* (12), 3659-3673.

29. Gao, H.-y.; Hu, Z.; Yang, J.-g.; Chen, J., $Li_{2-x}Fe_{1-x}Al_xSiO_4$/C nanocomposites cathodes for lithium-ion batteries. *Energy Technology* **2014,** *2* (4), 355-361.

30. Zhang, S.; Deng, C.; Fu, B. L.; Yang, S. Y.; Ma, L., Effects of Cr doping on the electrochemical properties of Li_2FeSiO_4 cathode material for lithium-ion batteries. *Electrochimica Acta* **2010,** *55* (28), 8482-8489.

31. Qiu, H.; Yue, H.; Zhang, T.; Ju, Y.; Zhang, Y.; Guo, Z.; Wang, C.; Chen, G.; Wei, Y.; Zhang, D., Enhanced electrochemical performance of Li_2FeSiO_4/C positive electrodes for lithium-ion batteries via Yttrium doping. *Electrochimica Acta* **2016,** *188*, 636-644.

32. Yang, J.; Zheng, J.; Kang, X.; Teng, G.; Hu, L.; Tan, R.; Wang, K.; Song, X.; Xu, M.; Mu, S.; Pan, F., Tuning structural stability and lithium-storage properties by d-orbital hybridization substitution in full tetrahedron Li_2FeSiO_4 nanocrystal. *Nano Energy* **2016,** *20*, 117-125.

33. Qiu, H.; Yue, H.; Wang, X.; Zhang, T.; Zhang, M.; Fang, Z.; Zhao, X.; Chen, G.; Wei, Y.; Wang, C.; Zhang, D., Titanium-doped Li_2FeSiO_4/C composite as the cathode material for lithium-ion batteries with excellent rate capability and long cycle life. *Journal of Alloys and Compounds* **2017,** *725*, 860-868.

34. Wang, K.; Teng, G. F.; Yang, J. L.; Tan, R.; Duan, Y. D.; Zheng, J. X.; Pan, F., Sn(II,IV) steric and electronic structure effects enable self-selective doping on Fe/Si-sites of Li_2FeSiO_4 nanocrystals for high performance lithium ion batteries. *Journal of Materials Chemistry A* **2015,** *3* (48), 24437-24445.

35. Yamashita, H.; Ogami, T.; Kanamura, K., Enhanced Energy Density of Li2MnSiO4/C Cathode Materials for Lithium-ion Batteries through Mn/Co Substitution. *Electrochemistry* **2018,** *86* (6), 324-332.

36. Wang, D. Y.; Li, H.; Shi, S. Q.; Huang, X. J.; Chen, L. Q., Improving the rate performance of $LiFePO_4$ by Fe-site doping. *Electrochimica Acta* **2005,** *50* (14), 2955-2958.

37. Li, H.; Cormier, M.; Zhang, N.; Inglis, J.; Li, J.; Dahn, J. R., Is Cobalt Needed in Ni-Rich Positive Electrode Materials for Lithium Ion Batteries? *Journal of The Electrochemical Society* **2019,** *166* (4), A429-A439.

38. Kageyama, H.; Hashimoto, Y.; Oaki, Y.; Imai, H., Six-armed twin crystals composed of lithium iron silicate nanoplates and their electrochemical properties. *Crystengcomm* **2015,** *17* (44), 8486-8491.

39. Yabuuchi, N.; Yamakawa, Y.; Yoshii, K.; Komaba, S., Hydrothermal synthesis and characterization of Li_2FeSiO_4 as positive electrode materials for Li-ion batteries. *Electrochemistry* **2010,** *78* (5), 363-366.

40. Islam, M. S.; Driscoll, D. J.; Fisher, C. A. J.; Slater, P. R., Atomic-scale investigation of defects, dopants, and lithium transport in the $LiFePO_4$ olivine-type battery material. *Chemistry of Materials* **2005,** *17* (20), 5085-5092.

41. Ong, S. P.; Wang, L.; Kang, B.; Ceder, G., Li−Fe−P−O_2 Phase Diagram from First Principles Calculations. *Chemistry of Materials* **2008,** *20* (5), 1798-1807.

42. Saracibar, A.; Wang, Z.; Carroll, K. J.; Meng, Y. S.; Dompablo, M. E. A.-d., New insights into the electrochemical performance of Li_2MnSiO_4: effect of cationic substitutions. *Journal of Materials Chemistry A* **2015,** *3* (11), 6004-6011.

43. Meng, Y. S.; Arroyo-de Dompablo, M. E., Recent Advances in First Principles Computational Research of Cathode Materials for Lithium-Ion Batteries. *Accounts Chem Res* **2013,** *46* (5), 1171-1180.

44. Fisher, C. A. J.; Kuganathan, N.; Islam, M. S., Defect chemistry and lithium-ion migration in polymorphs of the cathode material Li_2MnSiO_4. *Journal of Materials Chemistry A* **2013,** *1* (13), 4207-4214.

45. Chen, H.; Hautier, G.; Ceder, G., Synthesis, Computed Stability, and Crystal Structure of a New Family of Inorganic Compounds: Carbonophosphates. *Journal of the American Chemical Society* **2012,** *134* (48), 19619-19627.

46. Zeng, Y.; Chiu, H.-C.; Rasool, M.; Brodusch, N.; Gauvin, R.; Jiang, D.-T.; Ryan, D. H.; Zaghib, K.; Demopoulos, G. P., Hydrothermal crystallization of *Pmn*2_1 Li_2FeSiO_4 hollow mesocrystals for Li-ion cathode application. *Chemical Engineering Journal* **2019,** *359*, 1592-1602.

47. Kresse, G.; Furthmüller, J., Efficient iterative schemes for ab initio total-energy calculations using a plane-wave basis set. *Physical Review B* **1996,** *54* (16), 11169-11186.

48. Kresse, G.; Joubert, D., From ultrasoft pseudopotentials to the projector augmented-wave method. *Physical Review B* **1999,** *59* (3), 1758-1775.

49. Perdew, J. P.; Burke, K.; Ernzerhof, M., Generalized gradient approximation made simple. *Phys Rev Lett* **1996,** *77* (18), 3865-3868.

50. Jain, A.; Ong, S. P.; Hautier, G.; Chen, W.; Richards, W. D.; Dacek, S.; Cholia, S.; Gunter, D.; Skinner, D.; Ceder, G.; Persson, K. A., Commentary: The Materials Project: A materials genome approach to accelerating materials innovation. *APL Materials* **2013,** *1* (1), 011002.

51. Zhou, F.; Cococcioni, M.; Marianetti, C. A.; Morgan, D.; Ceder, G., First-principles prediction of redox potentials in transition-metal compounds with LDA+*U*. *Physical Review B* **2004,** *70* (23), 235121.

52. Eames, C.; Armstrong, A. R.; Bruce, P. G.; Islam, M. S., Insights into changes in voltage and structure of Li_2FeSiO_4 polymorphs for lithium-ion batteries. *Chemistry of Materials* **2012,** *24* (11), 2155-2161.

53. Walle, C. G. V. d.; Neugebauer, J., First-principles calculations for defects and impurities: Applications to III-nitrides. *Journal of Applied Physics* **2004,** *95* (8), 3851-3879.

54. Dominko, R.; Sirisopanaporn, C.; Masquelier, C.; Hanzel, D.; Arcon, I.; Gaberscek, M., On the origin of the electrochemical capacity of $Li_2Fe_{0.8}Mn_{0.2}SiO_4$. *Journal of The Electrochemical Society* **2010,** *157* (12), A1309.

55. Armstrong, A. R.; Sirisopanaporn, C.; Adamson, P.; Billaud, J.; Dominko, R.; Masquelier, C.; Bruce, P. G., Polymorphism in Li_2MSiO_4 (M = Fe, Mn): A variable temperature diffraction study. *Zeitschrift für anorganische und allgemeine Chemie* **2014,** *640* (6), 1043-1049.

56. Kleiner, K.; Strehle, B.; Baker, A. R.; Day, S. J.; Tang, C. C.; Buchberger, I.; Chesneau, F.-F.; Gasteiger, H. A.; Piana, M., Origin of high capacity and poor cycling stability of Li-rich layered oxides: A long-duration in situ synchrotron powder diffraction study. *Chemistry of Materials* **2018,** *30* (11), 3656-3667.

57. Momma, K.; Izumi, F., VESTA 3 for three-dimensional visualization of crystal, volumetric and morphology data. *Journal of Applied Crystallography* **2011,** *44* (6), 1272-1276.

58. Armstrong, A. R.; Kuganathan, N.; Islam, M. S.; Bruce, P. G., Structure and lithium transport pathways in Li_2FeSiO_4 cathodes for lithium batteries. *Journal of the American Chemical Society* **2011,** *133* (33), 13031-13035.

59. Arthur, Z.; Chiu, H.-C.; Lu, X.; Chen, N.; Emond, V.; Zaghib, K.; Jiang, D.-T.; Demopoulos, G. P., Spontaneous reaction between an uncharged lithium iron silicate cathode and a $LiPF_6$-based electrolyte. *Chemical communications* **2016,** *52* (1), 190-193.

60. He, G.; Popov, G.; Nazar, L. F., Hydrothermal synthesis and electrochemical poperties of Li_2CoSiO_4/C nanospheres. *Chemistry of Materials* **2013,** *25* (7), 1024-1031.

61. Orazem, M. E.; Tribollet, B., Time-Constant Dispersion. In *Electrochemical Impedance Spectroscopy*, John Wiley & Sons, Inc: 2017.

62. Minkyu, K.; Minkyung, K.; Heetaek, P.; Hong, L.; Byoungwoo, K., Unusual Activation of Cation Disordering by Li/Fe Rearrangement in Triplite $LiFeSO_4F$. *Advanced Energy Materials* **2018,** *8* (22), 1800298.

63. Metzger, M.; Strehle, B.; Solchenbach, S.; Gasteiger, H. A., Origin of H_2 Evolution in LIBs: H_2O Reduction vs. Electrolyte Oxidation. *Journal of The Electrochemical Society* **2016,** *163* (5), A798-A809.

64. Palacín, M. R.; de Guibert, A., Why do batteries fail? *Science* **2016,** *351* (6273).

65. Aurbach, D.; Markovsky, B.; Salitra, G.; Markevich, E.; Talyossef, Y.; Koltypin, M.; Nazar, L.; Ellis, B.; Kovacheva, D., Review on electrode–electrolyte solution interactions, related to cathode materials for Li-ion batteries. *Journal of Power Sources* **2007,** *165* (2), 491-499.

66. Assat, G.; Delacourt, C.; Corte, D. A. D.; Tarascon, J.-M., Editors' Choice—Practical Assessment of Anionic Redox in Li-Rich Layered Oxide Cathodes: A Mixed Blessing for High Energy Li-Ion Batteries. *Journal of The Electrochemical Society* **2016,** *163* (14), A2965-A2976.

67. Baker, D. R.; Li, C.; Verbrugge, M. W., Similarities and Differences between Potential-Step and Impedance Methods for Determining Diffusion Coefficients of Lithium in Active Electrode Materials. *Journal of The Electrochemical Society* **2013,** *160* (10), A1794-A1805.

68. Teufl, T.; Pritzl, D.; Solchenbach, S.; Gasteiger, H. A.; Mendez, M. A., Editors' Choice—State of Charge Dependent Resistance Build-Up in Li- and Mn-Rich Layered Oxides during Lithium Extraction and Insertion. *Journal of The Electrochemical Society* **2019,** *166* (6), A1275-A1284.

69. Arora, P.; Popov, B. N.; White, R. E., Electrochemical investigations of cobalt‐doped $LiMn_2O_4$ as cathode material for lithium‐ion batteries. *Journal of The Electrochemical Society* **1998,** *145* (3), 807-815.

70. Zaghib, K.; Ait Salah, A.; Ravet, N.; Mauger, A.; Gendron, F.; Julien, C. M., Structural, magnetic and electrochemical properties of lithium iron orthosilicate. *Journal of Power Sources* **2006,** *160* (2), 1381-1386.

71. Pretsch, E.; Bühlmann, P.; Badertscher, M., IR Spectroscopy. In *Structure Determination of Organic Compounds: Tables of Spectral Data*, Springer Berlin Heidelberg: Berlin, Heidelberg, 2009; pp 1-67.

72. Dippel, C.; Krueger, S.; Kraft, V.; Nowak, S.; Winter, M.; Li, J., Aging stability of Li_2FeSiO_4 polymorphs in $LiPF_6$ containing organic electrolyte for lithium-ion batteries. *Electrochimica Acta* **2013,** *105*, 542-546.

73. Wengao, Z.; Jianming, Z.; Lianfeng, Z.; Haiping, J.; Bin, L.; Hui, W.; H., E. M.; Chongmin, W.; Wu, X.; Yong, Y.; Ji-Guang, Z., High voltage operation of Ni-rich NMC cathodes enabled by stable electrode/electrolyte interphases. *Advanced Energy Materials* **2018,** *8* (19), 1800297.

74. Moulder, J.; Chastain, J.; King, R., *Handbook of X-ray Photoelectron Spectroscopy: a reference book of standard spectra for identification and interpretation of XPS data*. Physical Electronics: 1995.

75. Dedryvère, R.; Laruelle, S.; Grugeon, S.; Gireaud, L.; Tarascon, J.-M.; Gonbeau, D., XPS identification of the organic and inorganic components of the electrode/electrolyte interface formed on a metallic cathode. *Journal of The Electrochemical Society* **2005,** *152* (4), A689-A696.

76. Bolli, C.; Guéguen, A.; Mendez, M. A.; Berg, E. J., Operando monitoring of F^- formation in lithium ion batteries. *Chemistry of Materials* **2019**, , 31, 4, 1258-1267.

77. Ye, C.; Tu, W.; Yin, L.; Zheng, Q.; Wang, C.; Zhong, Y.; Zhang, Y.; Huang, Q.; Xu, K.; Li, W., Converting detrimental HF in electrolytes into a highly fluorinated interphase on cathodes. *Journal of Materials Chemistry A* **2018,** *6* (36), 17642-17652.

78. Fan, X.; Chen, L.; Borodin, O.; Ji, X.; Chen, J.; Hou, S.; Deng, T.; Zheng, J.; Yang, C.; Liou, S.-C.; Amine, K.; Xu, K.; Wang, C., Non-flammable electrolyte enables Li-metal batteries with aggressive cathode chemistries. *Nature Nanotechnology* **2018,** *13* (8), 715-722.

79. Ensling, D.; Stjerndahl, M.; Nyten, A.; Gustafsson, T.; Thomas, J. O., A comparative XPS surface study of Li_2FeSiO_4/C cycled with LiTFSI- and $LiPF_6$-based electrolytes. *Journal of Materials Chemistry* **2009,** *19* (1), 82-88.

80. Browning, J. F.; Baggetto, L.; Jungjohann, K. L.; Wang, Y.; Tenhaeff, W. E.; Keum, J. K.; Wood, D. L.; Veith, G. M., In situ determination of the liquid/solid interface thickness and composition for the Li ion cathode $LiMn_{1.5}Ni_{0.5}O_4$. *ACS Applied Materials & Interfaces* **2014,** *6* (21), 18569-18576.

81. Cherkashinin, G.; Motzko, M.; Schulz, N.; Späth, T.; Jaegermann, W., Electron spectroscopy study of Li[Ni,Co,Mn]O_2/electrolyte interface: Electronic structure, interface composition, and device implications. *Chemistry of Materials* **2015,** *27* (8), 2875-2887.

Chapter 5. Defect Engineering of Fe-Rich Orthosilicate Cathode Materials with Enhanced Li-Ion Intercalation Capacity and Kinetics

In Chapter 4, partial substitution of Fe(II) by other divalent cations in the matrix of stochiometric LFS was discussed, from which Co(II) showed the most promising results in terms of synthesis feasibility and electrochemical performance. The presence of Co(II) enhanced capacity retention substantially. Despite the good retention, Co-doped LFS was not able to deliver high capacity that is required for a practical Li-ion cathode. This low capacity is mainly due to the intrinsic low conductivities of LFS and the inaccessibility of the second Li. Thus, in this chapter, thinking "out of the box" moved away from the stoichiometric and Li-rich composition regions by designing non-stoichiometric Fe-rich LFS with a general formula $Li_{4-2x}Fe_xSiO_4$ ($1<x<2$). The benefits that could be possible materialized include the increased Fe content that gives higher theoretical capacity with only Fe^{2+}/Fe^{3+} redox couple, while more importantly, the alteration of local structures that will change the electronic structure and may change the electronic and Li transport dynamics. In terms of material synthesis, we have shown in Chapter 3 that Li-Fe antisite defects are favored to form during hydrothermal crystallization, which indicates the possibility of putting Fe on Li site to some extent.

It is shown in this chapter that Fe-rich and Li-rich (Fe-deficient) LFS with a certain level of solubility can be synthesized by the hydrothermal method developed in our previous work (Chapter 3). The electrochemical performances of stoichiometric and Fe-rich LFS are evaluated and compared. Fe-rich LFS, as hypothesized, delivers higher capacity than its stoichiometric counterpart as a result of facile Li transport kinetics and improved electronic conductivity. This is the first time that Fe-rich LFS is designed, synthesized, and tested, which with its promising results, opens a new direction for optimizing intercalation materials for energy storage.

This chapter was submitted as **Yan Zeng**, Hsien-Chieh Chiu, Bin Ouyang, Karim Zaghib, George P. Demopoulos. Defect Engineering of Fe-Rich Orthosilicate Cathode Materials with Enhanced Li-Ion Intercalation Capacity and Kinetics. (under review*)*

5.1 Abstract

Defect engineering via non-stoichiometric composition control can serve as an effective strategy to tune the electronic and crystal structures of intercalation compounds, as has been recently evidenced in Li-rich cathode materials. We have extended this strategy, but in another direction— Fe-rich as opposed to Li-rich, in improving the electrochemical performance of a promising cathode material, Li_2FeSiO_4 (LFS). Non-stoichiometric LFS compounds in orthorhombic *Pmn*2_1 phase with up to 8% Fe excess were successfully synthesized via controlled hydrothermal synthesis. We demonstrate that in addition to the higher electron capacity from the accessible Fe^{2+}/Fe^{3+} redox couple, the presence of excess Fe enhances the intercalation kinetics vis-à-vis the stoichiometric composition. From combined electrochemical evaluation and first principles DFT calculations, the enhanced kinetics are rationalized by the introduction of the $Fe_{Li}^{\bullet}$ + $V_{Li}^{\prime}$ defect pair and newly-generated electron conducting states from the creation of local Fe–O–Fe configurations. Moreover, we found the Fe-rich structure to facilitate Fe migration to Li-site due to lower energy barrier than stoichiometric LFS, hence apparently leading to faster phase transformation from *Pmn*2_1 towards the cycled inverse *Pmn*2_1 phase. More generally, this study opens alternative defect and compositional engineering approaches in designing next generation intercalation materials with improved electrochemical performance.

5.2 Introduction

In the paradigm of intercalation cathode materials for Li-ion batteries, most of research studies have focused on ordered and stoichiometric compounds, such as layered $LiNi_xCo_yMn_zO_2$ (NCM, x+y+z = 1), spinel $LiMn_2O_4$ (LMO), and olivine $LiFePO_4$ (LFP).[1-2] In the recent decade, there has been increasing interest in developing non-stoichiometric oxides as an attempt to enable high energy density of cathode materials.[3-6] Reversible oxygen redox activity, thanks to the Li-rich compositional design, adds extra capacity to what can be achieved with solely transition metal redox couple.[3, 7-8] It has been proven in these studies that compositional engineering can serve as an effective strategy for tuning the crystal and electronic structures and hence electrochemical properties of the intercalation materials.

Li_2FeSiO_4 (LFS) is a sustainable and promising high-energy density intercalation cathode material with theoretical energy density of 1120 Wh kg^{-1} because of having two Li per formula

unit.[9-10] Unfortunately, drawbacks such as low electronic and ionic conductivities and the difficulty in extracting reversibly more than one Li have hindered its development.[11] Performance of Li-ion batteries is highly correlated to the transport of electrons and Li-ions in the lattice of the electrodes. The lattice of stoichiometric LFS in $Pmn2_1$ structure can be viewed as assembling of corner-sharing tetrahedra of LiO_4, FeO_4, and SiO_4 occupying the hexagonal close-packed-based framework of oxygen.[12] Each FeO_4 is separated from the other by SiO_4 or LiO_4. This results in a large bandgap of about 3 eV[13] and a small electronic conductivity of about 6×10^{-14} S cm^{-1} at room temperature and about 2×10^{-12} S cm^{-1} at 60^{o}C[14]. Within this framework, Li could transport along the *a*-direction with a migration barrier of 0.83 eV or along a zigzag *c*-direction with a migration barrier of 0.74 eV.[15] Upon electrochemical cycling, LFS undergoes phase transformation to a cycled crystal structure with lower energy[16] that is associated with an enlarged migration barrier to 0.91 eV along a zigzag *c*-direction.[17] This Li migration barrier is high compared to those of other Fe-based cathode materials, for example, 0.55 eV for $LiFePO_4$[18] and 0.47 eV for $Li_2Fe(SO_4)_2$.[19] Meanwhile, it is also possible that the transport of electron and Li-ion is strongly coupled in LFS, referring to the formation of small-polaron that has been well-studied in LFP.[20-23]

To address the challenge of enhancing the electrochemical performance of LFS, introducing non-stoichiometric defects could serve as a powerful tool. There are two directions to tune the stoichiometry of LFS by varying Li/Fe ratio— either increase the content of Li while reduce Fe (Li-rich) or the other way around (Fe-rich). In the Li-rich direction, the chemical formula can be written as $Li_{4-2x}Fe_xSiO_4$ ($0<x<1$), thus the total cations ($Li^+ + Fe^{2+}$) to be placed in the lattice are more than the original tetrahedral sites for Li and Fe. In a recent study on Li-rich LFS, Billaud et al.[24] proposed that the excess Li could occupy the interstitial octahedral sites. Interestingly, the presence of excess Li was found to promote the Li transport during (de)intercalation and thus enhance the rate performance. Yet, Li-rich LFS failed to deliver higher capacity because introducing Li excess sacrifices the Fe^{2+}/Fe^{3+} redox capacity. In the Fe-rich direction, denoted as chemical formula $Li_{4-2x}Fe_xSiO_4$ ($1<x<2$), the excess Fe could occupy the Li-site while forming a Li-vacancy to maintain charge neutrality. To the best of our knowledge, Fe-rich LFS compounds have not been reported, but as discovered in the present work this strategy can prove highly rewarding via alteration of the bonding and defect chemistry in terms of increased storage capacity, electronic conductivity, and Li transport kinetics.

An attempt to prepare Fe-rich LFS was made by Zhu et al. using sol-gel method with reactants containing excess Fe.[25] However, the excess Fe resulted in the formation of $LiFeO_{2-x}$ as a secondary phase rather than being mixed in the LFS matrix. Li-rich Li_2MnSiO_4 was prepared by solid-state reaction via varying the stoichiometry of the reactants.[26] Yet Mn-rich composition was not achieved; one reason could be that both Mn and Li were in excess in the reactants, whereas the other reason could be the nature of the high-temperature solid-state reaction that does not favor the formation of certain defects such as Mn-Li antisites. For the purpose of preparing Fe-rich LFS, aqueous-based chemistry may open the possibility. Indeed, the presence of Fe on Li site associated with Li-vacancy within a few atomic percentages has been typically observed in LFS or LFP prepared by aqueous synthesis.[27-29] Fe-rich LFP was successfully produced by Axmann et al.[30] using co-precipitation method and this non-stoichiometric structure remained stable after subsequent annealing. In our previous work, we demonstrated that the concentration of Fe-Li antisites can be tuned by manipulating the chemical potentials of Li- and Fe-species in hydrothermal synthesis.[31]

In this study, a series of new compounds of non-stoichiometric $Li_{4-2x}Fe_xSiO_4$ (target composition range: $0.8 \leq x \leq 1.2$) are synthesized via hydrothermal crystallization featuring EDTA as a mesocrystal regulating agent.[31] Structural analysis by Rietveld refinement of X-ray diffraction (XRD) and chemical analysis by Inductively Coupled Plasma (ICP) are applied to determine the solubility limits of non-stoichiometric composition while understanding the effect of Fe-deficiency (used interchangeably with Li-rich) and Fe-excess on the crystal structure of LFS. Afterwards, particular attention is given to Fe-rich LFS with the objective of elucidating the origin of enhanced electrochemical functionality by relating the defect-engineered structure to properties such as charge-discharge capacity, voltage, and Li diffusion kinetics. Finally, first-principles DFT calculations are utilized to understand the change of local structure with excess Fe and its influence on the electronic conductivity as well as cation migration characteristics.

5.3 Experimental Section

5.3.1 Synthesis

Stoichiometric and nonstoichiometric lithium iron silicates were synthesized by hydrothermal process using as starting materials lithium hydroxide monohydrate (98% $LiOH{\cdot}H_2O$), fumed silica (99% SiO_2), and iron(II) sulfate heptahydrate (98% $FeSO_4{\cdot}7H_2O$).

Ethylenediaminetetraacetic acid calcium disodium salt (99% EDTA-Ca-2Na) was added as a chelating agent to control the reactive crystallization of lithium iron silicates.[27] All the chemicals were purchased from Sigma-Aldrich and used without further purification. The detailed synthesis procedure can be found in our previous work.[31] In a typical synthesis experiment, $LiOH{\cdot}H_2O$, SiO_2, and $FeSO_4{\cdot}7H_2O$ were dissolved and mixed in degassed deionized-water based on varied molar ratio of Li/Fe/Si as 4/*x*/1 (*x* = 0.8, 0.9, 0.95, 1, 1.05, 1.1, and 1.2). Hydrothermal syntheses were carried out in a 450 mL PTFE-lined stirred autoclave (Parr Instruments, Moline, IL) at 200ºC for 6 hours. The colors of the as-synthesized powders change from light beige to grey/brown from Li-rich to Fe-rich. After hydrothermal treatment, the obtained powders were annealed at 400ºC for 6 hours under 5% H_2 + 95% N_2 atmosphere.

5.3.2 Characterizations

Powder X-ray diffraction (PXRD) patterns were collected on a Bruker D8 Diffractometer with Ni-filtered CuKα radiation (λ = 1.5418 Å) and operated at 40 kV and 40 mA in a 2θ range between 10º and 100º with increment of 0.02º and a dwell time of 2.5 s per step. Phase quantification and crystal structures were determined from Rietveld refinement using TOPAS Academic V.5.0 program. Transmission electron microscope (TEM) and high-resolution TEM (HR-TEM) images were acquired using the FEI Tecnai 12 BioTwin at 200 kV. Brunauer–Emmett–Teller (BET) specific surface area measurements were performed using a TriStar 3000 analyzer (Micromeritics) in N_2 (−196°C). Inductively coupled plasma optical emission spectroscopy (ICP-OES, Thermo Scientific iCAP 6500 ICP spectrometer) was applied for elemental analysis. Dissolved LFS for ICP measurements was prepared by fusion method. 0.2 g LFS powder was mixed with fusion flux (containing 2 g $Na_2B_4O_7$, 0.02 g NH_4NO_3 and 0.2 g KI) and heated at 1000ºC in a Pt crucible. The molten mixture was then diluted with 2 vol.% HNO_3 and subjected to ICP analysis thereafter.

5.3.3 Electrochemistry

Electrochemical measurements were performed in Swagelok type cells assembled in an Ar-filled glovebox. Chemicals used in the electrode fabrication included acetylene black (AB, Sigma-Aldrich), polyvinylidene difluoride (PVDF, Sigma-Aldrich), 1-methyl-2-pyrrolidone (99.5% NMP, Sigma-Aldrich), lithium metal foil (Sigma-Aldrich), and a standard electrolyte solution made of 1 M $LiPF_6$ in ethylene carbonate (EC)/dimethyl carbonate (DMC) (1: 1 v/v) purchased

from BASF. The composite electrode materials were prepared by mixing the as-synthesized powders with acetylene black (AB) in a weight ratio of 0.8: 0.2 and ball milling in isopropanol at 250 rpm for 3 hours using planetary micro mill (Fritsch, Pulverisette 7 premium line). The working electrodes were prepared by spreading a slurry of the active material (ball-milled C-LFS), AB and PVDF in weight ratio of (C-LFS: AB: PVDF) 0.8: 0.1: 0.1 onto aluminum foil. Li metal was used as the counter electrode. Two pieces of polypropylene film (Celgard 2200) were used as separator in each cell. Each electrode contained approximately 2.5 mg/cm^2 of active LFS material.

Galvanostatic charge-discharge profiles were measured on an Arbin cycler at varied current rates between 1.5-4.5 V. Galvanostatic intermittent titration technique (GITT) was conducted on the Arbin cycler by applying a constant current at 0.02 C rate (3.32 mA g^{-1}) for 5 hours (corresponding to the removal of 0.1 Li), followed by relaxation for 24 hours. Cyclic voltammetry (CV) measurements were performed by using an electrochemical workstation (Bio-Logic). CV was performed between 2-4.5 V at a scan rate of 0.05 mV s^{-1} for 5 sweeps, followed by scanning at various rates from 0.1 to 0.5 mV s^{-1}. All the electrochemical measurements were performed at 45^{o}C.

5.3.4 Computational method

Spin polarized density functional theory (DFT) calculations were performed in the Vienna *ab initio* simulation package (VASP) using the projector augmented wave (PAW) method.[32-33] Generalized gradient approximation Perdew−Burke−Ernzerhof (GGA-PBE) functional was employed.[34] Hubbard parameter correlation (GGA + *U*) was used to correct the interactions inside the *d*-orbitals of the transition metals. *U* value used for Fe is 5.3 eV.[35-36] The cutoff energy was kept at 700 eV for all the calculations. Each calculation is treated as converged if the forces on all the nuclei were smaller than 0.01 eV/Å. A reciprocal space discretization of 25 Å is adapted in all structural optimizations while 45 Å is applied for self-consistent calculations to obtain accurate electronic structures. Kinetic calculations were performed by employing transition state theory. The climbed image Nudged Elastic Band (ci-NEB) method[37-40] was adopted to compute the minimum reaction paths (MEPs) and associated energy barriers.

The starting atomic configurations of stoichiometric and Fe-rich LFS were based on *Pmn*2$_1$ Li_2FeSiO_4 adopted from Eames *et al*.[41] All calculations were done in supercells containing sixteen formula unit (2×2×2 unit cells). For the investigation of Fe-rich LFS, one Li was substituted by

one Fe along with one Li-vacancy on the adjacent site for charge compensation, resulting in 6.25% Fe-rich ($Li_{1.88}Fe_{1.06}SiO_4$). Lattice parameters and atomic positions were fully relaxed prior to further calculations. To evaluate the phase stability of the Fe-rich structure, all the competing phases under the Li_2O-FeO-SiO_2 compositional space were involved to build the energy convex hull. In this case, the energy above the hull represents the thermodynamic driving force for a compound to decompose into the competing phases at the hull. This will therefore offer more accurate description about the stability and the potential phase transition of the compounds during synthesis. The structures of all the potential competing phases were taken from the Materials Project database[35] with followed-up convergence to ensure the higher precision criterion as described above.

5.4 Results and Discussion

5.4.1 Synthesis and structures of non-stoichiometric $Li_{4-2x}Fe_xSiO_4$

The phase diagram of the Li_2O-FeO-SiO_2 system (Figure 5.1a) was constructed by DFT calculations to represent thermodynamic solid phase equilibria in the corresponding chemical system. Thermodynamically stable solid compounds under the given conditions are labeled as grey nodes in the phase diagram. The positions of nonstoichiometric compounds $Li_{4-2x}Fe_xSiO_4$ are marked as dashed lines and can be separated to Li-rich (short-dashed blue line) and Fe-rich regions (dashed red line). In the Li-rich region, i.e. $0 < x < 1$, the potential decomposition phases for $Li_{4-2x}Fe_xSiO_4$ are Li_2FeSiO_4 and Li_4SiO_4. In the Fe-rich region, i.e. $1 < x < 2$, the potential decomposition phases for $Li_{4-2x}Fe_xSiO_4$ are Li_2FeSiO_4 and Fe_2SiO_4. It must be noted that the phase diagram in Figure 5.1a was constructed for systems at 0 K and 0 atm, which is different from actual experimental conditions (higher temperature and pressure, presence of aqueous solution, oxidizing or reducing environment, etc.). Thus, some differences between the calculations and the experiments are expected. Nonetheless, this phase diagram serves as a guide in understanding the compositional spaces of Li_2O-FeO-SiO_2 and gives insights into impurity phases that might be obtained from synthesis. Examples of constructing and interpreting these type of phase diagrams can be found elsewhere.[42-43]

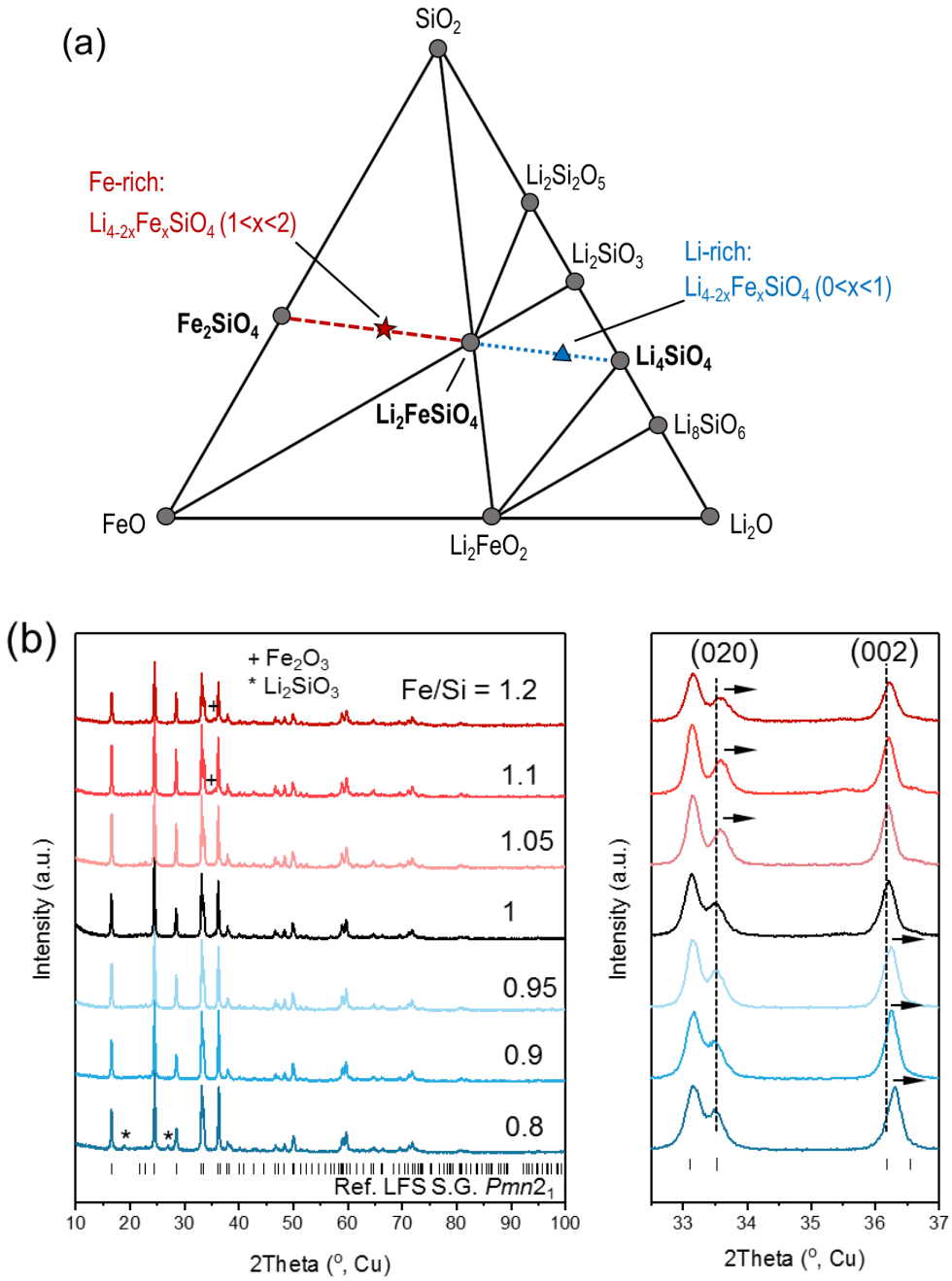

Figure 5.1. (a) Calculated phase diagram of the Li_2O-FeO-SiO_2 system. Non-stoichiometric compounds $Li_{4-2x}Fe_xSiO_4$ locates on the dashed lines in which dashed red line represents Fe-rich compounds (1<x<2) whereas short-dashed blue line represents Li-rich compounds (0<x<1). (b) Powder X-ray diffractograms (Cu-Kα radiation, λ = 1.5418 Å) of hydrothermal products synthesized from precursors with varied molar ratios of Li/Fe/Si = 4/*x*/1 (*x* = 0.8, 0.9. 0.95, 1, 1.05, 1.1, and 1.2). Black streaks at the bottom represent the Bragg peak positions of *Pmn*2_1 Li_2FeSiO_4 (reference PDF# 01-080-6279). Cross and star symbols represent second phases of Fe_2O_3 and Li_2SiO_3, respectively. Enlarged 2θ area on the right side illustrates peak shifts of the reflections corresponding to (020) and (002) lattice planes in Fe-rich and Fe-deficient compounds.

Stoichiometric and non-stoichiometric LFS compounds, $Li_{4-2x}Fe_xSiO_4$ (target composition range: $0.8 \leq x \leq 1.2$), with deficiency or excess in Fe, were synthesized by hydrothermal method. In the nominal formula $Li_{4-2x}Fe_xSiO_4$, the stable polyanion unit SiO_4 is used as the reference to determine the elemental composition of the non-stoichiometric compound. The content of Fe in the crystallized compound was adjusted by tuning the concentration therefore the chemical potential of Fe^{2+} in the precursor mixture. Figure 5.1b shows the measured powder XRD patterns of seven compounds from Li-rich to Fe-rich. It reveals that pure *Pmn*2_1 LFS-phase can be obtained when the precursors contained Fe concentrations ranging from 10% deficiency (x = 0.9) to 5% excess (x = 1.05). When Fe in precursor was 20% deficient (x = 0.8) from the stoichiometry, Li_2SiO_3 formed as the secondary phase. On the other side, when Fe in precursor was 10% or 20% excess (x = 1.1 or 1.2), small quantities of Fe_2O_3 formed. It is noted that the experimentally observed secondary phases, namely, Li_2SiO_3 and Fe_2O_3, are different to those predicted from DFT (Li_4SiO_4 and Fe_2SiO_4 as shown in Figure 5.1a). This can be attributed to the difference between the applied experimental conditions (hydrothermal at 473 K) and the calculation conditions (0 K and 0 atm) that could result in changes in total energies of solid compounds. To have a better understanding of the current solution system, Pourbaix diagrams in terms of the stability of Li_2SiO_3 and Fe_2SiO_4 in aqueous solutions at room temperature were constructed via the Materials Project.[44] As presented in Figure C1, under the experimental condition in aqueous solution with pH = 11-12, Li_4SiO_4 is unstable relative to Li_2SiO_3. While for Fe_2SiO_4, trace of oxygen could readily induce its decomposition to Fe_2O_3 and soluble SiO_4^{4-} species.

Rietveld refinement of XRD data combined with ICP elemental analysis were applied to quantify the phase fractions and hence determine the composition of $Li_{4-2x}Fe_xSiO_4$ in the synthesized products. The deduced purity and compositions of seven compounds are listed in Table 5.1. According to these analyses, the solubility limits of Fe-deficient and Fe-rich regions are about 13% and 8%, respectively, in the crystal lattice of *Pmn*2_1 LFS. That is to say, the composition range of synthesizable non-stoichiometric compounds $Li_{4-2x}Fe_xSiO_4$ at 200°C is $0.87 \leq x \leq 1.08$. We also calculated the energy above the hull of one Fe-rich composition $Li_{1.88}Fe_{1.06}SiO_4$ (i.e. 6.25% Fe-rich) and found it to be 15.97 meV/atom. According to Boltzmann distribution[45] for calculating the defect concentration, theoretically 4.5% of Fe-excess could be accommodated in the structure of LFS at 200°C.

Table 5.1. Target and determined compositions of hydrothermally synthesized $Li_{4-2x}Fe_xSiO_4$

Label of products	Target x in $Li_{4-2x}Fe_xSiO_4$	Fe/Si molar ratio from ICP	Weight percent from XRD	Determined composition [a]	Deviation from stoichiometry
LFS-Fe1.2	1.2	1.19	95.2%, 4.8% Fe_2O_3	$Li_{1.84}Fe_{1.08}SiO_4$	8% Fe-rich
LFS-Fe1.1	1.1	1.09	98.0%, 2.0% Fe_2O_3	$Li_{1.9}Fe_{1.05}SiO_4$	5% Fe-rich
LFS-Fe1.05	1.05	1.05	100%	$Li_{1.9}Fe_{1.05}SiO_4$	5% Fe-rich
LFS-stoi	1	1.00	100%	Li_2FeSiO_4	Stoichiometric
LFS-Fe0.95	0.95	0.96	100%	$Li_{2.08}Fe_{0.96}SiO_4$	4% Fe-deficient
LFS-Fe0.9	0.9	0.91	100%	$Li_{2.18}Fe_{0.91}SiO_4$	9% Fe-deficient
LFS-Fe0.85	0.85	0.83	92.2%, 7.8% Li_2SiO_3	$Li_{2.26}Fe_{0.87}SiO_4$	13% Fe-deficient

[a] The composition of LFS-based phase was determined by the Fe/Si molar ratio, the weight percentage of the phase, and considering charge neutrality.

Figure 5.2a shows the Rietveld refinement result of LFS-stoi refined by the reference structure of *Pmn*2_1 Li_2FeSiO_4. The lattice parameters of LFS-stoi were found to be a = 6.2660 Å, b = 5.34789 Å, c = 4.96323 Å, and V = 166.317 Å^3. Figure 5.2b presents the Rietveld refinement result of LFS-Fe1.2, which contains the highest level of Fe-excess in the products synthesized in this study. The refined lattice parameters of $Li_{1.84}Fe_{1.08}SiO_4$, the dominant phase in LFS-Fe1.2, are a = 6.26762 Å, b = 5.33556 Å, c = 4.96026 Å, and V = 165.878 Å^3. It is also resolved that 8% of Li-sites are partially occupied by Fe, whereas Fe-sites are fully occupied by Fe. Rietveld refinement results of other products are presented in Figure C2 with their corresponding lattice parameters. Figure 5.2c shows the variation of unit cell volumes with the deviation of Fe content from stoichiometry. In the Fe-rich region, the unit cell volume of $Li_{4-2x}Fe_xSiO_4$ decreases as x increases. LFS-Fe1.1 and LFS-Fe1.05 were found to have similar unit cell volume, which gives further evidence that the LFS phase in LFS-Fe1.1 contains the same Fe content as LFS-Fe1.05 (both are 5% Fe-rich) in the compounds. The residual Fe in LFS-Fe1.1 from precursor formed the secondary phase, Fe_2O_3. The shrinkage of unit cell associated with Fe-excess can be attributed to the Li vacancies created by substitution of Fe in Li. These Fe-rich compounds have less cations to be arranged than the available cation sites in the lattice. To keep the charge neutrality, the presence of excess Fe ($x > 1$ in $Li_{4-2x}Fe_xSiO_4$) requires formation of defects with a negative effective charge, which could be a cation vacancy or an excess oxygen on interstitial site. In a close-packed oxygen

sublattice, interstitial oxygen is expected to have a large free energy of formation compared to cation vacancy. Therefore, charge compensation of Fe-excess is most likely to be accomplished by Li^+ vacancies, generating defect pairs $Fe^{\bullet}_{Li} + V'_{Li}$ based on Kröger–Vink notation.[46] The solubility limit of these defect pairs in *Pmn*2$_1$ $Li_{4-2x}Fe_xSiO_4$ prepared by hydrothermal process were found to be approximately 8% as aforementioned. In the case of $LiFePO_4$, the same type of defect pairs (i.e. $Fe^{\bullet}_{Li} + V'_{Li}$) was found to have a concentration limit of 6.8%[30] when synthesized via a room-temperature coprecipitation route with subsequent annealing at 725°C.

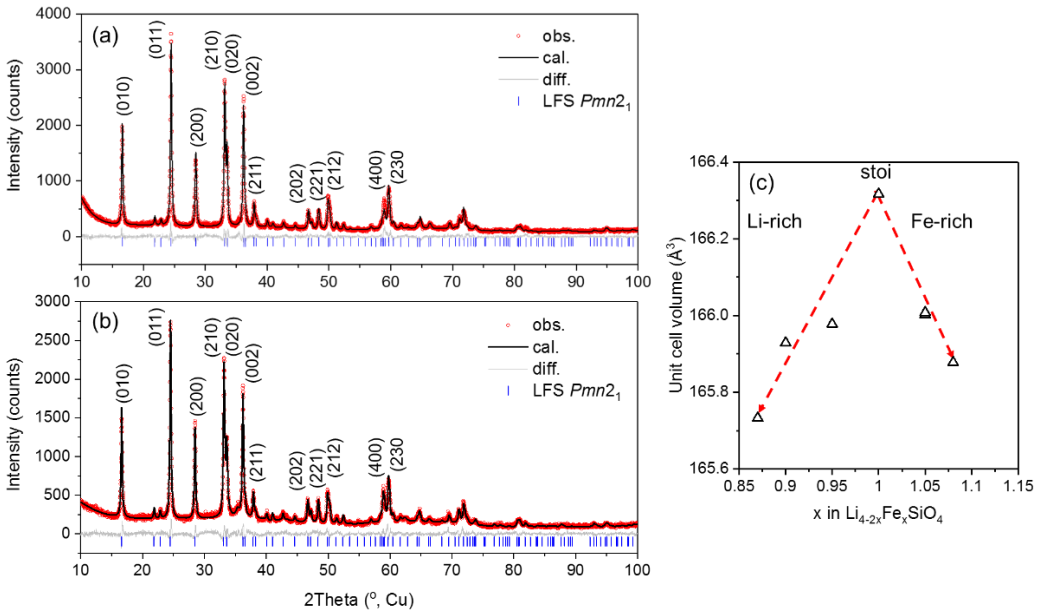

Figure 5.2. (a, b) Rietveld refinement of LFS-stoi and LFS-Fe1.2. Red scatters are experimental XRD results, black lines are calculated XRD results from Rietveld refinement, blue steaks at the bottom belong to reference pattern of *Pmn*2$_1$ Li_2FeSiO_4 (PDF# 01-080-6279), and grey lines are the differences between experimental and calculated results. Miller indices of major peaks are shown on the top. (c) Variation of unit cell volumes of $Li_{4-2x}Fe_xSiO_4$ with *x*. *x* represents the measured amount of Fe in $Li_{4-2x}Fe_xSiO_4$ compounds. Red dashed arrows are shown as a guide for view.

In the Fe-deficient region, the unit cell volume decreases with reducing Fe content (Figure 5.2b). This variation is consistent with that reported by Billaud et al.,[24] in which the unit cell volumes of Li-rich (i.e. Fe-deficient) LFS compounds in both *Pmnb* and *P*2$_1$/*n* phases were found to decrease with reducing Fe content. Because the total number of cations ($Fe^{2+} + Li^+$) is more than the original cation sites, the extra Li may occupy the interstitial Li octahedra sites which are not occupied in the stoichiometric LFS, as pointed out by Billaud et al.[24] The excess in Li could generate defect pairs of Li ions occupying an Fe-site plus an interstitial Li-site, denoted as Li'_{Fe} +

$Li_i^{\bullet}$. The solubility limit of this type of defects in Fe-deficient (Li-excess) $Li_{4-2x}Fe_xSiO_4$ ($x < 1$) in *Pmn*2_1 polymorph is about 13% based on the present study. In comparison, the Li-excess $Li_{4-2x}Fe_xSiO_4$ synthesized at high temperature in a mixed *Pmnb* - *P*2_1/*n* phase was found to accommodate excess Li up to 30%.[24] The larger Li-excess solubility compared to the present study could be attributed to higher processing temperatures that favors the formation of defects as well as the difference in crystal structures.

Figures 5.3a and 5.3d show that LFS-stoi and LFS-Fe1.2 have similar particle size and shape. Under the hydrothermal conditions applied in the present study, LFS with either stoichiometric or Fe-rich composition crystallizes as hollow mesocrystals that are assembled by smaller elongated nanocrystals aligned in the same crystallographic direction. Detailed analyses have been reported in a previous study.[31] High-resolution TEM images (Figures 5.3b, 5.3e) on the edges of particles demonstrate the characteristics of nanocrystals stacking on each other and having the same lattice fringe. The spacing of these lattice fringes is about 3.7 Å, corresponding to the (011) lattice planes in orthorhombic *Pmn*2_1 LFS (Figures 5.3c, 5.3f).

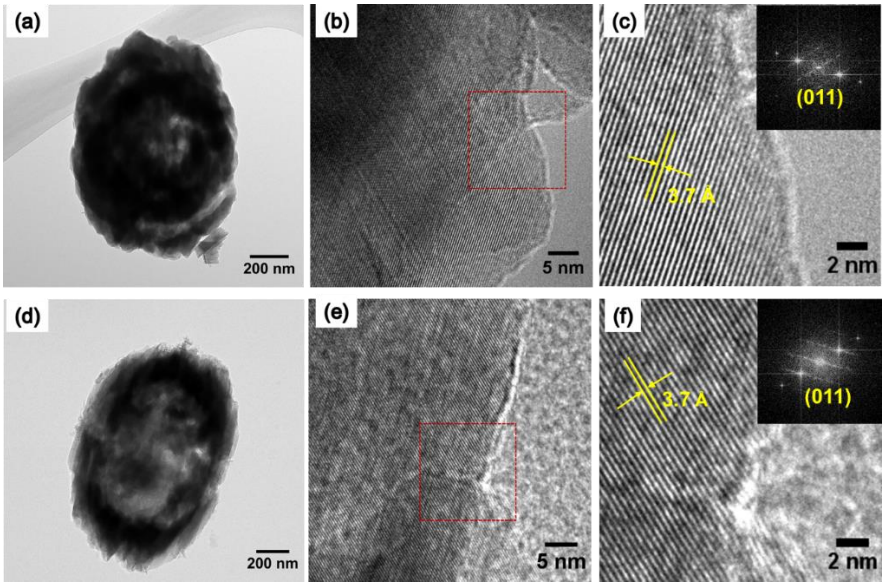

Figure 5.3. TEM and high-resolution TEM images of (a-c) LFS-stoi and (d-f) LFS-Fe1.2. High-resolution TEM images in (c) and (f) show lattice fringes with spacing of 3.7 Å, corresponding to the (011) lattice planes in orthorhombic *Pmn*2_1 LFS. Insets in (c) and (f) are the corresponding FFT patterns.

5.3.2 Electrochemical performance

Figure 5.4 presents the electrochemical performance of LFS-stoi and LFS-Fe1.2 evaluated via galvanostatic charge-discharge measurements. Half cells using Li-metal as the counter and reference electrode were firstly cycled at a low current rate of 0.02 C for 5 cycles, which were followed by cycling at 0.1 C and 1 C for 5 cycles at each rate, and finally at 0.1 C until 50 cycles are completed. As shown in Figure 5.4a, the stoichiometric LFS delivered a discharge capacity of 128.9 mAh g^{-1} in the 5^{th} cycle at 0.02 C (77% of the theoretical capacity), while this value decreased to 92 mAh g^{-1} at 0.1 C and 40.5 mAh g^{-1} at 1 C. The difference between the average charge and discharge voltages increases with the current rate due to increasing overpotential. As a comparison, Fe-rich compound LFS-Fe1.2 (Figure 4b) exhibited discharge capacities of 161.8 mAh g^{-1} (97% of the theoretical capacity), 125.2 mAh g^{-1}, and 65.3 mAh g^{-1}, respectively, at 0.02 C, 0.1 C, and 1 C. From LFS-stoi to LFS-Fe1.2, the discharge capacity increased by 25%, 36%, and 61% at 0.02 C, 0.1 C, and 1 C, respectively. Figure 5.4c presents the cycling performance of LFS-stoi and LFS-Fe1.2. While both cells went through capacity fading, LFS-stoi faded by 33% from the 6^{th} to the 50^{th} cycle at 0.1 C, which is almost double that of LFS-Fe1.2 (17%). The deterioration of capacity upon cycling could be mainly attributed to the side reactions between LFS and the $LiPF_6$-based electrolyte.[47] Nonetheless, Fe-rich LFS-Fe1.2 shows an improved cyclability which can be also confirmed when cycled at 0.02 C for the first 5 cycles (see Figure C3). The improved electrochemical performance of Fe-deficient (namely, Li-rich) LFS vis-à-vis the stoichiometric LFS studied by Billaud et al.[24], had been attributed to enhanced Li-ion transport. However, the Fe-deficient compounds are limited in terms of theoretical specific capacities. Thus the reported capacity of $Li_{2.6}Fe_{0.7}SiO_4$ studied by Billaud et al.,[24] was only ~120 mAh g^{-1} in the first cycle and quickly dropped to 105 mAh g^{-1} between 1.5-3.7 V at 0.06 C rate at 60°C. In this regard the superiority of Fe-rich LFS in terms of intercalation capacity and retention is really remarkable.

One may notice that nanosized LFS in monoclinic $P2_1/n$ structure with conductive carbon coating could deliver capacity corresponding to exchanging over one-electron per formula unit and show better rate capability than what have been achieved in the present study.[48-49] However, it remains unclear whether the extra capacity is from LFS redox activity or electrolyte degradation as such capacity was typically obtained when the cell was charged to a rather high voltage, e.g. 4.8

V vs. Li^+/Li.[50] Using a high-voltage electrolyte is necessary for confirming the achievability of extraction/insertion of more than one Li from/to LFS and the associated charge compensation mechanism.[51] As for the rate capability of stoichiometric or Fe-rich *Pmn*2_1 LFS, there is still room for improvement by surface modification with conductive coating.

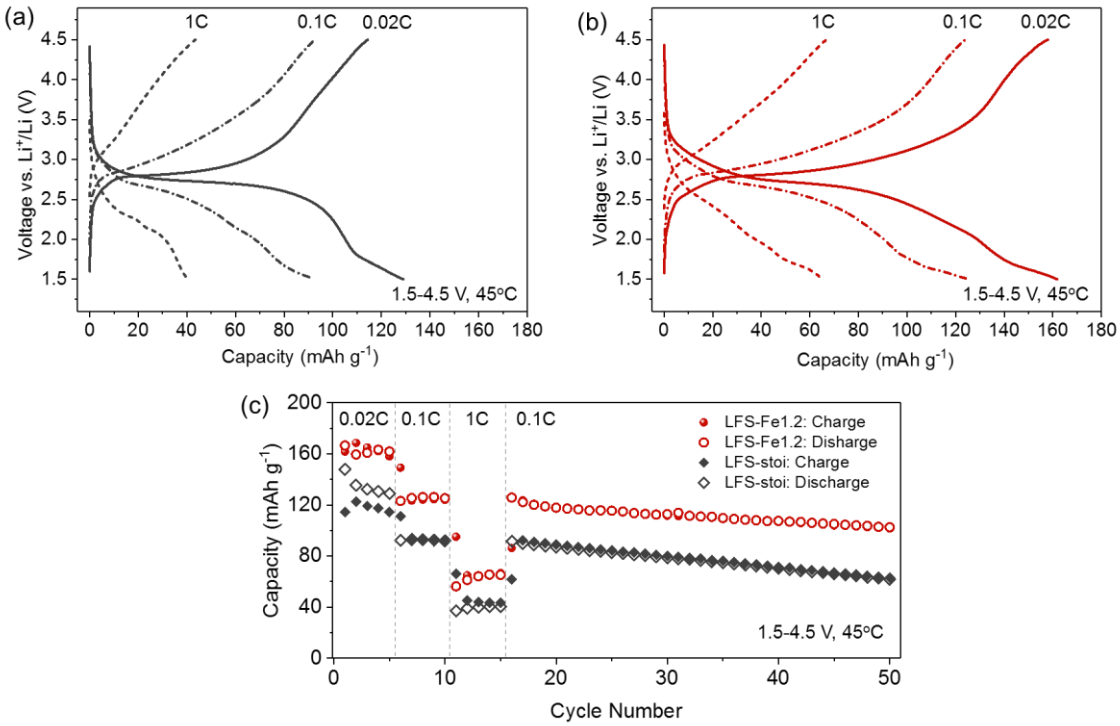

Figure 5.4. Electrochemical performance of LFS-stoi and LFS-Fe1.2. Galvanostatic charge-discharge profiles of (a) LFS-stoi and (b) LFS-Fe1.2 at 0.02 C, 0.1 C, and 1 C cycled from 1.5 V to 4.5 V at 45°C. For clarity, only the fifth cycle at each cycling rate is shown. (c) Cycling performance of LFS-stoi (black) and LFS-Fe1.2 (red) in 50 cycles. Charge capacities are shown in solid symbols whereas discharge capacities are shown in open symbols.

To compare Li diffusion kinetics between LFS-stoi and LFS-Fe1.2, cyclic voltammetry (CV) at different scan rates was performed to determine the apparent chemical diffusion coefficient of Li^+.[52] Figure 5.5a shows CV of LFS-stoi scanned between 2-4.5 V at various rates (0.05-0.5 mV s^{-1}). It is noted that the lower cut-off was chosen at 2 V for CV scans, which is different from the 1.5 V that was applied for galvanostatic charge-discharge tests. One reason is that the peak positions for both oxidation and reduction reactions during CV scans are above 2 V, thus a lower voltage is unnecessary. The other reason is that some unknown cathodic reactions may occur below 1.8 V, as observed in a recent study.[53] Considering that the main purpose of CV tests in the present study is to understand the kinetics of Li-ion diffusion, we chose 2 V as a more appropriate cut-off

voltage. Two oxidation peaks, denoted as I_{A1} and I_{A2}, are observed, with their intensities increasing with the scan rate, while I_{A2} increases faster than I_{A1}. In contrast to the oxidation process, only one peak, denoted as I_C, is seen in the reduction process. This might be explained by different diffusion kinetics between delithiation and lithiation processes, so that lead to different responses in the CV characteristics. LFS-Fe1.2 (Figure 5.5a), although showing some similar features with LFS-stoi, has lower I_{A2}/I_{A1} intensity ratio at all the scan rates. Particularly, at the lowest scan rate 0.05 mV s^{-1}, only I_{A1} is shown up in the oxidation curve of LFS-Fe1.2. Figure 5.5c compares CV of LFS-stoi to that of LFS-Fe1.2 at the same scan rate 0.05 mV s^{-1}. It is clearly shown that LFS-Fe1.2 exhibits more symmetric shape between oxidation and reduction peaks, as opposed to the asymmetric behavior of LFS-stoi, suggesting a better reversibility of Fe-rich LFS. Moreover, LFS-Fe1.2 has larger area under the current curve than LFS-stoi, indicating more capacity can be delivered. This is consistent with the galvanostatic charge-discharge measurements (Figure 5.4). Peak currents of the redox reaction are proportional to the square root of the scan rates if Li^+ diffusion is the rate-determining step, according to Randles-Sevčik equation (equation 1) shown below.[54]

$$I_p = 0.4463 \left(\frac{F^3}{RT}\right)^{1/2} n^{3/2} A D_{Li^+,CV}^{1/2} \Delta C_{Li^+} \upsilon^{1/2} \quad (5.1)$$

where I_p is the peak current (A), υ is the scan rate (V s^{-1}), F is Faraday's constant (96,485 C mol^{-1}), R is the gas constant of 8.314 J K^{-1} mol^{-1}, T is absolute temperature (318.15 K), n is the number of electrons involved in the redox reaction (n = 1 for Fe^{2+}/Fe^{3+}), and A is the surface area of the electrode (0.785 cm^2). ΔC_{Li^+} is the change in concentration of Li^+ before and after a sweep, which is approximately 0.0185 mol/cm^3 for either the anodic or the cathodic reaction assuming a complete one Li^+ insertion/extraction reaction per formula unit. $D_{Li^+,CV}$ is the chemical diffusion coefficient of Li^+ (cm^2 s^{-1}) determined by CV.

The calculated values of $D_{Li^+,CV}$ are listed in Table 5.2. For both anodic and cathodic reactions, $D_{Li^+,CV}$ of LFS-Fe1.2 are larger than those of LFS-stoi. This indicates that the diffusion kinetics during lithiation and delithiation are enhanced by introducing excess Fe in the crystal lattice. It should be mentioned that the value of $D_{Li^+,CV}$ determined by CV method represents an average performance of the whole lithiation/delithiation process. Using the same determination method, the calculated $D_{Li^+,CV}$ of LFS-Fe1.2 (5.96×10^{-11} cm^2 s^{-1} to 9.48×10^{-12} cm^2 s^{-1}) is higher

than that reported on 3DOM LFS/C composite (1.17 $\times 10^{-12}$ cm^2 s^{-1})[48] and LFS/C nanocrystals (~6 $\times 10^{-12}$ cm^2 s^{-1})[55].

Table 5.2. Calculated chemical diffusion coefficient $D_{Li^+,CV}$ of LFS-stoi and LFS-Fe1.2 based on cyclic voltammetry

Electrode	Peak	Slope of I_p vs. $v^{1/2}$	$D_{Li^+,CV}$, cm^2 s^{-1}
LFS-stoi	I_{A1}	0.0057	2.28×10^{-13}
	I_{A2}	0.0090	5.69×10^{-12}
	I_C	0.0118	9.68×10^{-12}
LFS-Fe1.2	I_{A1}	0.0200	9.48×10^{-12}
	I_{A2}	0.0246	1.44×10^{-11}
	I_C	0.0285	5.69×10^{-11}

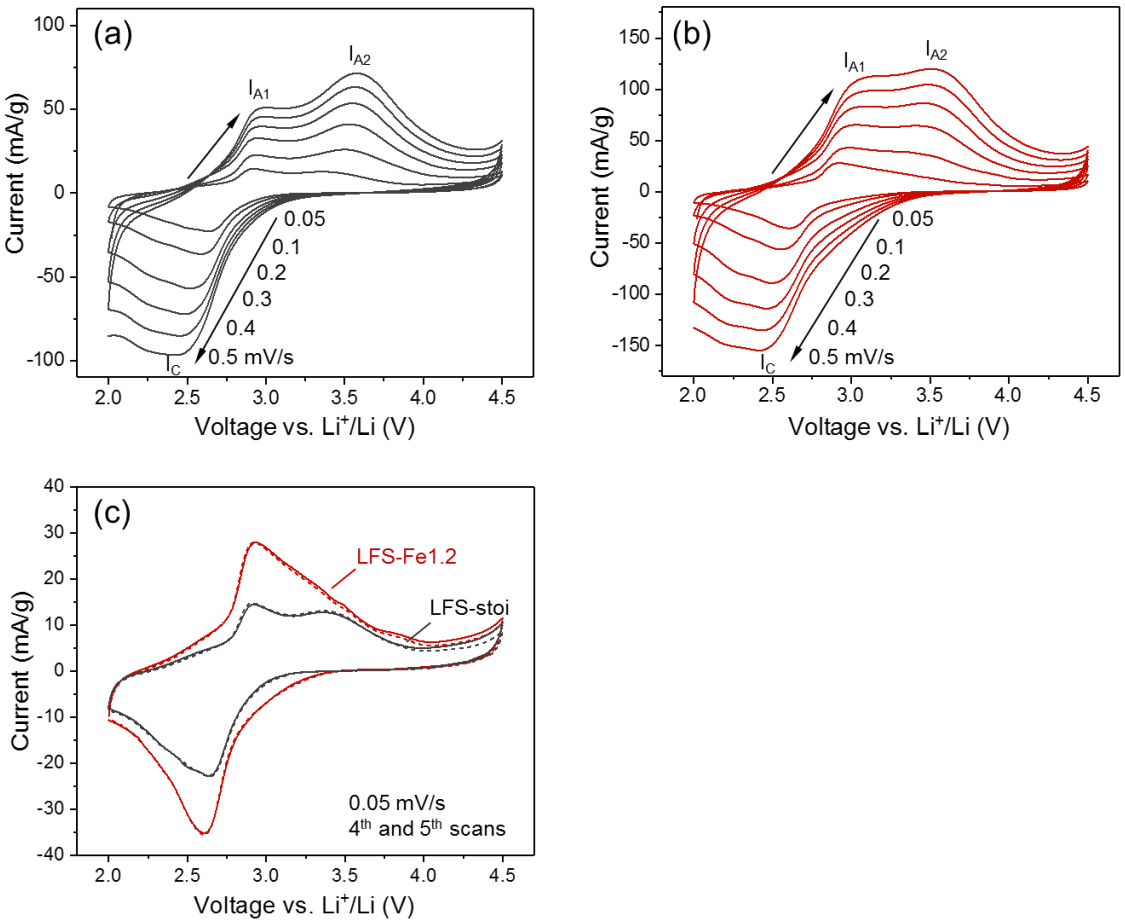

Figure 5.5. Cyclic voltammograms (CVs) of (a) LFS-stoi and (b) LFS-Fe1.2 between 2-4.5 V at scan rates from 0.05 to 0.5 mV s^{-1}. (c) Comparison of CVs between LFS-stoi and LFS-Fe1.2 scanned at 0.05 mV s^{-1}. Solid line represents the 4th scan while dashed line represents the 5th scan.

Galvanostatic intermittent titration technique (GITT) was conducted to gain insights into the diffusion kinetics at different Li^+ compositions and the difference between delithiation and lithiation processes in LFS-stoi and LFS-Fe1.2. The GITT curves show considerably less voltage polarization (voltage relaxation after each charge or discharge step) in LFS-Fe1.2 (Figure 5.6b) than in LFS-stoi (Figure 5.6a), particularly at the beginning of charging. This suggests that the mass-transfer resistance of Li^+ is decreased in the Fe-rich compound. For both cells, the largest polarization was observed at the end of charge and discharge. In the end of the first charge process, 1.1 Li was extracted from LFS-Fe1.2, whereas less than 0.8 Li was extracted from LFS-stoi. In addition, more Li ions were inserted back to LFS-stoi that those extracted, indicating that the pristine LFS-stoi material may have been partially oxidized due to exposure to air during handling or to spontaneous reaction with the electrolyte.[56]

The chemical diffusion coefficient of Li^+ can be deduced from GITT according to the following equation:[57-59]

$$D_{Li^+,GITT} = \frac{4}{\pi}\left(\frac{IV_M}{ZFS}\right)^2 \left[\frac{dE(x)}{dx} \Big/ \frac{dE(t)}{dt^{0.5}}\right]^2 \qquad (t \ll L^2/D_{Li^+,GITT}) \qquad (5.2)$$

where I is the applied current (A), V_M is the molar volume of the electrode material (about 54 cm^3/mol for Li_2FeSiO_4), Z is the charge number of active species ($Z = 1$ for Li^+), F is the Faraday's constant (96,485 C mol^{-1}), S is the electrochemical active area between the electrode and electrolyte (cm^2) that can be estimated by BET surface area measurements (21 $m^2\ g^{-1}$ for both products). $\frac{dE(x)}{dx}$ is the change of the steady-state voltage versus the change of Li^+ composition. $E(t)$ is the transient voltage during the constant current intervals, t is the time (s) when current is applied, and L is the characteristic length (cm) of the electrode material. The value of $\frac{dE(t)}{dt^{0.5}}$ was determined from the slope of the linear part of E versus $t^{0.5}$ in the fisrt 10 to 100 s after applying a current pulse. This time domain corresponds to the diffusion process.[60-61]

It should be noted that the employment of equation (2) in solving the chemical diffusion coefficient depends on multiple assumptions.[52, 62] Therefore, deviation of the investigated electrochemical system from the assumptions may lead to inaccuracy in the obtained values of $D_{Li^+,GITT}$ for the studied electrochemical system. Nevertheless, the scope of applying CV and GITT measurements in this study is not to quantify the absolute values of diffusivity, but rather to

characterize the impact of Fe-rich composition on Li diffusion kinetics in comparison to that of the stoichiometric LFS. The variation of $D_{Li^+,GITT}$ with the LFS composition is presented in Figure 5.6c. As it can be seen, $D_{Li^+,GITT}$ ranges from apporximately 10^{-17} to 10^{-22} cm^2 s^{-1} for LFS-Fe1.2, while is as low as 10^{-23} to 10^{-27} cm^2 s^{-1} for LFS-stoi. These results indicate that Fe-rich composition enhances the mass transfer of Li^+. This could be attributed to the presence of Li-vacancy sites generated by introducing extra Fe. These vacancies facilitate the transport of Li^+, particularly in the beginning of charge when the lattice is supposed to be fully occupied in the stoichiometric LFS.

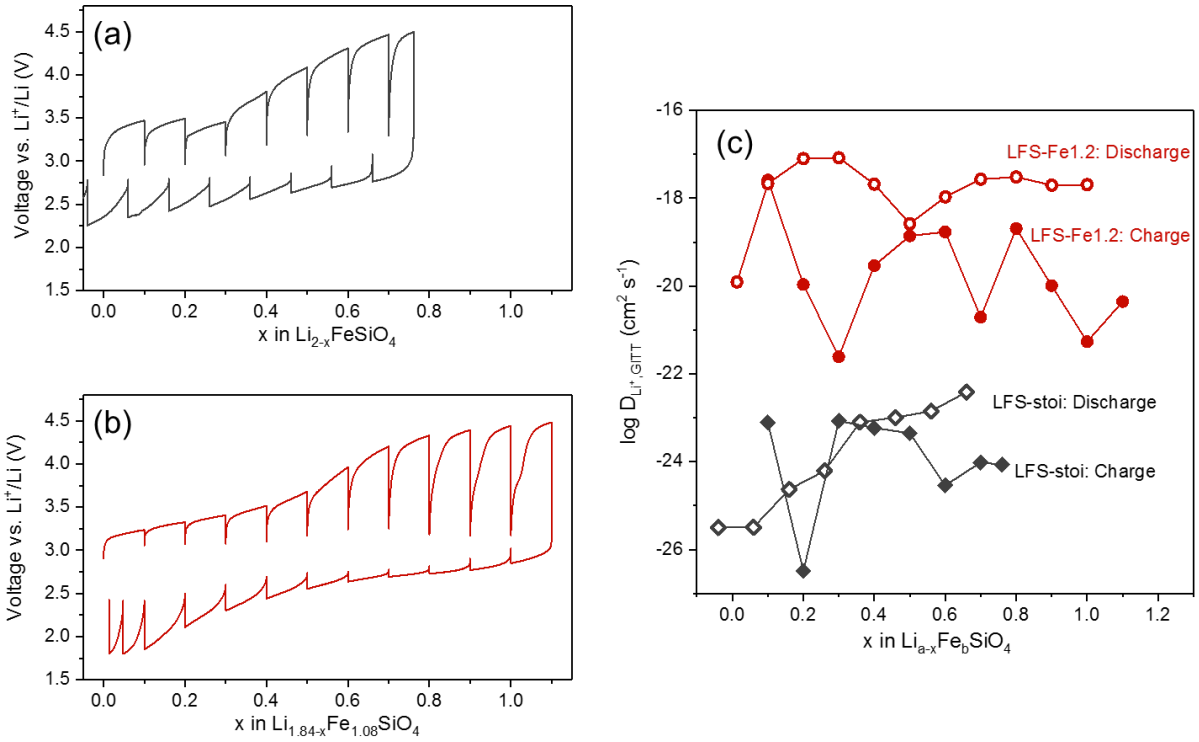

Figure 5.6. (a, b) GITT curves of the first charge-discharge cycle of LFS-stoi and LFS-Fe1.2. (c) Calculated diffusion coefficients $D_{Li^+,GITT}$ for the first charge (solid symbols) and discharge (open symbols) cycle based on GITT measurements. For LFS-stoi, a = 2 and b = 1; for LFS-Fe1.2, a = 1.84 and b = 1.08.

5.3.3 Electronic structure and Fe migration

In order to understand the influence of non-stoichiometry on the electronic structure of Fe-rich LFS, the projected density of states (PDOS) are calculated by DFT. The exact PDOS of LFS and Fe-rich LFS plotted in Figures 5.7a and 5.7b show a distinct gap between the conduction band minimum (CBM) and the valence band maximum (VBM). To make a direct comparison, PDOS

of the two materials are merged in the same figure (Figure 5.7c). For clarity, PDOS of majority and minority spins are summed up while the energy of Fermi level is placed on the top of the VBM of both materials. It should be noted that as we are trying to visualize the difference of energy level alignment, the absolute value of energy level does not matter. As indicated in Figure 5.7c, the bandgap of Fe-rich LFS (2.6 eV) is narrower than that of stoichiometric LFS (3.1 eV), mainly attributed to the emergence of a new peak at the conduction band. By projecting the charge density into the highlighted region of PDOS, it is clearly shown in Figures 5.7c and 5.7d that the new electron states in the conduction band originate from the $Fe_{Li}^{\bullet}$ defect and its immediate neighboring Fe atoms. These findings clearly demonstrate that $Fe_{Li}^{\bullet}$ defects in Fe-rich LFS are responsible for narrowing the bandgap of LFS. This is further confirmed by the darker color of the as-synthesized Fe-rich powders (LFS-Fe1.2) than the beige LFS-stoi, shown in the insets in Figures 5.7a and 5.7b.

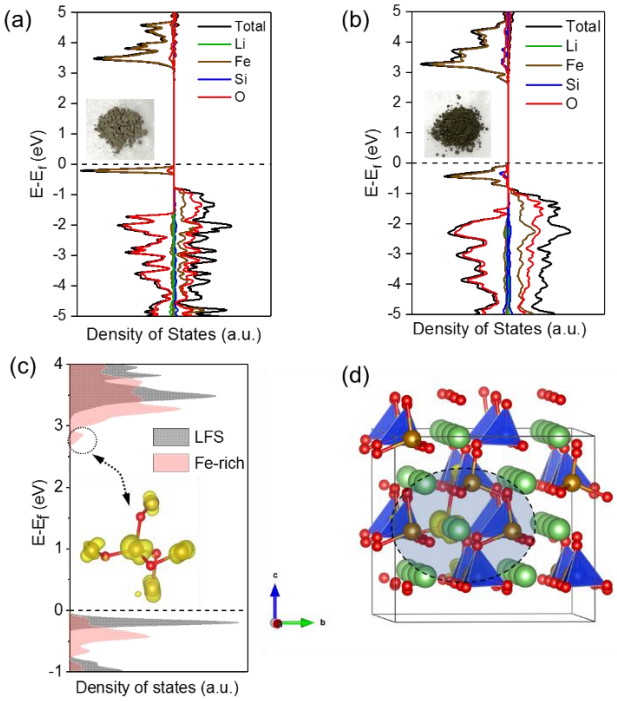

Figure 5.7. Effect of local Fe-rich configuration on the electronic structure of LFS. (a) Projected density of states (PDOS) of stoichiometric LFS. (b) PDOS of Fe-rich LFS. Insets in (a) and (b) are the corresponding images of the as-synthesized powders of LFS-stoi and LFS-Fe1.2. (c) Merged PDOS of LFS and Fe-rich LFS. Insect in (c) is the isosurface of the charge density around Fe–O–Fe coordination in Fe-rich LFS, which is found to contribute to the highlighted peak in the conduction band close to the Fermi level. (d) Atomic configuration of Fe-rich LFS (orthorhombic *Pmn*2_1) with highlighted region corresponding to the Fe–O–Fe coordination shown in (c).

During the initial charge-discharge, LFS experiences phase transformation to a new cycled phase associated with a ~0.3 V voltage drop.[16-17, 41] This phase transformation has been proposed to be triggered by Fe migration to Li-site. When all the Fe migrate to Li-site, the re-intercalated Li will occupy the Fe-site to form a new phase such as the so called inverse $Pmn2_1$. Thus, Fe migration is an important factor to understand the behavior of LFS upon cycling. Transition metal migration is also a key characteristic in other Li-containing compounds that affects their structural stability and Li storage kinetics.[63-65] Here, DFT calculations are performed to evaluate the change of Fe migration barrier in different local environments. The minimum diffusion pathways of Fe are demonstrated in Figures 5.8a and 5.8b respectively for LFS and Fe-rich LFS. The energy evolution during Fe migration is demonstrated in Figure 5.8c. As can be inferred from Figure 8c, the activation barrier of Fe migration in LFS is about 1.18 eV, whereas when comes to Fe-rich LFS, this barrier diminishes to 0.64 eV. The reduction of Fe activation barrier can be attributed to the presence of extra Fe and Li vacancies. By comparing Figure 5.8a with 5.8b, it shows that one of the immediate neighboring Li at the initial state of Fe migration is replaced by Fe as a result of non-stoichiometry. This results in a greater electrostatic repulsion that would destabilize the initial state. Similarly, the transition state and the final state would be stabilized by the adjacent Li-vacancy due to less electrostatic repulsion. As the Fe migration barrier is lowered, the phase transformation towards the cycled structure would be facilitated consuming less energy for the migration process.

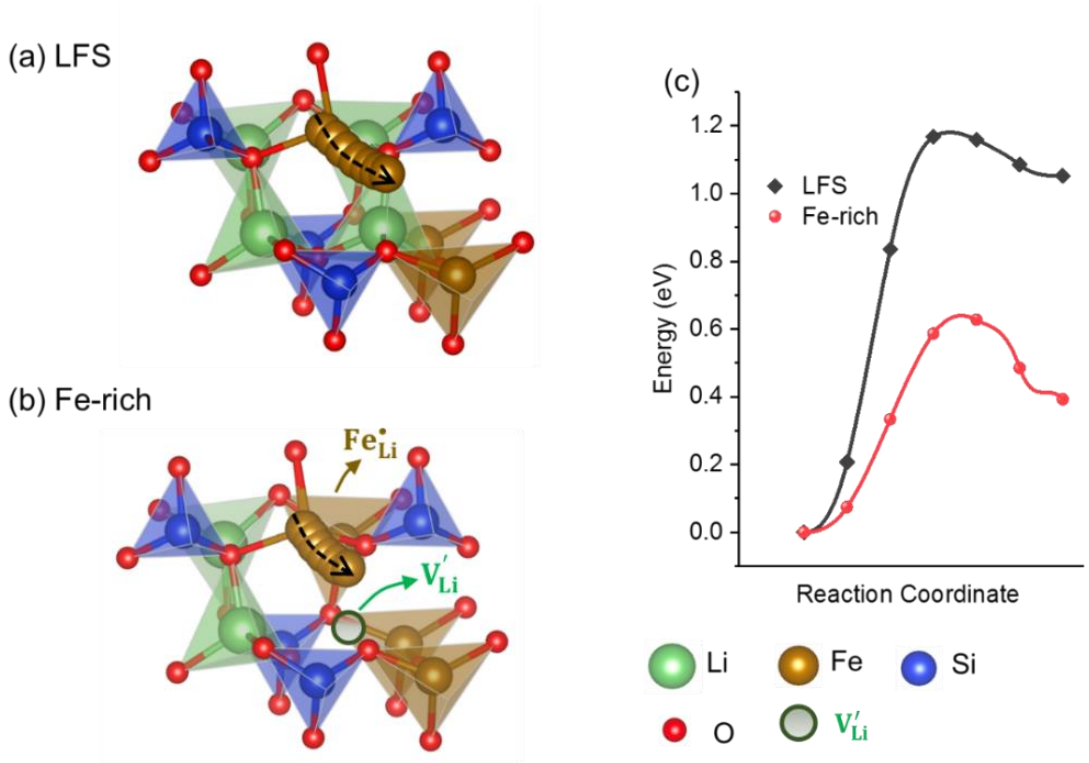

Figure 5.8. (a) and (b) Fe migration paths in LFS and Fe-rich LFS and (c) the corresponding energy barriers. The simulation is based on crystal structures in which one Li is extracted from a 2×2×2 supercell (i.e. $Li_{32}Fe_{16}Si_{16}O_{64}$ for LFS, $Li_{30}Fe_{17}Si_{16}O_{64}$ for Fe-rich LFS). Fe migrates from a Fe-site to an adjacent Li-site. In Fe-rich LFS, an antisite defect $Fe_{Li}^{\bullet}$ and a Li-vacancy V_{Li}' are pointed out.

5.5 Conclusions

Non-stoichiometric $Li_{4-2x}Fe_xSiO_4$ compounds were synthesized via hydrothermal method by varying the concentration ratio of precursors. Pure 5% Fe-rich and pure 10% Fe-deficient (Li-rich) compounds in *Pmn*2_1 structure were obtained, while higher extent of Fe-rich and Fe-deficiency resulted in the formation of secondary phases of Fe_2O_3 and Li_2SiO_3, respectively, as indicated by XRD. Rietveld refinement combined with compositional analyses revealed that the solubility limits of Fe-rich and Fe-deficiency in *Pmn*2_1 LFS are about 8% and 13% under the applied hydrothermal synthesis condition. As a result of Fe-rich composition, the formation of $Fe_{Li}^{\bullet} + V_{Li}'$ defect pair was induced which in turn leads to improvement of electrochemical performance in terms of higher capacity and facilitated Li^+ transport. This thesis was corroborated from the galvanostatic charge-discharge measurements that showed the Fe-rich LFS delivering higher capacity than the stoichiometric LFS from low to high current rates (161.8 mAh g^{-1} versus

128.9 mAh g^{-1} at 0.02 C, 65.3 mAh g^{-1} versus 40.5 mAh g^{-1} at 1 C). Furthermore, enhanced diffusion kinetics in Fe-rich LFS were observed by CV and GITT. First-principles DFT calculations revealed that the bandgap of LFS was narrowed from 3.1 eV to 2.6 eV by introducing excess Fe that generates local Fe–O–Fe configuration. In addition, the energy barrier for Fe migration to Li-site was found to be diminished in the Fe-rich compound thus facilitating phase transformation from $Pmn2_1$ towards the electrochemically cycled inverse $Pmn2_1$ phase. This study shows that the electrochemical performance of LFS can be largely improved by compositional engineering. Future work could be undertaken to investigate the effect of Fe-rich or Li-rich on the capacity beyond Fe^{2+}/Fe^{3+} redox reaction if a compatible and stable high-voltage electrolyte is available. It would be also interesting to synthesize LFS with even higher Fe-rich composition to further increase the Fe^{2+}/Fe^{3+} based capacity (e.g. 203 mAh g^{-1} for 33.3% Fe-rich) if the solubility limit can be elevated.

5.6 Acknowledgements

This work is funded by a Hydro-Québec/Natural Sciences & Engineering Research Council of Canada (NSERC) Collaborative R&D research grant (463484-2014). YZ and GPD acknowledge additional support by McGill Engineering International Tuition Award (MEITA) and McGill Sustainability Systems Initiative (MSSI) programs.

5.7 References

1. Etacheri, V.; Marom, R.; Elazari, R.; Salitra, G.; Aurbach, D., Challenges in the development of advanced Li-ion batteries: a review. *Energy & Environmental Science* **2011,** *4* (9), 3243-3262.

2. Li, M.; Lu, J.; Chen, Z.; Amine, K., 30 Years of Lithium-Ion Batteries. *Adv Mater* **2018,** *0* (0), e1800561.

3. Seo, D.-H.; Lee, J.; Urban, A.; Malik, R.; Kang, S.; Ceder, G., The structural and chemical origin of the oxygen redox activity in layered and cation-disordered Li-excess cathode materials. *Nature Chemistry* **2016,** *8*, 692.

4. Rozier, P.; Tarascon, J. M., Review—Li-Rich Layered Oxide Cathodes for Next-Generation Li-Ion Batteries: Chances and Challenges. *Journal of The Electrochemical Society* **2015,** *162* (14), A2490-A2499.

5. Nayak, P. K.; Erickson, E. M.; Schipper, F.; Penki, T. R.; Munichandraiah, N.; Adelhelm, P.; Sclar, H.; Amalraj, F.; Markovsky, B.; Aurbach, D., Review on Challenges and Recent Advances in the Electrochemical Performance of High Capacity Li- and Mn-Rich Cathode Materials for Li-Ion Batteries. *Advanced Energy Materials* **2018,** *8* (8), 1702397.

6. Lun, Z.; Ouyang, B.; Kitchaev, D. A.; Clément, R. J.; Papp, J. K.; Balasubramanian, M.; Tian, Y.; Lei, T.; Shi, T.; McCloskey, B. D.; Lee, J.; Ceder, G., Improved Cycling Performance of Li-Excess Cation-Disordered Cathode Materials upon Fluorine Substitution. *Advanced Energy Materials* **2019,** *9* (2), 1802959.

7. Li, X.; Qiao, Y.; Guo, S.; Jiang, K.; Ishida, M.; Zhou, H., A New Type of Li-Rich Rock-Salt Oxide $Li_2Ni_{1/3}Ru_{2/3}O_3$ with Reversible Anionic Redox Chemistry. *Advanced Materials* **2019,** *31* (11), 1807825.

8. Li, X.; Qiao, Y.; Guo, S.; Xu, Z.; Zhu, H.; Zhang, X.; Yuan, Y.; He, P.; Ishida, M.; Zhou, H., Direct Visualization of the Reversible O^{2-}/O^{-} Redox Process in Li-Rich Cathode Materials. *Advanced Materials* **2018,** *30* (14), 1705197.

9. Nytén, A.; Abouimrane, A.; Armand, M.; Gustafsson, T.; Thomas, J. O., Electrochemical performance of Li_2FeSiO_4 as a new Li-battery cathode material. *Electrochemistry Communications* **2005,** *7* (2), 156-160.

10. Ni, J.; Jiang, Y.; Bi, X.; Li, L.; Lu, J., Lithium Iron Orthosilicate Cathode: Progress and Perspectives. *ACS Energy Letters* **2017,** *2* (8), 1771-1781.

11. Islam, M. S.; Dominko, R.; Masquelier, C.; Sirisopanaporn, C.; Armstrong, A. R.; Bruce, P. G., Silicate cathodes for lithium batteries: alternatives to phosphates? *Journal of Materials Chemistry* **2011,** *21* (27), 9811-9818.

12. Mali, G.; Sirisopanaporn, C.; Masquelier, C.; Hanzel, D.; Dominko, R., Li_2FeSiO_4 polymorphs probed by Li-6 MAS NMR and Fe-57 Mössbauer spectroscopy. *Chemistry of Materials* **2011,** *23* (11), 2735-2744.

13. Arroyo-de Dompablo, M. E.; Armand, M.; Tarascon, J. M.; Amador, U., On-demand design of polyoxianionic cathode materials based on electronegativity correlations: An exploration of the Li_2MSiO_4 system (M = Fe, Mn, Co, Ni). *Electrochemistry Communications* **2006,** *8* (8), 1292-1298.

14. Dominko, R., Li_2MSiO_4 (M=Fe and/or Mn) cathode materials. *Journal of Power Sources* **2008,** *184* (2), 462-468.

15. Liivat, A.; Thomas, J. O., Li-ion migration in Li_2FeSiO_4-related cathode materials: A DFT study. *Solid State Ionics* **2011,** *192* (1), 58-64.

16. Seo, D.-H.; Kim, H.; Park, I.; Hong, J.; Kang, K., Polymorphism and phase transformations of $Li_{2-x}FeSiO_4$ ($0 \leqslant x \leqslant 2$) from first principles. *Physical Review B* **2011,** *84* (22), 220106.

17. Armstrong, A. R.; Kuganathan, N.; Islam, M. S.; Bruce, P. G., Structure and lithium transport pathways in Li_2FeSiO_4 cathodes for lithium batteries. *Journal of the American Chemical Society* **2011,** *133* (33), 13031-13035.

18. Islam, M. S.; Driscoll, D. J.; Fisher, C. A. J.; Slater, P. R., Atomic-scale investigation of defects, dopants, and lithium transport in the $LiFePO_4$ olivine-type battery material. *Chemistry of Materials* **2005,** *17* (20), 5085-5092.

19. Clark, J. M.; Eames, C.; Reynaud, M.; Rousse, G.; Chotard, J.-N.; Tarascon, J.-M.; Islam, M. S., High voltage sulphate cathodes $Li_2M(SO_4)_2$ (M = Fe, Mn, Co): atomic-scale studies of lithium diffusion, surfaces and voltage trends. *Journal of Materials Chemistry A* **2014,** *2* (20), 7446-7453.

20. Zaghib, K.; Mauger, A.; Goodenough, J. B.; Gendron, F.; Julien, C. M., Electronic, optical, and magnetic properties of $LiFePO_4$: Small magnetic polaron effects. *Chemistry of Materials* **2007,** *19* (15), 3740-3747.

21. Zheng, J.; Teng, G.; Yang, J.; Xu, M.; Yao, Q.; Zhuo, Z.; Yang, W.; Liu, Q.; Pan, F., Mechanism of exact transition between cationic and anionic redox activities in cathode material Li_2FeSiO_4. *The Journal of Physical Chemistry Letters* **2018,** *9* (21), 6262-6268.

22. Kieu My, B.; Van An, D.; Takahisa, O., Diffusion mechanism of polaron–Li vacancy complex in cathode material Li_2FeSiO_4. *Applied Physics Express* **2012,** *5* (12), 125802.

23. Lu, X.; Chiu, H.-C.; Bevan, K. H.; Jiang, D.-T.; Zaghib, K.; Demopoulos, G. P., Density functional theory insights into the structural stability and Li diffusion properties of monoclinic and orthorhombic Li2FeSiO4 cathodes. *Journal of Power Sources* **2016,** *318*, 136-145.

24. Billaud, J.; Eames, C.; Tapia-Ruiz, N.; Roberts, M. R.; Naylor, A. J.; Armstrong, A. R.; Islam, M. S.; Bruce, P. G., Evidence of enhanced ion transport in Li-rich silicate intercalation materials. *Advanced Energy Materials* **2017**, 1601043.

25. Zhou, H.; Einarsrud, M.-A.; Vullum-Bruer, F., High capacity nanostructured $Li_2Fe_xSiO_4$/C with Fe hyperstoichiometry for Li-ion batteries. *Journal of Power Sources* **2013,** *235*, 234-242.

26. Fleischmann, S.; Mancini, M.; Axmann, P.; Golla-Schindler, U.; Kaiser, U.; Wohlfahrt-Mehrens, M., Insights into the impact of impurities and non-stoichiometric effects on the electrochemical performance of Li_2MnSiO_4. *Chemsuschem* **2016,** *9* (20), 2982-2993.

27. Zaghib, K.; Guerfi, A.; Hovington, P.; Vijh, A.; Trudeau, M.; Mauger, A.; Goodenough, J. B.; Julien, C. M., Review and analysis of nanostructured olivine-based lithium recheargeable batteries: Status and trends. *Journal of Power Sources* **2013,** *232*, 357-369.

28. Jensen, K. M. Ø.; Christensen, M.; Gunnlaugsson, H. P.; Lock, N.; Bøjesen, E. D.; Proffen, T.; Iversen, B. B., Defects in hydrothermally synthesized $LiFePO_4$ and $LiFe_{1-x}Mn_xPO_4$ cathode materials. *Chemistry of Materials* **2013,** *25* (11), 2282-2290.

29. Sirisopanaporn, C.; Masquelier, C.; Bruce, P. G.; Armstrong, A. R.; Dominko, R., Dependence of Li_2FeSiO_4 electrochemistry on structure. *Journal of the American Chemical Society* **2011,** *133* (5), 1263-1265.

30. Axmann, P.; Stinner, C.; Wohlfahrt-Mehrens, M.; Mauger, A.; Gendron, F.; Julien, C. M., Nonstoichiometric $LiFePO_4$: Defects and related properties. *Chemistry of Materials* **2009,** *21* (8), 1636-1644.

31. Zeng, Y.; Chiu, H.-C.; Rasool, M.; Brodusch, N.; Gauvin, R.; Jiang, D.-T.; Ryan, D. H.; Zaghib, K.; Demopoulos, G. P., Hydrothermal crystallization of *Pmn*2_1 Li_2FeSiO_4 hollow mesocrystals for Li-ion cathode application. *Chemical Engineering Journal* **2019,** *359*, 1592-1602.

32. Kresse, G.; Furthmüller, J., Efficient iterative schemes for ab initio total-energy calculations using a plane-wave basis set. *Physical Review B* **1996,** *54* (16), 11169-11186.

33. Kresse, G.; Joubert, D., From ultrasoft pseudopotentials to the projector augmented-wave method. *Physical Review B* **1999,** *59* (3), 1758-1775.

34. Perdew, J. P.; Burke, K.; Ernzerhof, M., Generalized gradient approximation made simple. *Phys Rev Lett* **1996,** *77* (18), 3865-3868.

35. Jain, A.; Ong, S. P.; Hautier, G.; Chen, W.; Richards, W. D.; Dacek, S.; Cholia, S.; Gunter, D.; Skinner, D.; Ceder, G.; Persson, K. A., Commentary: The Materials Project: A materials genome approach to accelerating materials innovation. *APL Materials* **2013,** *1* (1), 011002.

36. Zhou, F.; Cococcioni, M.; Marianetti, C. A.; Morgan, D.; Ceder, G., First-principles prediction of redox potentials in transition-metal compounds with LDA+*U*. *Physical Review B* **2004,** *70* (23), 235121.

37. Hohenberg, P.; Kohn, W., Inhomogeneous Electron Gas. *Physical Review* **1964,** *136* (3B), B864-B871.

38. Sheppard, D.; Terrell, R.; Henkelman, G., Optimization methods for finding minimum energy paths. *J. Chem. Phys* **2008,** *128* (13), 134106.

39. Henkelman, G.; Uberuaga, B. P.; Jónsson, H., A climbing image nudged elastic band method for finding saddle points and minimum energy paths. *J. Chem. Phys* **2000,** *113* (22), 9901-9904.

40. Olsen, R. A.; Kroes, G. J.; Henkelman, G.; Arnaldsson, A.; Jónsson, H., Comparison of methods for finding saddle points without knowledge of the final states. *J. Chem. Phys* **2004,** *121* (20), 9776-9792.

41. Eames, C.; Armstrong, A. R.; Bruce, P. G.; Islam, M. S., Insights into changes in voltage and structure of Li_2FeSiO_4 polymorphs for lithium-ion batteries. *Chemistry of Materials* **2012,** *24* (11), 2155-2161.

42. Ong, S. P.; Wang, L.; Kang, B.; Ceder, G., Li−Fe−P−O_2 Phase Diagram from First Principles Calculations. *Chemistry of Materials* **2008,** *20* (5), 1798-1807.

43. Bianchini, M.; Wang, J.; Clément, R.; Ceder, G., A First-Principles and Experimental Investigation of Nickel Solubility into the P2 Na_xCoO_2 Sodium-Ion Cathode. *Advanced Energy Materials* **2018,** *8* (26), 1801446.

44. Persson, K. A.; Waldwick, B.; Lazic, P.; Ceder, G., Prediction of solid-aqueous equilibria: Scheme to combine first-principles calculations of solids with experimental aqueous states. *Physical Review B* **2012,** *85* (23), 235438.

45. Walle, C. G. V. d.; Neugebauer, J., First-principles calculations for defects and impurities: Applications to III-nitrides. *Journal of Applied Physics* **2004,** *95* (8), 3851-3879.

46. Kröger, F. A.; Vink, H. J., Relations between the Concentrations of Imperfections in Crystalline Solids. In *Solid State Physics*, Seitz, F.; Turnbull, D., Eds. Academic Press: 1956; Vol. 3, pp 307-435.

47. Li, W.; Dolocan, A.; Oh, P.; Celio, H.; Park, S.; Cho, J.; Manthiram, A., Dynamic behaviour of interphases and its implication on high-energy-density cathode materials in lithium-ion batteries. *Nat Commun* **2017,** *8*, 14589.

48. Ding, Z.; Liu, J.; Ji, R.; Zeng, X.; Yang, S.; Pan, A.; Ivey, D. G.; Wei, W., Three-dimensionally ordered macroporous Li_2FeSiO_4/C composite as a high performance cathode for advanced lithium ion batteries. *Journal of Power Sources* **2016,** *329*, 297-304.

49. Masese, T.; Tassel, C.; Orikasa, Y.; Koyama, Y.; Arai, H.; Hayashi, N.; Kim, J.; Mori, T.; Yamamoto, K.; Kobayashi, Y.; Kageyama, H.; Ogumi, Z.; Uchimoto, Y., Crystal structural changes and charge compensation mechanism during two lithium extraction/insertion between Li_2FeSiO_4 and $FeSiO_4$. *The Journal of Physical Chemistry C* **2015,** *119* (19), 10206-10211.

50. Liivat, A.; Thomas, J.; Guo, J.; Yang, Y., Novel insights into higher capacity from the Li-ion battery cathode material Li_2FeSiO_4. *Electrochimica Acta* **2017,** *223*, 109-114.

51. Zhang, C., High-voltage electrolytes. *Nature Energy* **2019,** *4* (5), 350-350.

52. Yang, X.; Rogach, A. L., Electrochemical Techniques in Battery Research: A Tutorial for Nonelectrochemists. *Advanced Energy Materials* **2019,** *9* (25), 1900747.

53. Zeng, Y.; Chiu, H.-C.; Ouyang, B.; Song, J.; Zaghib, K.; Demopoulos, G. P., Unveiling the mechanism of improved capacity retention in *Pmn*2_1 Li_2FeSiO_4 cathode by cobalt substitution. *Journal of Materials Chemistry A* **2019,** *7* (44), 25399-25414.

54. Elgrishi, N.; Rountree, K. J.; McCarthy, B. D.; Rountree, E. S.; Eisenhart, T. T.; Dempsey, J. L., A practical beginner's guide to cyclic voltammetry. *Journal of Chemical Education* **2018,** *95* (2), 197-206.

55. Qu, L.; Liu, Y.; Fang, S.; Yang, L.; Hirano, S.-i., Li_2FeSiO_4 coated by sorbitanlaurat-derived carbon as cathode of high-performance lithium-ion battery. *Electrochimica Acta* **2015,** *163*, 123-131.

56. Arthur, Z.; Chiu, H.-C.; Lu, X.; Chen, N.; Emond, V.; Zaghib, K.; Jiang, D.-T.; Demopoulos, G. P., Spontaneous reaction between an uncharged lithium iron silicate cathode and a $LiPF_6$-based electrolyte. *Chemical communications* **2016,** *52* (1), 190-193.

57. Wen, C. J.; Boukamp, B. A.; Huggins, R. A.; Weppner, W., Thermodynamic and Mass Transport Properties of "LiAl" *Journal of The Electrochemical Society* **1979,** *126* (12), 2258-2266.

58. Amin, R.; Chiang, Y.-M., Characterization of electronic and ionic transport in $Li_{1-x}Ni_{0.33}Mn_{0.33}Co_{0.33}O_2$ (NMC333) and $Li_{1-x}Ni_{0.50}Mn_{0.20}Co_{0.30}O_2$ (NMC523) as a function of Li content. *Journal of The Electrochemical Society* **2016,** *163* (8), A1512-A1517.

59. Shen, Z.; Cao, L.; Rahn, C. D.; Wang, C.-Y., Least Squares Galvanostatic Intermittent Titration Technique (LS-GITT) for Accurate Solid Phase Diffusivity Measurement. *Journal of The Electrochemical Society* **2013,** *160* (10), A1842-A1846.

60. Tang, K.; Yu, X.; Sun, J.; Li, H.; Huang, X., Kinetic analysis on $LiFePO_4$ thin films by CV, GITT, and EIS. *Electrochimica Acta* **2011,** *56* (13), 4869-4875.

61. Assat, G.; Delacourt, C.; Corte, D. A. D.; Tarascon, J.-M., Editors' Choice—Practical Assessment of Anionic Redox in Li-Rich Layered Oxide Cathodes: A Mixed Blessing for High Energy Li-Ion Batteries. *Journal of The Electrochemical Society* **2016,** *163* (14), A2965-A2976.

62. Zhu, Y.; Gao, T.; Fan, X.; Han, F.; Wang, C., Electrochemical techniques for intercalation electrode materials in rechargeable batteries. *Accounts Chem Res* **2017,** *50* (4), 1022-1031.

63. Kleiner, K.; Strehle, B.; Baker, A. R.; Day, S. J.; Tang, C. C.; Buchberger, I.; Chesneau, F.-F.; Gasteiger, H. A.; Piana, M., Origin of high capacity and poor cycling stability of Li-rich

layered oxides: A long-duration in situ synchrotron powder diffraction study. *Chemistry of Materials* **2018,** *30* (11), 3656-3667.

64. Kim, J. C.; Seo, D.-H.; Chen, H.; Ceder, G., The Effect of Antisite Disorder and Particle Size on Li Intercalation Kinetics in Monoclinic $LiMnBO_3$. *Advanced Energy Materials* **2015,** *5* (8), 1401916.

65. Kim, M.; Kim, M.; Park, H.; Li, H.; Kang, B., Unusual Activation of Cation Disordering by Li/Fe Rearrangement in Triplite $LiFeSO_4F$. *Advanced Energy Materials* **2018,** *8* (22), 1800298.

Chapter 6. Synopsis

In this final chapter, conclusions are drawn from the investigation that has been carried out on LFS, followed by *Claims to Originality* and suggestions to future work that could be further investigated.

6.1 Conclusions

In this thesis, a comprehensive study on how to synthesize LFS with controlled properties by hydrothermal approach and how to optimize the material properties as a Li-ion battery cathode via compositional engineering have been presented. The key findings are summarized below:

1. Time-resolved information on structure, composition and morphology revealed that hydrothermal formation of LFS has progressed through four steps: (1) spontaneous precipitation of hydrolysis products of Fe and Si, (2) phase transformation from metastable intermediates to the more stable phase LFS through dissolution-recrystallization, (3) initial growth of LFS nanoparticles and their assembly to mesocrystals by nearly-oriented attachment, and (4) growth of the outer shell promoted by dissolution of the core to form hollow structure.

2. Based on the formation pathways of LFS, particle size, which is controlled by the kinetics of nucleation and growth, can be effectively tailored by changing the precursor concentrations. Higher concentration yielded higher supersaturation which ultimately led to faster nucleation and hence smaller particles.

3. During hydrothermal synthesis of LFS, the presence of complexing agent EDTA can serve to regulate the activity of Fe ions via complexation and subsequent release, thereby enabling the prevention of iron oxides impurities as well as lattice defects in LFS. EDTA was also found to promote the formation of unique peanut shell-like hollow mesocrystals.

4. Substitution of Fe^{2+} by other divalent cations can be achieved to a certain extent by hydrothermal synthesis at 200^{o}C. Co^{2+} or Mg^{2+} with 6.25% doping concentration was incorporated into LFS lattice. Ni^{2+} or Sr^{2+}, however, was not miscible with LFS under aqueous hydrothermal environment.

5. Substitution of Co in LFS was found to facilitate phase transformation from $Pmn2_1$ to inverse $Pmn2_1$ during electrochemical cycling due to larger number of pre-existing transition

metal/Li antisites compared to un-doped LFS. The presence of Co also induced a full coverage of conductive and uniform protection cathode-electrolyte interphase (CEI) layer composed mainly by LiF, Li_2CO_3 and $Li_xPO_yF_z$ over the active particles. This CEI layer possessed lower interphase resistance that better facilitated charge-transfer compared to that in the undoped-LFS and also helped to prevent corrosion attack of the active material by HF. Thanks to the beneficial CEI layer, Co-doped LFS presented enhanced capacity retention as compared to LFS, namely, 95% versus 80% after 50 cycles.

7. Non-stoichiometric *Pmn*2_1 LFS compounds with up to 8% Fe excess were prepared by hydrothermal synthesis at 200°C. Using the same synthesis method, 13% Li excess could be sustained in the lattice of *Pmn*2_1 LFS.

8. Electrochemical analyses coupled with DFT computational study on stoichiometric and Fe-rich LFS revealed benefits brought by Fe-rich composition engineering. The excess Fe would take Li site thereby creating local Fe–O–Fe configurations that are absent in stoichiometric LFS structure. These bonding configurations result in new electron conducting states which could enhance electronic conductivity. Li vacancies are also created as another result of Fe-excess state. The introduction of $Fe_{Li}^{\bullet} + V_{Li}'$ defect pair enhanced the Li (de)intercalation kinetics resulting in higher capacity to be attained.

6.2 Claims of Originality

1. Crystallization mechanism of LFS particles during hydrothermal synthesis is unveiled for the first time.

2. First time the synthesis of LFS mesocrystals is achieved and explained.

3. EDTA chelating agent is employed for the first time in regulating the formation of unique barrel-like LFS particles with hollow structure.

4. Doping the low-temperature orthorhombic *(Pmn*2_1) LFS with divalent cations by hydrothermal synthesis is experimentally attempted for the first time. The limitation and effect of doping on LFS in *Pmn*2_1 structure rather than *P*2_1/*n* is also presented for the first time.

5. The mechanism of Co doping in enhancing the capacity retention is elucidated for the first time.

6. Fe-rich compositional design is exploited for the first time on LFS. The effect of excess Fe crystal structure, local bonding, electronic structure and Li transport kinetics of *Pmn*2_1 LFS is investigated for the first time.

7. Fe-rich strategy opens a new direction to enhance properties of intercalation compounds for energy storage.

6.3 Future Work

Herein, we obtained 162 mA h g^{-1} at an average voltage of 2.8 V at 45^{o}C, whereas the state-of-the-art value for LFP is at 165 mA h g^{-1} at 3.4 V at room temperature. To this end, deployment of LFS to a competitive Li-ion cathode is a desirable while challenging mission. Its intrinsic low ionic and electronic conductivities must be further improved so that sufficient rate capacities could be delivered. More importantly, it is still unclear if the second Li could be accessed in a reversible mode. Although in the literature the capacity corresponding to even 2 Li extraction has been reported, it is doubtful that the Fe^{4+} or O^{-} state can be achieved below 4.8 V vs. Li/Li^{+} because we must take into consideration the inductive effect caused by the strong covalency between Si and O. Nonetheless, the following suggestions are made for future work on LFS:

1. Post-synthetic treatment to coat LFS with a desired passivation layer may help to improve its chemical stability and redox stability on the interphase towards the common $LiPF_6$-based electrolytes. This layer is ideally a good ionic conductor to facilitate Li transport.

2. It is necessary to search for more suitable electrolytes that have higher oxidation limit, e.g. above 5 V vs. Li/Li^{+}, while will not react with LFS. If these electrolytes would be available, LFS could be charged to 5 V without triggering electrolyte decomposition. In this case, the viability of utilizing 2 Li/f.u. might be confirmed.

3. Non-stoichiometric LFS with higher Fe-rich content could be attempted by high-temperature synthesis approach. Thus, higher capacity based on only Fe^{2+}/Fe^{3+} redox couple can be achieved, for example, 203 mA h g^{-1} for 33.3% Fe-rich.

Appendix A for Chapter 3: Supporting Information for Hydrothermal Crystallization of *Pmn*2$_1$ Li_2FeSiO_4 Hollow Mesocrystals for Li-ion Cathode Application

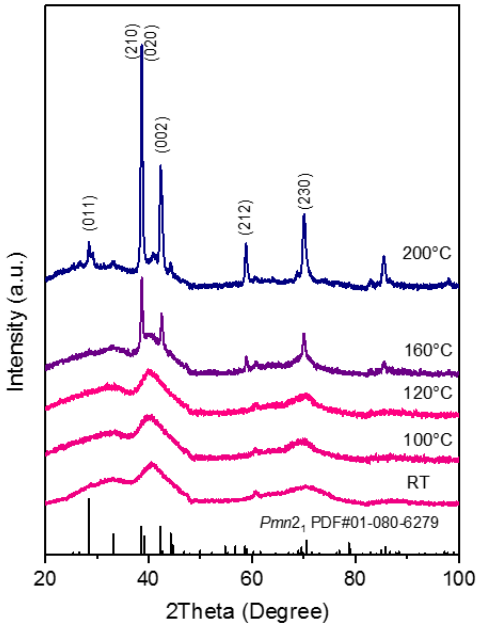

Figure A1. Laboratory XRD (Cobalt Kα radiation, λ = 1.788892 Å) patterns of powders obtained in hydrothermal synthesis of Li_2FeSiO_4 during heat-up from 25 to 200°C. Bragg peak positions of *Pmn*2$_1$ Li_2FeSiO_4.

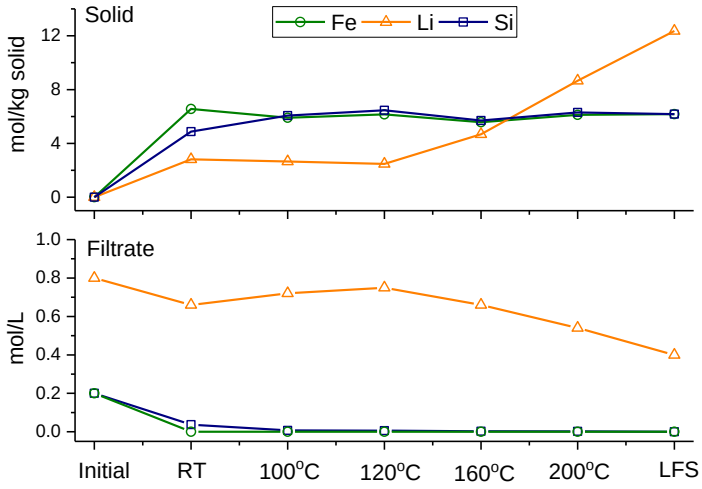

Figure A2. ICP elemental analysis results of LFS and the intermediates from hydrothermal synthesis.

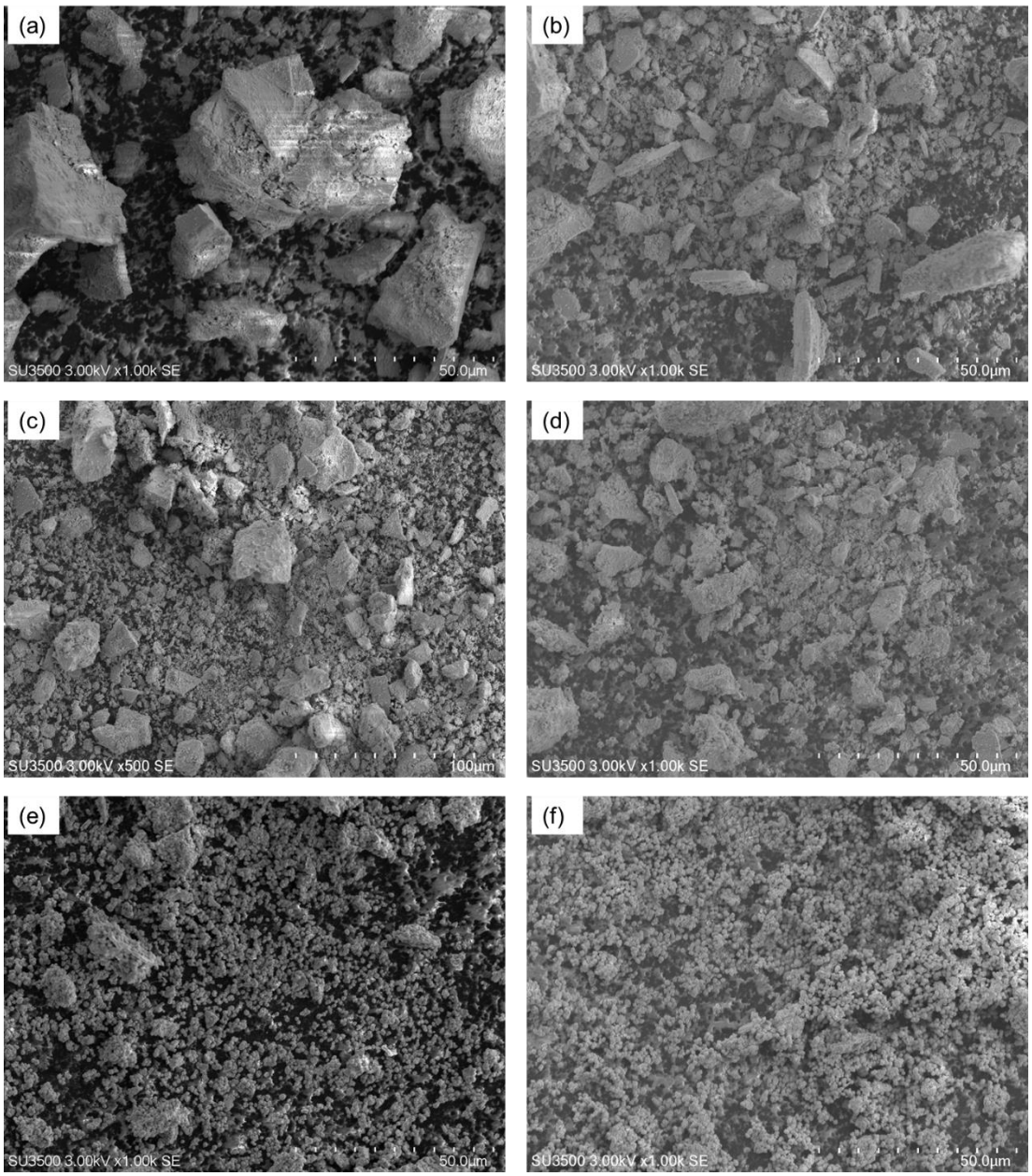

Figure A3. SEM images of hydrothermal intermediates precipitated during heat-up period. (a) LFSRT (precursor mixtures); (b) LFS100C (heat-up for 20 min); (c) LFS120C (heat-up for 30 min); (d) LFS160C (heat-up for 40 min); (e) LFS200C (heat-up for 50 min); and (f) LFS200C1H (hold at 200^{o}C for 1 hour).

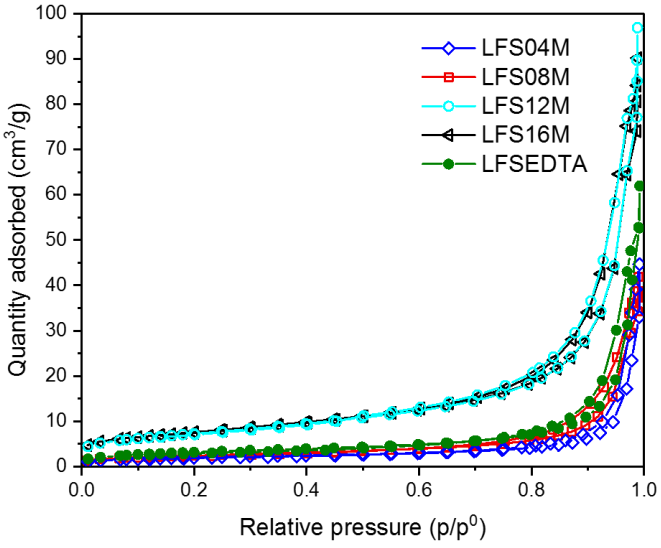

Figure A4. Nitrogen adsorption-desorption isotherms of LFS prepared at different concentrations.

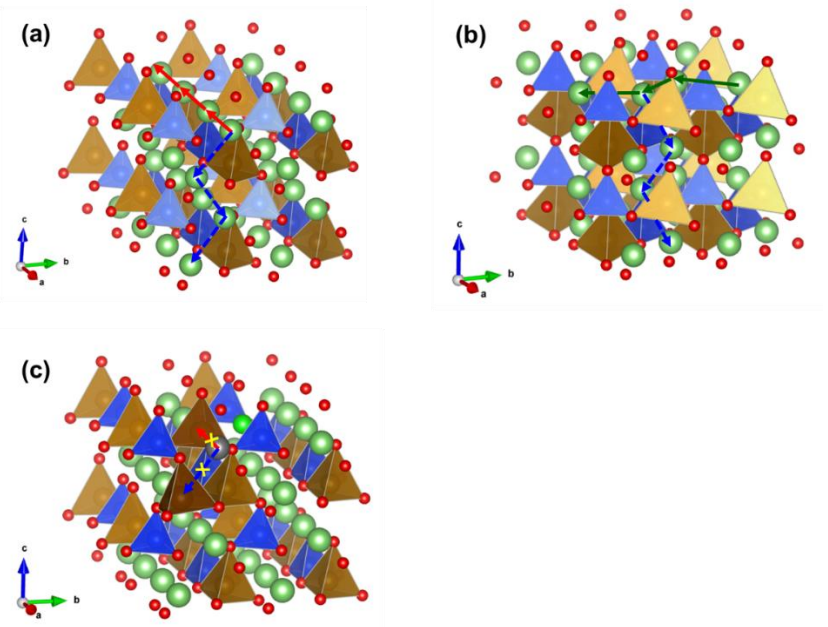

Figure A5. Li-ions transport pathways in different atomic configurations based on *Pmn*2_1 structure. (a) In the ideal *Pmn*2_1, where there is no antisite defects, Li-ions migrate along a straight *a*-direction (red arrows) or a zig-zag *c*-direction (blue arrows). (b) In the inverse *Pmn*2_1 (electrochemically cycled structure), where all the Fe-ions exchange site with half of the 2Li-ions, Li-ions migrate along a zig-zag *c*-direction (blue arrows) or a zig-zag *b*-direction (green arrows). (c) Local Fe/Li antisite leads to a blocked Li-ion (grey). Crystal structures were draw by VESTA software.

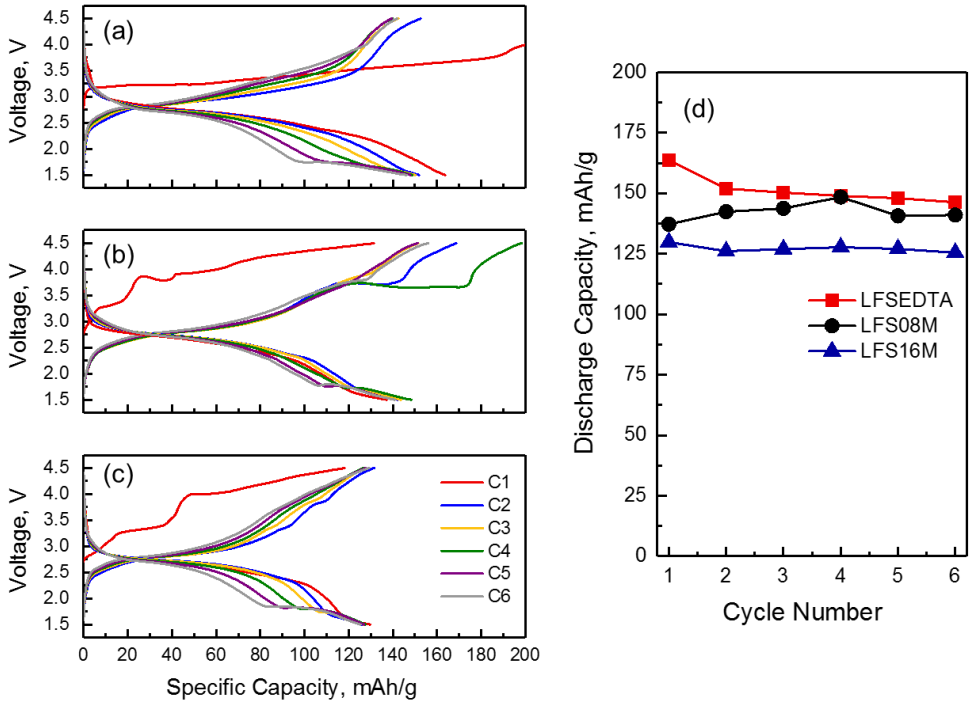

Figure A6. Galvanostatic charge and discharge curves of (a) LFSEDTA; (b) LFS08M; and (c) LFS16M at C/50 rate in the voltage range of 1.5 to 4.5 V at 55ºC. (d) Discharge capacity retention over the course of the first 6 cycles.

Table A1. Refined atomic fractional coordinates and site occupancies of LFSEDTA

Atom	Wyckoff	*x/a*	*y/b*	*z/c*	Occupancy
Li1/Fe2	4b	0.7623(17)	0.3370(12)	1.004(3)	0.9641(10)/0.0359(10)
Fe1/Li2	2a	0.00000	0.1705(3)	0.4837(7)	0.885(4)/ 0.115(4)
Si1	2a	0.00000	0.8270(6)	0.964(4)	1
O1	4b	0.7907(7)	0.7062(5)	1.0240(17)	1
O2	2a	0.00000	0.7966(17)	0.3537(11)	1
O3	2a	0.00000	0.1143(17)	0.8521(11)	1
R_{wp} = 3.821%, a = 6.26451(16) Å, b = 5.34467(15) Å, c = 4.96216(8) Å, V = 166.142(7) Å^3					

Table A2. Li/Fe antisite concentrations analysed by Rietveld refinement of synchrotron XRD data and iron valence states determined by ^{57}Fe Mössbauer spectroscopy

Product	Synchrotron XRD		Mössbauer	
	Fe on Li1, %	Li on Fe1, %	Fe^{2+}, %	Fe^{3+}, %
LFSEDTA	3.59(10)	11.5(4)	92.29	7.71
LFS08M	10.1(7)	22.8(16)	70.08	29.92
LFS16M	8.9(4)	30.3(6)	62.47	37.53

Table A3. Selected parameters from analysis of Mössbauer spectra

Product	Fe^{2+}			Fe^{3+}		
	IS, mm/s	QS, mm/s	*I*, at.%	IS, mm/s	QS, mm/s	*I*, at.%
LFSEDTA	0.991(1)	2.693(3)	92.29	0.28(2)	0.85(5)	7.71
LFS08M	0.986(3)	2.33(1)	70.08	0.330(8)	0.69(1)	29.92
LFS16M	0.959(3)	2.37(1)	63.47	0.307(6)	0.81(1)	37.53

Appendix B for Chapter 4: Unveiling the Mechanism of Improved Capacity Retention in *Pmn*2$_1$ Li_2FeSiO_4 Cathode by Cobalt Substitution

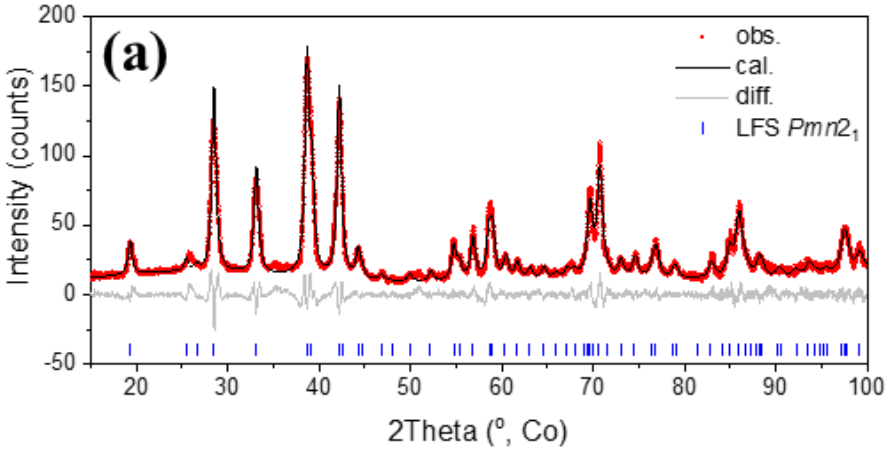

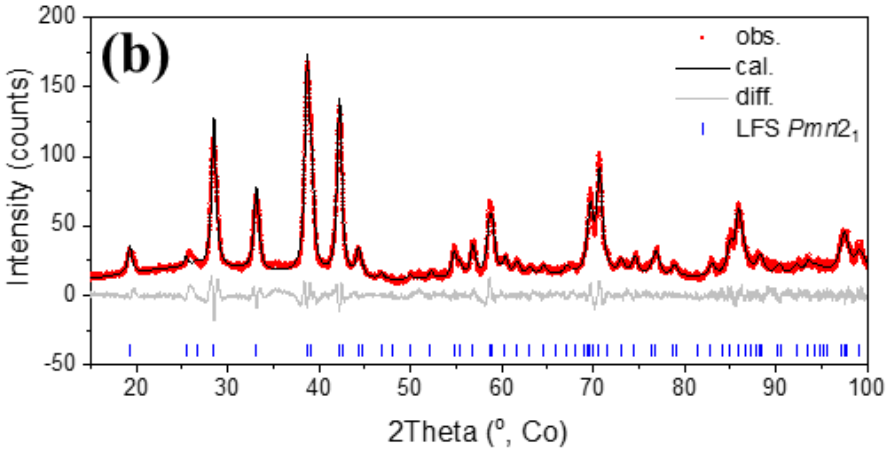

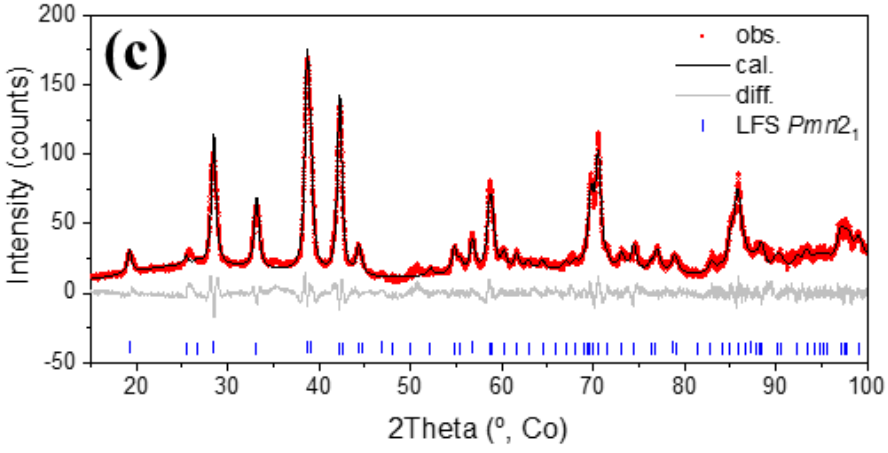

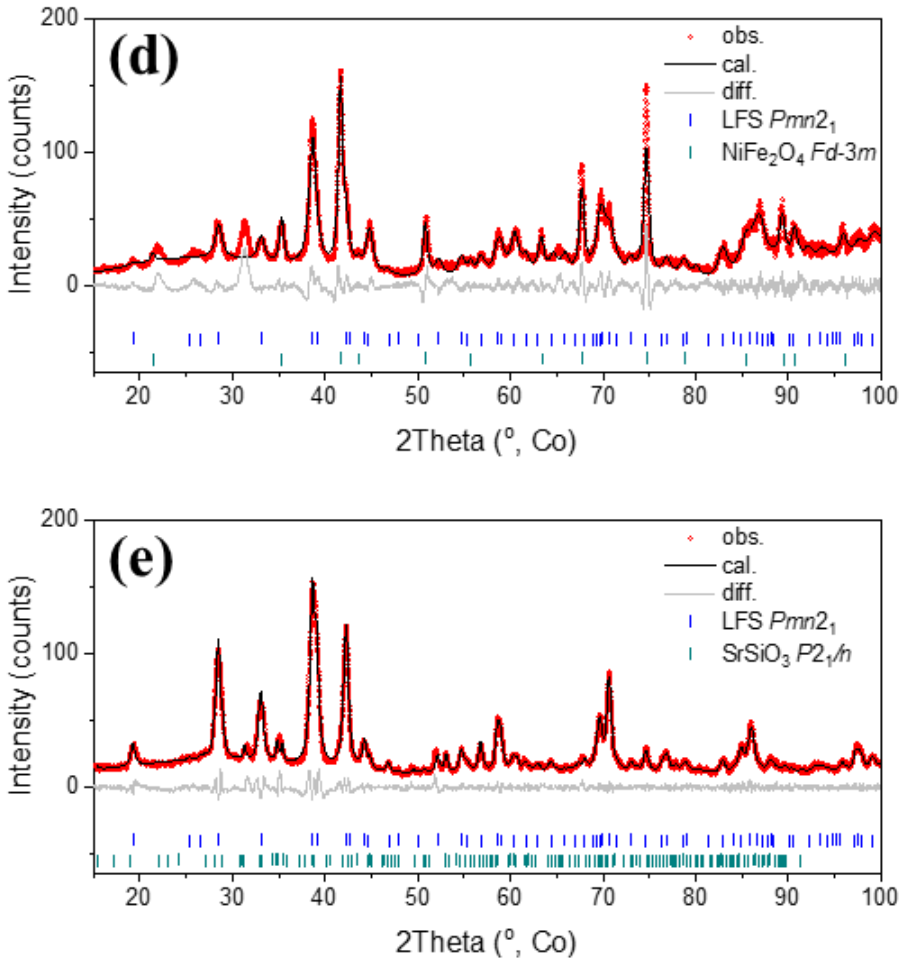

Figure B1. Le Bail refinement of powder X-ray diffractograms (Co-Kα radiation, γ = 1.7889 Å) of Mg, Co, Ni, or Sr-involved Li_2FeSiO_4 (LFS) samples obtained by hydrothermal synthesis at 200°C. (a) Undoped LFS with determined lattice parameters of a = 6.26873(21) Å, b = 5.33468(18) Å, c = 4.96970(18) Å, and V = 166.195(10) Å^3. (b) Mg-LFS with determined lattice parameters of a = 6.26586(23) Å, b = 5.33860(18) Å, c = 4.96815(18) Å, and V = 166.189(10) Å^3. (c) Co-LFS with determined lattice parameters of a = 6.25996(25) Å, b = 5.35188(19) Å, c = 4.96503(18) Å, and V = 166.341(11) Å^3. (d) Ni-LFS with determined lattice parameters of a = 6.27334(51) Å, b = 5.33224(42) Å, c = 4.97195(63) Å, and V = 166.316(28) Å^3. (e) Sr-LFS with determined lattice parameters of a = 6.27659(33) Å, b = 5.35413(27) Å, c = 4.96347(19) Å, and V = 166.801(14) Å^3. Note that LFS, Mg-LFS, and Co-LFS were refined with a single phase of Li_2FeSiO_4 in orthorhombic S.G. $Pmn2_1$ (01-080-3671), whereas Ni-LFS was refined with $Pmn2_1$ Li_2FeSiO_4 and $NiFe_2O_4$ in cubic Fd-3m (04-014-8286), and Sr-LFS was refined with $Pmn2_1$ Li_2FeSiO_4 and $SrSiO_3$ in monoclinic S.G. $P2_1/n$ (04-011-6968). The reported lattice parameters are for $Pmn2_1$ Li_2FeSiO_4 only. The refinement was performed using Academic TOPAS v.5.0 software.

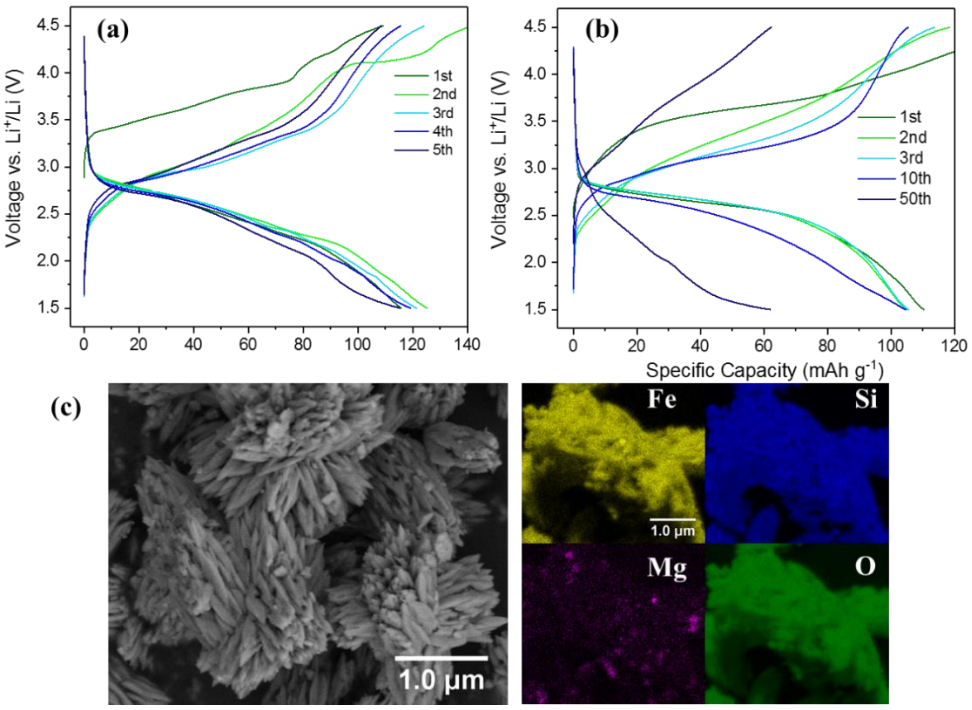

Figure B2. Galvanostatic charge-discharge curves of MgLFS at (a) C/30 and (b) C/10 between 1.5-4.5 V at 45ºC. (c) SEM and EDS mapping of MgLFS.

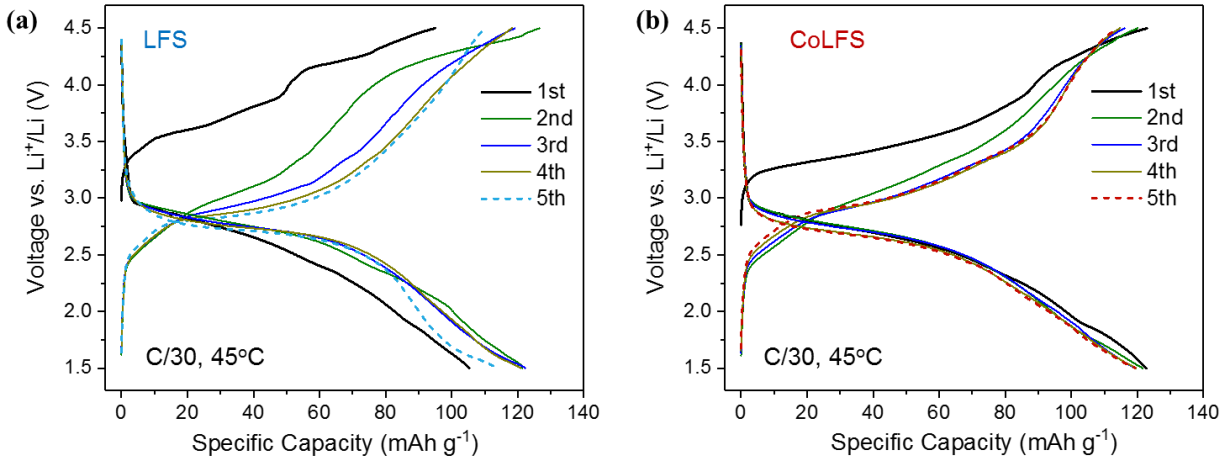

Figure B3. Galvanostatic charge-discharge curves of (a) LFS and (b) CoLFS at C/30 between 1.5-4.5 V at 45ºC.

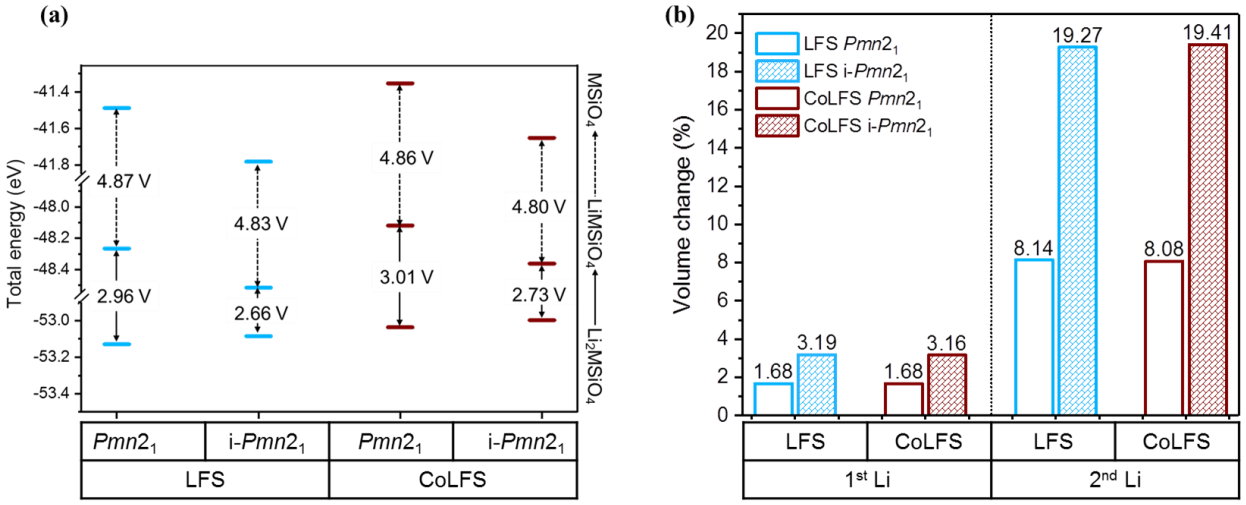

Figure B4. (a) Calculated total energies (eV/f.u.) of Li_2FeSiO_4 and $Li_2Fe_{0.94}Co_{0.06}SiO_4$ in *Pmn*2_1 and inverse-*Pmn*2_1 phases. (b) Calculated volume change (%) upon delithiation of $Li_yFe_{1-x}Co_xSiO_4$, where y = 0, 1, or 2, x is the doping concentration of Co. Solid and open symbols represent *Pmn*2_1 and inverse-*Pmn*2_1 phases, respectively. It should be mentioned here that extraction of the second Li-ion will only occur at voltages above 4.8 V vs. Li^+/Li. The removal of the second Li, although has not been achieved in the present study, was found to exhibit pronounced volume change of over 19% after full delithiation to $FeSiO_4$ in inverse-*Pmn*2_1 structure. Structural arrangement and thereby profound volume change during charging-discharging will be one of the major obstacles to extract the second Li from Li_2FeSiO_4. The strain caused by large volume change during electrochemical cycling would result in the failure of the cell. As the focus of the present work is to extract only the first Li, the volume change would not be an issue.

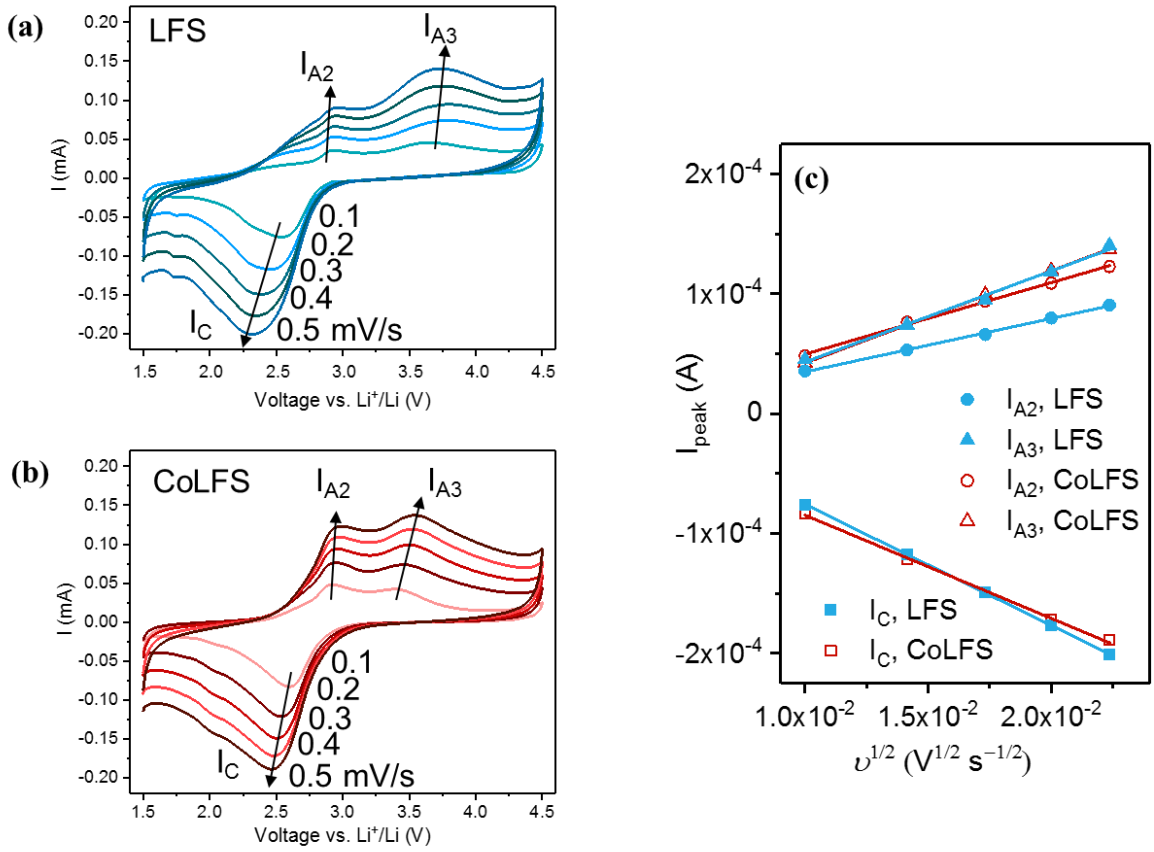

Figure B5. Cyclic voltammograms of (a) LFS and (b) CoLFS scanned at different rates from 0.1 mV s^{-1} to 0.5 mV s^{-1}. I_{A2}, I_{A4}, and I_C represent two anodic peaks and one cathodic peak, respectively. (c) Fitting of the peak currents vs. the square root of scan rate.

Note to Figure B5:

Figures B5a and B5b show the variation of CV at various scan rates from 0.1 to 0.5 mV s^{-1}. Faster scan rate leads to a faster mass transport of Li^+ and hence higher current can be obtained. Two anodic peaks and one cathodic peak can be observed despite the scan rate. The peak current, i.e., I_C, I_{A2}, or I_{A3}, is proportional to the square root of the scan rate $\upsilon^{1/2}$. The linear fitting results are shown in Figure B5c. Based on the Randles-Sevčik equation (eq B1) shown below, the chemical diffusion coefficient of Li^+ can be estimated from the slope of the linear lines.[B1-B2]

$$I_p = 0.4463\left(\frac{F^3}{RT}\right)^{1/2} n^{3/2} A D_{Li^+}^{1/2} C_{Li^+}^{*} \upsilon^{1/2} \quad \text{(B1)}$$

where I_p is the peak current in A, F is the faraday's constant of 96,485 C mol^{-1}, R is the gas constant od 8.314 J K^{-1} mol^{-1}), T is the temperature in Kevin, n is the number of electrons involved in the redox reaction, A is he surface area of the electrode in cm^2, D_{Li^+} is the chemical diffusion coefficient of Li^+ in cm^2 s^{-1}, $C^*_{Li^+}$ is the initial concentration of Li^+ in the bulk material in mol cm^{-3}, υ is the scan rate in V s^{-1}. A is 0.785 cm^2. $C^*_{Li^+}$ is approximately 0.0386 mol cm^{-3} for the anodic reaction and 0.0201 mol cm^{-3} for the cathodic reaction. The calculated results of D_{Li^+} are listed in Table B4. As it can be seen, diffusion coefficient D_{Li^+} of I_C (lithiation) is larger than that of I_A (delithiation) for both LFS and CoLFS, while CoLFS has larger D_{Li^+} of I_A than LFS.

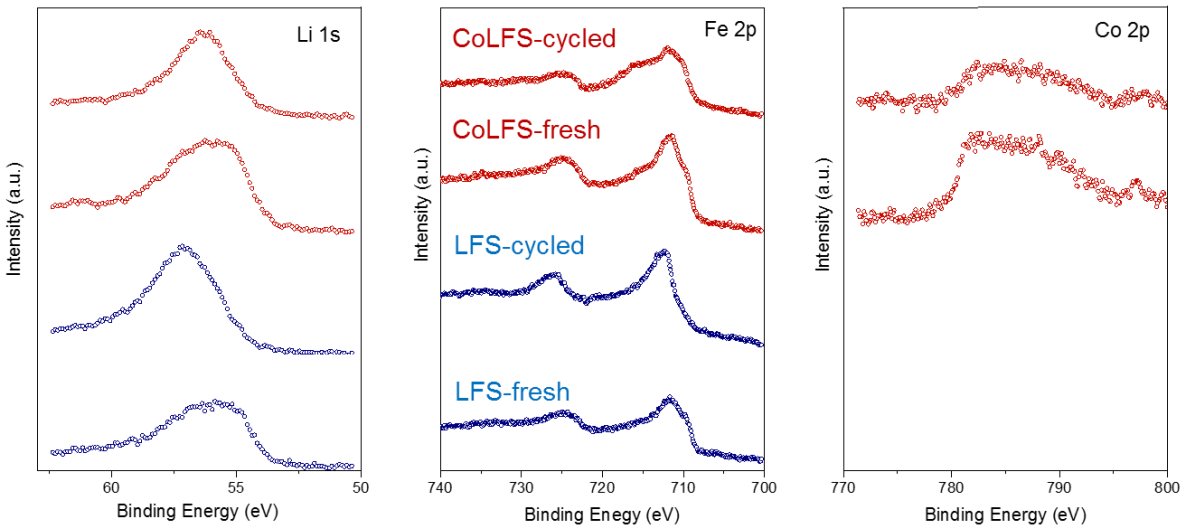

Figure B6. XPS spectra of Li 1s, Fe 2p, and Co 2p from the pristine and cycled electrodes of LFS and CoLFS (from bottom to top).

Table B1. Calculated total energies (eV/f.u.) of $Li_2Fe_{0.94}M_{0.06}SiO_4$ (M = Fe, Mg, Co, Ni, Sr, Ti, and Zr) in *Pmn*2_1 and inverse-*Pmn*2_1 phases

Compound	Total energy in $Pmn2_1$ (eV/f.u.)	Total energy in inverse-$Pmn2_1$ (eV/f.u.)
Li_2FeSiO_4	-53.13	-53.09
$Li_2Fe_{0.94}Mg_{0.06}SiO_4$	-53.03	-52.99
$Li_2Fe_{0.94}Co_{0.06}SiO_4$	-53.04	-53.00
$Li_2Fe_{0.94}Ni_{0.06}SiO_4$	-52.86	-52.77
$Li_2Fe_{0.94}Sr_{0.06}SiO_4$	-53.02	-52.96
$Li_2Fe_{0.94}Ti_{0.06}SiO_4$	-53.28	-53.24
$Li_2Fe_{0.94}Zr_{0.06}SiO_4$	-53.29	-53.25

Table B2. Calculated energies above the hull (meV/atom) and potential decomposition phases

Compound	Energy above the hull (meV/atom)	Decomposition phases
$Li_2Fe_{0.94}Mg_{0.06}SiO_4$	8.73	Li_2FeSiO_4, Li_2MgSiO_4
$Li_2Fe_{0.94}Mn_{0.06}SiO_4$	8.35	Li_2FeSiO_4, Li_2MnSiO_4
$Li_2Fe_{0.94}Co_{0.06}SiO_4$	8.65	Li_2FeSiO_4, Li_2CoSiO_4
$Li_2Fe_{0.94}Ni_{0.06}SiO_4$	12.10	Li_2FeSiO_4, Li_2SiO_3, NiO
$Li_2Fe_{0.94}Sr_{0.06}SiO_4$	14.57	Li_2FeSiO_4, Li_2SrSiO_4
$Li_2Fe_{0.94}Ti_{0.06}SiO_4$	33.03	Li_2FeSiO_4, Li_2SiO_3, Li_2TiSiO_5, Fe
$Li_2Fe_{0.94}Zr_{0.06}SiO_4$	583.19	Li_2FeSiO_4, Li_2SiO_3, ZrO_2, Fe

Table B3. Calculated cell voltage of Li_2FeSiO_4 and $Li_2Fe_{0.94}Co_{0.06}SiO_4$. The absolute values of cell voltage calculated in this work are 0.1-0.3 V lower than those reported in the literature, which can be attributed to different effective Hubbard *U* and total energy of Li metal used in the calculations

Compound	Phase	Cell voltage *V* (V vs. Li^+/Li)	ref.
	$Li_2Fe_{1-x}Co_xSiO_4 \rightarrow LiFe_{1-x}Co_xSiO_4$		
Li_2FeSiO_4	*Pmn*2_1	2.96	**this work**
		3.10	Soe *et al.*[B3]
		3.34	Eames *et al.*[B4]
	inverse-*Pmn*2_1	2.66	**this work**
		2.82	Soe *et al.* [B3]
		2.83	Saracibar *et al.* [B5]
		3.04	Eames *et al.* [B4]
$Li_2Fe_{0.94}Co_{0.06}SiO_4$	*Pmn*2_1	3.01	**this work**
	inverse-*Pmn*2_1	2.73	**this work**
	$LiFe_{1-x}Co_xSiO_4 \rightarrow Fe_{1-x}Co_xSiO_4$		
$LiFeSiO_4$	*Pmn*2_1	4.87	**this work**
		4.86	Saracibar *et al.* [B5]
	inverse-*Pmn*2_1	4.83	**this work**
		4.80	Soe *et al.* [B3]
		4.82	Saracibar *et al.* [B5]
$Li_2Fe_{0.94}Co_{0.06}SiO_4$	*Pmn*2_1	4.86	**this work**
	inverse-*Pmn*2_1	4.80	**this work**

Table B4. Chemical diffusion coefficient D_{Li^+} of LFS and CoLFS calculated from cyclic voltammetry measurements

Electrode	Peak	Slope of I_p vs. $\upsilon^{1/2}$	D_{Li^+}, cm^2/s
Li_2FeSiO_4	I_C	0.0101	6.07×10^{-12}
(LFS)	I_{A2}	0.0045	3.20×10^{-13}
	I_{A3}	0.0076	9.30×10^{-13}
$Li_2Fe_{0.94}Co_{0.06}SiO_4$	I_C	0.0086	4.41×10^{-12}
(CoLFS)	I_{A2}	0.0060	5.74×10^{-13}
	I_{A3}	0.0077	9.55×10^{-13}

Table B5. Binding energies (eV) and atomic percentages (%) of C, O, F, P, and Si from XPS spectra of the pristine and cycled electrodes of LFS and CoLFS

	binding energy, eV	LFS-p, eV	%	LFS-c, eV	%	CoLFS-p, eV	%	CoLFS-c, eV	%
C 1s			53.7		39.7		50.9		32.3
C-C	284.8	284.8	16.4	284.8	10.4	284.8	17.2	284.8	9.9
CH_2	~286	286.1	27.1	286.1	17.4	285.9	25.2	286.7	19.1
O-C=O	~288.5	289.2	2.2	287.6	5.9	289.2	2.1	289.7	0.1
CF_2	~292	291.1	8.0	290.9	5.0	291.1	6.4	291.0	3.2
O 1s			25.7		32.2		29		33.6
Li-O, Fe-O, Co-O	529-530	531.2	15.7	531.6	15.6	531.2	17.5	531.4	7.9
C-O, CO_3, SiO_4	531.5-532	532.6	10.0	532.7	11.3	532.7	11.5	532.6	18.9
P-O	534			534.1	5.3			534.0	6.8
F 1s			14.8		19.2		12.9		24
LiF	684-685.5	685.3	1.4	685.5	7.2	685.4	1.2	685.5	13.6
CF_2, $Li_xPO_yF_z$	688.8-689	688.2	13.4	687.9	12.0	688.2	11.7	688.1	10.4
P 2p									
$Li_xPO_yF_z$	135		0	135.1	3.6		0	135.3	5.9
Si 2p									
SiO_4, Si-F	101.6-103.8	102.2	5.9	102.6	5.5	102.3	7.3	102.9	4.2

Note to Figure 4.5:

CV deconvolution (Figures 4.5c and 4.5d) was performed with the pre-assumptions:

1. The I-V response follows the behaviours of thin-layer cyclic voltammetry where the bell-shaped (gaussian) curve applies. This is supported by the architecture of electroactive LFS as it is confined in the tens-of-micrometer space between the separator and Al current collector.

2. The redox reactions are exclusively from ferrous/ferric couple existing in LFS crystals.

3. Peak position reflects the coordination environment around Fe atoms in the crystal structure. Thus, different structure leads to different peak positions as reported by Sirisopanaporn et al.[B6]

4. LFS crystals are connected in parallel in the electrode.

In this context, each peak in cyclic voltammograms corresponds to a particular Li-ion intercalation process of the corresponding intermediate phase of LFS; the integrated intensity of the peak is related to the concentration of the electroactive ferrous/ferric couples in LFS. Hence, the newly formed intermediate LFS can be estimated through the peak area. It is worth mentioning that there exist almost infinite combinations of the peak selection, just like the equivalent circuit model for EIS. Therefore, only the most outstanding four peaks were selected for the peak deconvolution.

References B

B1. Elgrishi, N.; Rountree, K. J.; McCarthy, B. D.; Rountree, E. S.; Eisenhart, T. T.; Dempsey, J. L., A practical beginner's guide to cyclic voltammetry. *Journal of Chemical Education* **2018,** *95* (2), 197-206.

B2. Zhu, Y.; Gao, T.; Fan, X.; Han, F.; Wang, C., Electrochemical techniques for intercalation electrode materials in rechargeable batteries. *Accounts Chem Res* **2017,** *50* (4), 1022-1031.

B3. Seo, D.-H.; Kim, H.; Park, I.; Hong, J.; Kang, K., Polymorphism and phase transformations of $Li_{2-x}FeSiO_4$ ($0 \leq x \leq 2$) from first principles. *Physical Review B* **2011,** *84* (22), 220106.

B4. Eames, C.; Armstrong, A. R.; Bruce, P. G.; Islam, M. S., Insights into changes in voltage and structure of Li_2FeSiO_4 polymorphs for lithium-ion batteries. *Chemistry of Materials* **2012,** *24* (11), 2155-2161.

B5. Saracibar, A.; Van der Ven, A.; Arroyo-de Dompablo, M. E., Crystal structure, energetics, and electrochemistry of Li_2FeSiO_4 polymorphs from first principles calculations. *Chemistry of Materials* **2012,** *24* (3), 495-503.

B6. Sirisopanaporn, C.; Masquelier, C.; Bruce, P. G.; Armstrong, A. R.; Dominko, R., Dependence of Li_2FeSiO_4 electrochemistry on structure. *Journal of the American Chemical Society* **2011,** *133* (5), 1263-1265.

Appendix C for Chapter 5: Supporting Information for Defect Engineering of Fe-Rich Orthosilicate Cathode Materials with Enhanced Li-Ion Intercalation Capacity and Kinetics

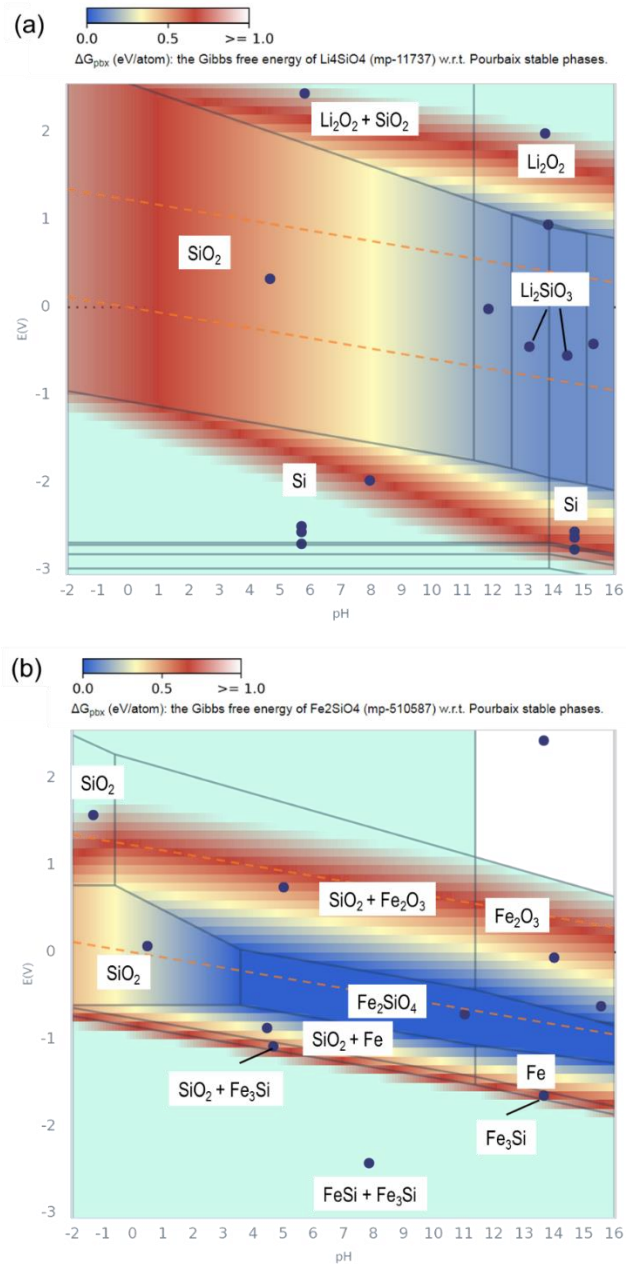

Figure C1. Calculated Pourbaix diagrams constructed via the Materials Project.[C1] Colors varying from blue to red represents a compound changing from stable to the most unstable. Only the stable solid phases are labeled. (a) Stability map of Li_4SiO_4 at concentrations of Li = 1M, Si = 0.1M. Li_4SiO_4 is unstable relative to Li_2SiO_3 in alkaline solution. (b) Stability map of Fe_2SiO_4 at concentrations of Fe = 1M, Si = 0.1M. Fe_2SiO_4 is unstable relative to Fe_2O_3 in alkaline and slight oxidative solution.

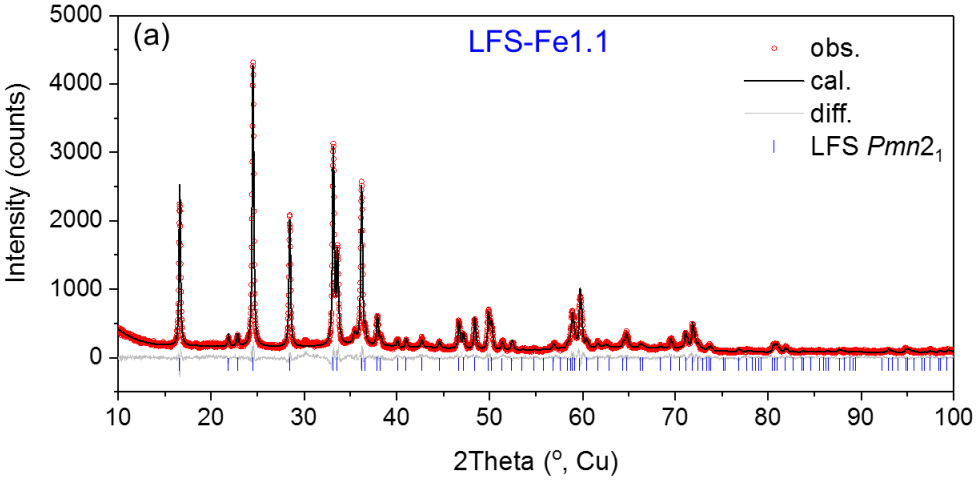
(a)
LFS-Fe1.1
obs.
cal.
diff.
LFS Pmn2$_1$
Intensity (counts)
2Theta (°, Cu)

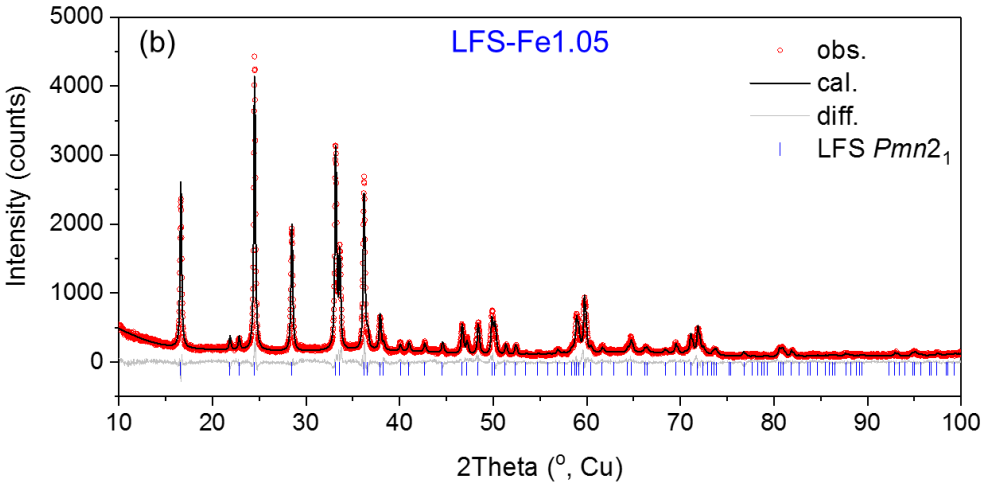
(b)
LFS-Fe1.05
obs.
cal.
diff.
LFS Pmn2$_1$
Intensity (counts)
2Theta (°, Cu)

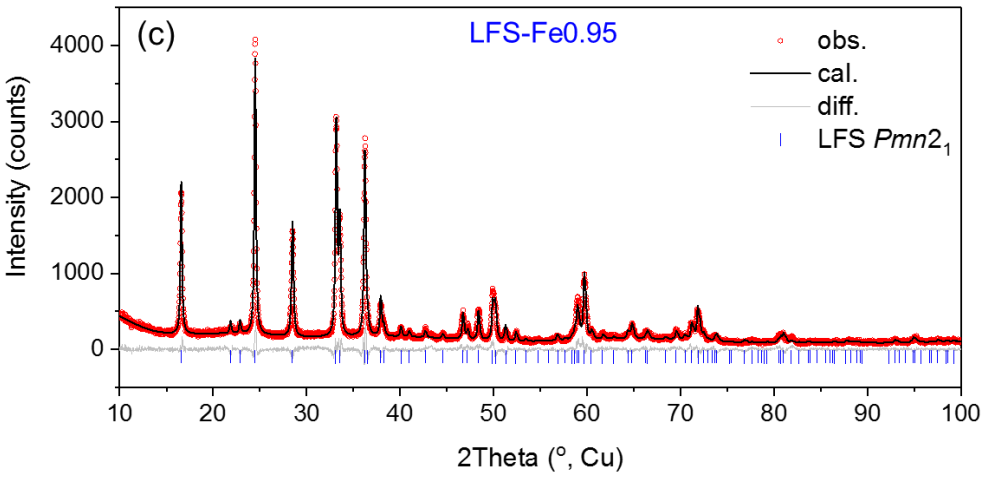
(c)
LFS-Fe0.95
obs.
cal.
diff.
LFS Pmn2$_1$
Intensity (counts)
2Theta (°, Cu)

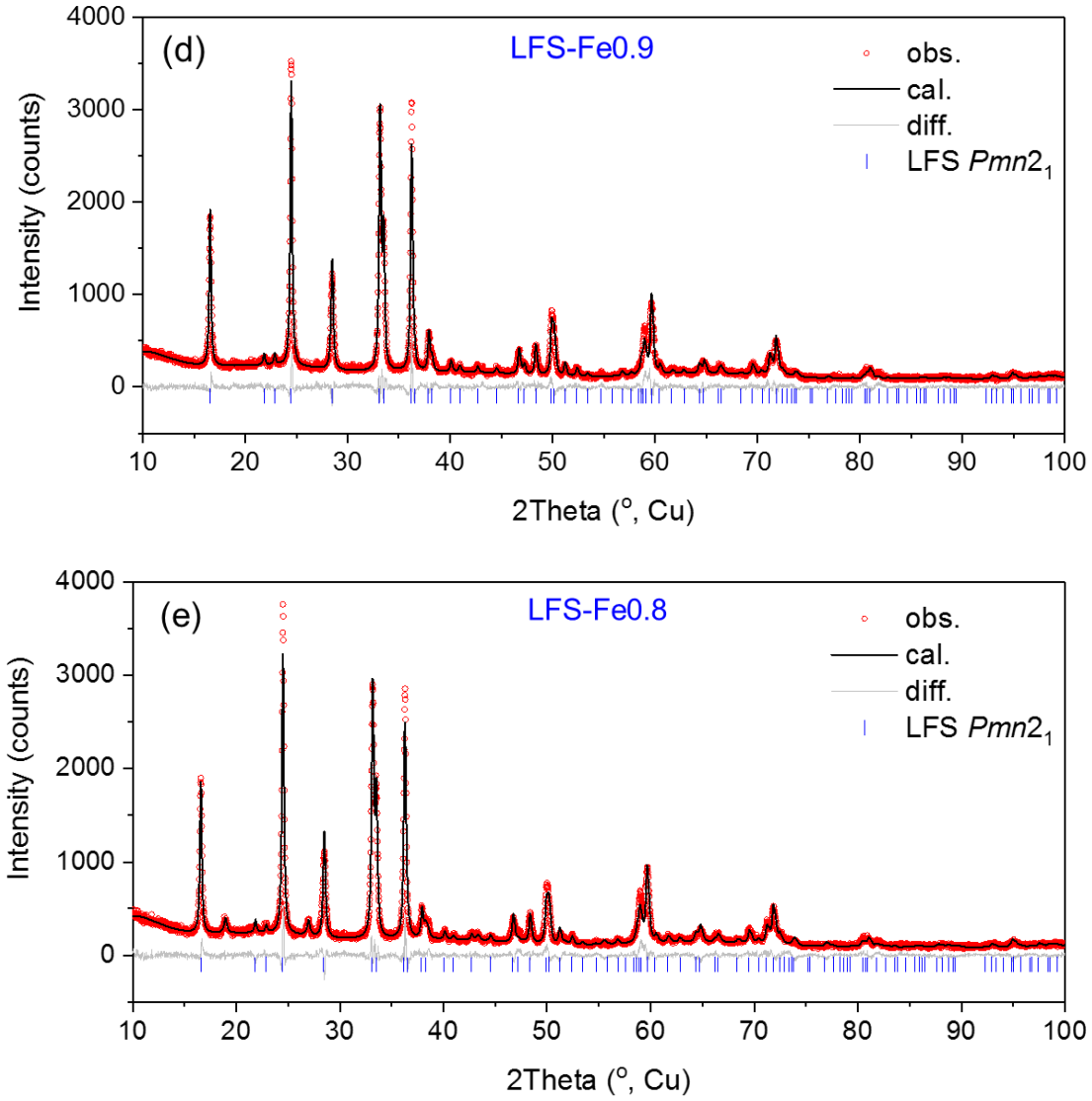

Figure C2. Rietveld refinement of powder X-ray diffractograms (Cu-Kα radiation, γ = 1.5418 Å) of non-stoichiometric $Li_{4-2x}Fe_xSiO_4$. (a) LFS-Fe1.1 with determined lattice parameters of a = 6.26927(16) Å, b = 5.33610(15) Å, c = 4.96236(14) Å, and V = 166.008(8) Å^3. (b) LFS-Fe1.05 with determined lattice parameters of a = 6.26722(17) Å, b = 5.33614(16) Å, c = 4.96375(15) Å, and V = 166.002(8) Å^3. (c) LFS-Fe0.95 with determined lattice parameters of a = 6.26224(19) Å, b = 5.34464(16) Å, c = 4.95910(15) Å, and V = 165.978(9) Å^3. (d) LFS-Fe0.9 with determined lattice parameters of a = 6.2599(2) Å, b = 5.34830(18) Å, c = 4.95608(15) Å, and V = 165.929(10) Å^3. (e) LFS-Fe0.8 with determined lattice parameters of a = 6.2605(3) Å, b = 5.3470(2) Å, c = 4.95091(19) Å, and V = 165.733(11) Å^3.

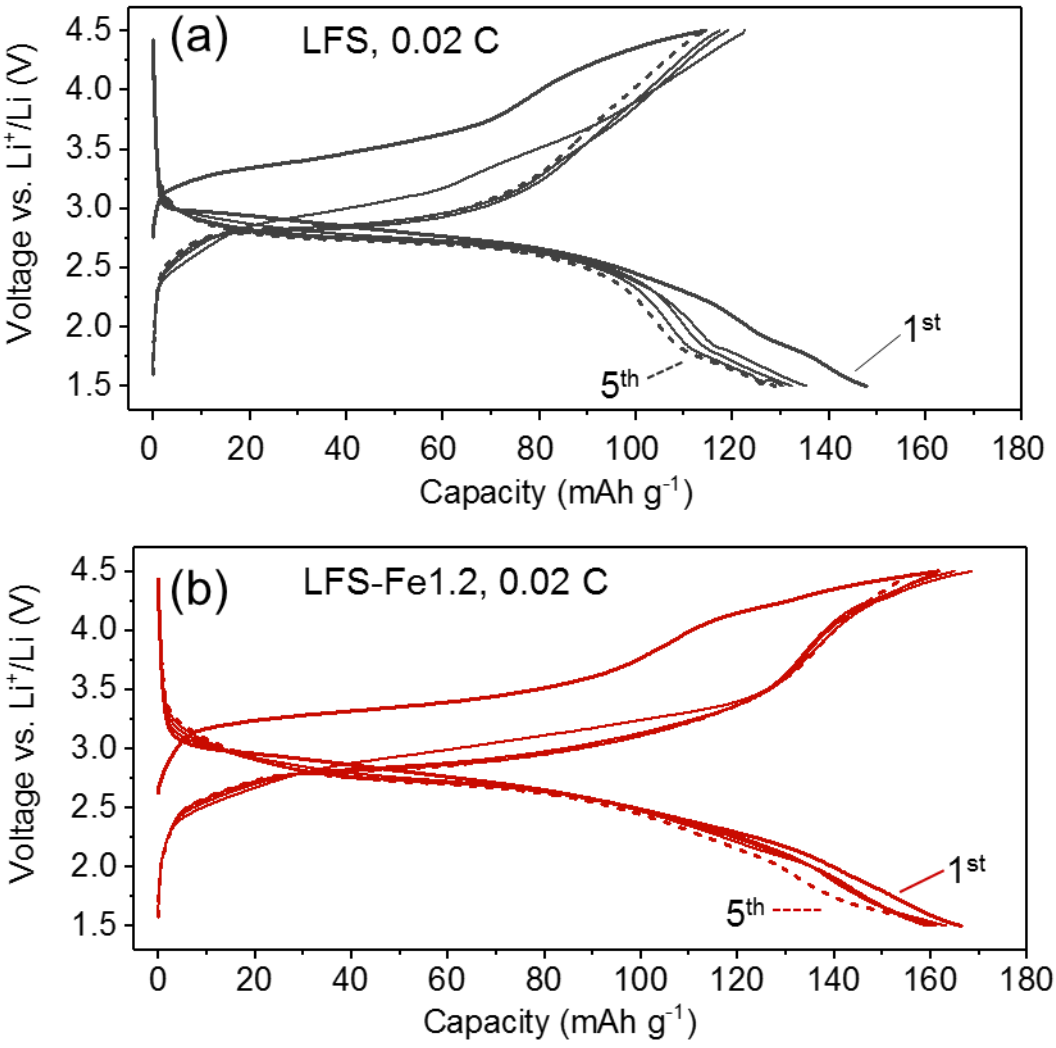

Figure C3. Galvanostatic charge-discharge profiles of (a) LFS-stoi and (b) LFS-Fe1.2 from the 1st to 5th cycles at 0.02 C between 1.5 – 4.5 V at 45ºC.

Reference C

C1. A. Jain, S. P. Ong, G. Hautier, W. Chen, W. D. Richards, S. Dacek, S. Cholia, D. Gunter, D. Skinner, G. Ceder, K. A. Persson, *APL Materials* **2013**, 1, 011002.